

**Best  
Available  
Copy**

AD-770 546

ELECTRICAL AND OPTICAL PROPERTIES  
OF AMORPHOUS MATERIALS

Charles Wood

Northern Illinois University

Prepared for:

Army Research Office-Durham  
Advanced Research Projects Agency

1973

DISTRIBUTED BY:

**NTIS**

National Technical Information Service  
U. S. DEPARTMENT OF COMMERCE  
5285 Port Royal Road, Springfield Va. 22151

AD 770546

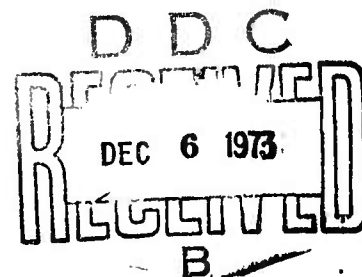
SIXTH AND FINAL SEMI-ANNUAL TECHNICAL REPORT

ELECTRICAL AND OPTICAL PROPERTIES OF AMORPHOUS MATERIALS\*

by

A Solid-State Group of the Physics Department  
Northern Illinois University  
DeKalb, Illinois 60115

\*Sponsored by  
Advanced Research Projects Agency  
ARPA Order No. 1562



The views and conclusions contained in this document are those of the authors and should not be interpreted as necessarily representing the official policies, either expressed or implied, of the Advanced Research Projects Agency or the U.S. Government.

"Approved for public release; distribution unlimited."

Reproduced by  
NATIONAL TECHNICAL  
INFORMATION SERVICE  
U S Department of Commerce  
Springfield VA 22151

269

GENERAL INFORMATION

ARPA Order Number	1562
Program Code Number	0D10
Name of Contractor	U.S. Army Research Office
Contracts	DA-ARO-D-31-124-70-G77 June 1, 1970 through June 29, 1971 \$57,820.00  DA-ARO-D-31-124-71-G132 June 30, 1971 through June 27, 1972 \$58,000.00  DA-ARO-D-31-124-72-G115 June 28, 1972 through September 27, 1973 \$39,000.00
Principal Investigator	Dr. Charles Wood (81S) 753-1773



## CONTENTS

ANALYSIS AND INTERPRETATION OF OPTICAL DATA	1
I.    Introduction	1
II.   Computational Developments	1
III.  Interpretation of Optical Data	2
IV.   Photoemission	3
V.    Photoconductivity	4
MATERIALS PREPARATION	5
TRANSPORT PROPERTIES	6
I.    Electrical Conductivity	6
II.   Thermo-emf Measurements	7
STRUCTURE	7
I.    Mössbauer Studies	7
II.   X-ray and Electron Diffraction Studies	8
FISCAL STATUS	10
PUBLICATIONS	11
APPENDICES	

## ANALYSIS AND INTERPRETATION OF OPTICAL DATA

### I. Introduction

During the period of this research grant considerable attention was focused upon the development of techniques for the analysis of optical data measured upon amorphous and related crystalline materials. In addition there was an effort to interpret the optical response of these systems in terms of their electronic states, chemical bonding, and possible microscopic structure. In what follows the results of this work are briefly described with references to the relevant publications included. In these publications, copies of which are attached to this report, can be found the details of methods and results.

### II. Computational Developments

The need to obtain the spectral distribution of the complex dielectric function provided strong motivation to develop a reliable computational method for Kramers-Kronig analysis. Thus a new technique for carrying out numerical Hilbert (Kramers-Kronig) transforms employing accurate expansion in Hermite functions evolved (A). In performing the Kramers-Kronig analysis of normal incidence reflectivity data a convenient method for extrapolating the data to high frequencies was employed (B), and reliable Kramers-Kronig data reductions can now be performed on a routine basis. The entire procedure was carefully tested (A,B) and has been applied to a number of material systems including (crystalline and amorphous)  $\text{Sb}_2\text{Se}_3$  (B); (amorphous)  $\text{Sb}_1\text{Se}_{1-x}$  (C); and (amorphous)  $\text{Ge}_x\text{Se}_{1-x}$ ,  $\text{Ga}_x\text{Se}_{1-x}$ , and  $\text{In}_x\text{Se}_{1-x}$  (D).

The frequency-dependent dielectric function obtained from the normal incidence reflectivity provides substantial information regarding the electronic structure of the material being studied. The use of sum rules, the f-sum rule and the relation

$$\epsilon_{1\text{eff}} = \frac{2}{\pi} \int_0^\omega \frac{\epsilon_2(\omega'')}{\omega''} d\omega''$$

both test the analysis and give information about the electronic structure particularly for the valence band. In the following paragraphs a brief outline of the type of information we have obtained and its interpretation is given. In addition where possible whatever insight this lends into the chemical bonding and structure is included.

### III. Interpretation of Optical Data

Optical data was obtained over a wide energy spectrum from ~30 eV, utilizing the University of Wisconsin Synchrotron Storage Ring as a radiation source, to the far IR, by employing Fourier Transform Spectroscopy. The systems that have been studied optically were all chosen from the chalcogenide semiconductors. In many instances these may be characterized as lone-pair semiconductors, i.e., there is evidence that the valence bands in these materials are principally composed of weakly-bonding p-electrons of the chalcogen atoms. The next lower valence bands also have primarily p-character but most likely have larger admixtures of s-electrons. It is these bands which correspond to the bonding electron states which are responsible for the cohesion in these solids.

In (B) it is demonstrated from the  $\epsilon_2$ -spectrum and related sum rules that both amorphous and crystalline  $\text{Sb}_2\text{Se}_3$  exhibit optical response in-

dicating the presence of both weakly bonding and bonding electrons. Furthermore, there are seen clear changes in the detailed optical response on the crystalline to amorphous transition which are consistent with a lack of long-range order upon this transition. In addition, there is a definite loss of oscillator strength in the lower frequency portion of the spectrum for the amorphous system.

In (C) the effect of compositional variation in the amorphous system  $\text{Sb}_{1-x}\text{Se}_x$  was studied. It was found that the two-absorption band spectrum characteristic of the lone-pair semiconductors was not found for Se compositions below  $x = 0.24$ . This behavior suggests that at these low Se compositions the amorphous material no longer contains any non-bonding p electrons, these having been exploited to satisfy the bonding and coordination requirements of the Sb atoms.

Finally in (D) similar considerations were applied to the systems  $\text{Ge}_{1-x}\text{Se}_x$ ,  $\text{In}_{1-x}\text{Se}_x$ , and  $\text{Ga}_{1-x}\text{Se}_x$  with similar conclusions. At sufficiently large Se concentrations the materials all exhibit spectra very similar to Se itself, the standard lone-pair semiconductor.

The optical data and its interpretation reported in this group of publications has been corroborated and extended by XPS (E) and photoemission (F) studies, particularly upon  $\text{Sb}_2\text{Se}_3$ .

#### IV. Photoemission

Ultraviolet photoemission spectroscopy (UPS) measurements were performed to determine the electronic structure and relate it to the chemical bonding model and to the bonding within the solid. A photoemission spectrometer of 0.1 eV resolution has been constructed and recently moved to the University of Wisconsin Physical Sciences Laboratory (UWPSL) on a permanent basis. The use of UPS with a synchrotron as a source of exciting radiation has the fol-

lowing advantages over other methods: (i) optical transitions can be followed over a large range (at least 30 eV) of photon energies, (ii) absolute energy positions of the maxima in the density of states (DOS) can be determined in both the valence band (VB) and the conduction band (CB) with a resolution of 0.2 eV or better. (iii) at higher values of photon energies (typically  $h\nu > 20$  eV) the experimental data can be related to the DOS of the VB. (iv) the natural polarization of the synchrotron radiation (with electrical vector  $\vec{E}_0$  in the median plane) allows the study of the crystal field effects on the matrix elements (F).

Amorphous and crystalline phases of  $\text{Sb}_2\text{Se}_3$  were investigated in great detail and the photoemission data has been published in (G,H). The UPS data confirm and further expand the DOS models based on the chemical bonding model conjectures. The bonding and weakly bonding bands are observed, with a well defined lone p-pair sub-band of the weakly bonding band. The structure of the lone p-pair band is extremely strongly affected at the crystalline to amorphous transition. This transition has a large effect of smoothing several DOS peaks in the non-bonding valence band as well as in the conduction band, but no UPS observation was made which would indicate a substantial tailing of the VB DOS in amorphous  $\text{Sb}_2\text{Se}_3$  in agreement with our photoconductivity and optical measurements.

The comparison of DOS data with those of Se (Schevchick et al., 1973) suggests that the lone pairs of chalcogen atoms play an important role in the formation of the upper VB of  $\text{V}_2\text{VI}_3$  compounds, both amorphous and crystalline, and that the basic features of the DOS are understandable in terms of chemical bonding.

## V. Photoconductivity

A specific measurement technique was developed (I) which allowed measure-

ments down to very low S/N values thus allowing measurements to be extended to the long wavelength part of the absorption edge. The photoconductivity measurements were performed (and correlated with the optical transmission) with particular attention to the vicinity of the fundamental absorption edge in order to obtain further information on the sharpness of the band edges.

In the case of properly prepared amorphous  $\text{Sb}_2\text{Se}_3$  films (J), no difference in the sharpness of the photoconductivity onset was observed (K). However, the product of mobility and the lifetime was found in the amorphous phase to be  $\sim 10^4$  times lower than in the crystalline  $\text{Sb}_2\text{Se}_3$ . It has been found, however, that deliberately introduced disorder in composition at a local scale results in less sharp edge in the photoconductivity (and optical) response (to be published).

In the case of  $\text{Sb}_2\text{O}_3$ , the photoconductivity with onset corresponding to the optical absorption edge (L) was observed in both crystalline modifications of  $\text{Sb}_2\text{O}_3$  (cubic and orthorhombic). The lack of the photoresponse in amorphous  $\text{Sb}_2\text{O}_3$  was explained by much lower value of the intrinsic photosensitivity (M).

#### MATERIALS PREPARATION

For reasons outlined in the initial proposal, most effort in the past three years has been devoted to the study of the binary amorphous system  $\text{Sb}_{1-x}\text{Se}_x$ , although other Sb-chalcogenides and Group III and Group IV - chalcogenides have been lightly surveyed. However, many of the developments in preparative techniques evolved from the study of the  $\text{Sb}_{1-x}\text{Se}_x$  system were carried over into these other systems.

At the outset, it was decided to concentrate on vacuum evaporation for reasons of high purity rather than employ the more contaminating methods such as sputtering, chemical vapor deposition or electrolytic deposition with their respective concomitant problems of inert gas, reactive gas or soluble impurity inclusions. Considerable emphasis was placed on obtaining known controllable compositions by physical evaporation. Although physical vapor deposition is a common method of preparation of amorphous materials not much attention had been paid in the literature to the resulting thin film compositions. Consequently, there were many reports in the literature on physical measurements of unknown compositions.

We were successful in overcoming this problem by three different techniques: (i) Single source evaporation from a solid using an electron beam (EB) gun (J), (ii) Controlled coevaporation from elemental sources to produce a particular composition (N), (iii) Controlled coevaporation from elemental sources employing an elongated substrate to prepare essentially the whole compositional system (O).

The last listed technique has been of considerable use in surveying other amorphous binary compounds and has been applied to the  $\text{Sb}_{1-x}\text{Te}_x$  (P),  $\text{Ge}_{1-x}\text{Se}_x$  (Q),  $\text{Ge}_{1-x}\text{Te}_x$  (Q),  $\text{Ga}_{1-x}\text{Se}_x$  (D) and  $\text{In}_{1-x}\text{Se}_x$  (D) systems in addition to  $\text{Sb}_{1-x}\text{Se}_x$  (N).

Single crystal growth of the Sb-chalcogenides (the only systems tackled) from the melt or the vapor presented no serious problems. An improved zone-refiner for single crystal growth was developed (R).

## TRANSPORT PROPERTIES

### I. Electrical Conductivity

Four-probe and sandwich-type conductivity measurements were made as a function of temperature on a number of amorphous systems. For the



two Sb-chalcogenide systems investigated:  $\text{Sb}_{1-x}\text{Se}_x$  (N) and  $\text{Sb}_{1-x}\text{Te}_x$  (P) a  $\ln\sigma$  vs  $T^{-1}$  dependence was obtained over a large temperature range, indicating that conduction occurred either in extended states or by hopping in localized states at the band edges. From optical data (N), (P), it was concluded that the former mechanism is the more likely.

In contrast, variable range hopping conductivity between localized states in the forbidden energy gap, i.e.,  $\ln\sigma$  vs  $T^{-1/4}$  behavior, was often observed in other amorphous systems e.g.,  $\text{Ge}_{1-x}\text{Se}_x$  (Q);  $\text{Ge}_{1-x}\text{Te}_x$  (Q);  $\text{Ga}_{1-x}\text{Se}_x$  (D) and  $\text{In}_{1-x}\text{Se}_x$  (D) although believable localized density of states values were not always obtained.

## II. Thermo-emf Measurements

The Seebeck coefficient was determined at room-temperature in a number of systems and when used in conjunction with  $\ln\sigma$  vs  $T^{-1}$  conductivity data yielded values for the Fermi-level position. Generally, the Fermi level was not found to be pinned in the gap center and so straightforward comparison between the thermal and optical band gaps could not be made. Some preliminary measurements were made of Seebeck coefficient as a function of temperature in the  $\text{Ge}_{1-x}\text{Se}_x$  system (to be published) but, for reasons we do not understand, the activation energies so obtained appeared to be somewhat higher than those determined from  $\ln\sigma$  vs  $T^{-1}$  measurements.

## STRUCTURE

### I. Mossbauer Studies

Amorphous films of  $\text{Sb}_{1-x}\text{Se}_x$  were studied with the Mossbauer effect (S). The spectra were all similar to each other, despite a large range in x-values, but was different from the single crystal, indicating that the environment of the Sb sites are homogeneous, i.e., they are characterized by a narrow range in coordination number and in bond length. Thus, the two sites in the



crystal are replaced by many closely similar sites in the glass, i.e., little site distortion.

A further Mossbauer investigation was conducted on Sn-doped  $\text{As}_2\text{Se}_3$  glass (T). The local environment about the Sn atoms was found to be similar for a wide range of Sn concentrations showing that a high degree of local chemical order exists in this glass. Further, it was confirmed that Sn displaces As in the glass, forming  $\text{SnSe}$  and, in addition, at higher Sn concentrations  $\text{SnSe}_2$ , i.e., changing its valency from 4 to 2 with increasing concentration.

Mossbauer studies of bond character, electronic structure and glass to crystalline transitions in amorphous semiconductors and oxide glasses have been reviewed (U). Based on the measured isomer shifts of the Sb-chalcogenides, it was concluded that the charge density at the Sb nuclei increases in magnitude in the sequence O, S, Se, Te. This conclusion is contradictory to optical bandgap data and is probably a result of a too simplistic view of the electronic configurations in a solid.

## II. X-ray and Electron Diffraction Studies

The crystallographic work was addressed mainly to two areas: to investigating the substitution of Se into the  $\text{Sb}_2\text{Te}_3$  structure and to investigating "amorphous" thin films of  $\text{Sb}_2\text{Se}_3$ .

By use of single crystal x-ray diffraction data and appropriate computer methods it was established that both  $\text{Sb}_2\text{Te}_3$  and  $\text{Sb}_2\text{Te}_2\text{Se}_1$  crystallize in the  $\text{Bi}_2\text{Se}_2\text{S}$  structure. In  $\text{Sb}_2\text{Te}_2\text{Se}_1$  the Se is substituted into the 0,0,0-position (corresponding to the S-position in  $\text{Bi}_2\text{Se}_2\text{S}$ ). In nonstoichiometric compounds  $\text{Sb}_2\text{Te}_{3-x}\text{Se}_x$ , with compositions  $0 < x < 1$ , the Se is substituted into the same 0,0,0 position. For compositions with  $x > 1$ , one formula unit of Se is substituted into the 0,0,0 position,

the excess Se into the other two positions. The lattice constants decrease continuously with increasing  $x$ , but one observes two distinct regions for  $x < 1$  and  $x > 1$  with almost linear lattice constant changes, but different slopes.

Amorphous  $\text{Sb}_2\text{Se}_x$  films were observed to rapidly crystallize in the electron beam of the electron microscope to single crystal sizes up to about  $100\mu$ . Astonishingly, within a wide range of composition, the predominant diffraction pattern was that of  $\text{Sb}_2\text{Se}_3$  with the crystallographic  $b$ -direction perpendicular to the films. However, the Se-rich samples predominantly crystallized in fibers which extended in the  $c$ -direction within the thin film. Sb-rich samples, on the other hand, formed very small crystals which gave a complicated powder pattern which was related to but not identical with that of  $\text{Sb}_2\text{Se}_3$ . Some deviation of the  $\text{Sb}_2\text{Se}_3$  pattern (for instance related to the systematical extinctions) was observed for almost all films even those of  $\text{Sb}_2\text{Se}_3$ . Astonishingly, the films even crystallized at low temperatures (down to  $-150^\circ\text{C}$ ). In some cases super-lattice formation took place (V).

## SUMMARY OF BUDGET AND EXPENDITURES

	1st Year		2nd Year		3rd Year	
	Budget	Costs	Budget	Costs	Budget	Costs
Salaries, including fringe benefits	\$31,368.00	\$31,354.60	\$38,995.00	\$40,059.45	\$31,825.00	\$31,953.47
Equipment	+3,670.00	3,714.03	6,120.00	2,218.40		
Supplies	-3,670.00 12,000.00	7,803.77	5,864.00	6,627.31	2,020.00	6,585.64
Travel	2,500.00	2,110.60	1,500.00	1,424.68	900.00	614.04
Other		885.00		112.16 2,037.00		
Total Direct Costs	45,868.00	45,868.00	52,479.00	52,479.00	34,745.00	39,153.15
Indirect Costs	11,952.00	11,952.00	5,521.00	5,521.00	4,255.00	0
TOTAL COSTS	57,820.00	57,820.00	58,000.00	58,000.00	39,000.00	39,153.15

Publications

- A) Hilbert Transformations of Densities of States Using Hermite Functions, J. Comp. Phys. 11 190 (1973), R. Afshar, F.M. Mueller and J.C. Shaffer.
- B) Electronic Structure of Single Crystal and Amorphous  $Sb_2Se_3$ , phys. stat. sol. (b) 54 511 (1972), J.C. Shaffer, B. Van Pelt, C. Wood, J. Freeouf, K. Murrese, and J.W. Osmun.
- C) Optical Properties of the Amorphous  $Sb_{1-x}Se_x$  System, phys. stat. sol. (b) 59 K17 (1973), R. Mueller, J.C. Shaffer and C. Wood.
- D) Amorphous Group III - Chalcogenides, Proceedings, 5th International Conference on Amorphous and Liquid Semiconductors, Garmisch-Partenkirchen, Germany, (Sept, 1973), C. Wood, L.R. Gilbert, C.M. Garner, and J.C. Shaffer.
- E) Electron Energy States in  $Sb_2Se_3$ , Phys. Rev. Letters 29, 485, (1972), C. Wood, J.C. Shaffer and W.G. Proctor.
- F) Photoemission Studies of Crystalline and Amorphous  $Sb_2Se_3$ , (submitted to Phys. Rev.), Z. Hurych, D. Buczek, C. Wood, G.J. Lapeyre and A.D. Baer.
- G) Strong Polarization Dependence and Selenium Lone-Pairs in the Photoemission Spectra of  $Sb_2Se_3$ , Solid State Communications (in print), Z. Hurych, D. Buczek, C. Wood, G.J. Lapeyre and A.D. Baer.
- H) Electronic Structure of Amorphous and Crystalline  $Sb_2Se_3$  From Photoemission Studies Using Synchrotron Radiation, Proceedings, 5th International Conference of Amorphous and Liquid Semiconductors, Garmisch-Partenkirchen, Germany, (Sept., 1973), Z. Hurych, C. Wood and J.C. Shaffer.
- I) A Method for Determining Photoconductive Response Times, J. Phys. E: Scient. Inst. 5, 11 (1972).
- J) Optical and Transport Properties of Amorphous  $Sb_2Se_3$ , J. Non-Cryst. Solids 8-10 209 (1972), C. Wood, Z. Hurych and J.C. Shaffer.
- K) Photoconductivity in Amorphous  $Sb_{1-x}Se_x$  Layers, J. Non-Cryst. Sol. 11 153, (1972), Z. Hurych, R. Mueller, C.C. Wang, and C. Wood.
- L) The Optical Properties of Amorphous and Crystalline  $Sb_2O_3$ , phys. stat. sol. (b) 54, 701 (1972), C. Wood, B. Van Pelt and A. Dwight.
- M) Photoconductivity in Crystalline and Amorphous  $Sb_2O_3$ , phys. stat. sol. (a) 16 K161 (1973), B. Wolffing and Z. Hurych.
- N) The Preparation of Amorphous Thin Films, J. Non-Cryst. Solids, 7 301 (1972), R. Mueller and C. Wood.
- O) The Amorphous Sb-Se System, J. Non-Cryst. Solids, 12 295 (1973), C. Wood, R. Mueller and L.R. Gilbert.

- P) The Amorphous  $Sb_{1-x}Te_x$  System, J. Non-Cryst. Solids (in print), C.M. Garner, L.R. Gilbert and C. Wood.
- Q) Amorphous Thin Films, J. Vac. Sci. Tech. 10, 739 (1973), C. Wood, L.R. Gilbert, R. Mueller and C.M. Garner.
- R) A Zone Refiner for Crystal Growth, Rev. Sci. Inst. 43 1374 (1972), C. Wood, B. Van Pelt, and E. Hyland.
- S) Mössbauer Studies of Amorphous and Crystalline Antimony Selenides, Phys. Lett. 37A 453 (1971), S.L. Ruby, L.R. Gilbert, and C. Wood.
- T) Mössbauer Investigation of  $Sn(As_2Se_3)_{1-x}$  Glasses, Phys. Chem. Glasses 13 153 (1972), S.P. Taneja, A.E. Dwight, L. Gilbert, W.C. Harper, C.W. Kimball and C. Wood.
- U) Mössbauer Spectroscopy of Amorphous Semiconductors and Glasses Containing Antimony, Tin and Iron: A Review, Mössbauer Effect Methodology 8, I.J. Gruverman, ed., Plenum Press, New York, 1973, p. 41.
- V) Mechanism of Crystal Growth in Thin Films of  $Sb_xSe_y$  Caused by Electron Irradiation, Ninth International Conference on Crystallography, Tokyo, Japan, August 1972.

Reprinted from JOURNAL OF COMPUTATIONAL PHYSICS  
All Rights Reserved by Academic Press, New York and London

Vol. 11, No. 2, February 1973  
Printed in Belgium

## Hilbert Transformation of Densities of States Using Hermite Functions\*

R. AFSHAR

*Department of Physics, Northern Illinois University, DeKalb, Illinois 60115*

F. M. MUELLER

*Argonne National Laboratory, Argonne, Illinois 60439 and  
Department of Physics, Northern Illinois University, DeKalb, Illinois 60115*

AND

J. C. SHAFER

*Department of Physics, Northern Illinois University, DeKalb, Illinois 60115*

Received December 17, 1971

It is shown that Hermite functions form a convenient representation of the Hilbert transform kernel (Kramers-Kronig transform). Application is made to two densities of states. The zeros and weight functions for Hermite integration for order  $n = 300$  are given in an appendix.

### I. INTRODUCTION

Analytic linear integral transforms are part of the working knowledge of almost all physicists. One learns of the usefulness and applicability of the Fourier integral transform, for example, at the earliest stages of one's training. However, rather less attention is given to other integral transform systems, and less still to specific techniques to use in formulating numerical procedures. The result is that often inappropriate numerical procedures have been used to carry out such integral transforms. The most problematic example, we believe, is the case of singular kernels such as numerical Kramers-Kronig [1, 2] or Hilbert transformation [3-5] which contain implicit principle value integrals.

\* Based on work performed under the auspices of the U. S. Atomic Energy Commission and also supported by the Advanced Research Projects Agency of the Department of Defense and was monitored by the Army Research Office, Durham.

We believe, however, that any ordinary integral transform may be handled in a completely straightforward manner. One has two systems of functions  $\Delta(\omega)$  and  $\psi(\omega')$  related through a linear kernel  $K(\omega, \omega')$  as

$$\psi(\omega) = \int K(\omega, \omega') \Delta(\omega') d\omega'. \quad (1)$$

The case of the symmetric kernel

$$K(\omega, \omega') = K(\omega', \omega) \quad (2)$$

has been treated exhaustively by Courant and Hilbert [4]. Simple numerical procedures consist of expanding  $\psi$  and  $\Delta$  in a complete, orthonormal set  $q_n(\omega)$ ,

$$\begin{cases} \psi(\omega) \\ \Delta(\omega) \end{cases} = \sum_n \begin{cases} \alpha_n \\ \beta_n \end{cases} q_n(\omega), \quad (3)$$

and the kernel as the Cauchy outer product

$$K(\omega, \omega') = \sum_{nm} S_{nm} q_n(\omega) q_m(\omega'), \quad (4)$$

so that the integral Eq. (1) is reduced to the linear matrix equation

$$\alpha_n = \sum_m S_{nm} \beta_m. \quad (5)$$

The problem of carrying out the numerical transform is thus reduced to the two mechanical operations of forming the expansion coefficients  $\beta$  in Eq. (3) and carrying out the matrix multiplication in Eq. (5).

In this paper, we will consider functions and kernels defined over the whole real line ( $-\infty < \omega < \infty$ ) and will thus focus on expansions in the complete set of Hermite functions  $\psi_n(\omega)$ . We will limit our discussion of the kernel to the important case of the Hilbert or Weyl-Kronig transform

$$K_H(\omega, \omega') = (P/\pi)[1/(\omega - \omega')], \quad (6)$$

where the  $P$  indicates that the principle value of the integral (1) is to be taken. Finally we limit ourselves here to consideration of cases where the function  $\Delta(\omega')$  is well defined everywhere. We will consider real experimental data and the special problems inherent in extrapolation elsewhere.

We consider a mathematically exact treatment of the problem of numerical Hilbert transformation which is simple to use, can be applied to a variety of cases, and automatically least-square-fits data. In Section II we discuss the formal deriva-

tion of our technique, and in Section III the application to Monte-Carlo derived densities of electron states for a simple cubic  $s$  band and face-centered-cubic palladium. Section IV summarizes our results and discusses application to other systems.

## II. FORMALISM

### A. The Hilbert Operator

As is well known, the Kramers-Kronig relation between the real and imaginary parts of a response function arise because of causality. If, in the long wave length limit, a time varying field  $E(t)$  is impressed upon a media starting at  $t = 0$ , then the linear response  $D(t)$  must also be zero for  $t < 0$ , and is given by

$$D(t) = \epsilon(t) E(t), \quad (7)$$

where  $\epsilon$  is the (complex) generalized susceptibility. Upon taking the complex Fourier transform of (7) we obtain the Kramers-Kronig relations [6]:

$$\begin{aligned} \epsilon_1(\omega) &= 1 - \frac{P}{\pi} \int_{-\infty}^{\infty} \frac{\epsilon_2(\omega') d\omega'}{\omega' - \omega}, \\ \epsilon_2(\omega) &= \frac{P}{\pi} \int_{-\infty}^{\infty} \frac{(\epsilon_1(\omega') - 1) d\omega'}{\omega' - \omega}, \end{aligned} \quad (8)$$

where  $\epsilon_1$  and  $\epsilon_2$  denote the real and imaginary parts, respectively, and  $\epsilon_1(\infty) = 1$ . If we regard the principle value integrals of (8) as an operator  $P$  then we have the functional relations

$$\begin{aligned} (\epsilon_1 - 1) &= P(\epsilon_2), \\ \epsilon_2 &= -P(\epsilon_1 - 1), \end{aligned} \quad (9)$$

or that

$$(\epsilon_1 - 1) = -P^2(\epsilon_1 - 1), \quad (10)$$

which makes manifest that  $P$  is an antiunitary operator.

The relations (8) form a Hilbert transform pair. The close connection between Hilbert and Fourier integral transformations is seen in that the (Dirichlet) kernel for (double) Fourier transformation is given by

$$K_F(\omega, \omega') = \frac{1}{\pi} \int_0^{\infty} dt \cos(\omega - \omega')t = \delta(\omega - \omega') \quad (11)$$



(a Dirac delta function), whereas the analogous kernel for Hilbert transformation is

$$K_H(\omega, \omega') = \frac{1}{\pi} \int_0^\infty dt \sin(\omega - \omega')t = \frac{1}{\pi} \frac{P}{\omega - \omega'}, \quad (12)$$

which we define as the (odd) function

$$\rho(\omega - \omega') = (1/\pi)[P/(\omega - \omega')]. \quad (13)$$

The relations (11) and (12) may be used to form representations of the operators  $K_F$  and  $K_H$ . Any denumerable, complete set of functions defined over the whole real line may be used to form a representation for (11) since in terms of any complete orthonormal set  $\psi_n(\omega)$  we have

$$\sum_n \psi_n(\omega) \psi_n(\omega') = \delta(\omega - \omega'), \quad (14)$$

where the sum extends over all of the members of the set. An analogous representation for the function  $\rho(\omega - \omega')$  may be constructed as follows:

From (12), or by direct integration, we have

$$\rho(\omega - \omega') = \frac{i}{2\pi} \int_{-\infty}^{\infty} dt \text{SGN}(t) e^{i(\omega - \omega')t} \quad (15)$$

where  $\text{SGN}(t)$  is the signature or signum function ( $-1$  for  $t < 0$  and  $+1$  for  $t > 0$  and  $0$ , say, if  $t = 0$ ). We recall that the signum function, like the delta function, is a generalized function [3] and has the property

$$(d/dx) \text{SGN}(x - x') = 2\delta(x - x'). \quad (16)$$

Equation (15) allows us to construct representations of the Hilbert operator from the representation for  $\exp(i\omega t)$ . In this paper, we will concentrate on a single representation, the Hermite functions  $\psi_n(\omega)$ . We recall [7] that the  $n$ th-order orthonormal Hermite function is found from the corresponding Hermite polynomial  $H_n(\omega)$  by

$$\psi_n(\omega) = N_n e^{-\omega^2/2} H_n(\omega), \quad (17)$$

where  $N_n$  is a normalization factor given by

$$N_n^2 = (2^n n! \sqrt{\pi})^{-1}. \quad (18)$$

For our purposes the most important property of the Hermite functions is that

up to a phase factor  $i^n$ , the Fourier transform of a Hermite function of order  $n$  is the same Hermite function

$$\frac{1}{\sqrt{2\pi}} \int_{-\infty}^{\infty} e^{i\omega't} d\omega' \psi_n(\omega') = i^n \psi_n(t). \quad (19)$$

Multiplying both sides of Eq. (19) by  $\psi_n(\omega)$  and utilizing Eq. (14), we have a representation for the Fourier kernel  $e^{i\omega t}$ :

$$e^{i\omega t} = \sqrt{2\pi} \sum_n i^n \psi_n(t) \psi_n(\omega) \quad (20)$$

and the conjugate relation for  $e^{-i\omega't}$ . Placing (20) in (15), we have

$$\rho(\omega - \omega') = (-i) \sum_n \sum_m (i)^n (-i)^m \psi_n(\omega) \psi_m(\omega') S'_{nm}, \quad (21)$$

where  $S'_{nm}$  is given by

$$S'_{nm} = \int_{-\infty}^{\infty} dt \operatorname{SGN}(t) \psi_n(t) \psi_m(t). \quad (22)$$

Thus  $S'_{nm}$  forms a representation of the signum operator in terms of the Hermite functions. Since the Hermite functions are simply odd or even,  $\psi_n(-t) = (-1)^n \psi_n(t)$ , the integral may be reduced to

$$S'_{nm} = [1 + (-1)^{m+n+1}] \int_0^{\infty} dt \psi_n(t) \psi_m(t). \quad (23)$$

$S'_{nm}$  is zero unless  $n + m$  is odd. Let us assume that this is true. We define a symmetric real matrix  $\sigma$  related to  $S'$  by

$$\sigma_{nm} = \int_0^{\infty} dt H_n(t) H_m(t) e^{-t^2}. \quad (24)$$

We recall [8] that the derivative  $d[e^{-x^2} H_{n-1}(x)]$  is given by  $e^{-x^2} H_n(x) dx$ . Applying an integration by parts, we find the double recursion formula on the matrix  $\sigma$ :

$$\sigma_{nm} = H_m(0) H_{n-1}(0) + 2m\sigma_{n-1, m-1}, \quad (25)$$

with a similar relation on interchanging  $n, m$ . Eliminating  $\sigma_{n-1, m-1}$  from the later two equations, and replacing the normalization factors, we find the symmetric matrix:

$$S'_{nm} = \sqrt{\frac{2^{-(n+m-2)}}{n! m! \pi}} \frac{n H_{n-1}(0) H_m(0) - m H_{m-1}(0) H_n(0)}{n - m}. \quad (26)$$

Let us define the antisymmetric matrix  $S$  such that

$$\rho(\omega - \omega') = \sum_{nm} S_{nm} \psi_n(\omega) \psi_m(\omega'). \quad (27)$$

Then the relation between  $S$  and  $S'$  with  $m = n + 2h + 1$  is given by

$$S_{nm} = (-1)^{h+1} S'_{nm}; \quad S_{nm} = -S_{nm} \quad (28)$$

The compactness of the matrix  $S$  can be seen either from Eq. (4) or from the fact that for fixed  $n$

$$\lim_{h \rightarrow \infty} S_{n, n+2h+1} \rightarrow 0 \quad \text{as } h^{-1}. \quad (29)$$

The latter is easily proved [9] by direct expansion of Eq. (26).

#### B. Hermite Integration

A separate report [10] gives the zeros and weight function for Hermite integration of order  $n = 20, 26, 50, 76, 150$ . Those for the 300-th order are given in an appendix. Also available are those of the 500-th and 1000-th order, which are probably high enough for any problem of practical interest. The Hermite function Fortran programs are also published in the Argonne report, and are available on request. Because there are no special problems in generating these functions, simple, upward recursion was used:

$$H_{n+1}(x) = 2xH_n(x) - 2nH_{n-1}(x). \quad (30)$$

The only numerical problem is the implicit factor of  $n!$  in the Hermite polynomials, which was treated by extending the exponential part of the double precision word of an IBM 360/50/75 to include arbitrarily high powers of 16. To avoid overflow/underflow problems the functions are replaced by zero if they are smaller than  $16^{**}(-17)$ .

A thorough discussion of Hermite integration has been given by Hochstrasser [11] and Davis and Polansky [12] based on the classic work of Russel [13] and Salzer *et al.* [14]. Our results differ from that of the previous authors only in that we have gone to higher order [15] and used a different weight function. Hermite integration of an arbitrary function  $f(x)$  is approximated, to order  $n$ , by

$$\int_{-\infty}^{\infty} e^{-x^2} f(x) dx \cong \sum_{i=1}^n W_n(x_i^n) f(x_i^n), \quad (31)$$

where  $x_i^n$  is the  $i$ -th zero of the  $n$ -th order Hermite polynomial  $H_n$ , and the weight factors  $W_n$  are given by

$$W_n(x_i^n) = 2^{n-1} n! \sqrt{\pi/n^2} [H_{n-1}(x_i^n)]^2. \quad (32)$$

A numerically more convenient representation for Hermite integration is achieved if we consider instead

$$\int_{-\infty}^{\infty} g(x) dx = \sum_{i=1}^n W_n'(x_i^n) g(x_i^n), \quad (33)$$

where  $W_n'$  is given by

$$W_n'(x_i^n) = W_n(x_i^n) \exp(x_i^{n2}) / (n\psi_{n-1}^2(x_i^n)), \quad (34)$$

where  $\psi_n$  is the  $n$ -th order orthonormal Hermite function. In the appendix we list the positive zeros and weight functions  $W_n'$  for the Hermite polynomials of order 300. For the overlapping case of  $n = 20$ , our results agree with those of Salzer *et al.* to at least 14 significant figures.

We have found the zeros of the Hermite polynomials (or Hermite functions) by noticing that the sequence of polynomials  $H_0, H_1, \dots, H_n$  form a Sturm sequence. Thus by counting the number of sign changes in the sequence, we know precisely, by Budan's Theorem, the number of zeros between a given point  $x$  and zero. (Infinitesimally above zero the sign of the Hermite polynomials is plus.) An estimate of the largest zero of the Hermite polynomial of order  $n$  is found by remembering that the Hermite functions are eigenfunctions (with eigenvalue  $E_n = (n + 1/2) \hbar \omega_c$ ) of the simple harmonic oscillator operator,  $H = p^2/2m + \frac{1}{2} k x^2$ , where  $\omega_c = \sqrt{k/m}$ . We recall that the last zero of the probability density of the  $n$ -th harmonic oscillator eigenfunction is bounded by the classical limit  $\sqrt{2E_n/k}$ , or in the appropriate units ( $m = k = 1$ ), by  $x_{\max} = \sqrt{2n+1}$ . Thus all of the zeros of the  $n$ -th order Hermite polynomial lie between  $-\sqrt{2n+1}$  and  $\sqrt{2n+1}$ .

Our computational procedure for evaluating the zeros of the  $n$ -th polynomial used the interval given by the absolute bounds  $\pm \sqrt{2n+1}$  and continuously subdivided this interval by a factor of 2. Each subinterval was selected for further operation depending on whether the Sturm sequence predicted an appropriate zero in the left or right-hand portions. Such a procedure quickly, and accurately converged to our results in the appendix. We have further tested our zeros through the sum rule:

$$\sum_{i=1}^n (x_i^n)^2 = \frac{n(n+1)}{2} \quad (35)$$

to an accuracy of at least 14 significant figures for all cases  $n$ .

In Table I we present the lowest 10 ( $10 \times 10$ ) elements of the antisymmetrical matrix  $S$ . Note that for finite order the operator Eq. (4) reduces to a matrix equation and that the square of  $S$  ( $= S^2$ ) is a matrix whose diagonal elements have an

## STATES USING HERMITE FUNCTIONS

TABLE I  
The first ten elements of the expansion coefficients of the anti unitary matrix  $S_{nm}$  for Hermite functions

$n$	$m$	0	1	2	3	4	5	6	7	8	9
0	0.0	-0.79788	0.0	0.0	-0.32574	0.0	-0.21851	0.0	-0.16858	0.0	-0.13907
1	0.79788	0.0	-0.56419	0.0	0.0	-0.16287	0.0	-0.08921	0.0	-0.05960	0.0
2	0.0	0.56419	0.0	0.0	-0.69099	0.0	-0.25752	0.0	-0.16689	0.0	-0.12644
3	0.32574	0.0	0.69099	0.0	0.0	-0.59841	0.0	-0.18209	0.0	-0.10720	0.0
4	0.0	0.16287	0.0	0.59841	0.0	0.0	-0.66905	0.0	-0.24088	0.0	-0.15330
5	0.21851	0.0	0.25752	0.0	0.0	0.66905	0.0	-0.61075	0.0	-0.19044	0.0
6	0.0	0.08921	0.0	0.18209	0.0	0.0	0.61075	0.0	-0.65969	0.0	-0.23324
7	0.16858	0.0	0.16689	0.0	0.0	0.24088	0.0	0.65969	0.0	-0.61708	0.0
8	0.0	0.05960	0.0	0.10220	0.0	0.0	0.19044	0.0	0.61708	0.0	-0.65451
9	0.13907	0.0	0.12644	0.0	0.0	0.15330	0.0	0.23324	0.0	0.65451	0.0

absolute value slightly less than 1. If we define the normalized trace  $T$  of the squared matrix  $S^2$  as

$$T = \frac{1}{N} \sum_{n=1}^N |(S^2)_{nn}|, \quad (36)$$

$T$  has the converging values of 0.885, 0.944, 0.970, 0.984, 0.992, for  $N$  of 10, 25, 50, 100 and 200, respectively, with the largest error in the last (biggest  $n$ ) term.

### C. Moments and Scaling

If we assume that the function we wish to transform ( $\equiv g(\omega')$ ) has a norm of 1, then we may think of  $g(\omega')$  as a distribution density and the transformed function  $F(\omega)$  as

$$F(\omega) = -\frac{P}{\pi} \int \frac{g(\omega') d\omega'}{\omega' - \omega}, \quad (37)$$

where  $F$  and  $g$  are real and imaginary parts of a self-energy, for example. Let us formally expand the kernel as

$$-\frac{P}{\omega' - \omega} = \frac{P}{\omega} \sum_{m=0}^{\infty} \left(\frac{\omega'}{\omega}\right)^m. \quad (38)$$

Then upon (carefully) interchanging summation and integration, Eq. (37) becomes

$$F(\omega) = \frac{P}{\pi\omega} \sum_{m=0}^{\infty} (\omega)^{-m} \int d\omega' \omega'^m g(\omega'), \quad (39)$$

which (formally) shows that Hilbert transformation may be thought of as merely interchanging the Taylor and Laurent expansions (assuming they exist) of the two functions about zero. In terms of the distribution density  $g$ , we can define the  $m$ -th moment

$$\mu_m = \int d\omega' \omega'^m g(\omega'), \quad (40)$$

so that

$$F(\omega) = \frac{P}{\pi\omega} \sum_{m=0}^{\infty} \mu_m (\omega)^{-m}. \quad (41)$$

It is clear from (40) and (41) that a further expansion of the Laurent representation of  $F(\omega)$  in Hermite functions yields a worse result for the low order terms. Better converged results would be achieved if we remove (analytically) as much of the low-order moments as we can from  $g(\omega)$ . In practice we do this by finding a simply

transformed analytic function  $g'(\omega)$  which resembles  $g(\omega)$  as closely as possible and expanding not the entire  $g(\omega)$  in Hermite functions but the difference as

$$\beta_n' = \int d\omega' (g(\omega') - g'(\omega')) \varphi_n(\omega'), \quad (42)$$

$$F(\omega) = \sum S_{nm} \beta_m' \varphi_n(\omega) + F'(\omega), \quad (43)$$

where  $F'(\omega)$  is the analytic transform of  $g'(\omega)$  and the difference  $g'(\omega') - g(\omega')$  has no zero-th moment. Thus a Laurent expansion of  $(F(\omega) - F'(\omega))$  begins with the second term ( $\sim \omega^{-2}$ ), in the general case, and with the third term ( $\sim \omega^{-3}$ ) when  $F(\omega)$  is odd. Further details are given in the results below.

Finally we consider the effects of scaling the expansion as

$$g(\omega) = \sum C_n(\alpha) \varphi_n(\alpha\omega), \quad (44)$$

where  $\alpha$  is a scaling constant. (Note that the form of our kernel is independent of scaling, providing that the scale factor in  $\omega$  and in  $\omega'$  has the same value. Therefore the same matrix  $S_{nm}$  may be used for all scaled cases.) It is clear from the completeness of the Hermite functions that convergence may be eventually obtained, independent of any particular  $\alpha$ , but practical considerations demand that the convergence of (42) be as rapid as possible. For functions defined only over a finite range, as in this paper, we find that a best scale factor is approximately achieved, if the highest zero of the highest expansion function is scaled to fall at about twice the range  $R$  as

$$\alpha = \sqrt{2N + 1}/2R, \quad (45)$$

where  $N$  is the order of the highest Hermite function.

Note that a best scale factor depends on the actual form of the function one wishes to transform. However, as discussed below, the exact value of  $\alpha$  is not critical, and our choice (45) will work well for many cases. The only important consideration is to avoid a confluence of the end of the function range ( $\sqrt{2N + 1}$ ) and the edge of the (finite) integration range.

## RESULTS AND APPLICATIONS

As a first example of our technique of Hilbert transformation, we consider two applications to densities of states: the model-system triple-cosine  $s$  band density of states, and that of a more realistic transition metal (palladium).

### A. *s*-band Density of States

We apply our technique to the important problem of deriving the "F" function for the density of *s* states in the simple cubic lattice:

$$F(\omega) = \frac{-P}{\pi} \int_{-\infty}^{\infty} d\omega' \frac{G(\omega')}{\omega' - \omega}, \quad (46)$$

where

$$G(\omega') = \frac{2}{(2\pi)^3} \int d\mathbf{k} \delta(E(\mathbf{k}) - \omega'), \quad (47)$$

$$E(\mathbf{k}) = 0 - \cos(k_x a) - \cos(k_y a) - \cos(k_z a), \quad (48)$$

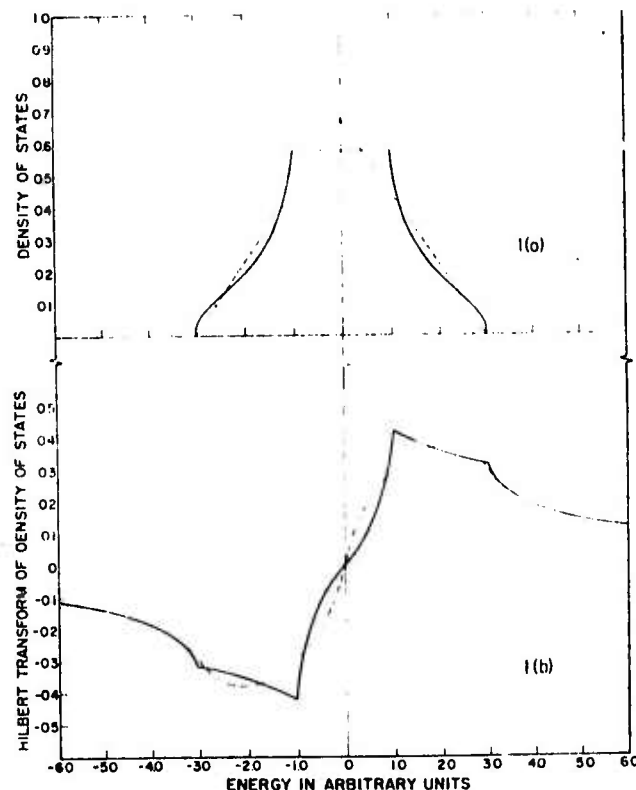


FIG. 1. The density of states (a) and Hilbert transform (b) of a simple cubic *s* band. Note that the density has a zero-th moment of 2. As explained in the text, removal of the analytic-zero-th moment function (dashed lines) greatly improves the convergence. Because of the small error, only the Hermite expansion function have been plotted. In the plot we have sharpened very small rounding errors at  $\pm 1.0$  and  $\pm 3.0$  due to the finite (250) order of the expansion.



and  $-(\pi/a) < k_x, k_y, k_z \leq \pi/a$ . In Fig. 1(a) we plot a three hundred histogram approximation to (47), where we have used one-million Monte Carlo points [16] to integrate (47). The functions  $F(\omega)$  and  $G(\omega)$  have the analytic [17] representation

$$\begin{cases} G(\omega) \\ F(\omega) \end{cases} = \frac{2}{\pi} \int_0^\omega dt J_0^3(t) \begin{cases} \cos(\omega t) \\ \sin(\omega t) \end{cases}. \quad (49)$$

In order to improve convergence of the function  $F(\omega)$ , we have subtracted out the zero-th moment as was discussed above. The function  $G(\omega)$  has a zero-th moment of  $2(\int G(\omega) d\omega = 2)$ . We have used the triangle-like function  $G_s(\omega)$

$$G_s(\omega) = \frac{2}{3}[1 - \text{SGN}(\omega) \omega/3] \quad (50)$$

which has the analytic transform

$$F_s(\omega) = -\frac{2}{3\pi} \left[ \ln \left| \frac{\omega - 3}{\omega + 3} \right| - \frac{\omega}{3} \ln \left| \frac{(\omega - 3)(\omega + 3)}{\omega^2} \right| \right]. \quad (51)$$

Note that to first order, the log poles in (51) at  $\pm 3$  cancel ( $F_s$  is log-singular in its derivatives) as is shown in Fig. 1(b). Should the presence of such poles prove detrimental, in given applications, a less singular function than (50) should be used. For the cases considered here (50) and (51) cause no problems.

TABLE II

Convergence error of the expansion of the density of cubic  $s$  states  $G$  and its Hilbert transform  $F$  in scaled Hermite functions of various order  $n$

$n$	$G(\omega)$		$F(\omega)$	
	$\mu_0 \neq 0$	$\mu_0 = 0$	$\mu_0 \neq 0$	$\mu_0 = 0$
25	0.0324	0.0097	0.1647	0.0099
50	0.0221	0.0055	0.1653	0.0071
100	0.0158	0.0028	0.1660	0.0064
150	0.0126	0.0022	0.1659	0.0065
200	0.0105	0.0018	0.1658	0.0066
250	0.0086	0.0016	0.1656	0.0066

In Table II we test the convergence of the Hilbert transform by listing the rms error (of both  $G$  and  $F$ ) as a function of total number of expansion terms. The error is defined as

$$\text{error}^2 = \frac{1}{N_i} \sum_i (G_A(\omega_i) - G(\omega_i))^2, \quad (52)$$

where  $G_A$  is the analytic function (49), and  $G$  is formed from the expansion procedure. The two separate cases cover the absence or presence of the zero-th moment function. Clearly the presence of the moment function is very helpful for the accurate evaluation of the  $F$  function, but makes little difference to the  $G$ .

TABLE III

The effect of scaling the expansion function on the residual fitting error

$\alpha$	$n = 100$	$(\mu_0 = 0)$	$F$
	$G$		
0.25	0.0237		0.0211
0.50	0.0096		0.0098
1.0	0.0060		0.0075
1.5	0.0044		0.0068
2.0	0.0034		0.0065
2.36	0.0028		0.0064
2.5	0.0027		0.0064
3.0	0.0024		0.0065
3.5	0.0022		0.0065
4.0	0.0021		0.0066
4.5	0.0020		0.0066
5.0	0.0040		0.0074

Table III shows the effect of scaling on the error. Here the number of expansion coefficients was fixed at 100, and  $\alpha$  was varied. The broad minimum around the value  $\alpha = 2.36$  suggests that the exact value of  $\alpha$  is not critical. If, however,  $\alpha$  deviated greatly from this minimal value, serious errors could result.

Finally we note a parenthetical result of our work: the function  $G(\omega)$  contains four types [18] of critical points and the function  $F(\omega)$  contains four critical points. We see that the four critical point in  $g(\omega)$  are mapped precisely into the four of  $F(\omega)$ , i.e., at exactly the same  $\omega$ , except that the types of critical points have interchanges under Hilbert transform as  $M_0 \leftrightarrow M_1$ ;  $M_2 \leftrightarrow M_3$ . We conclude from this simple example that critical point structure *cannot* shift in  $\omega$  under a proper Hilbert transform [19].

#### B. Transition Metal

For our second example we consider the more complicated case of electronic structure of the lowest 11 conduction electrons of a face-centered-cubic transition metal here palladium as calculated by Mueller, Freeman, Dimmock and

Furdyna [20]. We recall that the noninteracting electronic Greens' function in the momentum and frequency representation for  $n$  bands is given by [21]

$$G^0(\mathbf{k}, \omega) = \sum_n (\omega - E_n(\mathbf{k}) + i\eta \text{SGN}(E_n(\mathbf{k}) - \mu))^{-1}, \quad (53)$$

where  $\eta$  is an infinitesimal and  $\mu$  is the Fermi energy  $E_F$ . The imaginary part of (48) is given by

$$\text{Im}G^0(\mathbf{k}, \omega) = -\pi \sum_n \text{SGN}(E_n(\mathbf{k}) - \mu) \delta(E_n(\mathbf{k}) - \omega) \quad (54)$$

and the density of states of the lowest 11 electrons is given by

$$G(\omega) = \frac{-1}{\pi} \text{SGN}(\omega - \mu) \frac{2}{(2\pi)^3} \int \text{Im}G^0(\mathbf{k}, \omega) d\mathbf{k}. \quad (55)$$

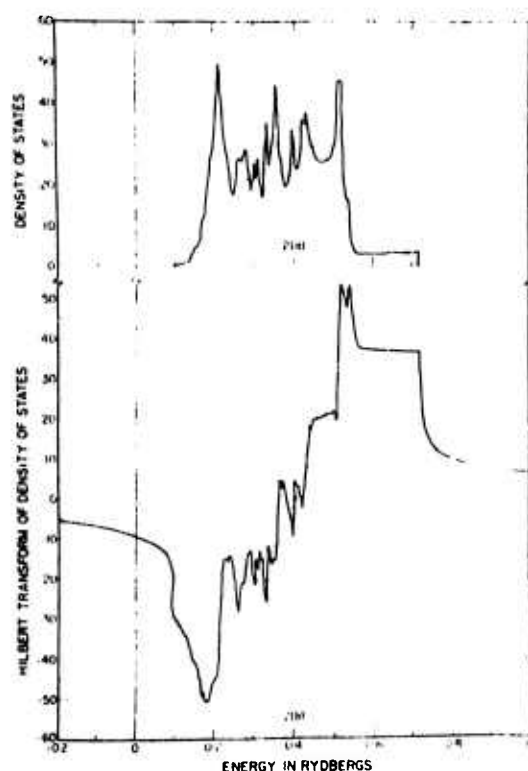


FIG. 2. The density of states (a) and Hilbert transform (b) of electrons in fcc palladium. The dashed line has a zero-th moment of 11. Because of the small error, only the expansion functions have been plotted.

and is plotted in Fig. 2(a). The dispersion relation for the Greens' function is given by

$$\text{Re } G^0(k, \omega) = \frac{P}{\pi} \int_{-\infty}^{\infty} d\omega' \frac{\text{Im } G^0(k, \omega') \text{SGN}(\omega' - \mu)}{\omega' - \omega}, \quad (56)$$

where the presence of signum function in (56) removes the signum function in (54), so that the integral to be performed in (56) is just the principal part of a delta function of a function of  $k$ . Here we consider only the  $\omega$  dependence of (56) by integrating (56) over the first BZ to produce the Hilbert transform pair  $G = G_R + iG_I$  where

$$\begin{Bmatrix} G_R(\omega) \\ G_I(\omega) \end{Bmatrix} = \frac{2}{(2\pi)^3} \int \begin{Bmatrix} \text{Re} \\ \text{Im} \end{Bmatrix} G^0(k, \omega) dk, \quad (57)$$

so that

$$G_I(\omega) = \pi \text{SGN}(\omega - \mu) G(\omega). \quad (58)$$

We have taken the signum function weighted Hilbert transform of  $G_I(\omega)$  using the method given in Section II by expanding  $g(\omega)$  in the first 250 Hermite functions. We have used a scale factor  $\alpha = 31.34$ . We notice that the fact that  $G(\omega)$  has no parity symmetry does not harm our completely general transformation, Eq. (27). We give our results in Fig. 2(b). Note that we have used atomic units of states per atom-Rydberg for both the real and imaginary parts. The total time for our routines for the 250 term expansion was 4 min on the IBM 360/50/75 at the Applied Mathematics Division at Argonne National Laboratory.

#### SUMMARY AND DISCUSSION

In this paper we have considered an exact numerical procedure for finding the Kramers-Kronig or Hilbert transform of a given function by means of an expansion in terms of Hermite functions. The practical advantage of removing the low-order moments of the initial function by means of an analytic fitting procedure have been stressed. Because of the simplicity and speed of expansion of numerical results in terms of Hermite functions, we believe that our procedures should prove useful in a wide variety of problems. Finally although all of our discussion of this paper has been couched in terms of the Hilbert transform, we point out that our expansion procedure in terms of Hermite functions are equally valid for the Fourier transform kernel, Eq. (20). Thus in contrast to Russel [22] who concluded in 1933 that "this use of Hermite functions (i.e., Fourier transformation) is, in general, not practicable," we believe that Hermite functions are eminently suitable for such numerical work.

## APPENDIX

The Positive Zeros and Weight Function for Hermite Integration for order 300.  
Note that the parentheses at the end of each number enclose a multiplication power of 10.

<hr/>		
<i>N</i> 300		
<i>i</i>	$X_i$	$W_i(X_i)$
1	0.06407 41472 40219(00)	0.12814 85862 78527(00)
2	0.19222 41925 71379(00)	0.12815 20880 83630(00)
3	0.32037 94910 76731(00)	0.12815 90929 38003(00)
4	0.44854 35469 46482(00)	0.12816 96033 31269(00)
5	0.57671 98674 84211(00)	0.12818 36230 01091(00)
6	0.70491 19643 56741(00)	0.12820 11569 37050(00)
7	0.83312 33548 48544(00)	0.12822 22113 85832(00)
8	0.96135 75631 21985(00)	0.12824 67938 57734(00)
9	0.10896 18121 48474(01)	0.12827 49131 34490(00)
10	0.12179 08571 66569(01)	0.12830 65792 78457(00)
11	0.13462 32466 10075(01)	0.12834 18036 43157(00)
12	0.14745 93369 22983(01)	0.12838 05988 85211(00)
13	0.16029 94858 80652(01)	0.12842 29789 77690(00)
14	0.17314 40527 22181(01)	0.12846 89592 24895(00)
15	0.18599 33982 84332(01)	0.12851 85562 78625(00)
16	0.19884 78851 37154(01)	0.12857 17881 55945(00)
17	0.21170 78777 21467(01)	0.12862 86742 58499(00)
18	0.22457 37424 88346(01)	0.12868 92353 93416(00)
19	0.23744 58480 40787(01)	0.12875 34937 95845(00)
20	0.25032 45652 77703(01)	0.12882 14731 53176(00)
21	0.26321 02675 40432(01)	0.12889 31986 30997(00)
22	0.27610 33307 61931(01)	0.12896 86969 00846(00)
23	0.28900 41336 18831(01)	0.12904 79961 69817(00)
24	0.30191 30576 86559(01)	0.12913 11262 12093(00)
25	0.31483 04875 97702(01)	0.12921 81184 02481(00)
26	0.32775 68112 03834(01)	0.12930 90057 52003(00)
27	0.34069 24197 41004(01)	0.12940 38229 45667(00)
28	0.35363 77079 99120(01)	0.12950 26063 82463(00)
29	0.36659 30744 95444(01)	0.12960 53942 17719(00)
30	0.37955 89216 52440(01)	0.12971 22264 07881(00)
31	0.39253 56559 80238(01)	0.12982 31447 57859(00)
32	0.40552 36882 63951(01)	0.12993 81929 71039(00)
33	0.41852 34337 56145(01)	0.13005 74167 02080(00)
34	0.43153 53123 74723(01)	0.13018 08636 12652(00)
35	0.44455 97489 06545(01)	0.13030 85834 30233(00)

---

$N = 300$		
$i$	$X_i^*$	$W_i(X^*)$
36	0.45759 71732 17077(01)	0.13044 06280 10123(00)
37	0.47064 80204 66418(01)	0.13057 70514 00859(00)
38	0.48371 27313 32040(01)	0.13071 79099 13169(00)
39	0.49679 17522 38613(01)	0.13086 32621 92688(00)
40	0.50988 55355 95289(01)	0.13101 31692 96599(00)
41	0.52299 45400 40867(01)	0.13116 76947 74446(00)
42	0.53611 92306 97249(01)	0.13132 69047 53321(00)
43	0.54926 00794 31646(01)	0.13149 08680 27683(00)
44	0.56241 75651 28007(01)	0.13165 96561 54062(00)
45	0.57559 21739 68179(01)	0.13183 33435 50938(00)
46	0.58878 43997 23317(01)	0.13201 20076 04081(00)
47	0.60199 47440 56127(01)	0.13219 57287 77684(00)
48	0.61522 37168 34511(01)	0.13238 45907 31631(00)
49	0.62847 18364 57277(01)	0.13257 86804 45272(00)
50	0.64173 96301 92552(01)	0.13277 80883 48087(00)
51	0.65502 76345 29639(01)	0.13298 29084 57699(00)
52	0.66833 63955 45051(01)	0.13319 32385 25665(00)
53	0.68166 64692 83536(01)	0.13340 91801 91540(00)
54	0.69501 84221 54947(01)	0.13363 08391 45774(00)
55	0.70839 28313 47863(01)	0.13385 93253 01981(00)
56	0.72179 02852 60936(01)	0.13409 17529 79220(00)
57	0.73521 13839 52988(01)	0.13433 12410 94941(00)
58	0.74865 67396 12971(01)	0.13457 69133 69326(00)
59	0.76212 69770 50959(01)	0.13482 88985 41787(00)
60	0.77562 27342 11436(01)	0.13508 73306 00484(00)
61	0.78914 46627 10220(01)	0.13535 23490 25737(00)
62	0.80269 34283 96470(01)	0.13562 40990 48361(00)
63	0.81626 97119 41308(01)	0.13590 27319 23935(00)
64	0.82987 42094 54720(01)	0.13618 84052 24215(00)
65	0.84350 76331 32506(01)	0.13648 12831 46922(00)
66	0.85717 07119 35176(01)	0.13678 15368 45252(00)
67	0.87086 41923 00860(01)	0.13709 93447 78620(00)
68	0.88458 88388 94404(01)	0.13740 48930 86255(00)
69	0.89834 54353 95049(01)	0.13772 83759 85364(00)
70	0.91213 47853 25241(01)	0.13805 99961 95847(00)
71	0.92595 77129 23309(01)	0.13839 99653 93597(00)
72	0.93981 50640 63013(01)	0.13874 85046 94727(00)
73	0.95370 77072 23158(01)	0.13910 58451 73204(00)
74	0.96763 65345 10753(01)	0.13947 22284 14639(00)
75	0.98160 24627 41485(01)	0.13984 79071 09224(00)
76	0.99560 64345 81581(01)	0.14023 31456 87203(00)
77	0.10096 49419 75549(02)	0.14062 82210 00407(00)
78	0.10237 32416 32419(02)	0.14103 34230 53899(00)

N 300		
$i$	$X_i''$	$W_n(X_i'')$
79	0.10378 56352 03934(02)	0.14144 90557 92188(00)
80	0.10520 22585 77901(02)	0.14187 54379 44763(00)
81	0.10662 31909 07108(02)	0.14231 29039 36427(00)
82	0.10804 85547 71127(02)	0.14276 18048 68347(00)
83	0.10947 84663 48299(02)	0.14322 25095 76357(00)
84	0.11091 30455 98719(02)	0.14369 54057 73886(00)
85	0.11235 24164 59115(02)	0.14418 09012 87641(00)
86	0.11379 67070 50575(02)	0.14467 94253 95006(00)
87	0.11524 60499 00201(02)	0.14519 14302 73312(00)
88	0.11670 05821 77869(02)	0.14571 73925 72203(00)
89	0.11816 04459 49367(02)	0.14625 78151 21696(00)
90	0.11962 57884 47361(02)	0.14681 32287 89954(00)
91	0.12109 67623 61745(02)	0.14738 41945 06735(00)
92	0.12257 35261 51134(02)	0.14797 13054 70132(00)
93	0.12405 62443 77416(02)	0.14857 51895 56805(00)
94	0.12554 50880 65523(02)	0.14919 65119 58192(00)
95	0.12704 02340 90794(02)	0.14983 59780 68361(00)
96	0.12854 18705 96601(02)	0.15049 47366 52432(00)
97	0.13005 01874 45190(02)	0.15117 23833 28534(00)
98	0.13156 53867 05064(02)	0.15187 09644 00786(00)
99	0.13308 76781 78634(02)	0.15259 09810 86028(00)
100	0.13461 72809 74304(02)	0.15333 33941 83268(00)
101	0.13615 44241 27682(02)	0.15409 92292 41913(00)
102	0.13769 93472 77255(02)	0.15488 95822 93313(00)
103	0.13925 23014 00482(02)	0.15570 56262 19885(00)
104	0.14081 35496 17129(02)	0.15654 86178 47856(00)
105	0.14238 44680 67554(02)	0.15741 99058 63159(00)
106	0.14396 20468 74742(02)	0.15832 09396 66510(00)
107	0.14554 98912 00145(02)	0.15925 32793 02607(00)
108	0.14714 72224 04828(02)	0.16021 86066 21943(00)
109	0.14875 43793 29162(02)	0.16121 87378 60854(00)
110	0.15037 17197 06303(02)	0.16225 56378 59006(00)
111	0.15199 96217 27093(02)	0.16333 14361 73422(00)
112	0.15363 84857 76849(02)	0.16444 84453 97047(00)
113	0.15528 87363 67860(02)	0.16560 91820 49064(00)
114	0.15695 08242 95442(02)	0.16681 63904 76960(00)
115	0.15862 52290 50238(02)	0.16807 30703 00110(00)
116	0.16031 24615 25285(02)	0.16938 25080 35034(00)
117	0.16201 30670 63404(02)	0.17074 83136 80970(00)
118	0.16372 76288 99143(02)	0.17217 44632 16932(00)
119	0.16545 67720 60003(02)	0.17366 53481 79044(00)
120	0.16720 11678 04732(02)	0.17522 58337 63597(00)
121	0.16896 15386 92596(02)	0.17686 13272 53247(00)

$N = 300$		
$i$	$X_i^n$	$W_n'(X_i^n)$
122	0.17073 86643 97687(02)	0.17857 78590 18452(00)
123	0.17253 33884 07672(02)	0.18038 21789 34597(00)
124	0.17434 66257 78456(02)	0.18228 18718 25591(00)
125	0.17617 93721 57181(02)	0.18428 54965 61106(00)
126	0.17803 27143 38727(02)	0.18640 27547 89126(00)
127	0.17990 78426 89313(02)	0.18864 46971 09744(00)
128	0.18180 60658 60659(02)	0.19102 39769 78230(00)
129	0.18372 88283 37200(02)	0.19355 51660 47093(00)
130	0.18567 77315 18488(02)	0.19625 51494 30925(00)
131	0.18765 45592 55524(02)	0.19914 36261 35969(00)
132	0.18966 13090 57773(02)	0.20224 37496 08365(00)
133	0.19170 02306 03538(02)	0.20558 29575 48059(00)
134	0.19377 38737 76303(02)	0.20919 40612 59533(00)
135	0.19588 51493 01395(02)	0.21311 66968 92843(00)
136	0.19803 74063 11253(02)	0.21739 92907 56593(00)
137	0.20023 45330 54717(02)	0.22210 17702 33716(00)
138	0.20248 10898 76033(02)	0.22729 93817 84612(00)
139	0.20478 24882 04038(02)	0.23308 81972 22952(00)
140	0.20714 52368 44350(02)	0.23959 32745 71523(00)
141	0.20957 72896 96028(02)	0.24698 11437 11762(00)
142	0.21208 85516 34067(02)	0.25547 96378 30989(00)
143	0.21469 16418 42953(02)	0.26541 08377 29415(00)
144	0.21740 30968 97619(02)	0.27724 88800 06507(00)
145	0.22024 53745 02475(02)	0.29172 85834 77932(00)
146	0.22325 04339 47069(02)	0.31006 84153 02829(00)
147	0.22656 67666 71338(02)	0.33448 59076 06618(00)
148	0.22997 51746 38731(02)	0.36961 00629 21528(00)
149	0.23393 23523 10660(02)	0.42754 81977 49874(00)
150	0.23874 80976 36942(02)	0.55859 77929 72507(00)

## ACKNOWLEDGMENTS

We wish to thank Professor C. Wood and Dr. G. Rubloff for stimulating our interest in this problem, and for helpful discussions. We would also like to thank Drs. B. Veal, J. E. Robinson, J. W. Garland, S. Kirkpatrick, W. E. Rudge and N. Dalton for useful conversations. Finally we wish to acknowledge W. J. Cody of the Applied Mathematics Division of Argonne National Laboratory for helpful consultations on the Hermite function generator programs, and the computation centers of Argonne National Laboratory and Northern Illinois University for excellent service.



## REFERENCES

1. R. KRONIG, *J. Opt. Soc. Amer.* **12** (1926), 547.
2. H. A. KRAMERS, *Atti. Congr. Intern. Fisici. Como.* **2** (1927), 545.
3. E. C. TITCHMARSH, "Introduction to the Theory of Fourier Integrals," Clarendon Press, Oxford, 1948; M. J. LIGHTHILL, "Introduction to Fourier Analysis and Generalized Functions," University Press, Cambridge, 1959.
4. R. COURANT AND D. HILBERT, "Methods of Mathematical Physics," Volume I, Interscience, New York, 1953.
5. N. DUNFORD AND J. T. SCHWARTZ, "Linear Operators Part II: Spectral Theory," Section XI.7, Interscience, New York, 1963.
6. See, for example, D. PINES, "Elementary Excitations in Solids" p. 288, W. A. Benjamin, New York, 1963.
7. E. C. TITCHMARSH, *ibid.*, p. 76.
8. W. MAGNUS, F. OBERHETTINGER, AND R. PAL SONI, "Die Grundlehren der Mathematischen Wissenschaften," Band 52, p. 249, Springer Verlag, New York, 1966. Note that the definition of the third Hermite polynomial  $H_3(x)$  on p. 250 is incorrect. The correct result is  $H_3(x) = 8x^3 - 12x$ .
9. N. DALTON AND W. E. RUDGE, private communications.
10. R. AFSHAR, F. M. MUELLER AND J. C. SHAFFER, ANL (unpublished).
11. V. W. HOCHSTRASSER, "Handbook of Mathematical Functions" (M. Abramowitz and I. A. Stegun, Eds.), Chapter 22, Dover, New York, 1965.
12. P. J. DAVIS AND I. POLANSKY, *op. cit.*, Chapter 25.
13. J. B. RUSSEL, *J. Math. Phys.* **12** (1933), 291.
14. H. E. SALZER, R. ZUKER AND R. CAPUANO, *J. Res. Nat. Bur. Sci.* **48** (1952), 111.
15. See also A. H. STROUD AND D. SECREST, "Gaussian Quadrature Formulas," Prentice-Hall, Englewood Cliffs, New Jersey, 1966, for 0 to 136, even to 30 decimal places where the weight factor (34) is used.
16. This point is discussed thoroughly in F. M. MUELLER, J. W. GARLAND, M. H. COHEN, AND K. H. BENNEMANN, to be published.
17. J. CALLAWAY AND A. J. HUGHES, *Phys. Rev.* **128** (1962), 134.
18. J. C. PHILLIPS, *Phys. Rev.* **104** (1956), 1263.
19. J. C. PHILLIPS, *Solid State Phys.* **18**, 63.
20. F. M. MUELLER, A. J. FREEMAN, J. O. DIMMOCK AND A. M. FURDYNA, *Phys. Rev.*, in press.
21. A. A. ABRIKOSOV, L. P. GORKOV, AND I. YE. DZHALOSHINSKI, "Quantum Field Theoretical Methods in Statistical Physics," p. 51, 2nd ed., Pergamon Press, Oxford, 1965.
22. J. B. RUSSEL, *J. Math. Phys.* **12** (1933), 274.

## Electronic Structure of Single Crystal and Amorphous $\text{Sb}_2\text{Se}_3$ <sup>1)</sup>

By

J. C. SHAFFER (a), B. VAN PELT (a), C. WOOD (a),  
J. FREEOUF (b), K. MURASE (b), and J. W. OSMUN (b)

The near normal incidence reflectivity of  $\text{Sb}_2\text{Se}_3$  has been measured upon both crystalline and amorphous samples. The data were obtained for two polarizations ( $E \parallel a$ ,  $E \parallel c$ ) in the cleavage plane of the crystal. The data were Kramers-Kronig analyzed and the implications of the results regarding the electronic structure of the compound were interpreted in terms of a valence bonding model. In particular the valence band electrons divide into those in weakly bonding resonance states and those in covalent bonding states. Upon the amorphous to crystalline transition it is the optical transitions originating in the resonance bonds which appear to be principally influenced.

Le degré de réflexion a été mesuré pour  $\text{Sb}_2\text{Se}_3$  cristallin et amorphe. Les données ont été obtenues pour deux polarisations ( $E \parallel a$ ,  $E \parallel c$ ) dans le plan de clivage du cristal. Les données ont été analysées d'après les relations Kramers-Kronig et les implications de la composition électronique du composé ont été interprétées suivant un modèle des liaisons de valence. En particulier les électrons de la bande de valence sont séparés en liaisons de résonance et liaisons covalentes. Avec la transition de l'état amorphe à l'état cristallin les transitions optiques tirent leur origine des liaisons de résonance qui sont principalement affectées.

### 1. Introduction

The optical properties of single crystal and amorphous  $\text{Sb}_2\text{Se}_3$  have been measured in the energy range 0 to 24 eV in order to characterize the influence of long range order on the electronic structure in this compound.

### 2. Experiment

Crystalline  $\text{Sb}_2\text{Se}_3$  is orthorhombic ( $a = 11.62 \text{ \AA}$ ,  $b = 11.77 \text{ \AA}$ ,  $c = 3.69 \text{ \AA}$ ) [1] of space group  $D_{2h}^{10}$ , type  $D_8^6$ , with 20 atoms, i.e., 4 molecules/unit cell. The atoms are arranged in a layer structure with layers  $\perp b$  and weak Sb-Se bonding [1] between layers and, therefore, the crystals exhibit natural cleavage  $\perp b$ . Excellent mirror-like surfaces for optical studies with polarizations  $E \parallel a$  and  $E \parallel c$  can be prepared by cleaving. However, great difficulty is experienced in preparing good surfaces perpendicular to the cleavage plane because the crystals are soft and easily deformed. Slight surface oxidation occurs if the crystals are exposed to air for long periods (days). Hence, all optical samples were either freshly cleaved or kept under an argon atmosphere prior to measurement.

<sup>1)</sup> This work was supported by the Advanced Research Projects Agency of the Department of Defense and was monitored by the Army Research Office, Durham, under Contract No. DA-ARO-D-31-124-71-01132. We wish, also, to acknowledge support by the U.S. Air Force Office of Scientific Research under contract numbers F44620-71-C-0025 and F44620-70-C-0020.

Single crystals of  $\text{Sb}_2\text{Se}_3$  were grown in a zone refiner [2] from 0.999999 purity elements after extensive zone refining of the compound. Amorphous films of  $\text{Sb}_2\text{Se}_3$  were prepared by controlled coevaporation of the elements [3] onto room-temperature fused quartz substrates.

Various spectrophotometers having overlapping energy ranges were used to cover the energy range 0 to 24 eV and comprised: a Cary 14R (0.4 eV to 6 eV); a McPherson 225 with Hinteregger Light Source<sup>2</sup> (4 to 12 eV); a McPherson 235 with Synchrotron Radiation Source (4 to 24 eV). Optical reflectivity was measured using the following apparatus: a Cary Model 1413 Reflectance Attachment (0.4 to 6 eV); a McPherson Reflectance Attachment (4 to 12 eV); reflectance apparatus described in [4] (4 to 24 eV). Sheet polarizers were used in the range 0.4 to 6 eV (Polaroid HR and Polarcote ultraviolet polarizers). The naturally occurring polarization of about 80% in the Synchrotron radiation and reflectance attachment obviated the need for polarizers in the range 4 to 24 eV.

### 3. Reflectance Results

The room-temperature reflectivity at near normal incidence of single crystal  $\text{Sb}_2\text{Se}_3$  in the energy range 0 to 5 eV is shown in Fig. 1 for both  $E \parallel a$  and  $E \parallel c$ . This data represents the maximum values obtained from measurements taken on five different single crystal samples of  $\text{Sb}_2\text{Se}_3$ . The reflectance values of the various samples were found to lie within a range  $\pm 2\%$ .

The structure displayed by the single crystals in the range of the broad reflectivity maxima, 1 to 6 eV, is in good general agreement [5] with the data of Shintov et al. [6] (see Table I) and is a result of structure in the joint density of states. The spectrum of  $\text{Sb}_2\text{Se}_3$  near the absorption edge indicates that the extremes of the valence and conduction bands occur at different points in the zone and that absorption begins with an indirect transition at 1.16 eV [7]; this is appreciably higher than the value of 0.89 eV reported by Sobolev et al. [8]. From

symmetry considerations on isostructural  $\text{Sb}_2\text{S}_3$ , Audzijonis et al. [9] have suggested that the maximum of the valence band at the center of the Brillouin zone  $\Gamma$  is split into subbands  $\Gamma_2$ ,  $\Gamma_6$ , and  $\Gamma_4$ . Correspondingly, Sobolev et al. have associated transitions between  $\Gamma_2(E \parallel a)$ ,  $\Gamma_6(E \parallel b)$ ,  $\Gamma_4(E \parallel c)$ , and the state  $\Gamma_1$  at the conduction band minimum with the lowest direct transition in  $\text{Sb}_2\text{Se}_3$ .

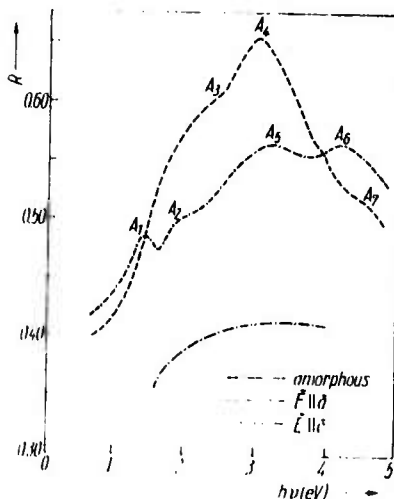
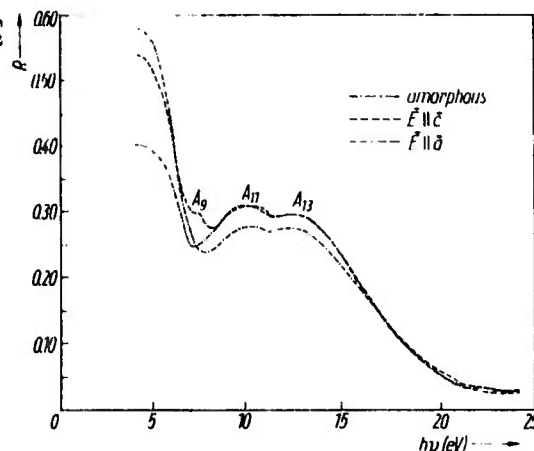


Fig. 1. Near-normal reflectance for single crystal ( $E \parallel a$ ,  $E \parallel c$ ) and amorphous  $\text{Sb}_2\text{Se}_3$  at low energy. The reflectances have been extrapolated parabolically below the low-energy cutoff of the data for purposes of performing the Kramers-Kronig analysis. The resultant static dielectric constants lie within the spread of experimentally measured values of the low frequency dielectric constant.

<sup>2</sup>) Instrument loaned by Dr. P. Yuster, Solid State Division, Argonne National Laboratory.

Fig. 2. Near-normal reflectance for single crystal ( $R \parallel a$ ,  $R \parallel c$ ) and amorphous  $\text{Sb}_2\text{Se}_3$  at higher energy



(peak  $A_1$  in Fig. 1). No assignments have been made for the higher energy structure in the broad reflectivity maximum.

In marked contrast, the broad reflectivity maximum of the amorphous form of  $\text{Sb}_2\text{Se}_3$  is featureless showing that the selection rules for these transitions are broken and/or the critical point structure in the densities of states is greatly smoothed in the absence of long range order. The absorption edge of amorphous  $\text{Sb}_2\text{Se}_3$  at approximately 1.26 eV [3] closely corresponds to the indirect edge in the crystalline material. In addition, as has been found in other V-VI compound semiconductors [10] as well as Te [11], the reflectance of the amorphous material is significantly lower than that of the crystal in the visible to near ultraviolet spectral range. Interference oscillations prevent extension of the reflectivity measurements below about 1.5 eV.

The near normal incidence reflectance measured in the range 4 to 24 eV using synchrotron radiation is shown in Fig. 2. At energies greater than 8 eV, a marked similarity exists between the reflectance of the crystalline and amorphous samples. The minima at 8 eV closely correspond to those of  $\text{As}_2\text{S}_3$  and  $\text{As}_2\text{Se}_3$  [10] and similarly, by Kramers-Kronig analysis, appear to be associated with the threshold of a new absorption process from a deeper lying valence band. In the region of this second broad maxima, two marked peaks are observed at 10 and 12.4 eV independent of the orientation of the  $E$ -vector or the absence of long range order.

#### 4. Kramers-Kronig Analysis

The normal incidence reflectivity data up to 24 eV described above have been Kramers-Kronig analyzed by the method described by Afshar et al. [12, 13]. The method essentially consists of two steps. First the Kramers-Kronig relation between the phase and the modulus of the complex reflection coefficient

$$\varphi(\omega) = \frac{P}{\pi} \int_{-\infty}^{+\infty} \ln r(\omega') \frac{\omega' d\omega'}{\omega' - \omega} \quad (1)$$

514 J. C. SHAFFER, B. VAN PELT, C. WOOD, J. FREBOUF, K. MURASE, and J. W. OSMUN

is separated into two portions, i.e.,  $\varphi(\omega) = \chi(\omega) + \theta(\omega)$ , where

$$\chi(\omega) = \frac{P}{\pi} \int_{-\infty}^{\infty} \frac{\ln \varrho(\omega') d\omega'}{\omega' - \omega} \quad (2)$$

and

$$\theta(\omega) = \frac{P}{\pi} \int_{-\infty}^{\infty} \frac{A(\omega') d\omega'}{\omega' - \omega} \quad (3)$$

In these relations  $\varrho(\omega')$  is the modulus of the complex reflectivity for a system of charged classical harmonic oscillators chosen to have a reflectivity  $\varrho^2(\omega')$  which closely fits the measured reflectivity data at the high and low frequency extremes of the measured range.  $\varrho^2(\omega')$  thus extrapolates the data into the unmeasured spectral regions. The  $\chi(\omega)$  can easily be computed from the appropriate dielectric function (which gives rise to  $\varrho^2(\omega')$ ) of the form

$$\epsilon(\omega) = 1 + \sum_{i=1}^N \frac{f_i}{(\omega_i^2 - \omega^2) + i I'_i \omega} \quad (4)$$

where the constants ( $f_i$ ,  $I'_i$ ) parametrize the strength and linewidth of the classical oscillator with resonant frequency  $\omega_i$ . In the analysis of the data presented here two oscillators are sufficient to fit the data at the extremes of the data

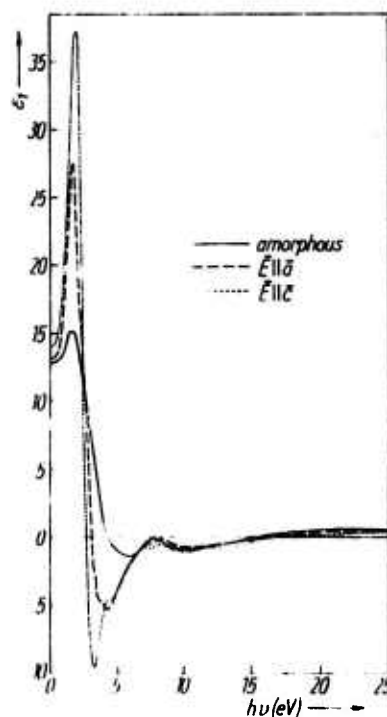


Fig. 3. Real part of dielectric function of crystalline ( $E \parallel a$ ,  $E \parallel c$ ) and amorphous  $\text{Sb}_2\text{Se}_3$ .

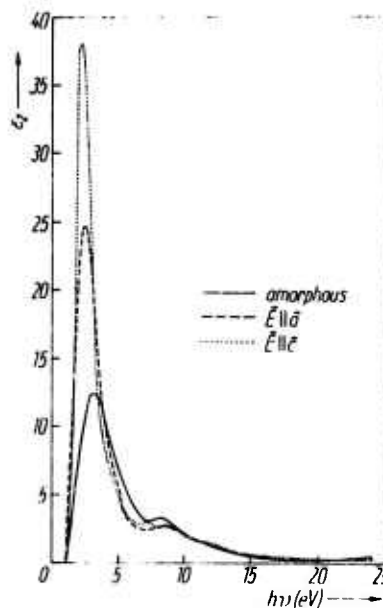


Fig. 4. Imaginary part of dielectric function of crystalline ( $E \parallel a$ ,  $E \parallel c$ ) and amorphous  $\text{Sb}_2\text{Se}_3$ .

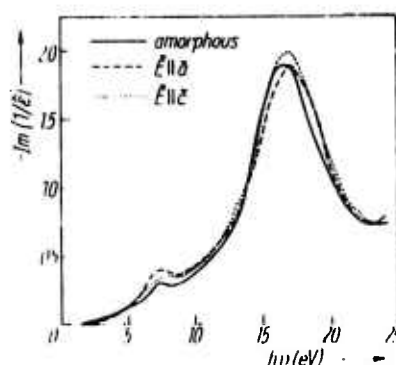


Fig. 5. Energy loss function of crystalline ( $E \parallel a$ ,  $E \parallel c$ ) and amorphous  $\text{Sb}_2\text{Se}_3$ .

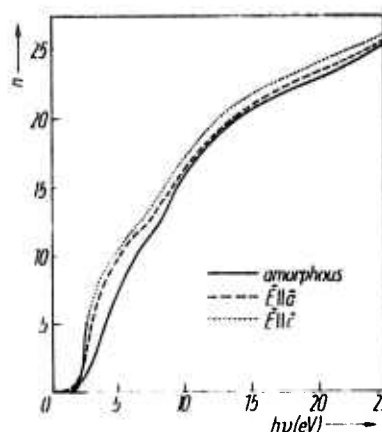


Fig. 6.  $n$  vs.  $h\nu$  from sum rule for crystalline ( $E \parallel a$ ,  $E \parallel c$ ) and amorphous  $\text{Sb}_2\text{Se}_3$ .

range.  $\theta(\omega)$  is computed by expanding  $\ln(\omega')$ , the residual portion of  $\ln r(\omega')$ , in Hermite functions, and using the Hermite representation of the Hilbert transform operator developed by Afshar et al. [12] to compute the integral in (3). All optical functions are obtainable from  $\rho(\omega) \exp\{i\phi(\omega)\}$ , the complex reflection coefficient.

In Fig. 3 the real part of the dielectric function  $\epsilon_1(\omega)$  is shown for the two polarizations  $E \parallel a$  and  $E \parallel c$  and for the amorphous film as computed from the reflectivity data above. In Fig. 4 the same display is made for  $\epsilon_2(\omega)$  and Fig. 5 shows a plot of the energy loss function  $-\text{Im } \epsilon^{-1}$  in each case.

An additional interesting feature is the comparison of the sum rules on  $\sigma_1(\omega) = \omega \epsilon_2(\omega)/4\pi$  for the three cases. Thus we have computed

$$\frac{2}{\pi} \int_0^\infty \omega' \epsilon_2(\omega') d\omega' = \frac{4\pi e^2}{m} \frac{1}{\Omega} n(\omega) \quad (5)$$

in each case, where  $n(\omega)$  is the number of electrons per molecule participating in transitions up to frequency  $\omega$ , and  $\Omega$  is the unit cell volume. Fig. 6 shows  $n(\omega)$  for both polarizations of the crystal as well as for the amorphous film. In each instance there is a discernible inflection in  $n(\omega)$  between 7.0 and 8.0 eV beyond which  $n(\omega)$  rises sharply with the onset of the  $A_{11}$  and  $A_{13}$  peaks. The inflection is slightly obscured for  $E \parallel c$  by the  $A_9$  peak as one might expect from Fig. 2 and 3. These results are similar to those reported on  $\text{As}_2\text{Se}_3$  and  $\text{As}_2\text{S}_3$  in [14]. In all cases, however,  $n(\omega)$  attains a value of about 25  $\rightarrow$  26 electrons/molecule for  $h\omega = 24$  eV. Since each molecule of  $\text{Sb}_2\text{Se}_3$  nominally contributes 28 valence electrons it is assumed that the sum rule will saturate at an energy slightly greater than 24 eV at 28 electrons/molecule.

### 5. Discussion of Results

It is reasonable to assume that the transitions which dominate up to 8 eV involve electrons associated with the weak resonating p-bonds which were hypothesized by Mooser and Pearson [15] to occur in  $\text{Sb}_2\text{Se}_3$  on the basis of the struc-

tural determinations of Tideswell et al. [1]. At energies greater than about 8 eV the onset of transitions from the energetically lower states associated with covalent bonds occurs. Study of the  $n(\omega)$  curves in Fig. 6 indicates that the lower frequency portion would saturate at about 16 electrons/molecule and the higher frequency portion at an additional 12 electrons/molecule. This compares favorably with the number of electrons/molecule associated with the weaker and stronger bonds in Table 6 of [1].

The suppression of the reflectivity of the amorphous sample in the visible and near ultra-violet arise from sensitivity of the transitions from the resonating p-bonds to the lack of long range order. This could result from a reduction of the average matrix element for these transitions or from reduction of the density of states in the conduction or valence bands in the appropriate energy range. XPS measurements [16] on amorphous and crystalline  $\text{Sb}_2\text{Se}_3$  indicate quite small differences in the magnitude of the valence band density of states in the energy range of interest. Thus this effect seems to be associated either with reduced matrix elements in the amorphous material or with some influence of the disorder on the conduction band density of states, perhaps through a reduction of Sb 5d-band overlap contributions.

The XPS data also locates the 4d bands of Sb at 33 eV below the top of the valence band thus obviating any direct influence of these levels on the optical properties in the spectral range studied. The results reported here on the sum rule confirm this.

As a check upon the accuracy of the Kramers-Kronig analysis and our low-frequency extrapolations of reflectivity we have directly computed  $\epsilon_1^f(0, \omega)$ , the "frequency-dependent" static dielectric constant, from the Kramers-Kronig formula

$$\epsilon_1^f(0, \omega) = 1 + \frac{2}{\pi} \int_0^{\omega} \frac{\epsilon_2(\omega')}{\omega'} d\omega', \quad (6)$$

where  $\epsilon_2(\omega)$  is the imaginary part of the dielectric function obtained from our Kramers-Kronig analysis of reflectivity. Since  $\epsilon_1(0)$  is fixed by the value of reflectivity in the low frequency limit we can compare  $\epsilon_1^f(0, \omega)$  with  $\epsilon_1(0)$ . In

Table I  
Reflectivity peaks energies (eV) of  $\text{Sb}_2\text{Se}_3$  \*

polarization	$A_1$	$A_2$	$A_3$	$A_4$	$A_5$	$A_6$	$A_7$	$A_8$	$A_9$	$A_{11}$	$A_{12}$	$A_{13}$
$E \parallel a$	1.36 (1.36)	2.00 (1.97)			3.30 (3.15)	4.15 (3.95)	— (4.56)			10.0		12.4
$E \parallel c$			2.30 (1.90)	3.00 (2.30)	— (2.95)	3.90 (3.20)	4.52 (4.0)	(5.6)	(7.4)	(9.5)	(10.8)	12.4

\*) The bracketed data are from the work of Shutov et al. [6] where the peaks  $A_8$  to  $A_{12}$  were measured with unpolarized light with  $E \perp c$  so that the structure in this spectral region is not strictly comparable with the present results.



every case we find that  $\epsilon_1^f(0, \omega)$  approaches the  $\epsilon_1(0)$  value assumed by extrapolating  $R(\omega)$  to low frequency and is equal to  $\epsilon_1(0)$  within 5% at the upper end of our data range.  $\epsilon_1^f(0, \omega)$  is found to be smaller for the amorphous sample reflecting the smaller overall magnitude of the low frequency reflectivity in this case.

### 6. Summary

To summarize, the following points are to be emphasized. In comparison with the work of Shutov et al. [9] this study shows some differences in the exact location of certain of the critical point structure in the reflectance of crystalline  $\text{Sb}_2\text{Se}_3$  (see Table I). In general, however, the agreement is quite close in the overlapping region studied. In regard to comparison of the amorphous and crystalline samples it is seen that the absorption, as characterized by  $\epsilon_2(\omega)$ , for example shows nearly complete smearing of the critical point structure in the amorphous material in the visible and near ultraviolet. Furthermore there is an overall suppression of the absorption in comparison with that of the crystalline samples in this range. Beyond about 8.0 eV the spectra of the crystalline material (for either polarization) and the amorphous film are virtually identical. The close similarity of the energy loss function. In  $\epsilon^{-1}$  for the three cases (there is a near coincidence of the valence band plasma peaks at about 17 eV) suggests that the occupied bands have similar overall properties in the amorphous and crystalline material, e.g., number of states/volume and average effective mass. We conclude, therefore, that the influence of the lack of long range order upon the electronic structure of  $\text{Sb}_2\text{Se}_3$  is confined, for all practical purposes, to the conduction bands and higher valence bands of the material, and that loss of long range order alters the weakly bonding resonance electron states producing a substantial change in the optical properties.

### Acknowledgements

We wish to thank Dr. H. Fritzsche and Dr. F. M. Mueller for their valuable comments and suggestions and the staff of the Wisconsin Physical Science Laboratory for their experimental assistance.

### References

- [1] N. W. TIDESWELL, F. H. KRUSE, and J. C. McCULLOUGH, *Acta Cryst.* **10**, 99 (1957).
- [2] C. WOOD, B. VAN PELT, and E. HYLAND, *Rev. Sci. Instrum.* **43**, 1374 (1972).
- [3] R. MUELLER and C. WOOD, *J. Non-Cryst. Solids* **7**, 301 (1972).
- [4] U. GERHARDT and G. W. RUDLOFF, *Appl. Opt.* **8**, 305 (1969).  
G. W. RUDLOFF, H. FRITZSCH, U. GERHARDT, and J. FREEDER, *Rev. Sci. Instrum.* **42**, 1507 (1971).
- [5] C. WOOD, Z. HURYCH, and J. C. SHAFFER, *J. Non-Cryst. Solids*, **8** 209 (1972).
- [6] S. D. SHUTOV, V. V. SOBOLEV, Y. V. POPOV, and S. N. SHESTATSKII, *phys. stat. sol.* **31**, K23 (1969).
- [7] B. VAN PELT and C. WOOD, to be published.
- [8] V. V. SOBOLEV, S. D. SHUTOV, and S. N. SHESTATSKII, *Moldavian Acad. Sciences, USSR*, 183 (1969).
- [9] A. AUDZIJONIS, J. BATAJUNAS, A. KARPUS, and S. KUDZMANSKAS, *Lietuvos Fizikos Rinkiny* **5**, 481 (1965).
- [10] R. ZALLEN, R. E. DREWS, R. L. EMERALD, and M. L. SLADE, *Phys. Rev. Letters* **26**, 1564 (1971).



- [11] J. STUKE, *J. non-cryst. Solids* **4**, 1 (1970).
- [12] R. AFSHAR, F. M. MUELLER, and J. C. SHAFFER, *J. Comp. Phys.*, in the press.
- [13] R. AFSHAR, F. M. MUELLER, and J. C. SHAFFER, to be published.
- [14] R. E. DREWS, R. L. EMERALD, M. L. SLADE, and R. ZALLEN, *Solid State Commun.* **16**, 293 (1972).
- [15] E. MOOSER and W. B. PEARSON, *J. Phys. Chem. Solids* **7**, 65 (1958).
- [16] C. WOOD, J. C. SHAFFER, and W. V. PROCTOR, *Phys. Rev. Letters* **29**, 485 (1972).

*(Received August 8, 1972)*

Subject classification: 2, 13, 20.1

Physics Department, Northern Illinois University, DeKalb

Optical Properties of the Amorphous System  $\text{Sb}_{1-x}\text{Se}_x$

By

R. MUELLER, J.C. SHAFFER, and C. WOOD

A study of optical properties as a function of composition for the amorphous system  $\text{Sb}_{1-x}\text{Se}_x$  has been made. The reflectivities of thin films from this system with  $x = 0.24$ ,  $0.60$ , and  $0.97$  were measured over a range of photon energies limited at low frequency by interference oscillations and at high frequency by the spectrometer cutoff at  $11.0$  eV. The films were prepared by an evaporation technique (1) which allowed simultaneous preparation of samples with widely varying compositions. The reflectivities of the three samples are shown in Fig. 1. The data for the Se rich ( $x = 0.97$ ) film resembles previous results (2,3) on amorphous Se. The film ( $x = 0.60$ ) shows a reflectivity similar to previous results reported for amorphous  $\text{Sb}_2\text{Se}_3$  (4). The Sb-rich ( $x = 0.24$ ) sample has a reflectivity fundamentally different from those of the other samples. This indicates that chemical alterations as a function of composition occur in this system. These probably include conversion of Se p-electrons from lone-pair to bonding character with increasing Sb concentration.

In order to employ the reflectivity for further study of these effects we have performed Kramers-Kronig inversions on these data using a technique outlined previously (4,5). Here we present two results of the analysis, the imaginary part of the dielectric constant  $\epsilon_2(\omega)$ , and results obtained from the frequency dependence of the f-sum rule

$$\int_0^\omega \omega' \epsilon_2(\omega) d\omega' = \frac{2\pi^2}{m_0} e^2 N(\omega) \quad , \quad (1)$$

where  $e$  is the electronic charge,  $m_0$ , the (free) electronic mass, and  $N(\omega)$  the number of electrons per unit volume participating in transitions up to

frequency,  $\omega$ .

Fig. 2 shows the  $\epsilon_2(\omega)$  spectra for the three samples. The extrapolations into the unmeasured ranges were made as in (4). In the overlapping range, the  $\epsilon_2$  spectrum for the sample with  $x = 0.60$  closely matches that reported previously (4) for a different sample of amorphous  $\text{Sb}_2\text{Se}_3$  for which reflectivity data extended to 24.0 eV. The samples with  $x = 0.60$  and  $x = 0.97$  show two main peaks in their  $\epsilon_2$  spectra, consistent with the division of the valence band p-electrons into lone-pair and bonding states. The sample with  $x = 0.24$  exhibits no discernible division. The low frequency spectra exhibit edges in  $\epsilon_2(\omega)$  which compare favorably with the fundamental absorption edges obtained from reflectivity and transmission measurements (1).

Fig. 3 presents the results from the f-sum rule (eq. 1) in terms of the number of electrons per formula unit ( $\text{Sb}_{1-x}\text{Se}_x$ ),  $n(\omega)$ , exhausted in electronic transitions up to frequency  $\omega$ . To compute these results it is required that the mass density of each sample be known. The densities were estimated from a linear extrapolation fitted to the crystalline densities of Se and  $\text{Sb}_2\text{Se}_3$ . The absolute values of  $n(\omega)$  are lower than those which would be obtained from the correct densities of the amorphous films. As the principal interest is in trends in the system and the existence and frequency location of structure in  $n(\omega)$  this expedient is justified.

The following conclusions are inferred from the analysis. No clear separation of the Se p-electrons into bonding and non-bonding states is present for  $x \leq 0.24$ . The reflectivity and  $\epsilon_2$  spectra show such separation of these states for the  $x = 0.60$  and  $x = 0.97$  samples. The sum rule exhibits inflections at  $h\omega = 6.7$  eV and 6.5 eV for  $x = 0.60$  and 0.97, respectively, but no inflection for the  $x = 0.24$  sample. We conclude that at lower Se compositions the p-electrons of Se are all in bonding states in order to satisfy

the valence requirements of the Sb atoms. It is also evident that  $n(\omega)$  for the  $\text{Sb}_{0.40}\text{Se}_{0.60}$  sample rises above the same quantity for  $\text{Sb}_{0.03}\text{Se}_{0.97}$  in the low frequency region. This suggests that, for the former, not only Se lone p-pairs but other p-electrons of both Se and Sb parentage contribute to the low frequency absorption band. A similar conclusion has been made from photoemission studies on  $\text{Sb}_2\text{Se}_3$  (6). Also the recent electronic structure calculation of Chen (7) indicates considerable overlap of lone pair and bonding states for elemental amorphous Se.

#### Acknowledgements

We wish to thank Dr. P. Yuster for the use of the McPherson 225 Monochromator and to acknowledge financial support from A.R.P.A. Research Grant No. DA-ARO-D31-124-72-G115.

References

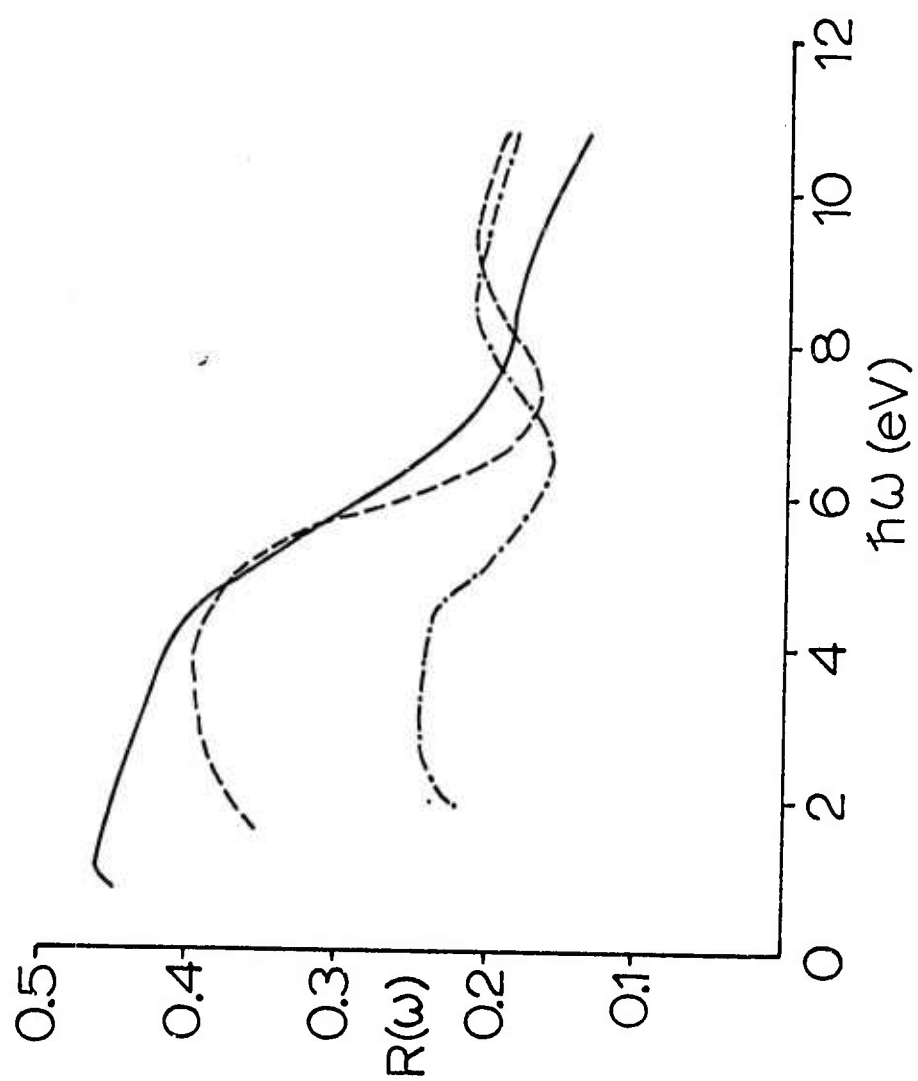
- (1) C. WOOD, R. MUELLER, and L.R. GILBERT, J. Non.-Cryst. Solids (to be published).
- (2) A.C. LEIGA, J. Opt. Soc. Amer. 58, 1441 (1968).
- (3) J. STUKE, Adv. Solid State Phys. - Festkörper problem IX, Pergamon Press  
Vedweg (Braunschweig) 1969.
- (4) J.C. SHAFFER, B. VAN PELT, C. WOOD, J. FREEOUF, K. MURASE, and J.W. OSMUN,  
phys. stat. sol. (b) 54, 511 (1972).
- (5) R. AFSHAR, F.M. MUELLER, and J.C. SHAFFER, J. Comp. Phys. 11, 190 (1973).
- (6) Z. HURYCH, D. BUCZEK, C. WOOD, G.J. LAPTYERE, and A.D. BAER, Solid State  
Comm. (to be published).
- (7) I. CHEN, Phys. Rev. (to be published).

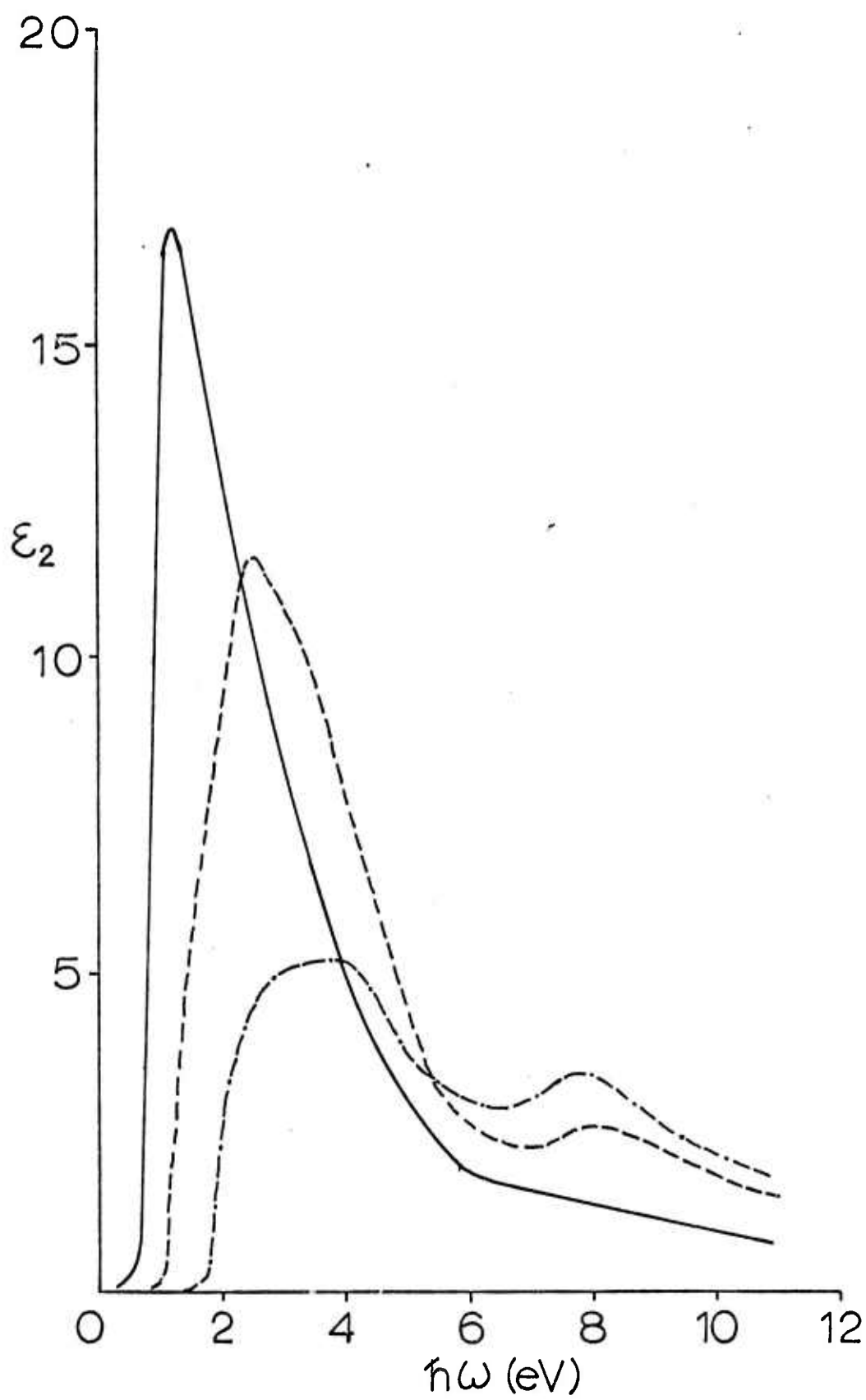
Figure Captions

Fig. 1. Front surface reflectivity  $R(\omega)$  versus photon energy  $(h\omega)$  for film compositions:  $x = 0.24$  (—);  $x = 0.60$  (----); and  $x = 0.97$  (-·-·-·-·-).

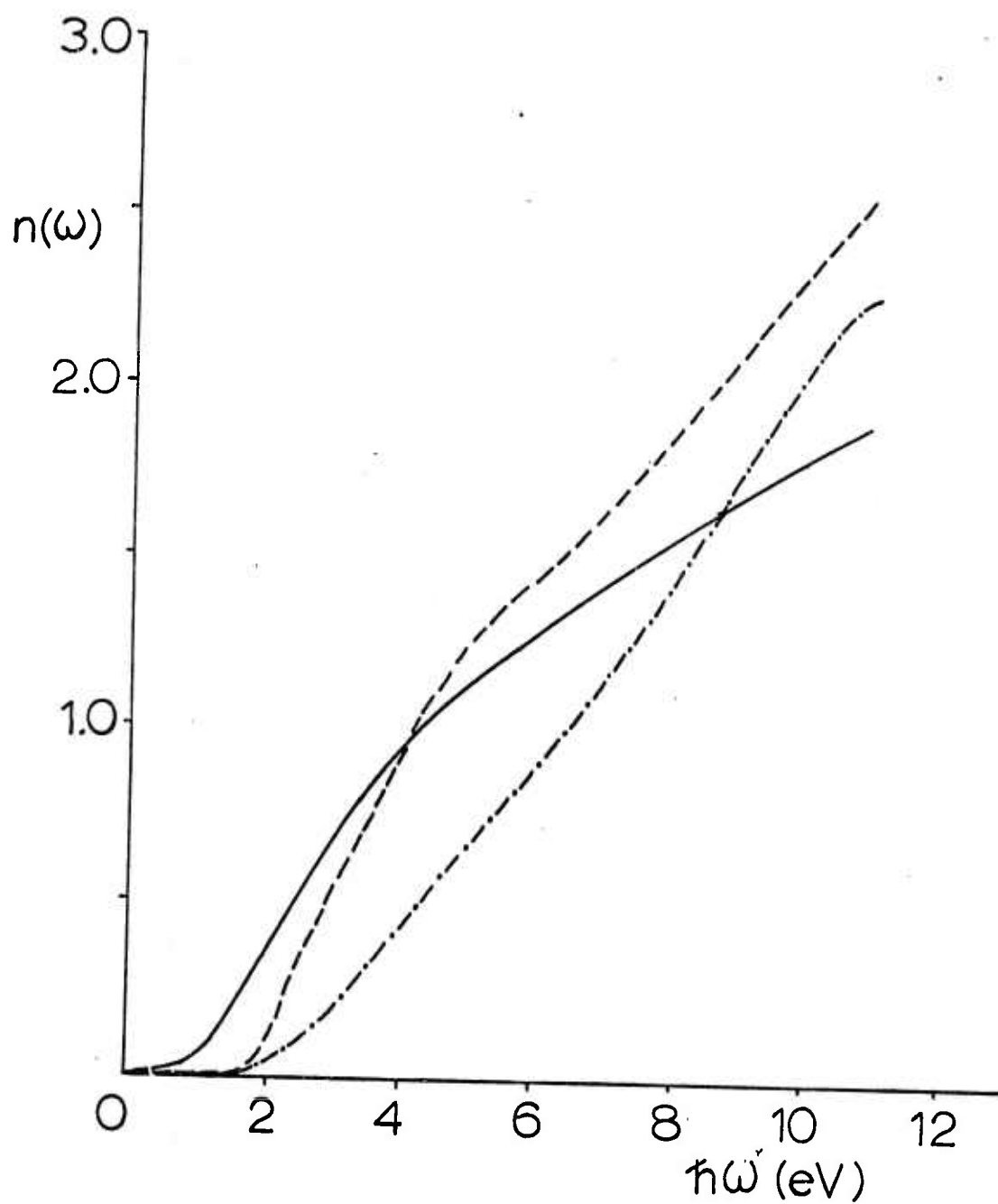
Fig. 2. Imaginary part of the dielectric constant  $\epsilon_2(\omega)$  versus  $(h\omega)$  for  $x = 0.24$  (—);  $x = 0.60$  (----); and  $x = 0.97$  (-·-·-·-·-).

Fig. 3. Number of electrons  $n(\omega)$  versus  $(h\omega)$  for  $x = 0.24$  (—);  $x = 0.60$  (- - - -); and  $x = 0.97$  (-·-·-·-·-).









AMORPHOUS GROUP III - CHALCOGENIDES\*

C. Wood, L.R. Gilbert, C.M. Garner, and J.C. Shaffer

Department of Physics  
Northern Illinois University  
DeKalb, Illinois 60115

Abstract

A vacuum co-evaporation technique has been developed based on an elongated substrate, whereby essentially the complete compositional range of an amorphous binary system can be prepared in one evaporation. The method is particularly suited to the preparation of amorphous films, wherein the systems are not governed by equilibrium phase diagram considerations.

This "elongated substrate" technique has been applied to the Ga- $\text{Sb}$  and In- $\text{Sb}$  systems, and by investigating the optical and transport properties by means of transmittance, reflectance, electrical conductivity and thermoelectric measurements as a function of temperature the effects of compositional variations on the distribution of electronic states have been determined. Particular attention has been paid to compositional regions in which delocalization of electronic states could occur. The results have been compared with studies we have made on other binary systems, i.e.,  $\text{Sb-Te}$  and  $\text{Ge-Te}$ , and interpreted in terms of the chemical bonding.

\* This work was supported by the Advanced Research Projects Agency of the Department of Defense, Office under

## 1. Introduction

This work is part of a continuing study to compare the properties of the amorphous and crystalline phases of binary chalcogenide systems and to determine the influence of chemical bonding on the properties of the binary amorphous solids. To this end, we have previously (Wood et al. 1973a) selected several binary systems  $Sb_{1-x}Se_x$ ,  $Ge_{1-x}Se_x$  and  $Ge_{1-x}Te_x$  on the basis of the molecular ionization energies of the end components and attempted to trace the development of these energies across the whole phase diagram. Here we report similar studies on the Group III - chalcogenides:  $Ga_{1-x}Sb_x$  and  $In_{1-x}Se_x$ .

We have developed a vacuum co-evaporation technique to perform these studies whereby essentially the whole compositional range of an amorphous binary system can be prepared in one evaporation. This greatly facilitates the investigation of a continuous change in physical properties over a wide compositional range and, since amorphous systems are not governed by equilibrium phase diagram considerations, the method is particularly suited to the preparation of amorphous materials.

## 2. Experimental Procedures

Basically, the apparatus for this coevaporation technique consisted of a Varian ion-pumped bell-jar system with two widely-spaced Airco-Thamesal 270° electron beam (EB) guns, each gun being controlled by modified Sloan Omni IIA quartz-crystal oscillator evaporation-rate controllers (Wood et al. 1973b). An elongated substrate holder of length equal to the spacing between the EB guns, i.e., nearly the width of an 18" bell jar, and capable of being maintained at any temperature between room and liquid  $N_2$  temperature, was situated above and in line with the EB guns. A series (~ 28) of fused quartz substrates, in which each alternate substrate was electroded, was held in

juxtaposition in the holder. Thus each substrate received a different ratio of the two elements because of differing proximity to the two EB guns (the exact ratio being controlled by the settings of the evaporation rate controllers), i.e., compositions over a wide range were prepared simultaneously.

Our present system incorporated two such holders situated at different heights above the crucibles. Hence, for a given ratio of evaporation rates from the two EB guns, a broad sampling of compositions in thick films was obtained in a lower substrate rack and a smaller compositional gradient about a preselected composition was obtained in thin films from the upper rack.

In this experiment the elements used for evaporation were of high purity (6-9's) and the evaporations were carried out in a pressure of  $\sim 10^{-7}$  mm Hg, or lower, at extremely low evaporation rates ( $\sim 1$  to  $2 \text{ \AA/sec}$ ). The compositions of selected films were determined by electron microprobe analysis and, from the geometry of the system and the measured evaporation rates, the composition was calculated (Wood et al. 1973b) as a function of position in the holder. The films were determined to be amorphous or crystalline by x-ray diffraction.

Details of measurement of optical, electrical and thermo-emf measurements have been reported elsewhere (Wood et al. 1973b), only the results of these measurements will be reported here.

### 3. The $\text{Ga}_{1-x}\text{Se}_x$ System

There are very few references in the literature to amorphous modifications of  $\text{Ga}_{1-x}\text{Se}_x$ . Thomas, 1971, states that diffractometer traces taken from GaSe films deposited on room-temperature substrates in some cases showed no diffraction peaks. Electron-diffraction studies have been made by

52

Tatarinova, 1956, on evaporated films of a-GaSe and by Andrievskii et al., 1963, on evaporated films of a-Ga<sub>2</sub>Se<sub>3</sub>. In both instances the nearest neighbor distance was found to be considerably less than that of its crystalline counterpart although, in contrast with GaSe, the short-range order in a-Ga<sub>2</sub>Se<sub>3</sub> was similar to that of c-Ga<sub>2</sub>Se<sub>3</sub>. However, from the method of preparation great reliance cannot be placed on the stated compositions in any of the above references (Mueller and Wood, 1972).

### 3.1 Preparation

Three evaporation runs were carried out for this system. In the first evaporation, the substrates were held at room-temperature and the film thicknesses were  $\sim 1.2$  microns and  $\sim 3000$  Å for the lower and upper substrates, respectively. Over a considerable range of Ga-rich compositions the films appeared visually to be nonspecularly reflecting, i.e., as if partially crystalline, although x-ray diffraction measurements showed no evidence of crystallinity. Optical and electron microscopic examination of the surface of a film of composition  $x = 0.18$  revealed randomly spaced globular outgrowths, of  $\sim 40$  microns diameter, on a background having a pebbled appearance (fig. 1). These outgrowths were revealed to be predominantly Ga by focussing on one in a scanning electron microscope (Breton) and examining the omitted x-ray spectra. The outgrowths were not observed in films in the more Se-rich ( $x > 0.55$  and  $0.39$  for lower and upper racks, respectively) composition ranges.

Two subsequent evaporations were carried out with the substrates cooled by liquid N<sub>2</sub>. The surface temperatures of the substrates were  $\sim 120^\circ$  K during evaporation. Here the thicknesses for both runs were  $\sim 6000$  Å and  $\sim 1500$  Å for the lower and upper substrate racks, respectively. Again, all films were amorphous by x-ray diffraction although compositions with  $x < 0.35$  for the lower rack were non-specularly reflecting. For the whole upper rack  $x$  was  $> 0.35$ .

### 3.2 Optical and Transport Properties

Optical and transport measurements were made only on films which did not exhibit surface outgrowths, i.e., in the composition range  $x > 0.38$ .

The optical absorption coefficients ( $\alpha$ ) for most films ranged between  $10^3$  to  $10^5$   $\text{cm}^{-1}$  and, when plotted against photon energy ( $h\nu$ ), fitted well to an  $(\alpha h\nu)^{1/2}$  vs  $h\nu$  relationship for non-direct transitions (Davis and Mott 1971; Tauc, 1970). The absorption edge positions were determined from the intercept of the curves with the  $\alpha = 0$  axis and these values for the optical energy gap,  $E_g$ , are shown in fig. 2 as a function of composition.  $E_g$  was found to decrease non-linearly with increasing temperature in the range  $100^\circ \text{K}$  to  $300^\circ \text{K}$ .

Optical reflectivity measurements were extended to 12 eV (Yuster) on two films of composition  $x = 0.52$  and  $0.87$  and the results Kramers-Kronig analyzed to yield values of  $\epsilon_2$  (fig. 8) for comparison with other amorphous chalcogenide systems. Details of these measurements are reported elsewhere (Mueller et al., 1973).

Lateral-type four-probe conductivity measurements were made only on films in the composition range  $0.38 < x < 0.67$ , although the resistances of several films in this range were too high ( $> 10^{15}$  ohms) to be measured. No systematic trend in conductivity with composition was apparent. All other films were either too high in resistance to be measured ( $x > 0.67$ ) or exhibited outgrowths ( $x < 0.38$ ). The conductivity generally showed a temperature dependence of  $T^{-1/2}$  in the range  $200^\circ \text{K}$  to  $300^\circ \text{K}$  (fig. 3) suggesting a variable range hopping mechanism (Davis and Mott, 1971) to be predominant but, as Table 1 shows, the densities of states are generally unrealistically low. Annealing tended to increase the resistance of the films beyond the measureable range.

For several selected thick films ( $\sim 6000 \text{ \AA}$  thickness) of widely differing composition the conductivity measurements were extended to above room-temperature. A marked increase in conductivity over one or several orders of magnitude at a particular temperature was taken as an approximate indication of the amorphous-crystalline phase transformation. The crystallization temperature was taken to be at the point of maximum slope and this data is plotted as a function of composition in fig. 4. Crystallization was confirmed to have occurred by x-ray diffraction measurements.

We were unable to make thermo-electric measurements on any films because of their high resistances.

#### 4. The $\text{In}_{1-x}\text{Se}_x$ System

There are two references in the literature to amorphous modifications of  $\text{In}_{1-x}\text{Se}_x$ . These are the electron diffraction studies of Tartarinova and Kazmazovskaya, 1962, on a-InSe and of Andrievskii et al., 1963, on a- $\text{In}_2\text{Se}_3$ .

##### 4.1 Preparation

In view of our experience with the  $\text{Ga}_{1-x}\text{Se}_x$  system we did not attempt to use room-temperature substrates in the preparation of the  $\text{In}_{1-x}\text{Se}_x$  system. Only one evaporation was performed onto liquid  $\text{N}_2$  cooled substrates. Films were found to be amorphous by x-ray diffraction over the composition range:  $x > 0.88$  for the lower substrate films,  $\sim 9000 \text{ \AA}$  thickness, and  $x > 0.48$  for the upper substrate films,  $\sim 2500 \text{ \AA}$  thickness. No globular outgrowths were observed for any compositions, however, partially crystalline films did exhibit pebbled surfaces.

##### 4.2 Optical and Transport Properties

In the composition range  $0.49 < x < 0.78$  the optical absorption was found to obey an  $(ah\nu)^n$  vs  $h\nu$  relationship with  $n = 1/2$ . Beyond this range, for  $0.78 < x < 0.9$ , the exponent  $n$  appeared to be  $\sim 2/3$  instead of  $1/2$ . For

$x > 0.9$ ,  $n$  was  $\sim 1$ . The values of  $E_g$ , determined from the intercepts with the  $\alpha = 0$  axis are plotted in fig. 5. Again,  $E_g$  was found to decrease with increasing temperature in the range  $100^\circ \text{ K}$  to  $300^\circ \text{ K}$  and to vary non-linearly with temperature.

Values for  $\epsilon_2$  determined from reflectivity measurements on two films of composition  $x = 0.49$  and  $0.96$  are shown in fig. 8.

For this system a  $\ln \sigma \sim$  vs  $T^{-1/2}$  behavior was obtained only for indium-rich compositions  $x < 0.54$ . A transition between the  $T^{-1/2}$  and  $T^{-1}$  dependences occurred at the composition  $x = 0.54$  with the conductivity obeying the  $T^{-1}$  relationship near room-temperature. For  $x > 0.54$ , the conductivity obeyed a  $\ln \sigma \sim$  vs  $T^{-1}$  relationship with the slope, i.e., thermal activation energy at absolute zero,  $\Delta E_0$  increasing with increasing Se content. The results for typical films are shown in fig. 6, with the compositional dependence of  $\Delta E_0$  compared with that of  $E_g$  in fig. 5. Values of the intercepts with the  $T^{-1} = 0$  axis in fig. 5, i.e.,  $\sigma_0$  are listed in Table 2. Several films gave unrealistically high values.

The crystalline temperatures determined from high temperature conductivity measurements, as for the  $\text{Ga}_{1-x}\text{Se}_x$  system, are plotted in fig. 4.

Seebeck coefficients could be measured in this system. They were p-type for all films and the values are shown in fig. 7 as a function of composition.

## 5. Discussion and Conclusions

Crystalline GaSe is built-up of 4-fold layers, each containing two close-packed gallium layers and two close-packed selenium layers with covalent bonding within and van der Waals bonding between layers.



(InSe has a similar structure). From infrared and Raman studies, Wieting and Verble, 1972, proposed that there is an appreciable ionic or coulombic interlayer interaction. The coordination numbers of gallium and selenium atoms are four and three respectively. Three crystallographically distinct polytypes of GaSe have been reported in the literature (Shubert et al. 1955; Basinski et al., 1961). The  $\beta$  ( $D_{6h}^4$ ) and  $\epsilon$  ( $C_{3h}^1$ ) structures have two-layer hexagonal stacking sequences whereas the  $\gamma$  ( $C_{3v}^5$ ) structure has a three-layer rhombohedral stacking sequence. Basinski et al., 1961, have suggested that the stacking fault energy in GaSe is very low and that transformation from one modification to another can readily take place.

The other major compound in the  $Ga_{1-x}Se_x$  system is  $Ga_2Se_3$  which is of cubic 3 B-type structure with some metal atom sites vacant (Hahn and Klinger, 1949). The coordination numbers for Ga and Se in this structure are 4 and 2.6, respectively according to Andrievskii et al., 1963. Thus, one third of the cation sites are vacant. Palatnik et al. 1967, have proposed that each Se donates two electrons to two Ga atoms forming  $sp^3$  hybrid bonds thus leaving a lone p-pair on the Se atoms which is directed towards the Ga vacancy.

Although we have direct evidence of phase-segregation occurring only for compositions with  $x < \sim 0.4$ , the strong tendency for Ga (and In) to take up a tetrahedral coordination in the crystalline form and the ease with which various modifications are produced is strongly suggestive that phase segregation could be occurring in other composition regions of these systems. Phase-segregation is a possible explanation for the unrealistically low values calculated for the densities of states in the variable range hopping conductivity mode in  $Ga_{1-x}Se_x$ . Preliminary annealing experiments did not improve these density of states values (Lewis, 1972) and, e.g., Ga rejection in the Ge-rich region and Se rejection for the Se-rich compositions

tended to raise the resistances beyond the measurable range. A Poole-Frenkel type mechanism has been invoked to explain the conduction behavior of GaSe (Tatsuyama et al. 1971). The conductivity vs field (F) dependence in a broad sample of films was not exponential; the dependence was ohmic at low fields and approximately  $F^{1.6}$  at high ( $F \sim 3000$  volts  $\text{cm}^{-1}$ ) fields.

The room temperature resistivities of the amorphous and crystalline phases, where  $x = 0.5$  and  $0.6$ , closely corresponded except for  $\text{In}_2\text{Se}_3$  where the value was about  $10^5$  lower in crystal.

No discontinuities in physical properties occurred in  $\text{Ga}_{1-x}\text{Se}_x$  system over the measured composition range. However in the  $\text{In}_{1-x}\text{Se}_x$  system a marked discontinuity occurred in optical and electrical properties at  $x \sim 0.78$ . Below this composition the values of  $\sigma_0$  were  $< 10^2$   $\text{ohm}^{-1} \text{cm}^{-1}$  which suggests hopping-type conductivity at band edges (Davis and Mott, 1971) whereas for  $x \geq 0.79$  the values of  $\sigma_0$  jumped to improbably high numbers. (Approximate values of  $\exp(\gamma/k)$ , determined from the temperature dependence of  $E_g$ , i.e.,  $\gamma \sim \beta/2$ , although large (up to  $\sim 10^{-3}$  eV  $^\circ\text{K}^{-1}$ ) were insufficiently large to reduce  $\sigma_0$  to commonly occurring values). The values of  $E_g$ ,  $\Delta E_0$ ,  $B$  and  $n$  (Table 2) also rose rapidly at this composition. Band calculations for GaSe by Bassini and Parravicini, 1967, indicate that the bottom of the conduction band is formed from the  $p_x$  and  $p_y$  orbitals of both the Ga and Se atoms whereas the valence band is formed from the  $p_z$  orbitals of Se and the  $s$  orbitals of Ga. Similar considerations should apply to InSe. As the concentration of Se increases to high values, from the relative ionization energies of In and Se, one would expect the lone-pair  $p$ -electrons of Se to form the valence band (Kastner, 1972). Perhaps this occurs at  $x \sim 0.78$ . We do see evidence of this in the  $\epsilon_2$  spectra (see below, fig. 8) as we have for other amorphous systems (Mueller et al. 1973).

The optical energy gaps,  $E_g$ , for the  $\alpha\text{-Ga}_{1-x}\text{Se}_x$  system agree reasonably

well with crystalline phases for corresponding values of  $x$ . For example, the absorption edge in c-GaSe arises from direct exciton transitions (Brebner and Mooser, 1967) and has been reported to have values ranging from 2.01 to 2.139 eV (Grandolfo et al., 1971). For a-GaSe,  $E_g$  is  $\sim 1.9$  eV. This shift to lower energies may be ascribed to the difference in short-range order (according to Tartarinova, 1956, there are 6 atoms in the first coordination sphere of a-GaSe).

Electroabsorption measurements by Askerov et al., 1972, on c-Ga<sub>2</sub>Se<sub>3</sub> showed the optical absorption edge to occur at 2.13 eV and arise from indirect transitions. In contrast to GaSe, no exciton line structure was observed. Its absence was ascribed to the strong defect nature of the lattice, which would obviously apply to the amorphous structure. For a-Ga<sub>2</sub>Se<sub>3</sub>,  $E_g$  is  $\sim 2.3$  eV. This higher value is consistent with the fact that although a tetrahedral coordination of atoms is maintained in the amorphous state (Andrievskii et al., 1963) the radius of the first coordination sphere ( $2.25\text{\AA}$ ) is less than the Ga-Se distance in the crystalline state.

The absorption edge in a-InSe begins with indirect transitions at  $\sim 1.19$  eV (Andriyashik et al., 1968) and again shows exciton structure, as in GaSe. This value is considerably higher than the optical gap of a-InSe, where  $E_g \sim 0.7$  eV, which is surprising in view of the identical tetrahedral coordination of the amorphous and crystalline phases (Tartarinova and Kazmazovskaya, 1962). Much better agreement is obtained between the optical gaps of c-In<sub>2</sub>Se<sub>3</sub> ( $E_g \sim 1.2$  eV, Nasledov et al., 1958) and a-In<sub>2</sub>Se<sub>3</sub> where the short range order closely corresponds.

The  $\epsilon_2$ -spectra in fig. 8 were obtained from Kramers-Kronig analyses of the reflectivities of a collection of samples chosen to indicate the trends occurring in each of the four binary amorphous systems studied. For each of the systems, Sb<sub>1-x</sub>Se<sub>x</sub>, Ge<sub>1-x</sub>Se<sub>x</sub>, and In<sub>1-x</sub>Se<sub>x</sub>, a similar pattern appears. As

the Se content increases the lower band in the spectrum shifts upward in energy and reduces in strength. At sufficiently large Se concentrations in these three systems a second higher energy band appears, and the spectra appear qualitatively similar to that of amorphous Se (Leiga, 1968; Stuke, 1969). For these systems it is conjectured that two phenomena are occurring with increasing Se content. The p-electron contribution to the occupied densities of states is splitting into two parts associated with bonding and weakly bonding (lone pairs) states. Secondly, the bonding ( $\sigma$ ) and anti-bonding ( $\sigma^*$ ) states are separating from one another producing a larger energy gap. The weakly bonding states are assumed more or less stationary in energy between the  $\sigma$  and  $\sigma^*$  states. For the  $\text{Ga}_{1-x}\text{Se}_x$  system there is no clear separation between the lone pair and  $\sigma$  states with Se concentration as for the other systems. It appears that at lower Se concentration for the systems  $\text{M}_{1-x}\text{Se}_x$  studied here the Se p-electrons are primarily utilized in M-Se bonds. At higher Se concentrations significant Se-Se bonding and/or M-Se bonding with Se in 2-fold coordination occurs. This results in a separation of the p-electron states in weakly bonding and bonding types. Also the decreased metallic character of the M-Se and Se-Se bonding relative to the M-M bonding produces wider  $\sigma$ - $\sigma^*$  gaps as evidenced by the shifts with increasing Se concentrations of the lower peaks in the optical spectra to higher energy.

- Andrievskii, A.I., Nabitovich, I.D., and Voloshchuk, Ya. V., 1963, *Soviet Physics-Crystallography*, 7(6), 704.
- Basinski, Z.S., Dove, D.B., Mooser, E., 1961, *Copte rendu de la reunion de la Societe Suisse de Physique*, 34.
- Bassini, F., and Parravicini, G.P., 1967, *Nuovo Cim.*, B50, 95.
- Breton, B.: Scanning electron microscopy was kindly performed by B. Breton of Kent-Cambridge Electronics.
- Davis, E., and Mott, N.F., 1971, Electronic Processes in Non-Crystalline Materials (Clarendon, Oxford, 1971).
- Kastner, M., 1972, *Phys. Rev. Letters*, 28, 355.
- Leiga, A.C., *J. Opt. Soc. Amer.*, 58, 1441 (1968).
- Lewis, A., 1972, *Phys. Rev. Letters*, 29, 1555.
- Mueller, R., and Wood, C., 1972, *J. Non-Cryst. S.*, 7 (1972), 301.
- Mueller, R., Shaffer, J., Wood, C., 1973, *Phys. Status Solidi*, in print.
- Palatnik, L.S., Koshkin, V.M., and Komnik, Yu. F., 1967, Chemical Bonds in Semiconductors and Solids, N. Sirota ed.
- Shubert, K., Dorro, E., and Kluge, M., 1955, *Z. Metallkunde*, 46, 216.
- Stuke, J., *Adv. Solid State Phys. - Festkörper problem IX*, Pergamon Press Vedweg (Braunschweig) 1969.
- Tartarinova, L.I., 1956, *Soviet Physics-Crystallography*, 1 (5), 423.
- Tartarinov, L.I., and Kazmazovskaya, T.S., 1962, *Soviet Physics-Crystallography*, 6 (3), 538.
- Tatsuyama, C., Hamuguchi, C., Tomita, H., 1971, *Jap. J. of App. Phys.*, 10 (12), 1698.
- Tauc, J., 1970, Optical Properties of Solids, ed. by F. Abeles (North-Holland, Amsterdam, 1970).
- Thomas, M.B., 1971, *Thin Solid Films*, 9 (1971) 273.
- Wieting, and Verble, 1972, *Phys. Rev. B.*, 5 (4), 1473.
- Wood, C., Gilbert, L.R., Mueller, R., and Garner, C.M., 1973a, *J. Vac. Sci. Tech.* (in print).
- Wood, C., Mueller, R., and Gilbert, L.R., 1973b, *J. Non-Cryst. S.* (in print).
- Yuster, P.: We wish to acknowledge the loan of a McPherson 225 monochromator.

Table 1

Optical and Electrical Parameters of  $\alpha\text{-Ga}_{1-x}\text{Se}_x$   
Films as a Function of Composition

Film #	x	$E_g$ (eV)	B $\text{eV}^{1-\frac{1}{n}}\text{-cm}^{-1}$	n	Hopping Activation Energy $\Delta W$ (eV) $\times 10^{-3}$	Density of States ( $\text{cm}^{-3}$ )
1L12	.38				1.5	$6.6 \times 10^4$
2U6	.40				10	$2.5 \times 10^{16}$
2U7	.42	1.39	3.4	$\frac{1}{2}$		
2U11	.49	1.77	4.1	$\frac{1}{2}$		
1L14	.50				3.3	$1.1 \times 10^7$
2U13	.52	2.03	4.4	$\frac{1}{2}$		
2U17	.60	2.27	5.2	$\frac{1}{2}$		
2U19	.63	2.22	4.9	$\frac{1}{2}$		
1L16	.64				4.7	$6.8 \times 10^6$
2U21	.66	2.15	4.4	$\frac{1}{2}$		
2L16	.67				6.8	$5.5 \times 10^{13}$
2U23	.69	2.12	4.1	$\frac{1}{2}$		
2U25	.72	2.03	3.8	$\frac{1}{2}$		
2U27	.74	1.95	3.5	$\frac{1}{2}$		
2L21	.87	1.99	6.6	$\frac{2}{3}$		
2L25	.93	2.08	7.4	1		

Optical and Electrical Parameters of  $\alpha\text{-In}_{1-x}\text{Se}_x$   
Films as a Function of Composition

Film #	x	$E_g$ (eV)	$B \times 10^5$ $\text{eV}^{-1}\text{-}\frac{1}{n}\text{cm}^{-1}$	n	$\Delta E_0$ (eV)	$\sigma_0$ $\Omega^{-1}\text{cm}^{-1}$	Seebeck Coefficient ( $\mu\text{V}/^\circ\text{C}$ )
U7	.49	.73	3.5	$\frac{1}{2}$			
U8	.51				$1.83 \times 10^{-3}$ *	$1.68 \times 10^{11}$ *	+57
U9	.53	.75	2.9	$\frac{1}{2}$			
U10	.55				.20	$1.1 \times 10^{-2}$	+153
U11	.56	1.04	3.1	$\frac{1}{2}$			
U12	.58				.49	$1.2 \times 10^1$	+408
U13	.60	1.21	3.5	$\frac{1}{2}$			
U14	.62				.52	$6.6 \times 10^1$	+563
U15	.64	1.39	3.6	$\frac{1}{2}$			
U16	.65				.49	$1.4 \times 10^2$	+676
U17	.67	1.59	3.9	$\frac{1}{2}$			
U18	.69				.37	$5.7 \times 10^1$	+524
U19	.70	1.82	4.3	$\frac{1}{2}$			
U20	.71				.41	$2.6 \times 10^0$	+660
U21	.73	1.76	4.1	$\frac{1}{2}$			
U23	.75	1.69	3.8	$\frac{1}{2}$			
U24	.76				.57	$8.0 \times 10^1$	+56
U25	.78	1.63	3.7	$\frac{1}{2}$			
U26	.79				1.39	$1.3 \times 10^{11}$	
U27	.79	1.98	6.4	$\frac{2}{3}$			
L21	.90	2.04	6.9	1			
L22	.92				1.47	$1.6 \times 10^{12}$	
L23	.93	2.03	7.2	1			
L25	.95	2.03	6.9	1	1.36	$1.1 \times 10^{10}$	
L26	.95						
L27	.96	2.06	6.8	1			

\* Arrhenius activation energy and intercept at  $T^{-1} = 0$  obtained from  $T^{-1}$  plot

Figure Captions

1. Surface of  $\text{Ga}_{0.82}\text{Se}_{0.18}$  film taken by a scanning electron microscope
  - a. Globular outgrowths on background field (x 50).
  - b. Pebbled structure of background field (x5000).
2. Room temperature optical activation energy ( $E_g$ ) versus composition for  $\text{Ga}_{1-x}\text{Se}_x$  system.
3. Log electrical conductivity ( $\sigma$ ) versus  $T^{-1/2}$  for  $\text{Ga}_{1-x}\text{Se}_x$  system.
4. Crystalization temperature versus composition for  $(\Delta)\text{Ga}_{1-x}\text{Se}_x$ ,  $(O)\text{In}_{1-x}\text{Se}_x$ .
5. Optical activation energy at room temperature (O) and thermal activation energy ( $\Delta$ ) extrapolated to  $0^\circ\text{K}$  versus film composition for the  $\text{In}_{1-x}\text{Se}_x$  system.
6. Log electrical conductivity ( $\sigma$ ) versus reciprocal of absolute temperature ( $T$ ) for  $\text{In}_{1-x}\text{Se}_x$  system.
7. Room temperature Seebeck coefficient versus film composition for  $\text{In}_{1-x}\text{Se}_x$  system.
8. Imaginary part of the dielectric constant ( $\epsilon_2$ ) versus photon energy for systems  $\text{Ga}_{1-x}\text{Se}_x$ ,  $\text{In}_{1-x}\text{Se}_x$ ,  $\text{Ge}_{1-x}\text{Se}_x$ , and  $\text{Sb}_{1-x}\text{Se}_x$ .



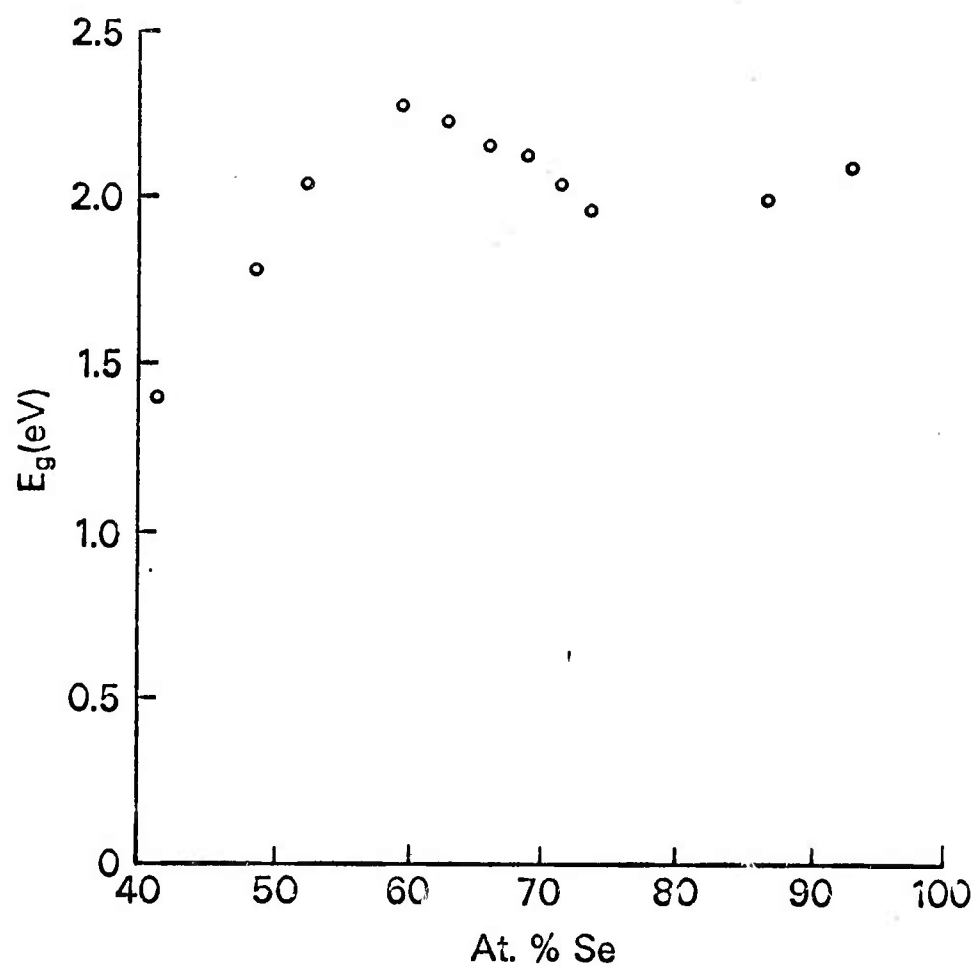
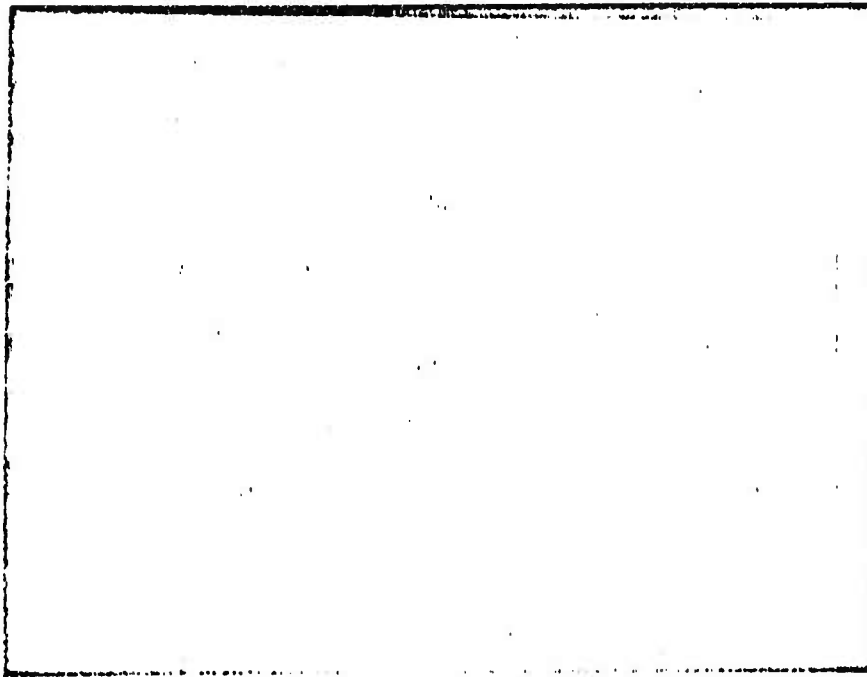
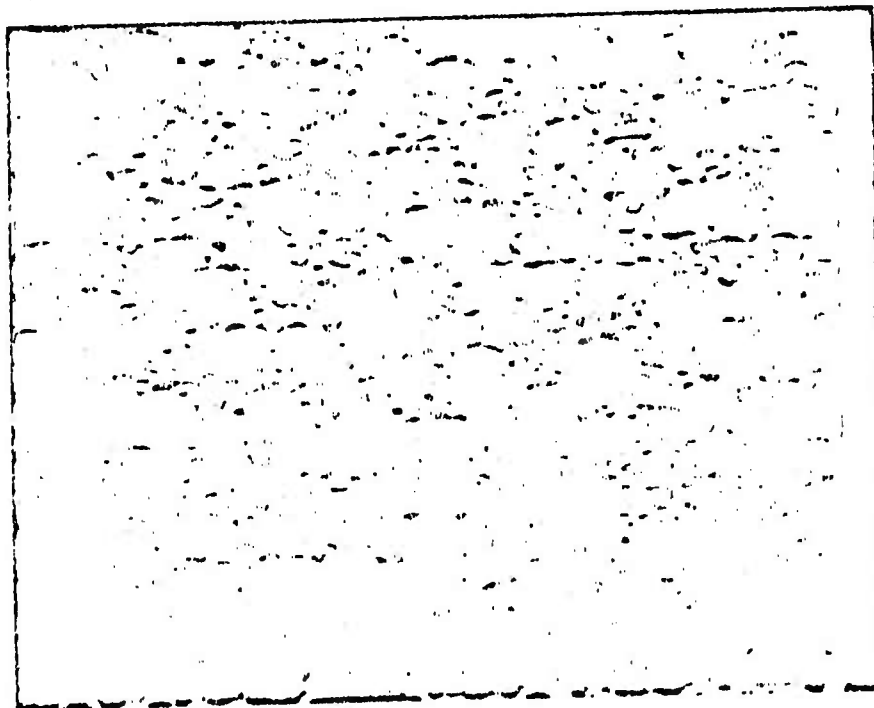


fig. 2

a



b



Reproduced from  
best available copy.



Fig 1 wood et al

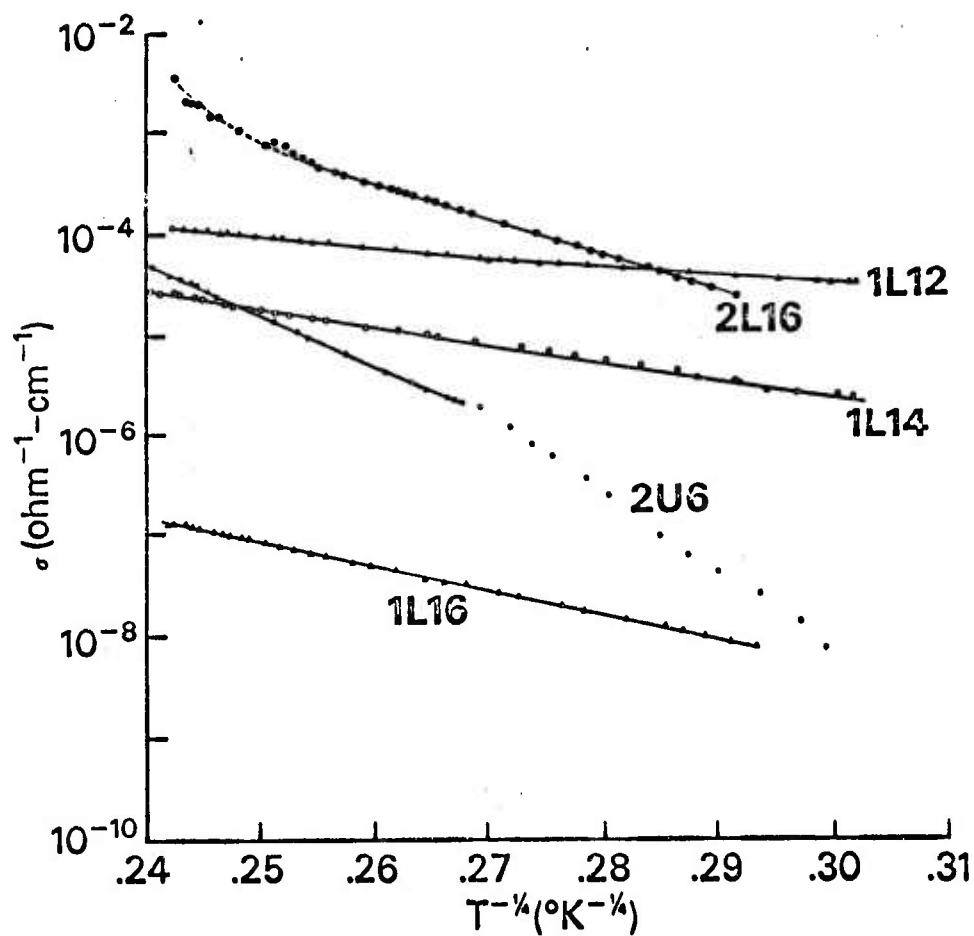


fig. 3

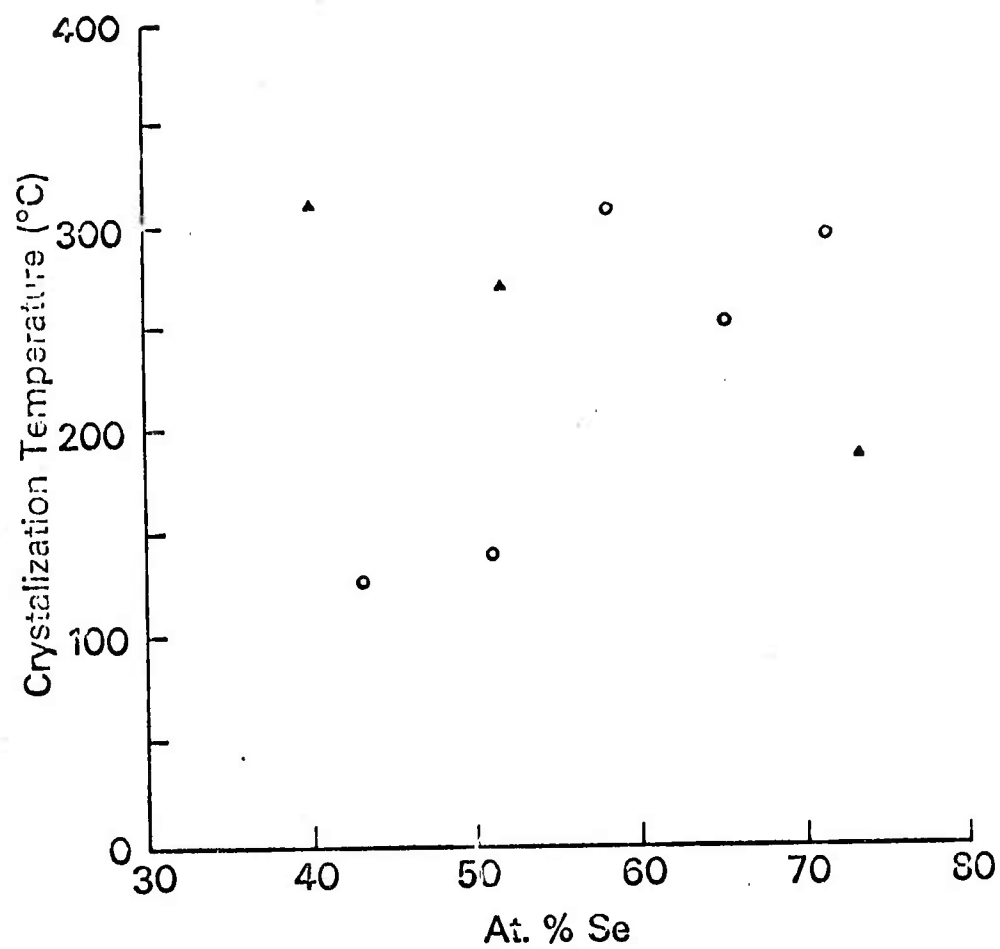


fig 4

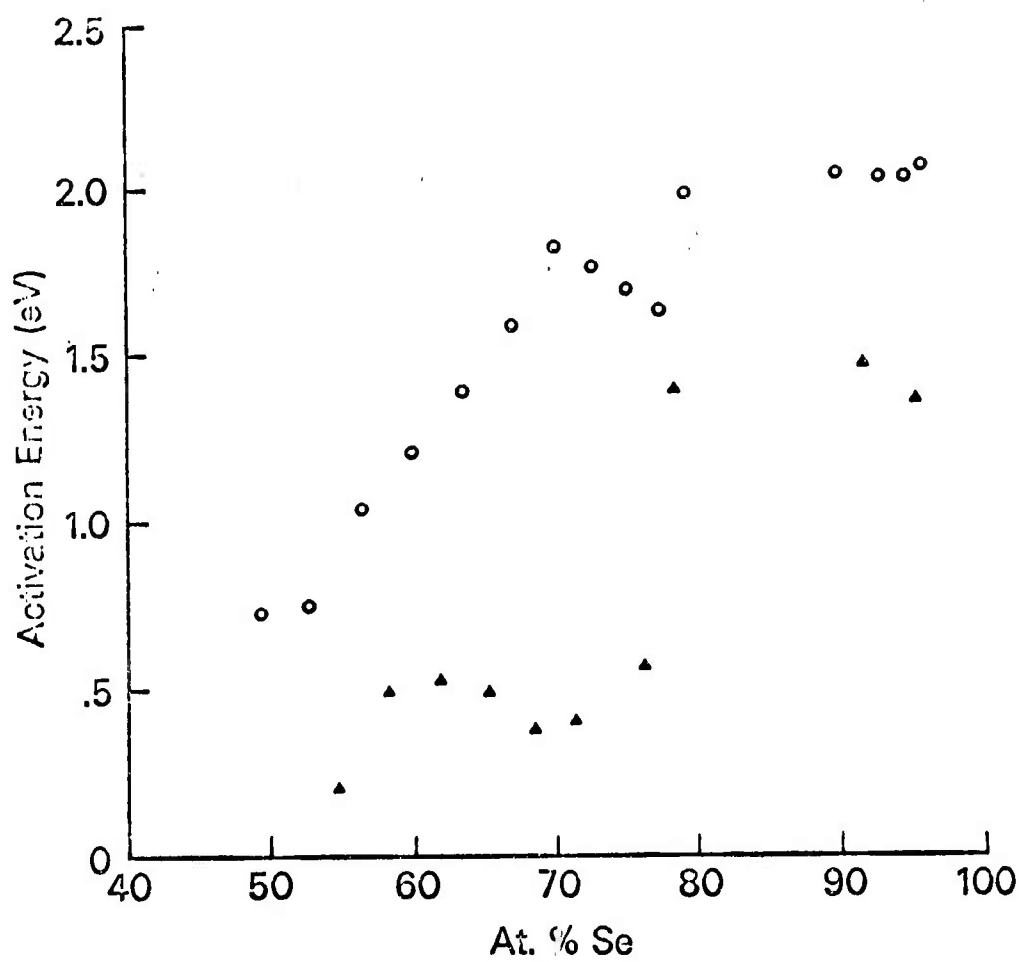


fig. 5

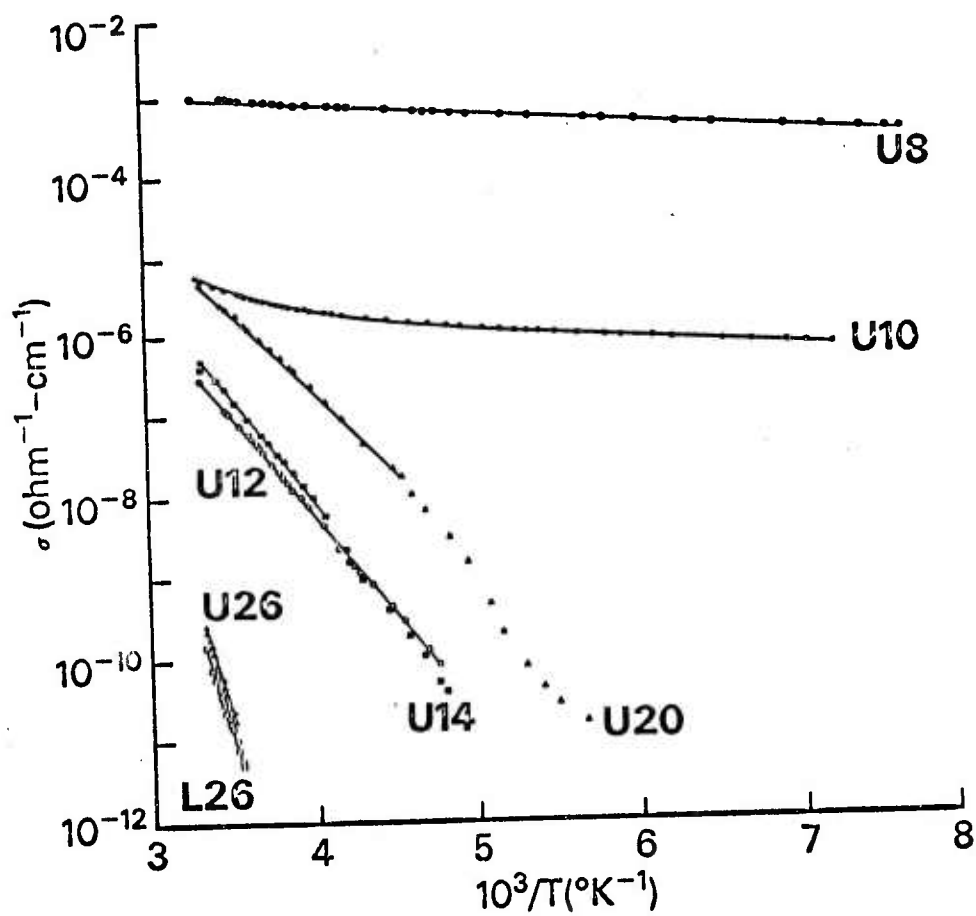


Fig. 6

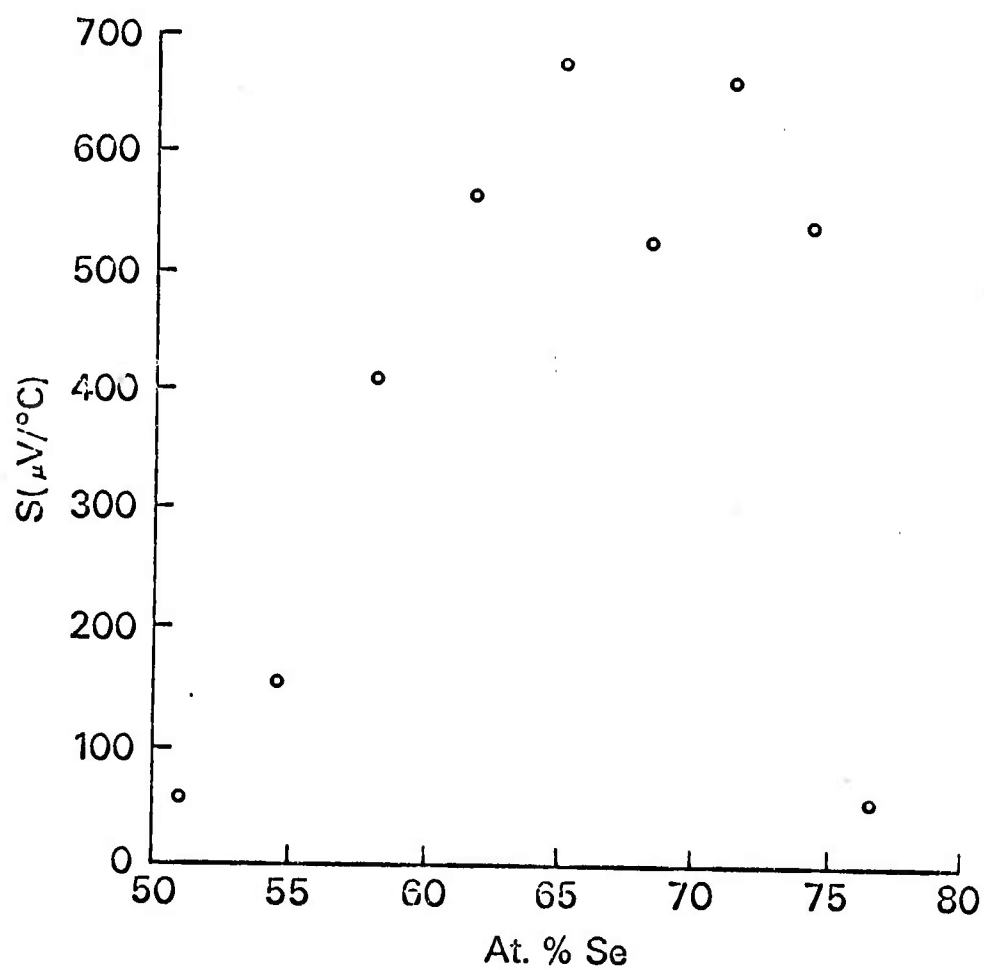


Fig. 7

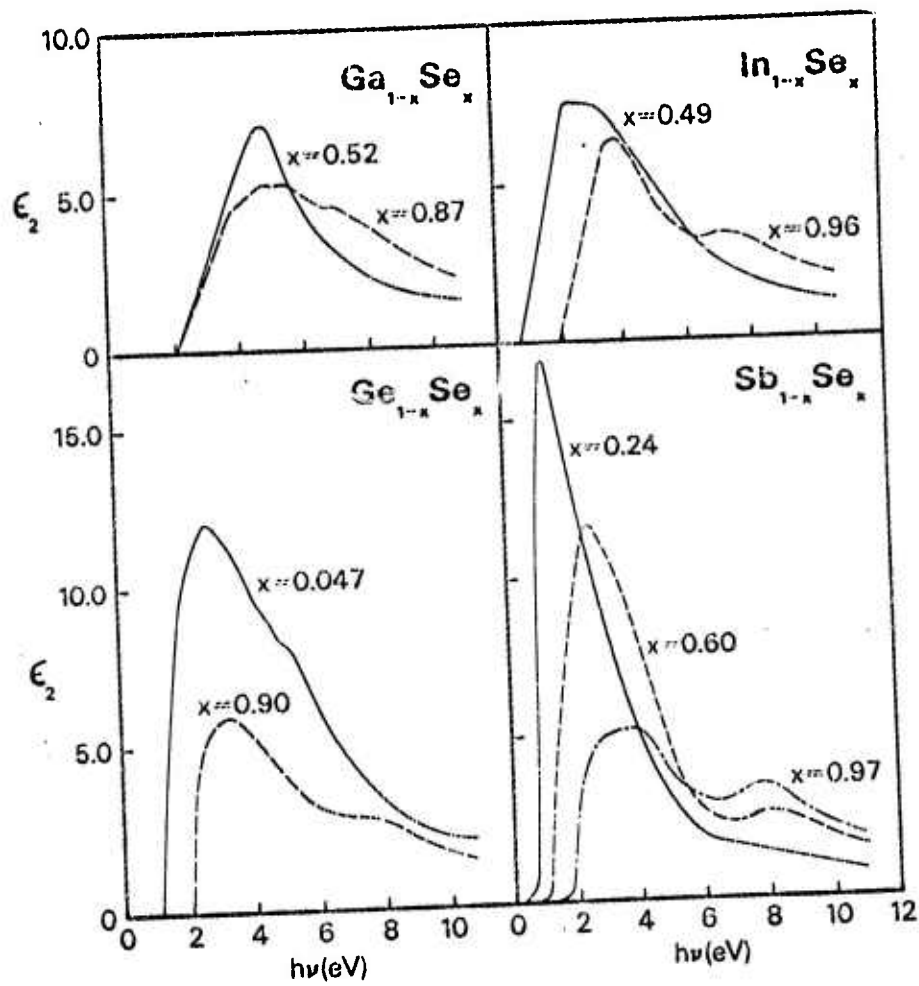


Fig. 8



## Electron Energy States in $\text{Sb}_2\text{Se}_3$ †

C. Wood and J. C. Shaffer

*Physics Department, Northern Illinois University, DeKalb, Illinois 60115*

and

W. G. Proctor

*Instrument Division, Varian Associates, Palo Alto, California 94303*

(Received 19 June 1972)

The transition strength  $(h\nu)^2\epsilon_2$ , computed by Kramers-Kronig analysis of optical reflectance spectra, is compared with x-ray photoelectron spectra for both single-crystal and amorphous  $\text{Sb}_2\text{Se}_3$ . The similarity of the data from x-ray photoelectron spectra for the two modifications suggests that the valence-band structure is essentially the same, whereas differences in the spectral dependence of  $(h\nu)^2\epsilon_2$  suggest that the conduction-band density of states is lower in the amorphous material, or that the matrix elements for optical transitions are suppressed.

As part of a study of the optical properties of  $\text{Sb}_2\text{Se}_3$ , we have compared the energy dependence of the transition strength  $(h\nu)^2\epsilon_2$  with x-ray photoelectron spectra (electron spectroscopy by chemical analysis) for both the amorphous and orthorhombic crystalline ( $D_{2h}^{10}$ ) modifications of the same composition. The single crystals were prepared in a horizontal zone refiner<sup>1</sup> and the amorphous films by vacuum evaporation<sup>2</sup> onto room-temperature fused quartz for the optical reflectance spectra, or aluminum substrates for the x-ray photoelectron spectra (XPS). An electrically conducting substrate of aluminum was used to

facilitate cleaning by sputtering. The films were verified to be amorphous by x-ray diffraction.

Values for the function  $(h\nu)^2\epsilon_2$ , where  $h\nu$  is the photon energy, were calculated by Kramers-Kronig analysis<sup>3</sup> of reflectivity data from 0 to 24 eV<sup>4</sup> and are plotted in Fig. 1. The most striking difference between the amorphous and single-crystal curves is that the peak observed at ~3 eV for both polarizations of the electric light vector for the single crystal appears to be strongly depressed for the amorphous material. This peak and the next major one at ~9 eV also are less well resolved for the amorphous solid.

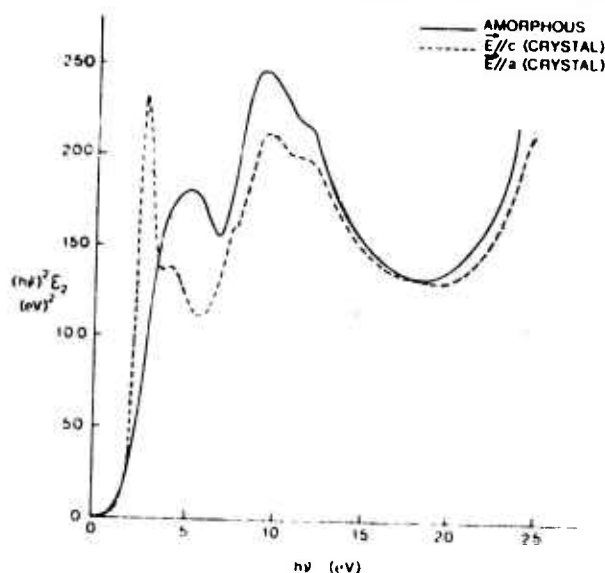


FIG. 1. Energy dependence of the optical transition strength for amorphous  $\text{Sb}_2\text{Se}_3$  and for two orientations of single-crystal  $\text{Sb}_2\text{Se}_3$  with the electric vector  $E \parallel a$  and  $E \parallel c$ .

The XPS data were taken on freshly sputtered single-crystal and amorphous specimens. Argon sputtering removed surface-impurity photoelectron peaks, but did not appear to change the overall shape of the spectra of either the amorphous or single-crystal specimens.

In Fig. 2 the x-ray photoelectron energy distribution curves are plotted in the range 0 to 45 eV, with the zero of energy at the Fermi level. The curves for the single-crystal and amorphous specimens are in general remarkably similar. A triplet structure appears in the XPS data for the crystalline samples at about 14 eV. This structure was not resolved as a triplet in the amorphous data. The spectrometer resolution for this measurement was  $\sim 1$  eV (full width at half-maximum). The strong triplet peak at  $\sim 24$  eV which appears for both the amorphous and crystalline samples in the XPS data and, therefore, in the valence-band density of states, we associate with the rising  $(h\nu)^2\epsilon_2$  beyond 20 eV. The doublet at  $\sim 33$  eV we associate with the  $\text{Sb } 4d_{3/2, 5/2}$  levels. The ratio of intensities should be 2:3, and probably is, since the weaker line is riding on the shoulder of the stronger.

As expected, good correspondence was obtained between the structure for amorphous and single-crystal material at higher energies, such as the  $\text{Se } 3d_{5/2, 3/2}$  doublet at  $\sim 53$  eV and the  $\text{Sb } 3d_{3/2, 5/2}$  doublet at 537 and 528 eV shown in Fig. 3. The oxygen  $1s_{1/2}$  level lies in the range of the latter

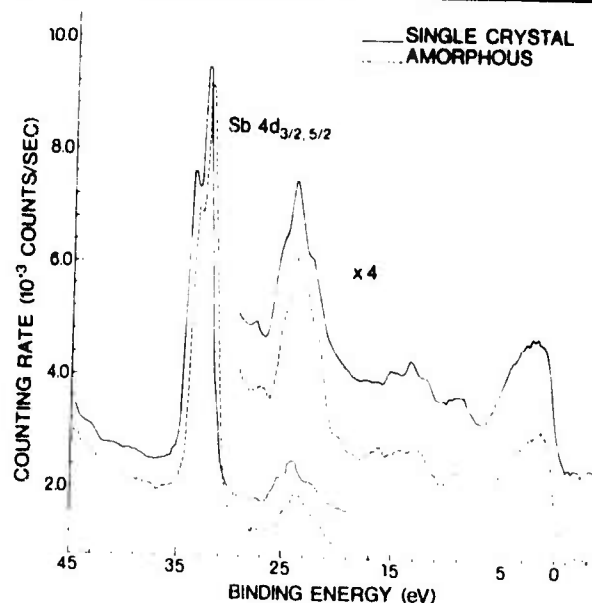


FIG. 2. X-ray photoelectron spectra between 0 and 45 eV binding energy for a single crystal and an amorphous sample of  $\text{Sb}_2\text{Se}_3$ . The ordinate scale applies only to the single-crystal counting rate. The counting rate for the amorphous sample has been scaled and displaced in order to facilitate comparison.

doublet and a small amount of oxygen remaining on the surface of the amorphous sample after sputtering could be detected by the weak shoulder at 532 eV.

Since  $(h\nu)^2\epsilon_2$ , the transition strength, is representative of the joint density of electronic states for optical transitions (assuming constant matrix elements), and since XPS data portray the structure of the occupied bands,<sup>5</sup> in particular, the valence band, we conclude that the peak at  $\sim 9$  eV in the  $(h\nu)^2\epsilon_2$  data arises from the conduction band because of the absence of any corresponding structure in the XPS data. This peak is unlikely to arise from nonconstant matrix elements since it appears with equal strength in the optical data for both crystalline orientations and amorphous material, and thus is insensitive to lack of long-range order.

The major effect of the crystalline-to-amorphous transition appears to be a general decrease of  $(h\nu)^2\epsilon_2$  at the lower energy range coupled with a smearing of most structure. Since the XPS measurements show no large changes in the structure of the valence band between the crystalline and amorphous material (fine structure of width  $< 1$  eV would not be resolved), we conclude that the lower observed values of  $(h\nu)^2\epsilon_2$  arise either from a lower conduction-band density of

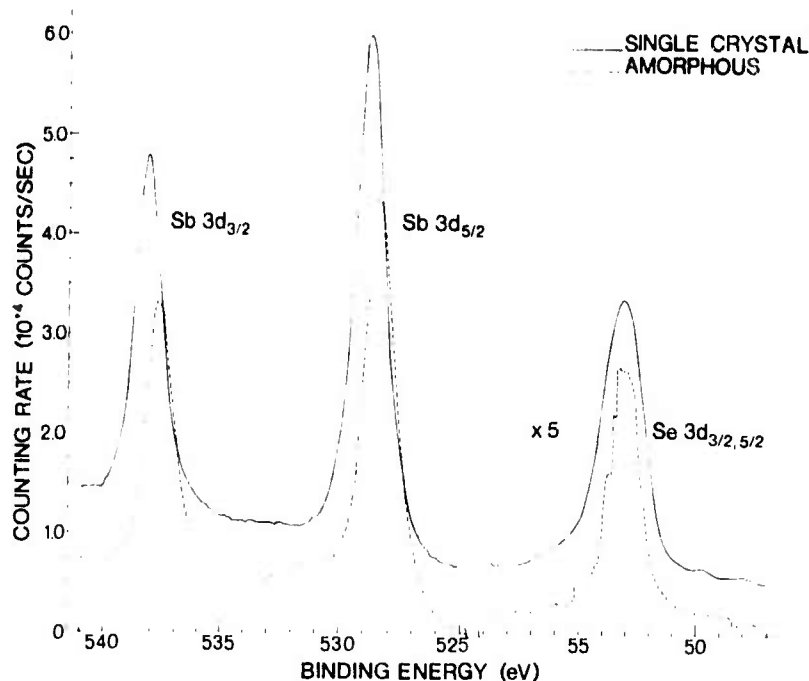


FIG. 3. X-ray photoelectron spectra for two designated energy regions for a single crystal and an amorphous sample of  $\text{Sb}_2\text{Se}_3$ . As in Fig. 2, the ordinate scale applies only to the single-crystal data, and the data for the amorphous sample have been scaled and displaced to facilitate comparison.

states or from a suppression of matrix elements in the amorphous material.

†Research supported by the Advanced Research Projects Agency of the Department of Defense, and monitored by the U. S. Army Research Office (Durham) under Contract No. DA-ARO-D-31-124-71-G132.

<sup>1</sup>C. Wood, B. Van Pelt, and E. Hyland, to be pub-

lished.

<sup>2</sup>R. Mueller and C. Wood, *J. Non-Cryst. Solids* **7**, 301 (1972).

<sup>3</sup>R. Afshar, F. M. Mueller, and J. C. Shaffer, to be published.

<sup>4</sup>C. Wood, Z. Hurych, and J. C. Shaffer, *J. Non-Cryst. Solids* **8/9**, 56 (1972); J. C. Shaffer, B. Van Pelt, C. Wood, J. Freeouf, K. Murase, and J. W. Os-  
mun, to be published.

<sup>5</sup>Y. Baer, P. F. Heden, J. Hedman, M. Klasson, C. Nordling, and K. Siegbahn, *Phys. Scr.* **1**, 56 (1970).

PHOTOEMISSION STUDIES  
OF CRYSTALLINE AND AMORPHOUS  $\text{Sb}_2\text{Se}_3$

Z. Hurych, D. Davis, D. Buczek and C. Wood†  
Physics Department  
Northern Illinois University  
DeKalb, Illinois 60115

and

G.J. Lapeyret† and A.D. Baer  
Physics Department  
Montana State University  
Bozeman, Montana 59715

†This work was supported by the Advanced Research Projects Agency of the Department of Defense and was monitored by the Army Research Office, Durham, under Contract N. DA-ARO-D-31-124-71-G132. We wish, also, to acknowledge the support of the Synchrotron Radiation Laboratory, University of Wisconsin, under Air Force contract No. F44620-70-C-0029.

††Supported by Air Force Office of Scientific Research, Office of Aerospace Research, USAF under Grant No. AFOSR-71-2061.

PHOTOEMISSION STUDIES  
OF CRYSTALLINE AND AMORPHOUS  $\text{Sb}_2\text{Se}_3$

Z. Hurych, D. Davis, D. Buczek and C. Wood  
Physics Department  
Northern Illinois University  
DeKalb, Illinois 60115

and

G.J. Lapeyre and A.D. Baer  
Physics Department  
Montana State University  
Bozeman, Montana 59715

Abstract

The photoemission energy distribution curves (EDC's) of crystalline and amorphous  $\text{Sb}_2\text{Se}_3$  were measured in the photon energy range  $h\nu = 7$  to 35 eV using polarized radiation from a synchrotron storage ring. The polarization dependence of the EDC's is much stronger than that of the reflectance spectra. The EDC's show several regions of high density of states in both the valence and conduction bands, with the structure strongly smeared-out in amorphous  $\text{Sb}_2\text{Se}_3$ . The region of the upper 2 eV of the valence band with six electrons per  $\text{Sb}_2\text{Se}_3$  molecule attributed primarily to the selenium lone p-pairs, is clearly separated from the remaining part of the EDC's in crystalline  $\text{Sb}_2\text{Se}_3$ . The optical transitions in crystalline  $\text{Sb}_2\text{Se}_3$  occur with matrix elements strongly dependent on the orientation of the electrical vector of the polarized radiation as a result of crystal field effects. Model densities of states are constructed for both crystalline and amorphous  $\text{Sb}_2\text{Se}_3$ .

## INTRODUCTION

$\text{Sb}_2\text{Se}_3$  belongs to V-VI compound semiconductors, a group of materials whose optical and transport properties have been widely investigated. However, there is available little data on band structure of these compounds due to the complicated primitive cell (comprised of 112 valence electrons in the case of  $\text{Sb}_2\text{Se}_3$ ), and the density of states models are generally derived from the molecular orbital approach, with the bonding and weakly-bonding bands usually adjusted to fit the reflectance spectra (1).

The typical features of the reflectance spectra of these compounds in both crystalline and amorphous form are two reflectivity bands, the first occurring in the near IR and visible region, and the second in the vacuum UV region of the spectrum (2), (3), (4), with onset at  $\sim 7$  eV in the case of  $\text{Sb}_2\text{Se}_3$ . These two reflectivity bands are usually interpreted (1), (4), as originating from splitting of the valence band into strongly bonding and weakly bonding states. Kastner (5) has recently pointed out the important role of the lone (unshared) p-electrons of chalcogen atoms in forming the weakly bonding band in these compounds. More detailed knowledge of the valence band structure, particularly its upper part formed by the lone-pairs, should be useful in explaining many physical properties of these materials. However, the above reflectivity-based model is of rather conjectural character, since the reflectivity (and associated optical constants) provide information on the joint density of states (JDOS) only, without determining absolutely either the initial or the final energy of states involved. In addition, it is generally difficult to determine which structure in the optical data is due to

the band density of states and which is due to enhancement by the critical points in JDOS or by matrix elements, although the critical points contribution is generally unimportant in amorphous materials as a result of lack of the long range order. This question of matrix elements is further complicated by low symmetry of these crystals, since some transitions could be either allowed or prohibited by the symmetry of the initial and final states. Such effects should show up when polarized light is used where the matrix elements would depend, in general, both on the wave vector  $\underline{k}$  and on the orientation of the electrical vector  $\underline{E}_0$ .

We have employed photoemission spectroscopy, which is capable of locating the absolute position of structures in either valence or conduction band, to substantially refine the existing density of states model and to obtain information of the character of the matrix elements. Due to the high resolution (0.2 eV), we have been able to determine several fundamental features in the upper (i.e., weakly bonding) valence band as well as a conduction band structure, unresolved previously in the x-ray photoemission studies (6). Application of polarized radiation from the synchrotron storage ring also reveals a strong effect of the crystal field which shows up as a strong dependence of the energy distribution curves (EDC's) on the orientation of  $\underline{E}_0$ .

## EXPERIMENTAL

1) Photoemission Apparatus and Light Source

The 240 MeV storage ring of synchrotron radiation at the Physical Science Laboratory of the University of Wisconsin was used as a continuum light source. The beam was focussed at the entrance slit of a monochromator optically equivalent to the McPherson 225 model. Upon reflection and dispersion at the grating, the beam is focussed at the exit slit of the monochromator and then diverges again ( $f = 10.4$ ). Therefore, an elliptical mirror was used to refocus the light beam to a spot of approximately 1 mm in diameter which illuminated the sample. Even though the beam is naturally polarized in the median plane of the storage ring, some depolarization occurs after reflections at focussing mirrors and the grating. The polarization of the light illuminating the sample was estimated to be  $\sim 80\%$ .

A double-pass cylindrical electrostatic mirror with a spiraltron electron multiplier was used as an electron energy analyzer. This analyzer which is described in detail elsewhere (7) detects only electrons of a certain velocity and which originate from a small volume (of linear dimensions  $\sim 1$  mm) surrounding a focal point; the focal point was positioned at the center of the light spot. By moving the sample with respect to the focal point of the analyzer it was possible to select the best surface area of the sample, the criterion being that the ratio of the high energy end of EDC's to the low energy peak due to scattering be maximized. For good crystal cleavages and uniform films this was only of a secondary importance. The sampling of the velocity of electrons was done by sweeping a retarding or accelerating voltage between two concentric



hemispheres located in the region between the electron source and the analyzer entrance. Analyzer resolution was then independent of the electron energy. In the present work the analyzer was set to pass 20 eV electrons and the resolution was 0.2 eV for all electron energies. This pass energy gave the most favorable condition for high transmittance of the analyzer while retaining good resolution. Digital processing of the signal at the output of the channeltron eliminated the vibrational, electrical and Johnson noise; the dark count was less than 1 cps. The primary source of noise was the statistical error which was 1% of full scale or better. This resulted in the necessity of a longer counting time for  $h\nu > 20$  eV where the light intensity began to decrease.

## 2) Sample Preparation

Orthorhombic single crystals of  $\text{Sb}_2\text{Se}_3$  (space group  $D_{2h}^{16}$ ,  $a = 11.62 \text{ \AA}$ ,  $b = 11.77 \text{ \AA}$ ,  $c = 3.96 \text{ \AA}$ ) were grown from the melt in a horizontal zone-refiner by the method described in (8) from 6-9's purity elements. Samples  $\sim 9 \text{ mm} \times 9 \text{ mm} \times 3 \text{ mm}$  were cut from ingots of  $\sim 1/2$ " diameter and 10" long. The base pressure in the photoemission chamber was  $8 \times 10^{-10}$  torr and did not change substantially during the cleaving. Excellent mirror-like cleaved surfaces  $\perp b$  were obtained which enabled the sample to be illuminated  $\underline{E}_0 \parallel a$  or  $\underline{E}_0 \parallel c$ , respectively. ( $\underline{E}_0$  is the electric vector of polarized light). The sample was positioned in such a manner that the incident light was always s-polarized, i.e.,  $\underline{E}_0$  was parallel only with one of the three orthorhombic axes at a time.

Amorphous  $\text{Sb}_2\text{Se}_3$  films of thickness  $\sim 200$  to  $500 \text{ \AA}$  were prepared in situ by evaporation of  $\text{Sb}_2\text{Se}_3$  from an electron-beam gun at very small rates ( $\sim 1 \text{ \AA/sec}$ ) onto nickel and quartz substrates with Pt contacts. This method of evaporation had been developed earlier (9) to produce amorphous stoichiometric  $\text{Sb}_2\text{Se}_3$  films within the 1% error in composition

as determined by electron microprobe. After the photoemission measurements, the films were checked by x-ray diffraction and were found to be amorphous. The pressure before the evaporation was  $5 \times 10^{-10}$  torr rising to  $4 \times 10^{-9}$  torr during the evaporation and decreasing back to  $8 \times 10^{-10}$  torr immediately after the electron beam gun was turned off.

### THEORY

Since there are several detailed treatments of the theory of the photoemission process (10), (11), (12), only conclusions pertinent to our results will be mentioned here. In addition some features of photoemission when polarized radiation is used will be discussed qualitatively.

The transition rate for the optical excitation is proportional to the square of the electric dipole matrix elements  $M_{if}(h\nu, \underline{k}, \underline{E}_0) = \langle \psi_i | H' | \psi_f \rangle$  where  $H'$  is the light perturbation Hamiltonian,  $\underline{k}$  is the crystal momentum, and  $\underline{E}_0$  is the electrical vector of polarized light. The form of the  $\underline{k}$  dependence of  $M_{if}$  depends on the character of the wave functions  $\psi_i$  and  $\psi_f$  in the initial and final states. If these are properly described by Bloch functions, and  $\underline{k}$  dependence of  $M_{if}$  includes the term  $\delta(\underline{k}_i - \underline{k}_f)$  (direct transition), and the excitation is described in terms of  $M_{if}$  and the JDOS. If Bloch functions do not properly describe either the initial or final states, the  $\underline{k}_i = \underline{k}_f$  condition for nonzero  $M_{if}$  is relaxed. The optical transitions are then termed as nondirect, and their rate can be expressed in terms of  $M_{if}$  and band densities of initial and final states.

The dependence of  $M_{if}$  on  $\underline{E}_0$  arises from the  $\underline{A} \cdot \underline{p}$  term in  $H'$ ,  $\underline{A}$  being the vector potential of the exciting radiation. The  $\underline{E}_0$  dependence can be very important

in an anisotropic solid such as  $\text{Sb}_2\text{Se}_3$ . This  $E_0$  dependence of  $M_{if}$  arises from the symmetry of the initial and final states rather than from the detailed character of  $\psi_i$  and  $\psi_f$ , reflecting the effect of crystal symmetry and field and can occur both for direct and nondirect transitions. Treatment of this problem in the case of wurtzite CdS can be found in (13).

In addition to the dependence on  $|M_{if}|^2$ , the photoemission EDC's depend also on the scattering factor  $S(h\nu, k_f, E)$  (10), which describes the transport and escape of electrons excited to final energy  $E$ . The  $k_f$  dependence of  $S$  gives rise to angular dependence of the photoemitted electrons. Several experiments have been performed to investigate this angular dependence of photoemission in the case of Cu (14), Ag (15), and Au (16). In the case of free-electron-like metals this angular dependence of photoemitted electrons has been treated theoretically by Mahan (17) from first principles.

Since  $k_f$  depends on the orientation of  $E_0$  through the  $\underline{A.p}$  term and some relation between  $k_i$  and  $k_f$ , it is appropriate to incorporate the  $E_0$  dependence also into the scattering function  $S(h\nu, E, k_f, E_0)$ . The EDC's then include <sup>a</sup> twofold dependence on the orientation of  $E_0$ :

(i) through the probability of the optical excitation proportional to  $(M_{if})^2$  (at any  $h\nu$  the transition can be allowed for one polarization and forbidden for the other as a result of symmetry);

(ii) through the transport and escape function  $S$ , where the angular distribution of emitted electrons depends upon  $E_0$  through the  $k_f$  dependence on  $E_0$  as a result of the term  $\underline{A.p}$ . This dependence would generally be much weaker in the case of nondirect transitions for which  $k_i \neq k_f$ .

While effect (ii) is not generally considered when EDC's are measured using the retarding field analyzer (which yields an "averaged" angular

distribution) it should be considered in the case of directional analyzers such as the double-pass electrostatic mirror used in this work. It is then desirable to separate the part due to  $M_{if}$  and to the  $S$  dependence on  $\underline{E}_0$  in the family of EDC's with different  $h\nu$  at constant polarization and constant angle of collection. Since there is no theory similar to that of Mahan (17), which would treat this problem in the case of complex semiconductors like  $\text{Sb}_2\text{Se}_3$ , we used, as a first approximation, the following criteria for the separation of the  $M_{if}$  and  $S$  dependence.

(i) The  $M_{if}$  dependence on  $(\underline{E}_0)$  can strongly modulate the intensity of peaks in the EDC's as  $h\nu$  is varied at constant polarization, since even a small change in  $h\nu$  can result in transitions between initial and final states of different symmetry, which could change from allowed to forbidden or vice-versa. Peaks in the EDC's may then suddenly appear and disappear when  $h\nu$  is changed by a small amount, i.e., the peaks may behave similar to those in the case of direct transitions.

(ii) Since the angular dependence of  $S$  is rather smooth and it is a continuous function of  $k_f$  as contrasted to the "0 to 1" type behavior of  $M_{if}(\underline{E}_0)$ , and since the overall momentum distribution  $k_f$  of all excited electrons would also change with  $h\nu$  more gradually than the "0 to 1" changes in  $M_{if}$ , one may expect rather weak and gradual modulation of structure in the EDC's due to the  $S(k_f, h\nu, E, \underline{E}_0)$  term as  $h\nu$  is varied at given polarization. This  $S(k_f, h\nu, E, \underline{E}_0)$  term would be expected to have a very small effect in the case of nondirect transitions.

#### EXPERIMENTAL RESULTS

The experimental data (EDC's) are presented at figs. 1-6 for crystalline  $\text{Sb}_2\text{Se}_3$  for two orientations of the electrical vector  $\underline{E}_0$  of the polarized light

$E_D||c$ ,  $E_D||a$ , and for amorphous  $Sb_2Se_3$ . It is seen that the EDC's exhibit the sharpest and richest structure in the photon energy range between 7 eV and 15 eV. At higher photon energies, the structure (peaks, shoulders, valleys) is getting progressively less sharp as a result of the increasing contribution of scattered electrons which build a structureless background at the lower energy part of EDC's and decrease the signal at the high energy end. Starting at  $h\nu \sim 20$  eV an additional overall decrease of the signal occurs as a result of decreasing efficiency of the normal incidence grating monochromator. Therefore, primarily the 7 to 20 eV region of  $h\nu$  will be used for further analysis. The EDC's for  $h\nu \geq 20$  eV look similar to those for 20 eV but the signal was considerable weaker. The main purpose of taking the EDC's for  $h\nu > 20$  eV was to obtain information on possible contribution from core d-levels (the 4d level of Sb). Our results show no core d-bands in the 7 to 30 eV region which indicates that the optical properties of  $Sb_2Se_3$  in reference 4 are due to the s and p valence electrons only.

Since there is present a large amount of structure in our data as a result of strong polarization dependence, a large span of photon energy, and a complex band structure, it is advantageous to identify briefly the most prominent structure, in Figs. 1-6. Analysis of the EDC's shows that most of the structure can be related to the constant energy of either initial or final states. Therefore, two sets of EDC's will be presented: one with EDC's arranged with respect to the initial energy, suitable for determining the valence band structure, and the other set arranged with respect to the final states energy, suitable for determining the conduction band structure.

The structure of constant initial state energy (figs. 1, 3, and 5) includes a weak shoulder S on the sharp leading edge, and two sharp peaks A and B in crystalline  $Sb_2Se_3$  (or one broad peak AB in amorphous  $Sb_2Se_3$ ) at the high

energy end of EDC's for  $h\nu$  in the 8 eV to 20 eV range; these structures are separated from the rest of the EDC's by a valley V located 2 eV below the high energy end of the EDC's. Additional peaks C and D are located at  $\sim 0.6$  eV and 1.3 eV below the valley V for crystalline  $\text{Sb}_2\text{Se}_3$ . The structure with the constant final state energy (figs. 2, 4, and 6) is observable at the low energy end of the EDC's. It includes five shoulders and peaks  $P_0$  to  $P_4$  in crystalline  $\text{Sb}_2\text{Se}_3$ , and two structures P and  $P^1$  in amorphous  $\text{Sb}_2\text{Se}_3$ . For further presentation and analysis of the EDC's we will also use the standard method of structure plots where the final energy E of each element of the structure is plotted vs. the photon energy  $h\nu$  (figs. 7-9), with the energies referred to the valence band maximum (VBM). The high (and energy independent) resolution of the analyzer used provides rather sharp leading edges of the EDC's which can be easily extrapolated to define the top of the valence band. The very weak tail at the high energy end of the EDC's is due to both intrinsic broadening (as a result of the electrical field penetration) as well as to the instrumental broadening (nonuniform work function of the analyzer, finite bandwidth of the exciting radiation, finite resolution of the analyzer).

#### CRYSTALLINE $\text{Sb}_2\text{Se}_3$

$$E_D || c$$

In the region between the threshold energy and  $h\nu = 8$  eV, a peak in the EDC's occurs close to the top of the valence band (fig. 1, also line  $\alpha'$  in fig. 7). This structure is attributed to direct transitions since it does not correspond to the slope of the  $E = h\nu$  line in the structure plot (fig. 7) and ends at  $h\nu = 8$  eV. At  $h\nu = 8$  eV a sharp peak A occurs in the EDC. Figs. 1 and 7 show that this peak keeps a

constant energy of initial states in the entire photon energy range up to 20 eV, but the intensity of this peak is strongly varying with  $h\nu$ ; in the 9.5 to 11.5 eV this peak almost disappears. Another structure of constant energy of the initial states, is peak B, starting at  $h\nu \sim 8.6$  eV as a weak shoulder. The intensity of this peak is again strongly varying with photon energy. The high resolution of this experiment shows this peak B as a doublet  $\sim 0.3$  eV wide in the  $h\nu \sim 9$  eV to 13 eV region. A weak shoulder S on the leading edge of most of the EDC's can be also observed. Peaks A and B are separated from the remaining part of EDC's by a valley V at 2 eV below VBM. This valley V is one of the most prominent features of EDC's for crystalline  $\text{Sb}_2\text{Se}_3$ . Since the two peaks A and B occur in extremely large photon energy range ( $\sim 20$  eV) with constant and well defined initial energy, we conclude that they correspond to high density of states regions in the valence band arising from flat E vs k parts of the band. In the  $h\nu = 8$  to 15 eV region the intensity of these two peaks is strongly varying with  $h\nu$  due to the effect of matrix elements. In the case of optically isotropic materials, this feature would be a clear indication of direct, i.e.,  $\underline{k}$  conserving optical transitions. In the case of such a strongly anisotropic material as  $\text{Sb}_2\text{Se}_3$  it is possible, however, that this matrix elements modulation could be due to the  $E_0$  rather than the  $\underline{k}$  dependence of matrix elements. Therefore the only definite indication that the transitions are direct is that the slope differs from  $45^\circ$  in the structure plot for peak A in the small photon energy range between the threshold and 8 eV.

Starting at  $h\nu \sim 10$  eV, fig. 1 shows two other peaks C and D of strongly varying intensity in the region 0.4 eV to 1.3 eV below the valley V. A slope differing from the  $E = h\nu$  slope in the corresponding structure plot (fig. 7), indicates that these peaks are associated with direct



optical transitions. There is a suggestion of another deeper lying structure in the valence band (labeled F), obscured by the background of inelastically scattered electrons and by the overlapping conduction band structure. This background is also partially obscuring an onset of another region of high density of states starting at about 6 eV below VBM (point G in fig. 1) for EDC's at  $h\nu > 15.5$  eV. We suggest that the sharp change of the slope at point G corresponds to an increase of the valence band densities of states, yet superimposed on a background of conduction band structure and scattered electrons since: (i) point G corresponds to a constant energy of initial states, and is therefore a property of the valence band; (ii) the inelastically scattered electrons would form a smooth background, dependent on the final rather than on initial energies. In amorphous  $\text{Sb}_2\text{Se}_3$ , (fig. 5) this deeper new band is much better resolved in the EDC's due to much weaker conduction band structure (fig. 5). This assignment of point G to the onset of a deeper valence band is further confirmed by the x-ray photoemission spectra (6) which portrays the structure of the occupied states.

The conduction band structure can be conveniently determined from the EDC's arranged with respect to the final energies of photoelectrons (fig. 2). Five regions of higher density of states (labeled  $P_0$  to  $P_4$ ) superimposed on a background of inelastically scattered electrons can be determined from fig. 2 between 6 and 10 eV above VBM. In general, such conduction band density-of-state-maxima can be filled either directly by optical excitation, or by photoexcited electrons which are inelastically scattered down from higher energies (19). Since the intensity and shape of these five peaks or shoulders is strongly dependent on the photon energy, these structures in EDC's obviously correspond to the optically excited



electrons rather than to the filling of these states by scattered electrons. This is best shown by observing the crossings of the lines representing the peaks A, B, C, and D with lines representing  $P_0$  to  $P_4$  in the structure plot (fig. 7). At several photon energies, corresponding to these crossings, strong interband optical transitions, enhanced by high density of states in both band, occur and show up in the EDC's as strong peaks, modulated further by the matrix elements  $M(h\nu, \underline{k}, \underline{E}_0)$ . For  $\underline{E}_0 || c$ , such strong peaks in the EDC's occur for example at  $h\nu = 8$  eV (transition from A to  $P_3$ ) and  $h\nu = 10$  eV (from B to  $P_1$ ). A complete list of such transitions is in table 1.

The lower part of the conduction band is not accessible due to the photoelectric threshold of  $\sim 5.9$  eV, as determined from the spectral distribution of the yield  $Y$  using a linear  $(Y h\nu)^{3/2}$  vs  $h\nu$  extrapolation (20).

$$\underline{E}_0 || a$$

The EDC's for  $\underline{E}_0 || a$  (figs. 3 and 4) bear resemblance to EDC's for  $\underline{E}_0 || c$ . The high energy side of the EDC's shows four peaks A, B, C, D of constant and rather well defined initial state energy (fig. 3, 8). A shoulder S can be observed on the leading edge of EDC's. These four peaks are attributed again to the valence band density-of-states maxima originating from flat  $E$  vs  $k$  portions of the band. In the EDC's these maxima are then strongly modulated by the matrix elements  $M(h\nu, \underline{k}, \underline{E}_0)$ . For example, the very sharp peak A at 10 eV is changing into a very weak shoulder in the 11.5 eV to 15 eV region (21). Peaks A and B are again clearly separated from the rest of EDC's by the valley V located 2 eV below VBM which is also one of the most prominent features of the EDC's for  $\underline{E}_0 || a$ . A weak structure F and an onset of a deeper valence band at G are also observed at Fig. 3. Contrary to the  $\underline{E}_0 || c$  polarization, peaks C and D keep a constant initial

state energy in this polarization for the entire photon energy range where they are present (see also fig. 8). Five regions  $P_0$  to  $P_4$  of high density of states in the conduction band are observed in the low energy side of EDC's (fig. 4) superimposed on a smooth background of scattered electrons. These conduction band densities are again coupled in optical transitions from the states in the upper valence band (Table 1).

Comparing the EDC's for  $\underline{E}_0 || a$  with  $\underline{E}_0 || c$  shows the dependence of the relative intensity of these peaks on the orientation of  $\underline{E}_0$  (see fig. 10). This indicates that the matrix elements include dependence on both  $\underline{k}$  and  $\underline{E}_0$ , the latter dependence arising as a result of the crystal field effect. Due to the differential character of the photoemission method, this  $\underline{E}_0$  dependence is much more pronounced in the EDC's than in the reflectance data (fig. 11). The EDC's are strongly polarization dependent in the photon energy range from 8 to  $\sim 15$  eV where the reflectance shows very little polarization dependence. While, for example, the reflectivity and the optical transition strength  $\omega^2 \epsilon_2$  (i.e., JDOS) exhibit the same two peaks at  $\sim 10$  eV and 12.5 eV for both polarizations (fig. 11) the EDJDOS (the energy distribution of JDOS) is quite different for these two polarizations (fig. 10). The reflectivity peak at  $\sim 10$  eV has strong contribution from peak A in EDC's for  $\underline{E}_0 || a$  and from peak B for  $\underline{E}_0 || c$ . The reflectivity peak at  $\sim 12.5$  eV has a large contribution from peaks B and C in EDC's for  $\underline{E}_0 || a$ , and approximately equal contributions from A and B for  $\underline{E}_0 || c$ . It is primarily the upper 3 eV of the valence band which produces a strong polarization and photon energy dependence of the EDJDOS which is not detectable in the reflectance data.

AMORPHOUS  $\text{Sb}_2\text{Se}_3$ 

The total photoemission yield of amorphous  $\text{Sb}_2\text{Se}_3$  films was lower than that of crystalline  $\text{Sb}_2\text{Se}_3$ , and the low energy part of the EDC's was partially obscured by the background of photoelectrons emitted from the analyzer (22). A correction for this effect at several photon energies is shown in figs. 5 and 6 (dashed line). These corrected EDC's still include, however, the secondary (scattered electrons originating in the conduction band of  $\text{Sb}_2\text{Se}_3$  films.

The structure of the EDC's for amorphous  $\text{Sb}_2\text{Se}_3$  is much less complicated than for crystalline, yet the main features are similar. There is again a shoulder S and a peak AB at the high energy end separated from the rest of the EDC's by the valley V. However, the two very sharp peaks A and B in crystalline  $\text{Sb}_2\text{Se}_3$  are now replaced by the broad peak AB, and the peaks C and D at the low energy side of V are completely missing. Both peak AB and valley V indicate again a constant initial state energy which is primarily attributable to the valence band structure. Of particular interest are the changes of the shape of the EDC's at  $h\nu = 8 \text{ eV}$  and  $9 \text{ eV}$ , where some sharpening of the peak AB occurs. The occurrence of such sharp peaks is rather unusual for an amorphous material, and in this case it is plausible to explain such peaks in the EDC's by a high density of states in the conduction band. Figures 6 and 9 indeed show

two weak regions of high density of states, P and P' in the conduction band at  $\sim 7$  and 8 eV above the top of the valence band. Their energy position corresponds to regions  $P_2$  and  $P_3$  of high density of states in the crystalline  $Sb_2Se_3$ , but their intensity is much weaker. The weakness of the conduction band structure in amorphous  $Sb_2Se_3$  is a property of the amorphous films, rather than an instrumental resolution effect, since the lower part of the valence band (point G) is resolved more sharply in amorphous than crystalline  $Sb_2Se_3$  despite the lower yield of films. Similar smoothing of the high density of the conduction band states in the amorphous phase of Se and Te have been reported by Laude and Pitton (23). Results (18) indicate that the difference between EDC's for crystalline and amorphous  $Sb_2Se_3$  is not due to collecting electrons under specific solid angle which would average out the structure in amorphous  $Sb_2Se_3$ .

Since the only two appreciable changes of the shape of the peak AB in the EDC's at  $h\nu \sim 8$  and 9 eV can be explained by the higher conduction band density of states, the otherwise constant shape and relative intensity of the peak AB suggest that it is due to nondirect transitions. It is interesting to note that within the resolution (0.2 eV) of the experiment, both crystalline and amorphous  $Sb_2Se_3$  exhibit very sharp high energy ends of the EDC's, particularly there is no direct evidence of the density of states tailing in amorphous stoichiometric  $Sb_2Se_3$  in agreement with previous findings from the optical and photoconductivity data (24).

#### DISCUSSION

One important feature of the EDC's is the strong structure in their upper 2 eV region. In the case of crystalline  $Sb_2Se_3$ , this region is strongly polarization dependent and split into peaks A and B, and

is clearly separated from the rest of EDC's by the valley V. The peaks A and B are rather narrow, their full width at half-maximum above the valley V being  $\sim 0.4$  eV. Such narrow bands would be consistent with rather low hole mobility  $\sim 40$  cm<sup>2</sup>/V sec (25) in crystalline Sb<sub>2</sub>Se<sub>3</sub>. We associate these two peaks A and B with two regions of valence band density-of-states maxima, arising from flat E vs. k bands. In agreement with this interpretation, the energy position of these two peaks from the VBM is the same for both polarizations. In the EDC's these valence band density-of-states maxima are modulated by the matrix elements  $M(h\nu, \underline{k}, \underline{E}_0)$  and to some extent by the escape function S and also by the conduction band density of states for  $8 \text{ eV} < h\nu < 15 \text{ eV}$ . In view of the atomic states configuration of Sb and Se, these flat bands are attributed primarily to p-electrons which would be rather localized at atoms. Peaks A and B in the EDC's of crystalline Sb<sub>2</sub>Se<sub>3</sub> merge into one broad peak AB in amorphous Sb<sub>2</sub>Se<sub>3</sub>. This peak AB does not allow for a very flat E vs  $\underline{k}$  band, and its behavior suggests that it is due to nondirect transitions with constant matrix elements, modulated by the conduction band density of states at  $h\nu \sim 8$  and  $9$  eV.

The other portion of the valence band being strongly affected by the phase transition is located between 2.0 and 3.3 eV below the VBM in crystalline Sb<sub>2</sub>Se<sub>3</sub> (peaks C and D in the EDC's). Optical transitions from these states are again strongly dependent on the orientation of  $\underline{E}_0$ . Behavior of these peaks in the structure plot (fig. 7) for  $\underline{E}_0 \parallel c$  again indicate that the corresponding optical transitions are direct in crystalline Sb<sub>2</sub>Se<sub>3</sub>. In the EDC's for amorphous Sb<sub>2</sub>Se<sub>3</sub> these two peaks C and D are completely missing.

Even though the effect of polarized light on the EDC's in the case of optically anisotropic materials has been reported earlier (13), (16), (26), the effects observed here are far stronger. It is also interesting to note that the polarization dependence is strongest for electrons excited from flat

bands at the upper  $\sim 3$  eV part of the valence band. In view of the discussion in the theoretical section, it is believed that this strong polarization dependence of the EDC's is due primarily to the  $M_{if}$  term with the S term giving possibly a weak background dependence such as observed in the EDC's at  $h\nu > 16$  eV. Even though a rigorous proof of this statement requires a detailed knowledge of the band structure, there are some experimental facts in its support: (i) the reflectance spectra in the visible range shows clearly strong  $M_{if}(\underline{E}_0)$  dependence for states within the upper  $\sim 3$  to 4 eV of the valence band, and (ii) the main features of the EDC's are independent of the type of analyzer used (18). This observed  $\underline{E}_0$  dependence of  $M_{if}$  shows the effect of crystal field and symmetry. The strong polarization dependence of EDC's makes it difficult to determine whether the transitions are direct, since the strong  $\underline{E}_0$  dependence of  $M_{if}$  obscures any possible  $\underline{k}$  dependence. There are indications of direct transitions such as the slope in the structure plots but only in a limited range of  $h\nu$  (e.g. peaks C and D for  $E_0 \parallel c$  in fig. 7). The question of direct transition is further complicated by the flatness of the bands corresponding to the initial states.

An additional increase of the density of states for both crystalline and amorphous  $Sb_2Se_3$  starts at  $\sim 6$  eV deep in the valence band (point G) which is seen as a sharp change of the slope of the EDC's in figs. 1, 3 and 5 at  $h\nu > 17.5$  eV. It is reasonable to assume that this lower portion of the valence band contributes significantly to the reflectivity rise at  $h\nu \sim 7$  eV even though the onset of these transitions cannot be seen in the EDC's due to the work function limitation.

The conduction band shows five closely spaced regions of higher density of states between 6.5 and 9.5 eV above VBM ( $P_0$  to  $P_4$ ) for both polarizations in crystalline  $Sb_2Se_3$ , and two weak structures P and P' at about 7 eV and 8 eV for amorphous  $Sb_2Se_3$ . The energy position of these conduction band densities of states

and their coupling in optical transitions to various regions of the valence band are presented in table 1. The existence of these conduction band density of states in  $\text{Sb}_2\text{Se}_3$  has further been confirmed by comparing the optical transition strength  $\omega^2\epsilon^2$  with the x-ray photoemission spectroscopy (6). One interesting feature of the conduction band structure is that it shows up much weaker for amorphous than for crystalline  $\text{Sb}_2\text{Se}_3$ . This can be explained by the lack of matrix element enhancement, or by a strong effect of the long range disorder on the higher conduction band. In particular, the effect of the long range disorder on the smoothing of the conduction band structure is much stronger than on the sharpness of the valence band edge.

At higher photon energies ( $h\nu > 16$  eV), the high energy end of the EDC's changes very little with  $h\nu$ , and similarly to other works (27,28), portrays the basic feature of the valence band density of states (DOS). The derived model DOS for crystalline and amorphous  $\text{Sb}_2\text{Se}_3$  are presented in fig. 12. The relative intensity of individual peak in this model cannot be determined accurately due to several unknown factors like  $M_{if}$  and  $S$ . Since the scattering length necessary to subtract the low energy peak due to inelastically scattered electrons is not available, the model densities in fig. 12 are "normalized" with respect to the optical sum rules from reference (4); also some cross features of the XPS spectra (6) are used in this model. It is interesting to note that due to improved resolution, the EDC's reveal more detailed structure (e.g., the valley V) in the densities of states for crystalline and amorphous  $\text{Sb}_2\text{Se}_3$  than the XPS data (6).

Since the valley V, separating the upper 2 eV of the valence band, is one of the most prominent features of EDC's for both polarizations, some physical interpretation of this structure is appropriate. This can be done by application of the optical sum rules, which determines that there are six electrons per molecule located between the VBM and the valley V, participating in the optical transitions from  $h\nu = 1.2$  eV (the bandgap of  $\text{Sb}_2\text{Se}_3$ ) to  $h\nu = 3.2$  eV.



Certain caution has to be exercised when using the optical sum rules, since it provides the "effective number" as determined from the total oscillator strength. This effective number can differ from the true number of valence electrons, particularly when the upper limit  $h\nu$  lies within the region of optical transitions. This has been observed in the case of Ge and VI-V compounds due to the core d-levels contribution to the total oscillator strength (29). In  $\text{Sb}_2\text{Se}_3$ , however, the highest occupied levels are the Sb 4d states at  $\sim 33$  eV below the VBM, (6) and the optical sum rules up to  $h\nu = 25$  eV do not exhibit any contribution due to these d-bands (4). Therefore, within the numerical accuracy of the optical sum rules (30), we consider  $n_{\text{eff}}$  as a reasonable and useful first order approximation.

Since there has been done no band structure calculation for  $\text{Sb}_2\text{Se}_3$  or similar orthorhombic V-VI compounds (primarily due to its very complicated primitive cell containing 112 valence electrons), the only theoretical model for the electronic structure of  $\text{Sb}_2\text{Se}_3$  at present is the conjecture resulting from the molecular orbital approach (5), (31). Our results can then be interpreted in the following way. The upper part (first 6 eV) of the valence band is attributed to weakly-bonding states which have strong p-like character as evidenced by several flat bands. According to the sum rule calculation (4) it includes a total of 12 electrons per  $\text{Sb}_2\text{Se}_3$  molecule with six electrons per molecule being located within the upper 2 eV region between the VBM and the valley V. These six electrons per molecule can be attributed primarily to the three lone (unshared) p-pairs of selenium electrons (32) whose existence in this class of compounds has been suggested by Kastner(5). At this point it should be mentioned that such separation of the group of  $\sim 6$  electrons/molecule by the valley V in the EDC's derived DOS was found also for other V-VI crystals  $\text{Bi}_2\text{Te}_3$  and  $\text{Sb}_2\text{Te}_3$  of rhombohedral  $D3m$  structures (33), and seems to be a general feature of the V-VI compounds indicating the presence



of the lone p-pairs. Also we would like to note the striking similarity of the DOS model of  $\text{Sb}_2\text{Se}_3$  to those of Shevchick et al. for Se (28) particularly the separation of the lone-pair band. This suggests the important role of the lone pairs on chalcogen atoms in forming the weakly bonding band of  $\text{VB}_2\text{VIB}_3$  compounds. The lone p-pair band in orthorhombic  $\text{Sb}_2\text{Se}_3$  is further split by the crystal field (peaks A,B) resulting from the low symmetry; this splitting is not observed in trigonal Se. Whereas the entire nonbonding band of  $\text{VB}_2\text{VIB}_3$  compounds has been previously referred to as the "lone-pair band" (5), the combination of the photoemission and XPS data, together with the sum rules, shows that in addition to the three lone-pairs, this nonbonding band contains approximately another six electrons per molecule, clearly separated from the lone-pair by the valley V. Similarly to the lone p-pairs those deeper states have again a strong contribution from flat E vs k band (peaks C and D) indicating strong p character with large contribution probably from the Sb 5 p-states.

The lower part of the valence band (bonding) starting at about 6 eV below VBM arises from the bonding states and corresponds to the  $\sigma$  orbitals of the molecular states. According to the sum rule (4) this band, including 16 electrons per molecule, can extend up to 25 eV below the VBM. This band should include the remaining p-states of Se and Sb, 5s states of Sb and possible the deep 4s states of Se. Due primarily to the difference in the strength of the conduction band structure, the onset of this bonding band is resolved better in the EDC's for amorphous than for crystalline  $\text{Sb}_2\text{Se}_3$ . In the x-ray photoemission spectrum, which is sensitive primarily to the valence band structure, the onset of this band is resolved equally well for both amorphous and crystalline  $\text{Sb}_2\text{Se}_3$  (6). The 4d states of Sb, according to present results as well as to (4) and (6), do not contribute to this band.

The lowest part of the conduction band would correspond to  $\sigma^*$  antibonding molecular states. The EDC's show several additional regions of well localized higher densities of states in the conduction band in the region 6 to 10 eV above the VBM superimposed on a more or less smooth conduction band. The small width of these states and their strong optical coupling to the p-type states at the upper (weakly bonding) valence band suggests d-like character of these higher conduction states  $P_0$  to  $P_4$ . The intensity and sharpness of these states is much lower in the amorphous phase.

It would be very interesting to correlate the electronic states to the different type of bonds, particularly in regard to different bond strengths in the case of this pseudo-two dimensional crystal consisting of  $Sb_4Se_6$  units (34). The x-ray diffraction data of Tideswell et al. (34) shows that the bond character is very complex since the bond distances occur anywhere between the sum of covalent radii ( $\sim 2.6 \text{ \AA}$ ) and  $\sim 3.8 \text{ \AA}$  (the sum of the van der Waals radii for Sb and Se is  $4.20 \text{ \AA}$ ). The 6 electrons in the upper 2 eV (primarily lone-pairs) of the weakly bonding band can be considered to play some role in forming the six weakest bonds per molecule (bond distances  $3.74 \text{ \AA}$  and  $3.46 \text{ \AA}$ ), holding the crystal and only a small amount of the electronic charge participates in forming the bonds, as the bond number is  $\sim 0.01$ . The crystal field and symmetry determine the direction of these bonds and their energy levels (rather flat E vs k bands giving rise to peaks A and B) so that the total crystal energy is minimized. Another six weak bonds per  $Sb_2Se_3$  molecule (bond distances  $3.26 \text{ \AA}$  and  $3.27 \text{ \AA}$ , bond number  $\sim 0.1$ ) responsible for bonding infinitely long Sb-Se chains into crystal layers can be associated, at least in part, with another six weakly bonding electrons located between the valley V and the point G. The direction of these bonds and

corresponding electronic energy levels are again determined by the crystal field which shows up in the EDC's via the strong  $E_0$  dependence of matrix elements. The  $\sigma$  (bonding) states are involved in forming the strong Sb-Se bonds of distances 2.57 to 2.98 Å (bond number  $\sim 1.0$ ) within infinitely long chains, parallel with the c-axis (34).

In amorphous  $\text{Sb}_2\text{Se}_3$  these weakly bonding states are determined by the local potential instead of the crystal field. The weak bonds, responsible formerly for holding together or forming the crystal layers, are now randomly oriented in space, and their energy levels, determined locally, lose their resonant character and the bands consequently become wider. This is clearly reflected in the EDC's for amorphous  $\text{Sb}_2\text{Se}_3$  where the sharp peaks A and B are replaced by one broad peak AB, and peaks C and D are completely missing. The separation of the lone-pairs by the valley V from the rest of the weakly bonding band is also very weak in amorphous  $\text{Sb}_2\text{Se}_3$ .

The effect of the crystal field and the similarity between the major features of the DOS of crystalline and amorphous  $\text{Sb}_2\text{Se}_3$  are consistent with the model of both phases displaying properties characteristic of molecular solids; the crystal containing  $\text{Sb}_4\text{Se}_6$  units bonded rather weakly to one another (34) and amorphous films being a random aggregate of  $\text{Sb}_4\text{Se}_6$  molecules (35).

#### CONCLUSION

The EDC's present a considerable extension of the DOS model derived from the general molecular orbital approach. It is shown that the upper  $\sim 3$  eV region of the weakly bonding band has a strong p-type character with flat bands, whose states are strongly affected by the crystal field as evidenced by a strong polarization dependence of matrix elements. This

region of the valence band is also very strongly affected by the transition to the amorphous phase, where the local potential results in smearing of the fine details of the valence band DOS. The similarity between the lone pair bands in the DOS of  $\text{Sb}_2\text{Se}_3$  and Se (28) suggests the role of the chalcogen lone p-pairs in forming the weakly bonding band of  $\text{Sb}_2\text{Se}_3$  and other  $\text{VB}_2\text{VIB}_3$  compounds.

1. K. Murase, J.W. Osmun, J. Freeouf, M. Kastner and C. Wood, Bull. APS 17, (3) 345 (1972).
2. S.D. Shutov, V.V. Sobolov, Y.V. Popov and S.N. Shestatskii, Phys. Stat. Sol. 31, K23 (1969).
3. R. Zallen, R.E. Drews, R.L. Emerald and M.L. Slade, Phys. Rev. Lett. 26, 1564 (1971).
4. J.C. Shaffer, B. Van Pelt, C. Wood, J. Freeouf, K. Murase and J.W. Osmun, Phys. Stat. Solidi (b), 54, 511 (1972).
5. M. Kastner, Phys. Rev. Lett. 28, 6, 355 (1972).
6. C. Wood, J.C. Shaffer and W.G. Proctor, Phys. Rev. Lett. 29, 485 (1972).
7. G.J. Lapeyre, A.D. Baer, P.L. Gobby and C.F. Badgley, to be published.
8. C. Wood, B. Van Pelt and E. Hyland, Rev. Sci. Instr., 43, 1374 (1972).
9. R. Mueller and C. Wood, J. Noncryst. Solids 7, 301 (1972).
10. W.F. Krolikowski and W.E. Spicer Phys. Rev. 185, 882 (1969).
11. J.F. Janak, O.E. Eastman and A.R. Williams, Solid State Comm., 8, 271 (1970).
12. N.V. Smith, Phys. Rev. B, 5, 4, 1192 (1972).
13. G.F. Derbenwick, Ph.D. Thesis, Stanford University (unpublished).
14. U. Gerhardt and E. Dietz, Phys. Rev. Lett. 26, 1477 (1971).
15. T. Gustafssons, P.O. Nilsson and L. Wallden, Phys. Lett., 37A, 121 (1971).
16. R.Y. Koyama and L.R. Hughey, Phys. Rev. Lett. 29, 1518 (1972).
17. G.D. Mahan, Phys. Rev. B, 2, 4334 (1970).
18. The EDC's of  $\text{Sb}_2\text{Se}_3$  taken with the retarding field analyzer and the electrostatic double pass cylindrical mirror analyzer support this criterion. There is some difference in the relative intensity of the peaks taken with the two different analyzers, but this difference is varying rather smoothly with photon energy. Z. Hurych, D. Davis and T. Knecht, to be published.
19. R.A. Powell, W.E. Spicer and J.C. McMenamin, Phys. Rev. B, 6, 3050 (1972).
20. J.M. Ballantyne, Phys. Rev. B, 6, 1436 (1972).
21. It is possible that this weak shoulder is due to the nonpolarized component (approx. 20%) of the radiation and that it would disappear if 100% polarized radiation were used. (B. Van Pelt, private communication).

22. Even though the analyzer used detects only the electrons originating at its focal point, it is not able to discriminate against electrons emitted from other parts of space yet having a virtual origin at its focal point. Most of the background electrons come from the two screens used to define the field free region and the region of acceleration or deceleration.
23. L.D. Laude and B. Fitton, J. Noncryst. Solids 8-10, 971 (1972).
24. Z. Hurych, C. Wang, R. Mueller and C. Wood, J. Noncryst. Solids, 11, 153 (1972).
25. J. Black, E.M. Conwell, L. Seigle and C.W. Spencer, J. Phys. Chem. Solids, 2, 240 (1957).
26. G.J. Lapeyre, T. Huen and F. Wooten, Solid State Comm. 8, 1233 (1970).
27. W.D. Grobman and D.E. Eastman, Phys. Rev. Lett. 29, 1508 (1972).
28. N.J. Schevchnik, J. Tejeda, M. Cordona and D.W. Langer, Solid St. Comm. 12, 1285 (1973).
29. H.R. Phillip and H. Ehrenreich, Phys. Rev. 129, 1550 (1963).
30. 5 to 10% (J.C. Shaffer, private communication).
31. E. Mooser and W.B. Pearson, J. Phys. Chem. Solids, 7, 65 (1958).
32. Z. Hurych, D. Buczek, C. Wood, G.J. Lapeyre and A.D. Baer, Solid St. Comm., in press.
33. Z. Hurych, D. Davis and T. Knecht, to be published.
34. N.W. Tideswell, F.H. Kruse and J.C. McCullough, Acta Cryst. 10, 99 (1957).
35. Z. Hurych, J.C. Shaffer, C. Wood, J.G. Lapeyre and A.D. Baer, Proceedings of the 5th International Conference on Amorphous and Liquid Semiconductors, to be published.

## CAPTIONS

- Figure 1. Energy distribution curves (EDC's) for  $E_0//c$ , with respect to the initial states.
- Figure 2. EDC's for  $E_0//c$ , with respect to the final states.
- Figure 3. EDC's for  $E_0//a$ , with respect to the initial states.
- Figure 4. EDC's for  $E_0//a$ , with respect to the final states.
- Figure 5. EDC's for amorphous  $Sb_2Se_3$ , with respect to the initial states.
- Figure 6. EDC's for amorphous  $Sb_2Se_3$ , with respect to the final states.
- Figure 7. Structure plot for  $E_0//c$ .
- Figure 8. Structure plot for  $E_0//a$ .
- Figure 9. Structure plot for amorphous  $Sb_2Se_3$ .
- Figure 10. Polarization dependence of the EDC's.
- Figure 11. Reflectance spectrum of  $Sb_2Se_3$  (after Reference 4).
- Figure 12. Model density of states for  $Sb_2Se_3$ .

Table 1a

Position of the Density of States Maxima in (eV)  
With Respect to the VBM

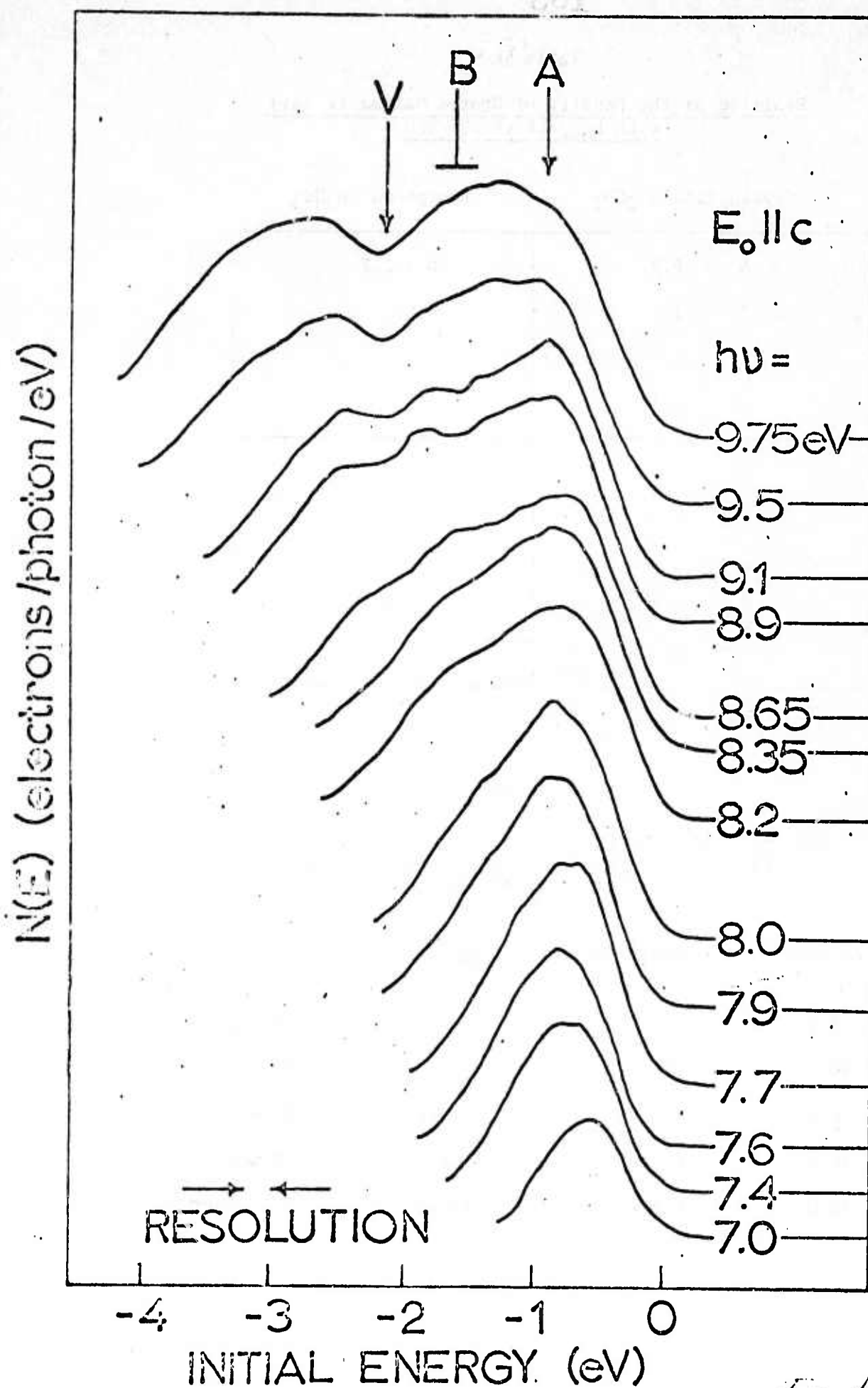
Crystalline $\text{Sb}_2\text{Se}_3$	Amorphous $\text{Sb}_2\text{Se}_3$
A ~ 0.8	AB ~ 1.2
B 1.6	
C 2.6	
C 3.3	
P <sub>4</sub> 6.4	P' 7
P <sub>3</sub> 7.2	
P <sub>2</sub> 7.8	
P <sub>1</sub> 8.5	
P <sub>0</sub> 9.3	
	P' 8

Table 1b

The Polarization Dependence of the Transition Between  
the Valence and Conduction Band DOS Maxima  
in Crystalline  $\text{Sb}_2\text{Se}_3$

h $\nu$ (eV)	Transition	$E_0    a$	$E_0    c$
8.0	A $\rightarrow$ P <sub>3</sub>	Weak	Strong
10.1	B $\rightarrow$ P <sub>1</sub>	Weak	Strong
10.1	D $\rightarrow$ P <sub>3</sub>	Strong	Weak
10.6	D $\rightarrow$ P <sub>1</sub>	Weak	Strong
12.0	C $\rightarrow$ P <sub>0</sub>	Strong	Not Observed





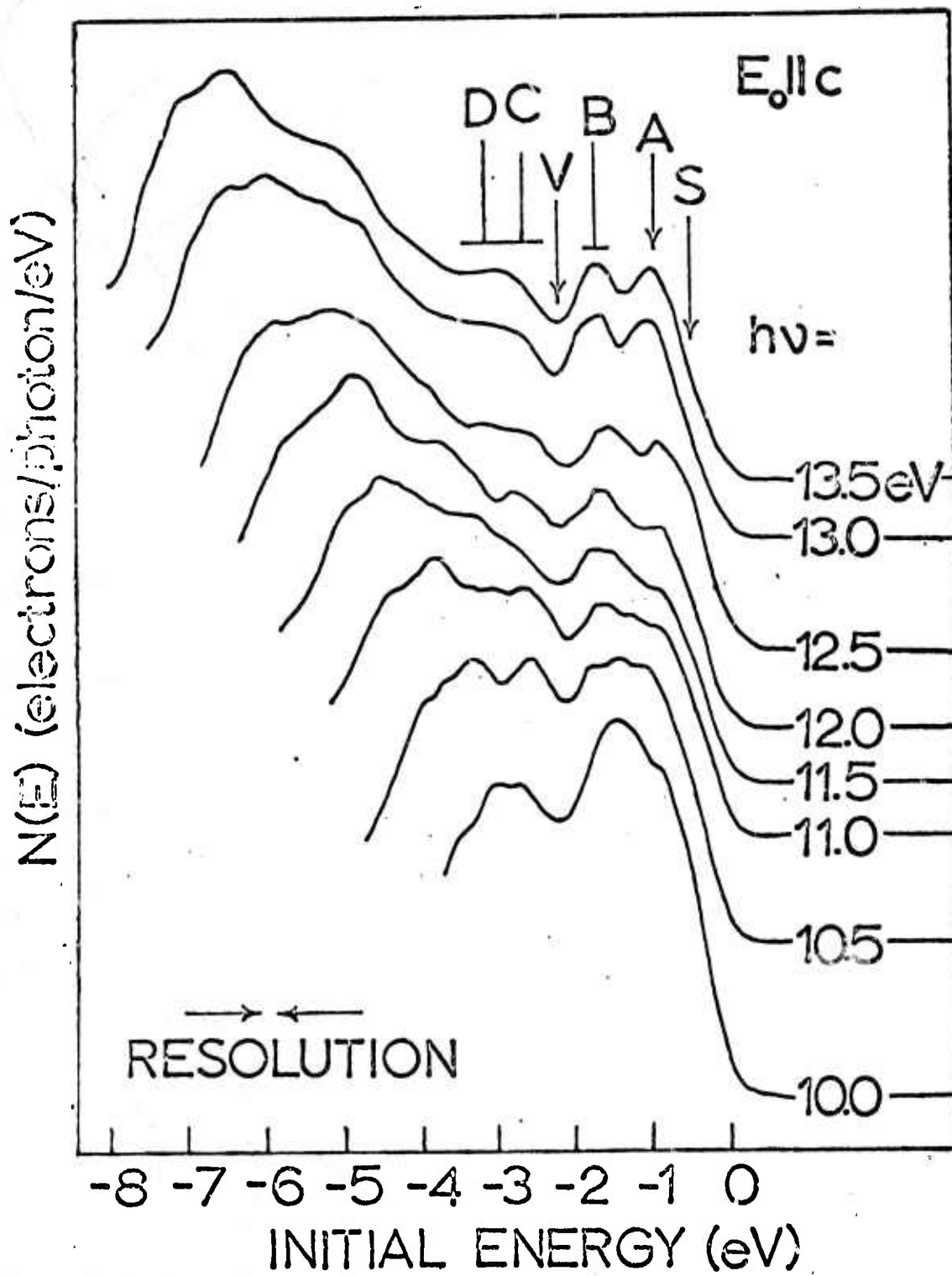
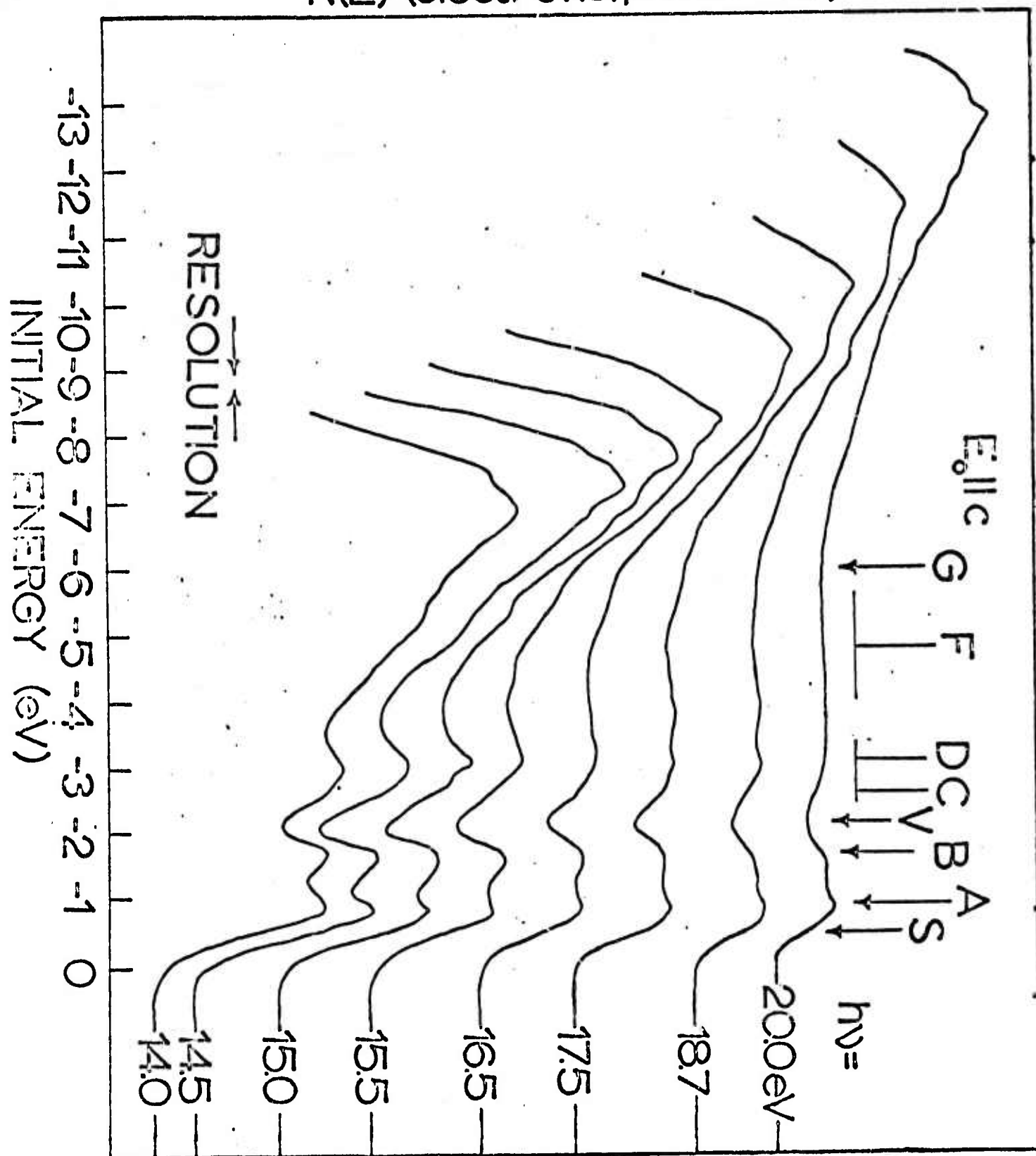
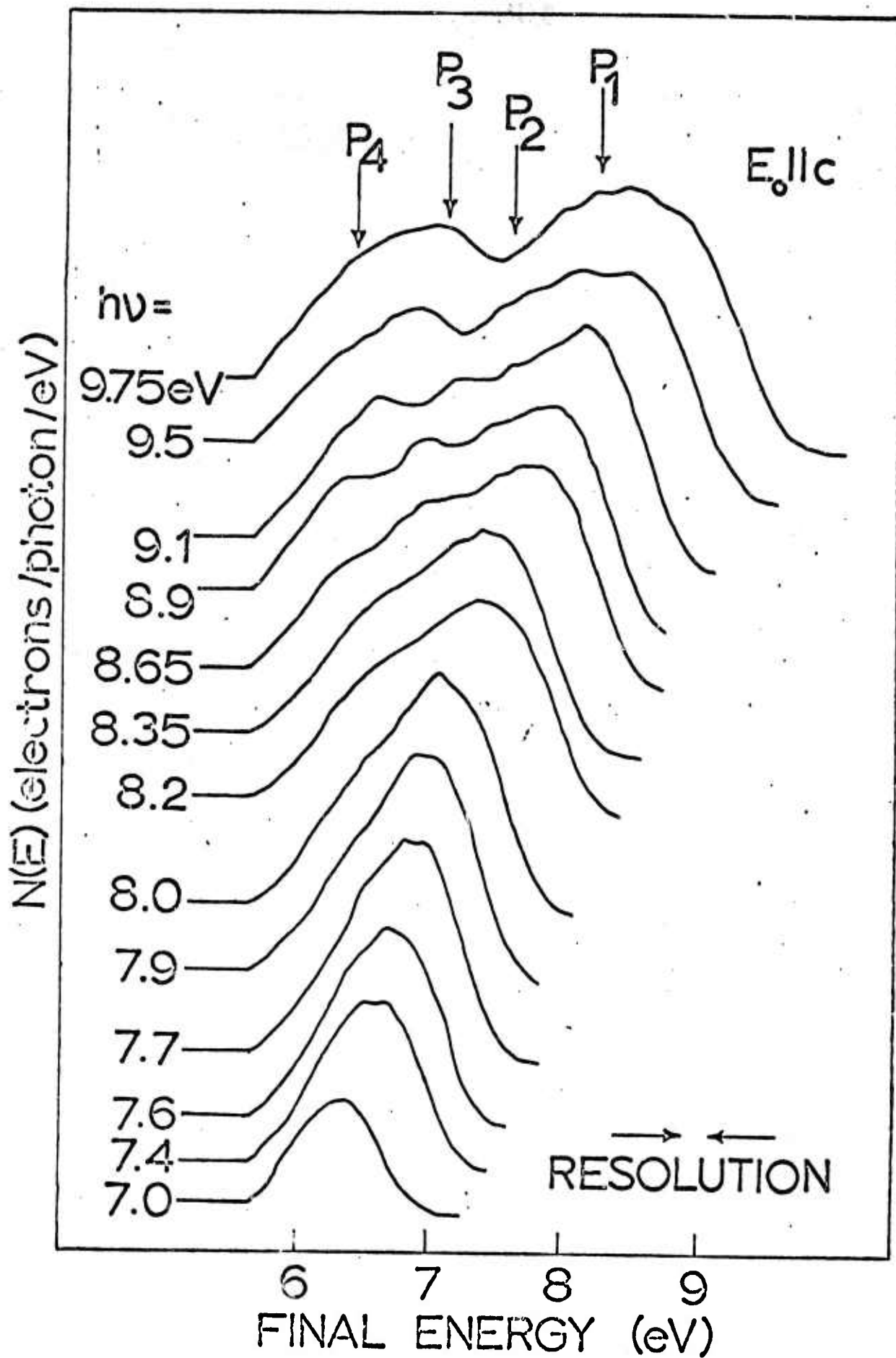


Fig. 1b

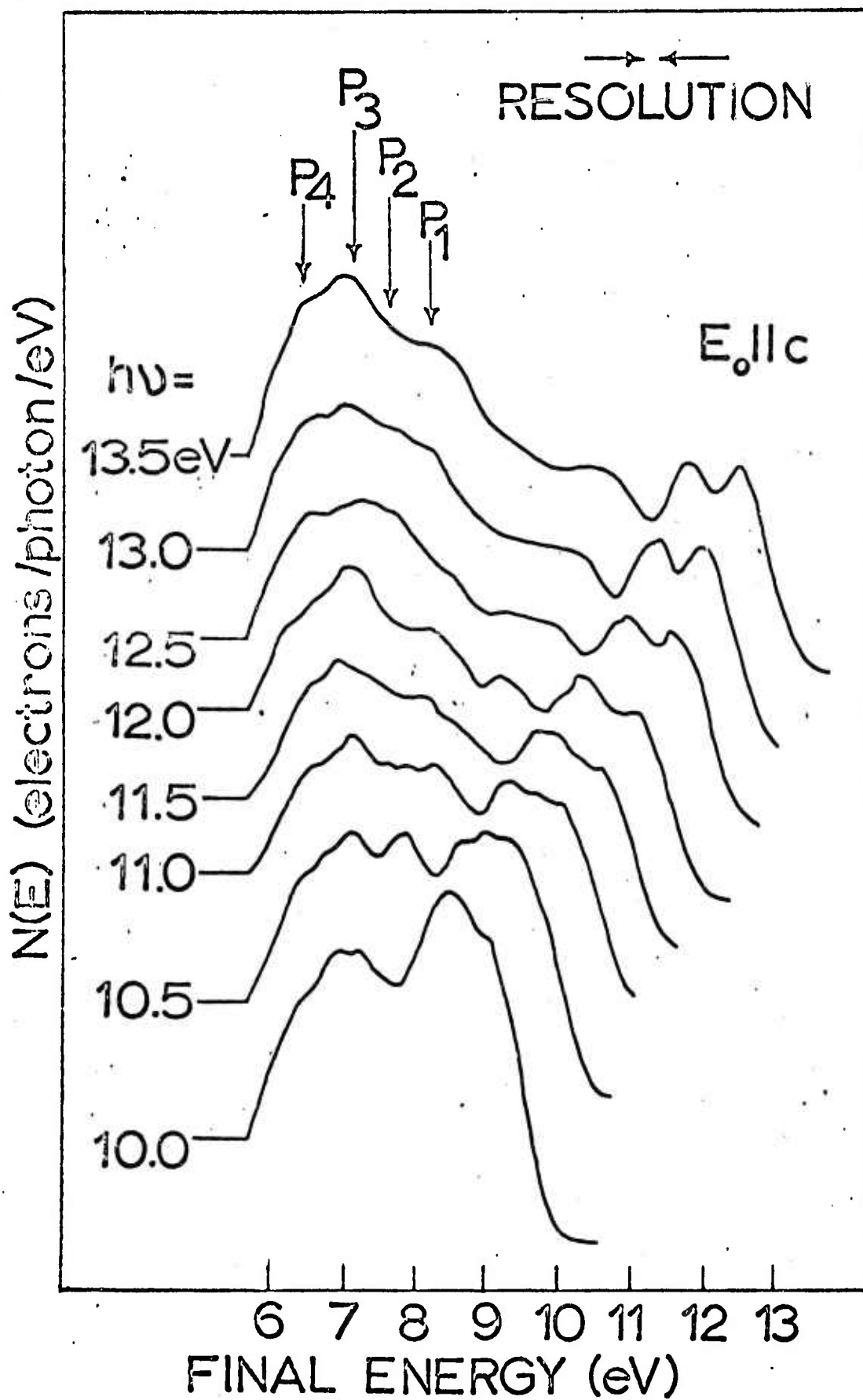
$N(E)$  (electrons/photon/eV)

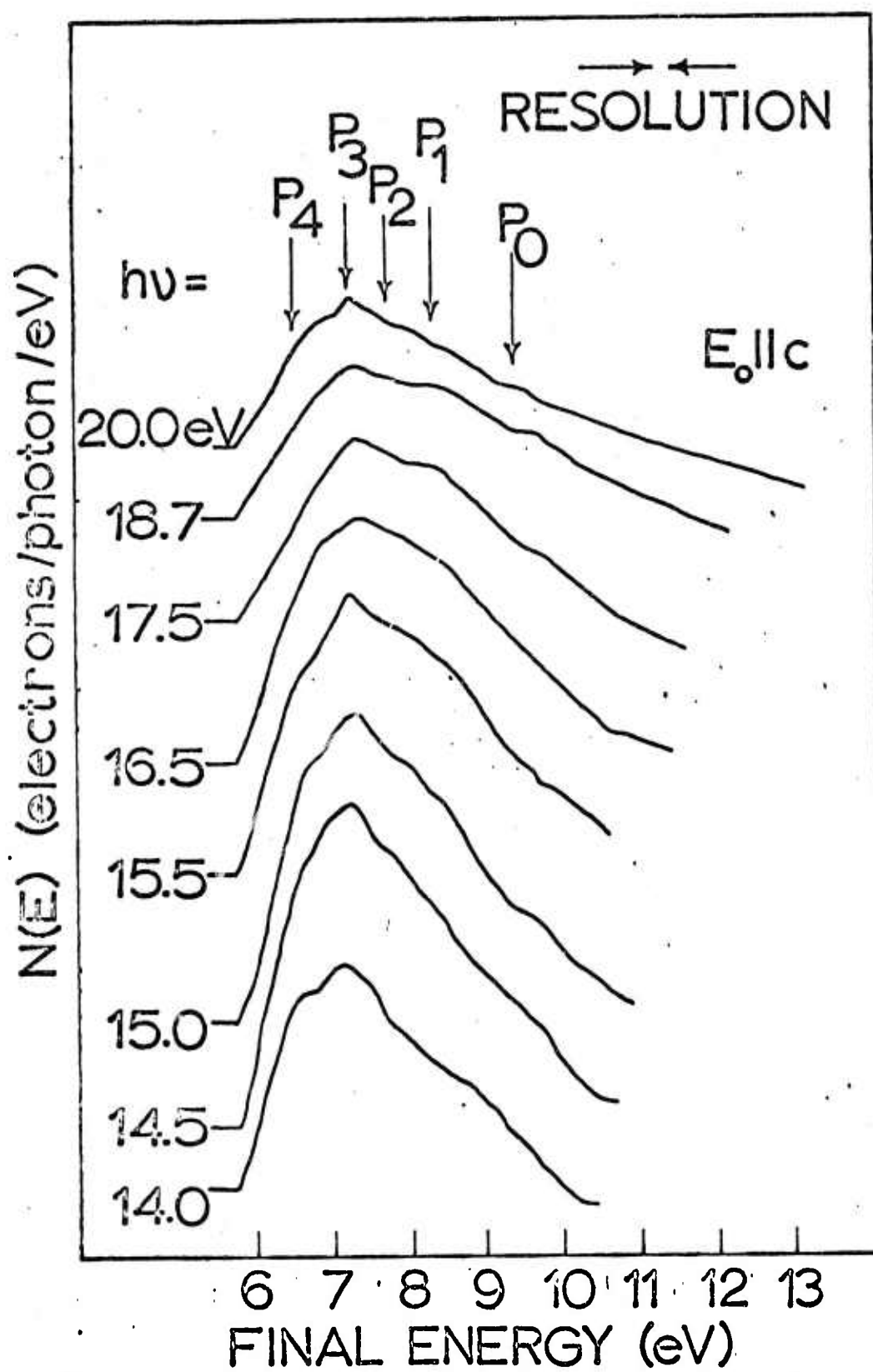


*Fig. 10*



Reproduced from  
best available copy.







$N(E)$  (electron/photon/eV)

Reproduced from  
best available copy.

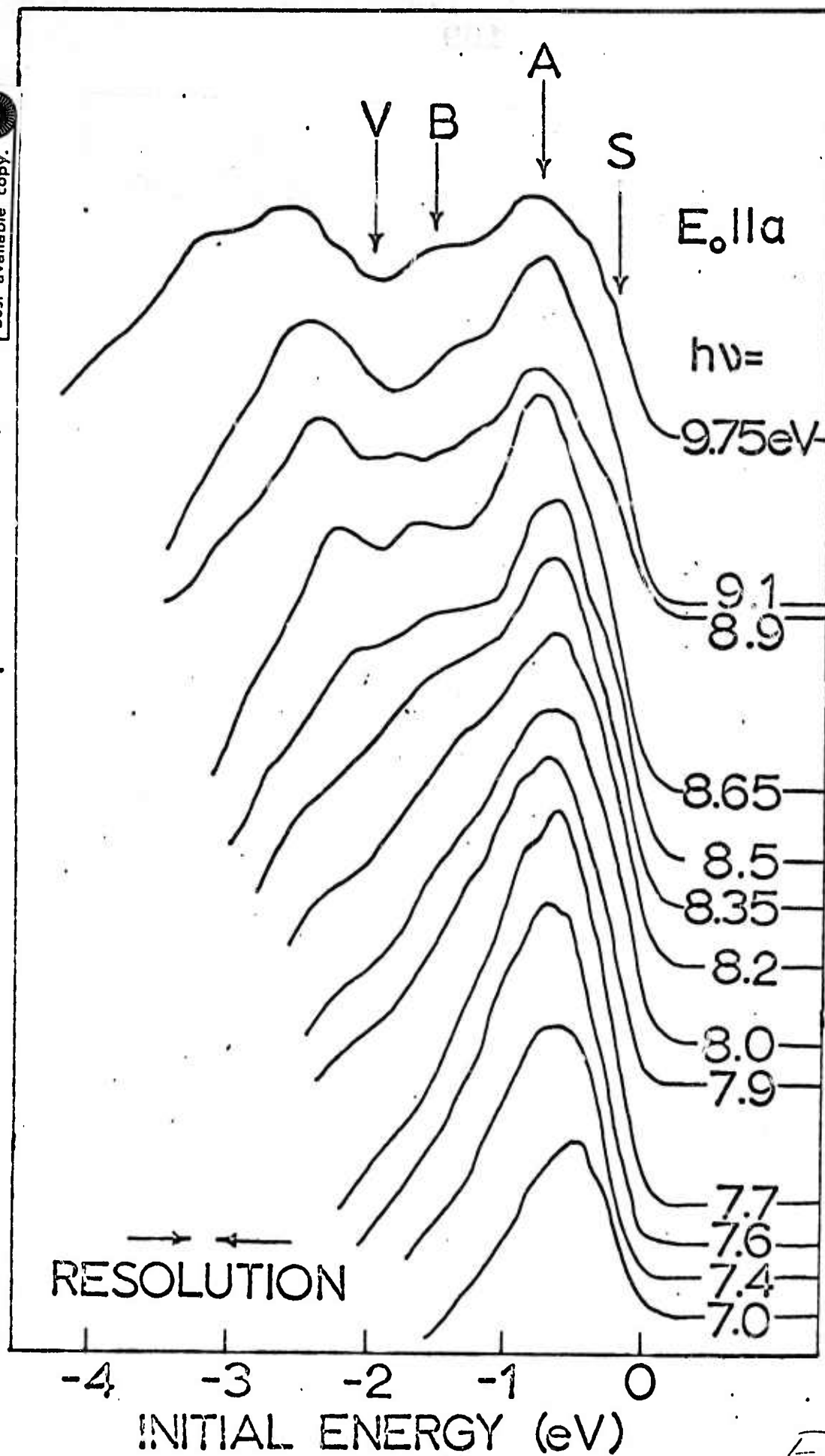
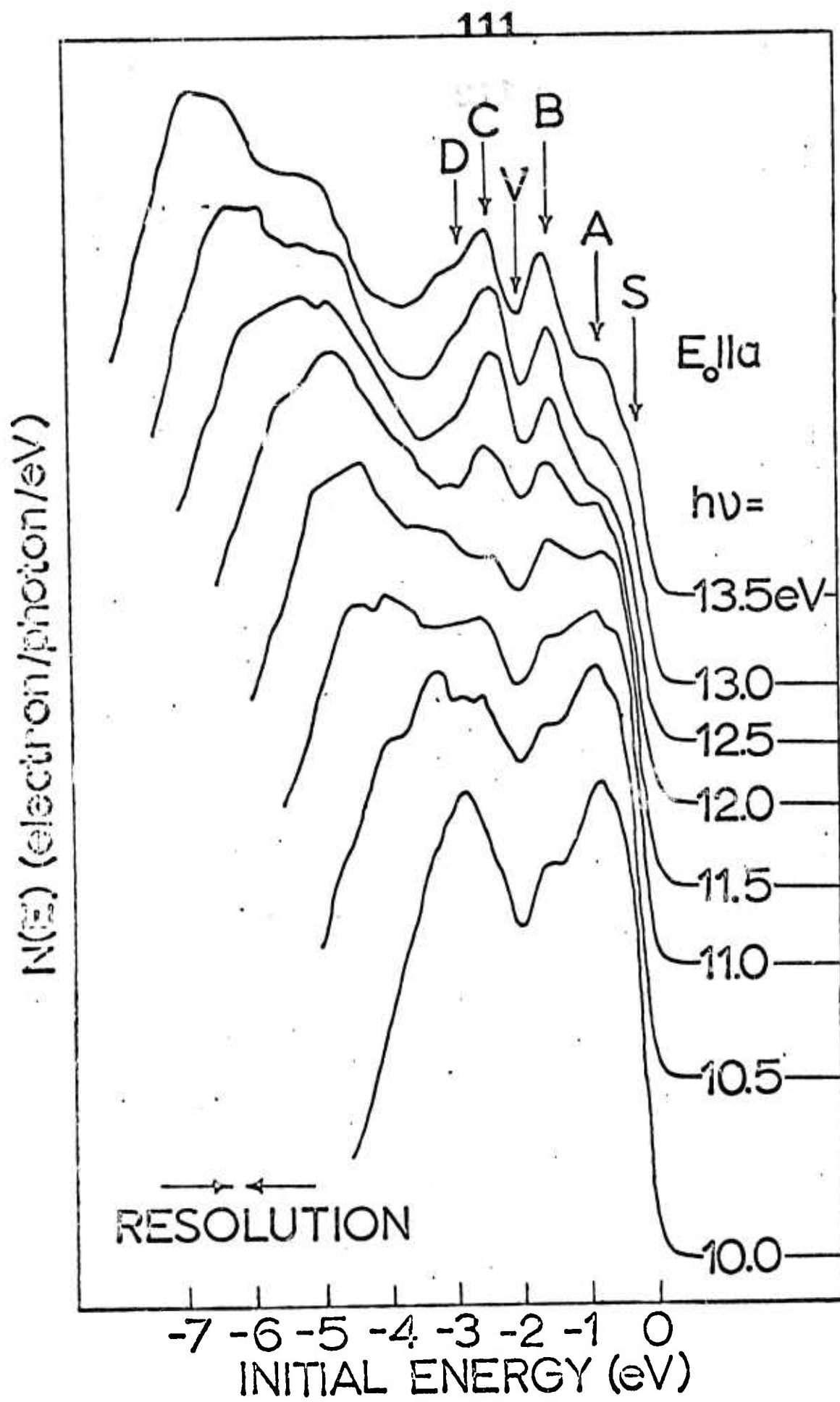
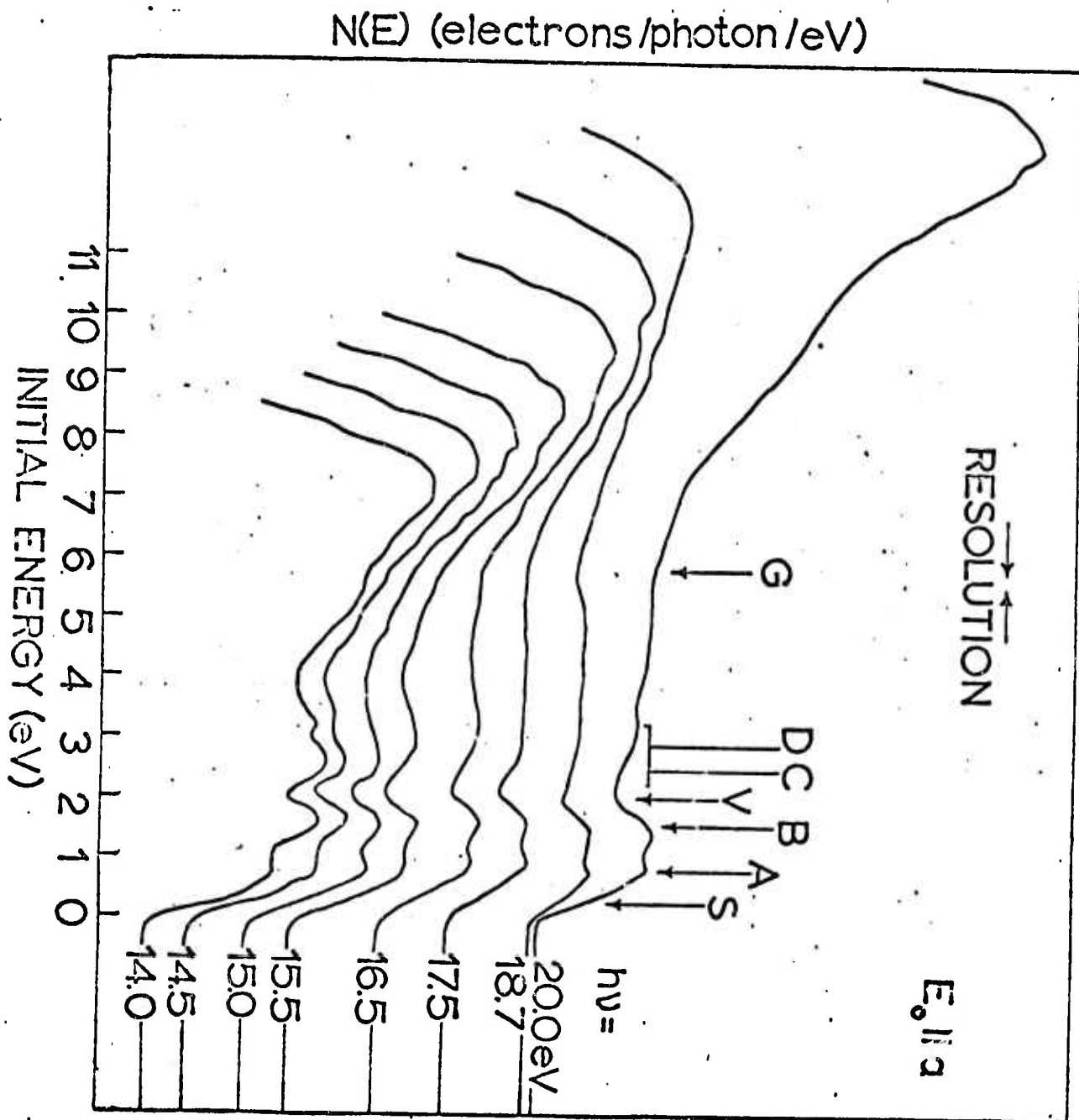
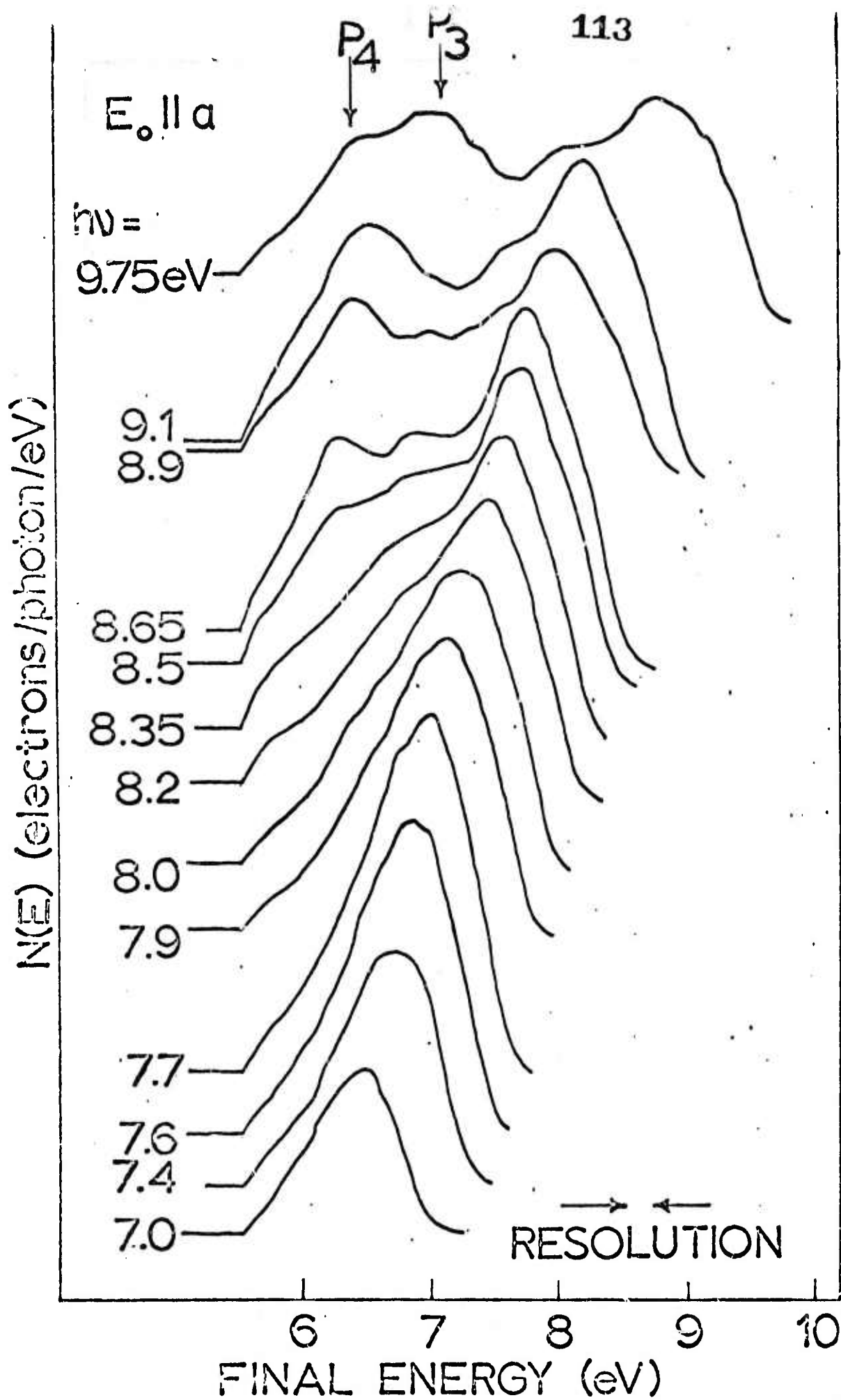


Fig. 3a





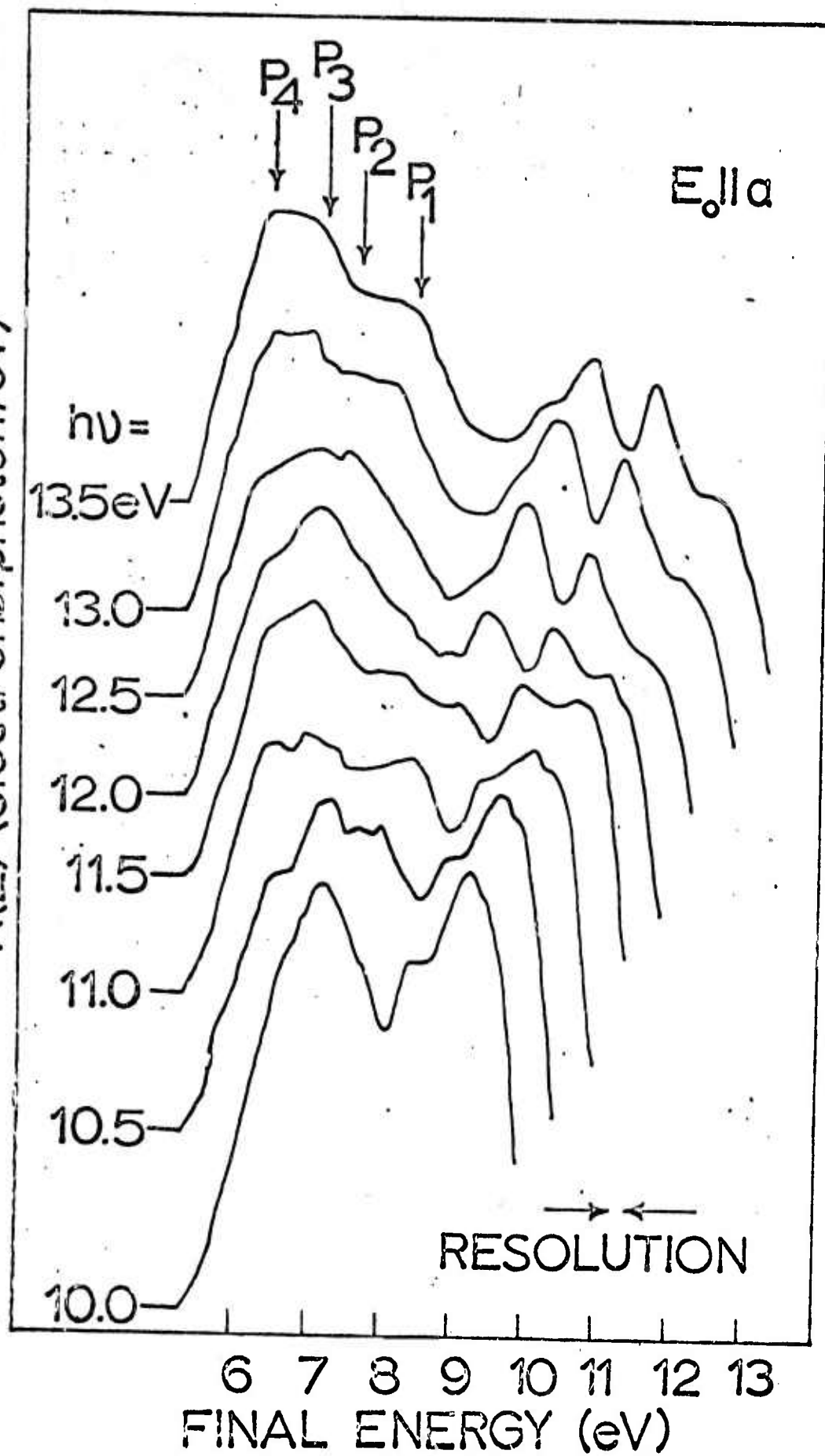


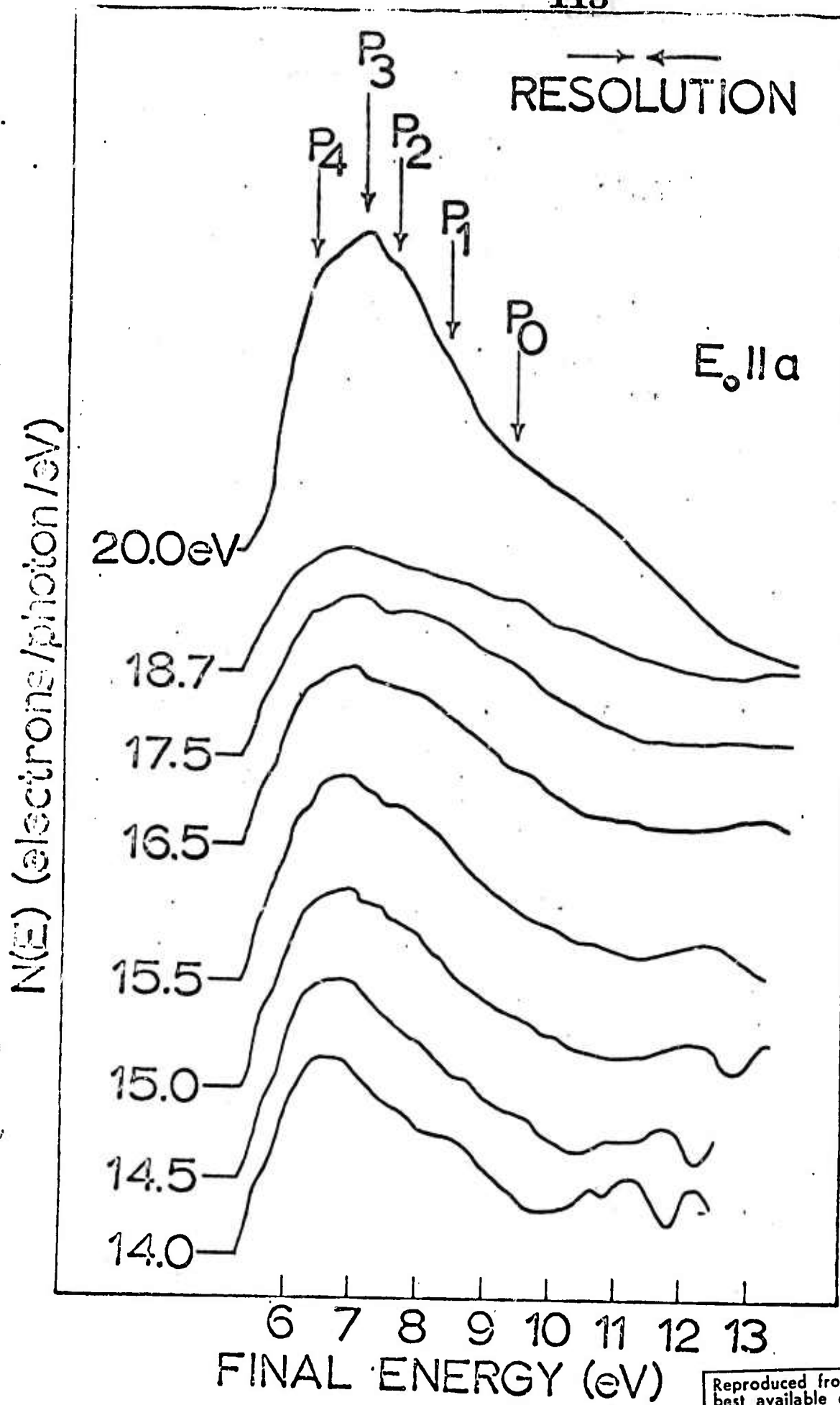


Reproduced from  
best available copy.

Reproduced from  
best available copy.

$N(E)$  (electrons/photon/eV)





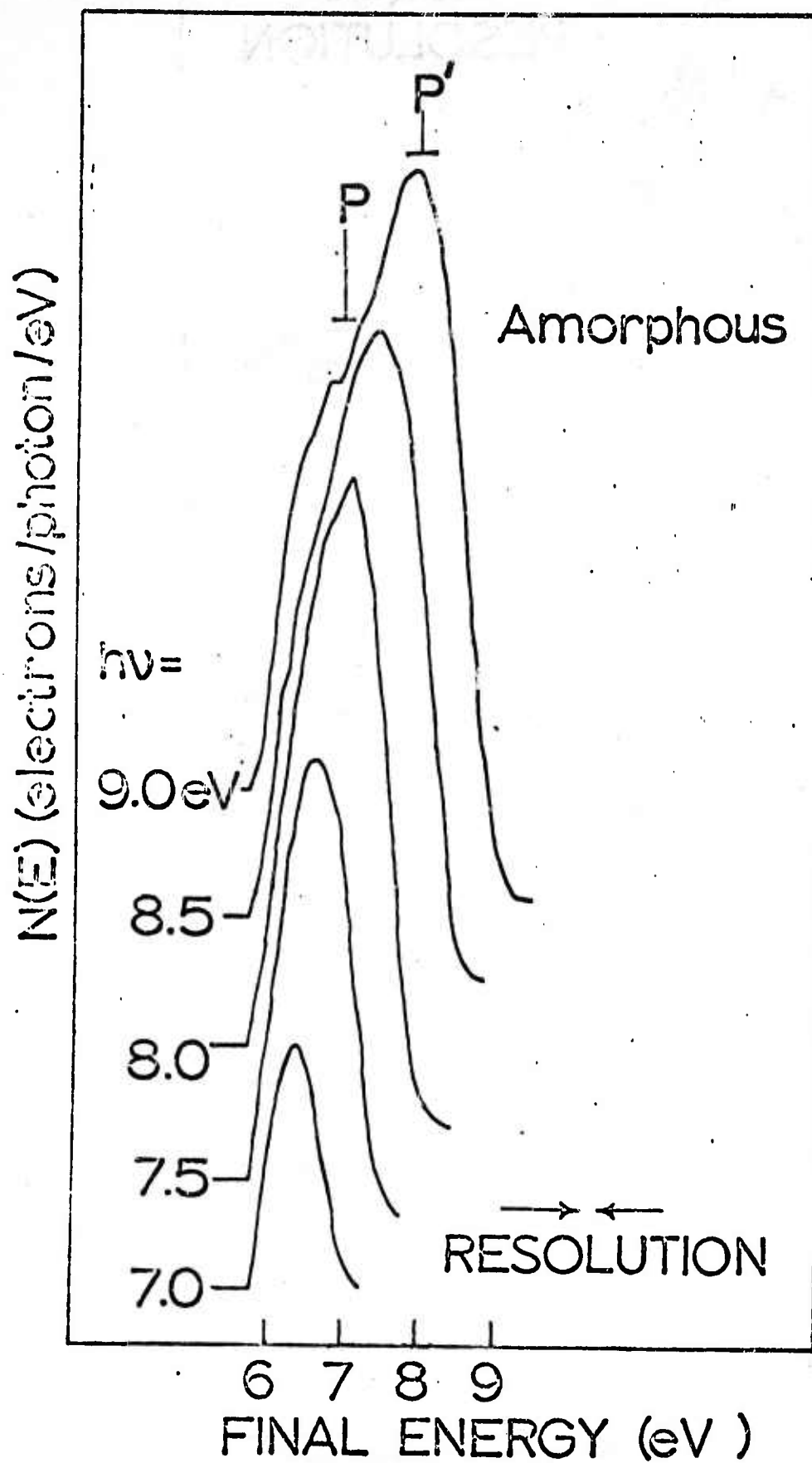
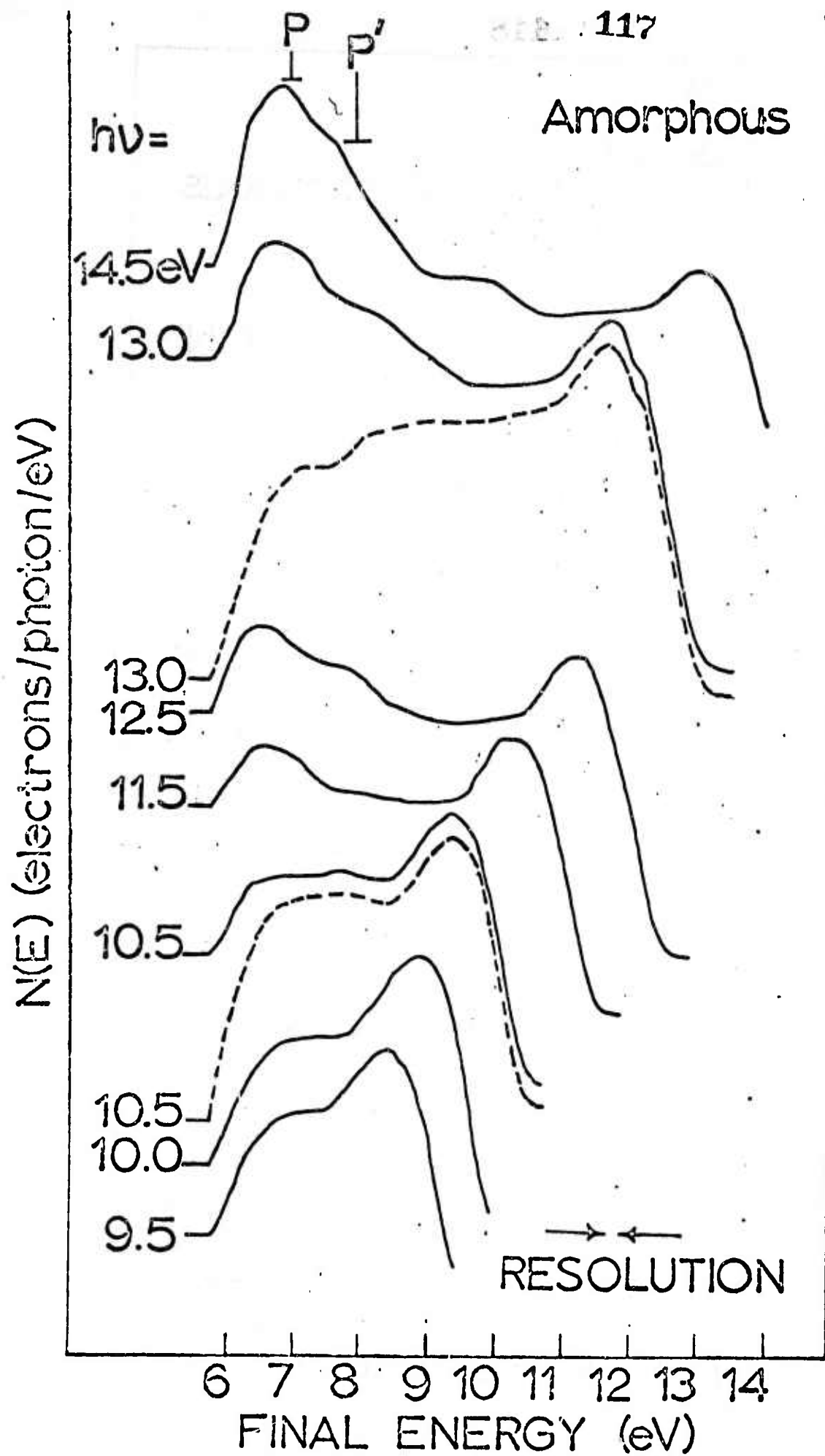
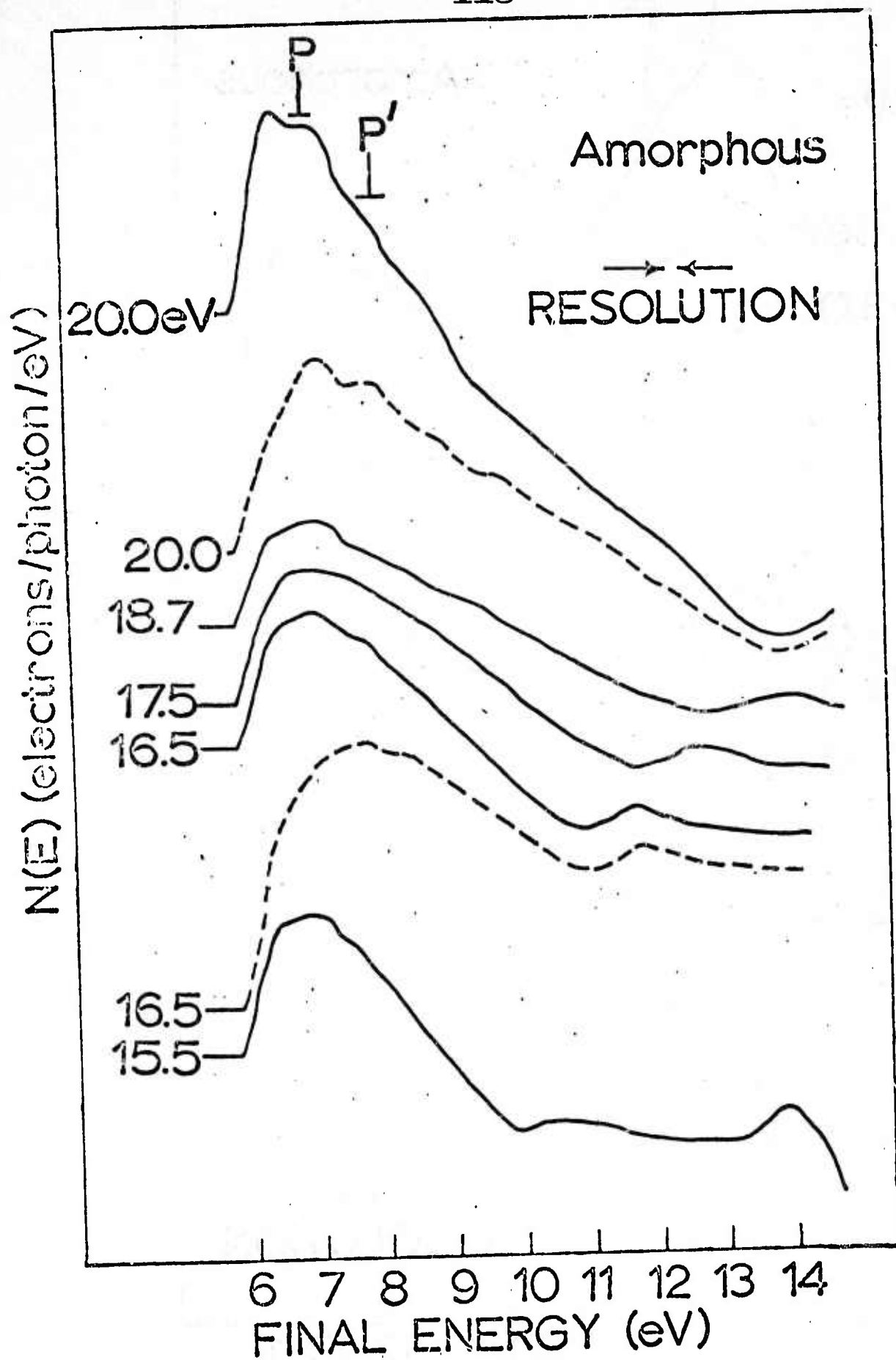


Fig. 6a







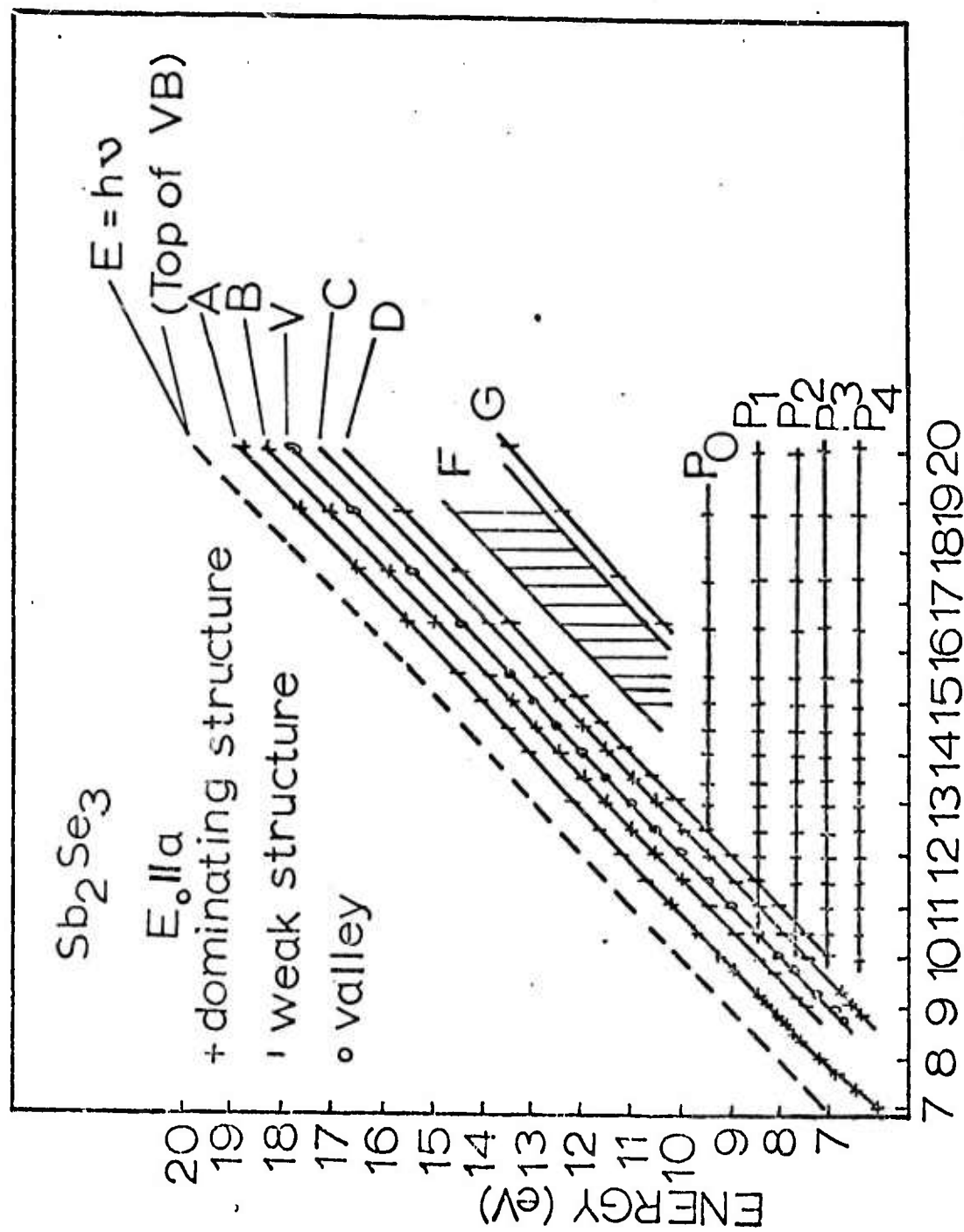
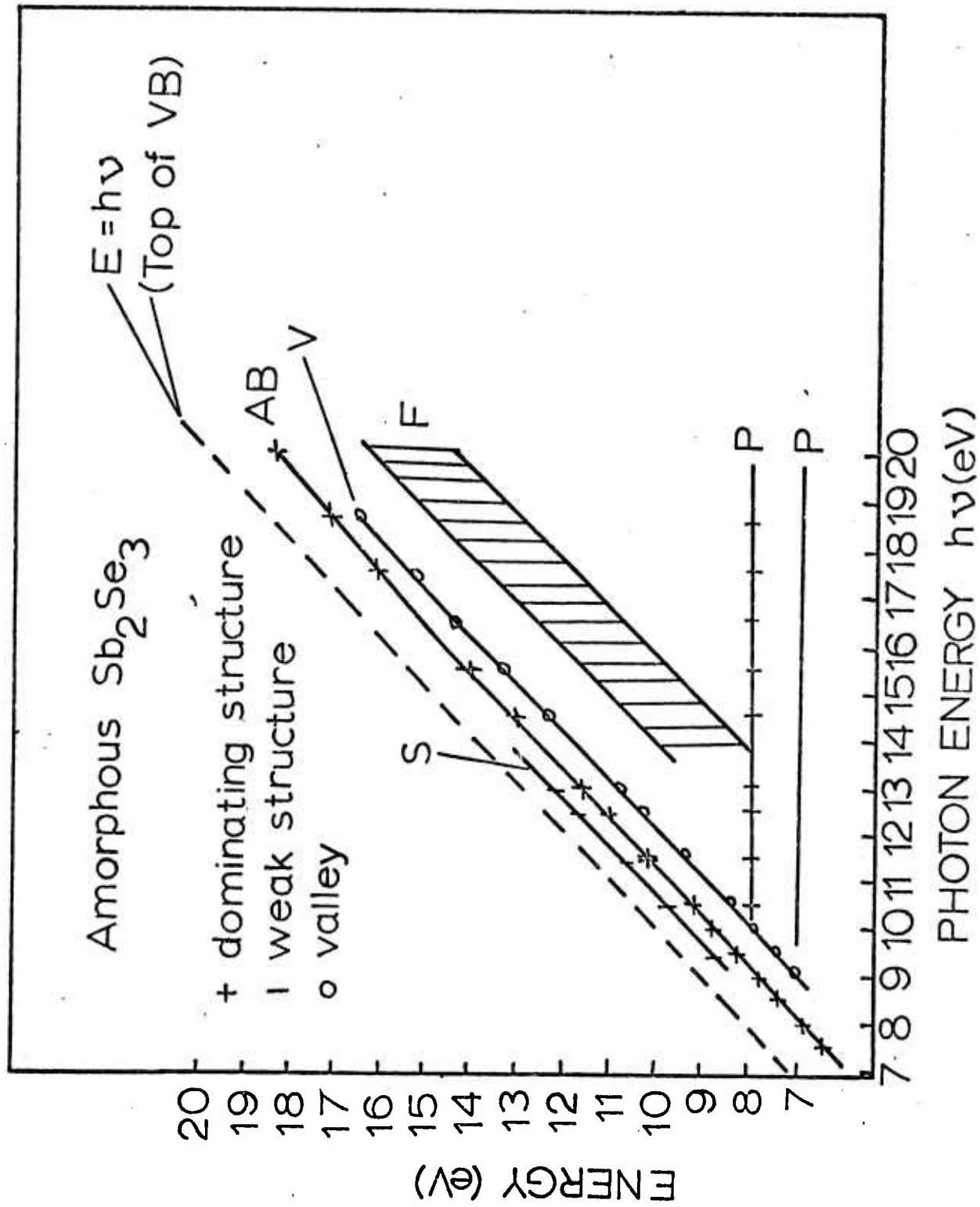
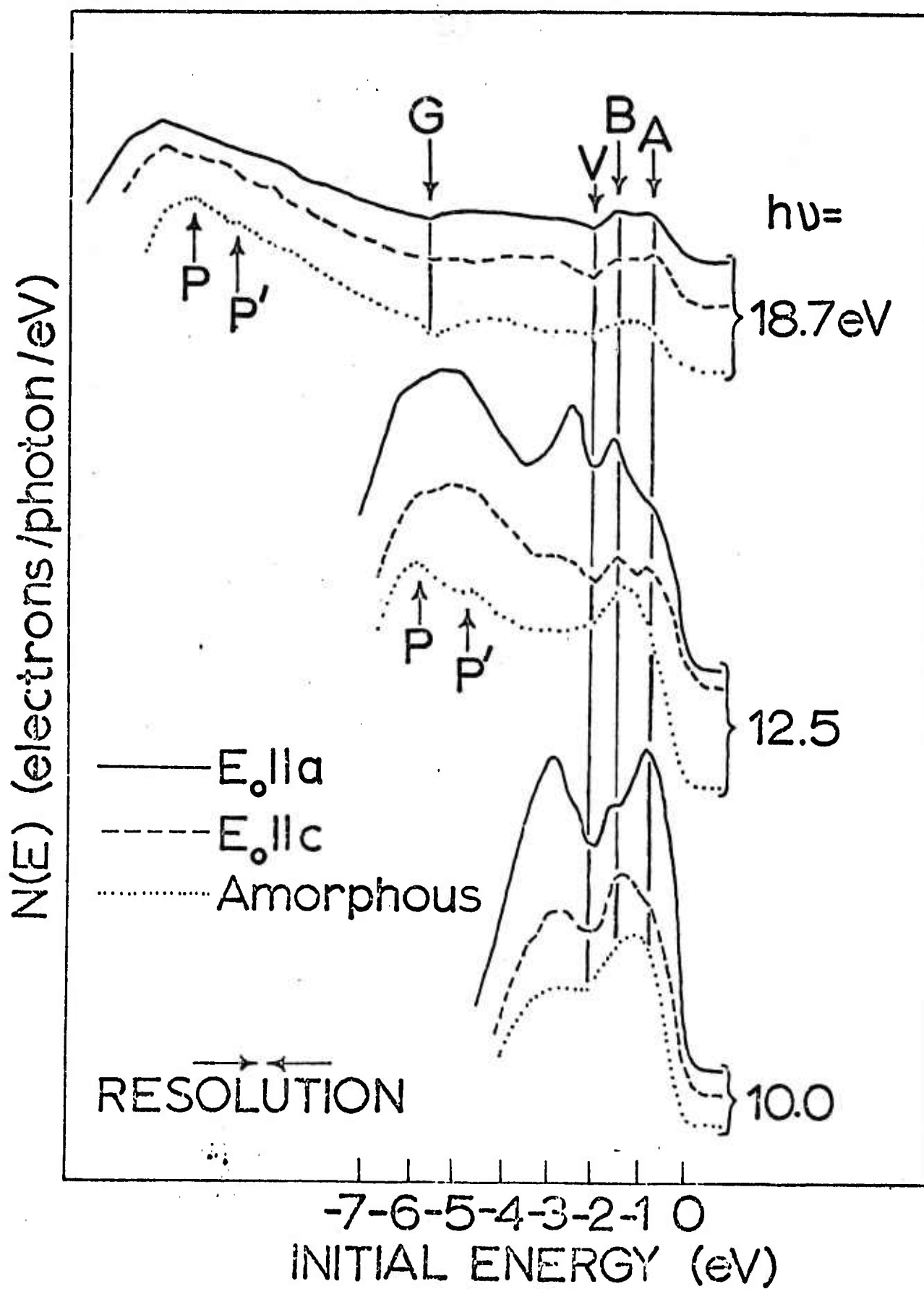


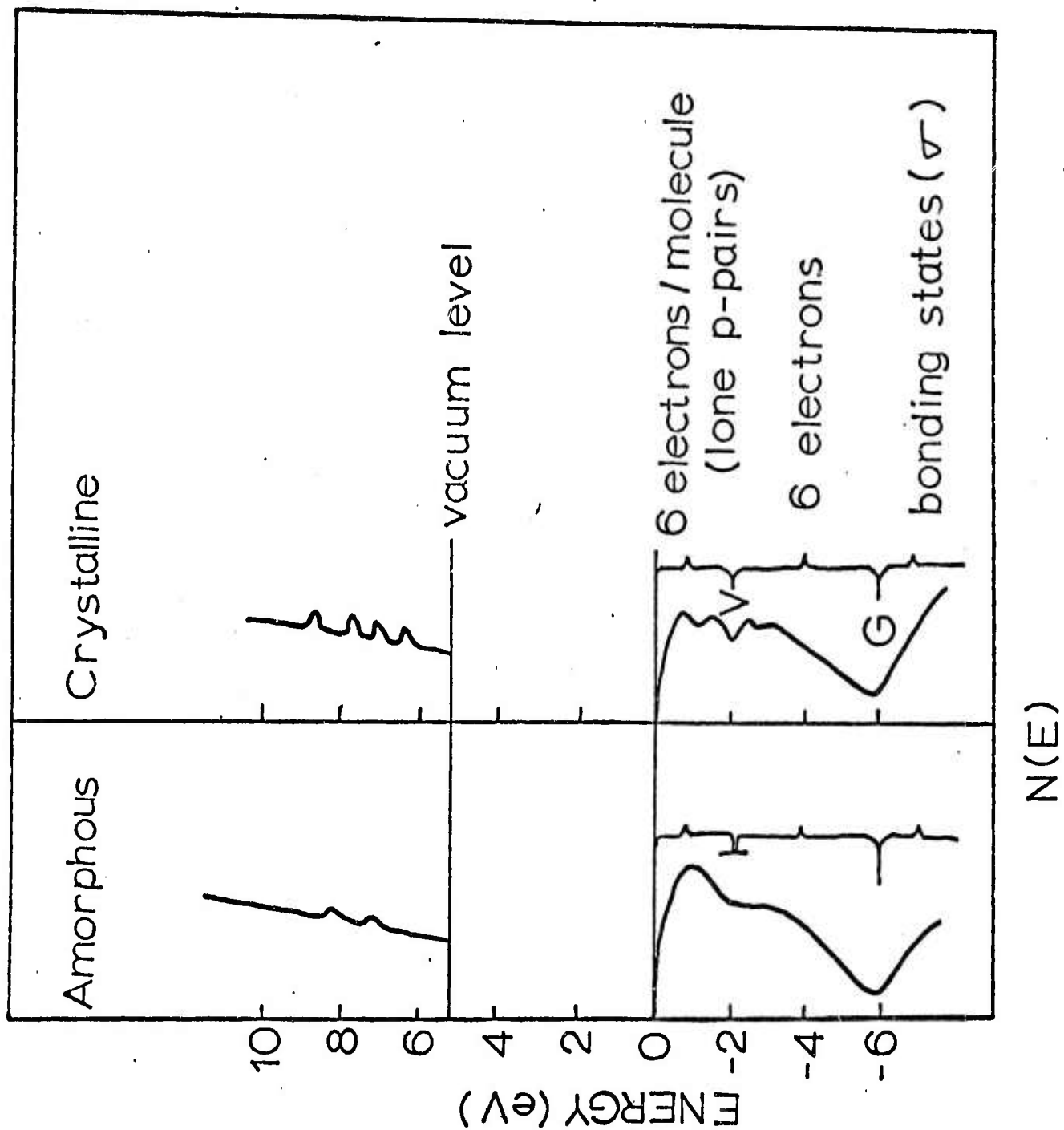
Fig. 8

PHOTON ENERGY  $h\nu$  (eV)









Strong Polarization Dependence and Selenium Lone-Pairs  
in the Photoemission Spectra of  $\text{Sb}_2\text{Se}_3$

Z. Hurych, D. Buczek and C. Wood<sup>†</sup>  
Physics Department  
Northern Illinois University  
DeKalb, Illinois 60115

and

G.J. Lapeyre and A.D. Baer<sup>††</sup>  
Physics Department  
Montana State University  
Bozeman, Montana 59715

<sup>†</sup>This work was supported by the Advanced Research Projects Agency of the Department of Defense and was monitored by the Army Research Office, Durham, under Contract No. DA-ARO-D-31-124-71-G132. We wish, also, to acknowledge the support of the Synchrotron Radiation Laboratory, University of Wisconsin, under Air Force contract no. F44620-70-C-0029.

<sup>††</sup>Work supported by the Air Force Office of Scientific Research, Office of Aerospace Research, USAF under Grant No. AFOSR-71-2061.

## Abstract

The photoemission energy distribution curves (EDC's) of crystalline and amorphous  $\text{Sb}_2\text{Se}_3$  were measured in the photon energy range  $h\nu = 7$  to 20 eV using polarized radiation from a synchrotron storage ring. The EDC's show that the six electrons per  $\text{Sb}_2\text{Se}_3$  molecule, attributed primarily to the selenium p-pairs, are clearly separated from the remaining part of the valence band of crystalline  $\text{Sb}_2\text{Se}_3$ . The optical transitions from these states occur with matrix elements strongly dependent on the orientation of the electrical vector of the polarized radiation as a result of crystal field effects. Model densities of states are constructed for both crystalline and amorphous  $\text{Sb}_2\text{Se}_3$ .

## Résumé

Les courbes de distribution des photoelectrons émis par  $\text{Sb}_2\text{Se}_3$  cristalline et amorphe ont été mesurés dans l'intervalle de  $h\nu = 7 \text{ eV}$  à  $h\nu = 20 \text{ eV}$ . Les mesures ont été effectuées pour la radiation polarisée émise par un synchrotron. Les courbes obtenues indiquent que six électrons de la molécule de  $\text{Sb}_2\text{Se}_3$ , sont bien séparés de la bande des électrons de la bande de valence de  $\text{Sb}_2\text{Se}_3$  cristalline. Les transitions optiques de ces états sont caractérisés par des probabilités de transitions fortement dépendant de l'orientation du vecteur du champ électrique. Ce phénomène dépend des effets du champ cristallin. Les densités des états ont été construites pour l'état cristallin et l'état amorphe de  $\text{Sb}_2\text{Se}_3$ .

Orthorhombic  $\text{Sb}_2\text{Se}_3$  (space group  $D_{2h}^{16}$ ) belongs to the group V-VI compound semiconductors, a class of materials whose optical and transport properties have been widely investigated. However, little data is available on band structure of these compounds, primarily because of their complicated primitive cells (comprising 112 valence electrons in the case of  $\text{Sb}_2\text{Se}_3$ ). Densities of states are generally derived from a molecular orbital approach, with the bonding and weakly-bonding bands adjusted to fit the reflectance spectra (1). This method is necessarily conjectural since the reflectance data does not allow the determination of the absolute energy levels of the states involved.

We have employed photoemission spectroscopy to determine absolute energies and some fundamental features of the structure of the upper valence band and conduction band of amorphous and crystalline  $\text{Sb}_2\text{Se}_3$  and so determine the influence of disorder on the electronic structure. The measurements were made in the photon energy range 7 to 20 eV using the University of Wisconsin 240 MeV synchrotron storage ring. The radiation incident onto the sample was naturally polarized  $\sim 80\%$  with the electrical vector  $\vec{E}_0$  in the median plane of the storage ring. A double-pass cylindrical electrostatic mirror (2) with a spiraltron was used as an electron energy analyzer, having a constant resolution of 0.2 eV.

Single crystals of  $\text{Sb}_2\text{Se}_3$  were grown in a zone refiner (3), and were cleaved in situ in a vacuum of  $\sim 10^{-10}$  torr. The natural cleavage plane (010) produced excellent mirror-like surfaces which allowed the measurement of the photoemission energy distribution curves (EDC's) for  $\vec{E}_0 \parallel a$  and  $\vec{E}_0 \parallel c$ . Amorphous  $\text{Sb}_2\text{Se}_3$  films of thickness 200 to 500 Å were evaporated in situ from an electron-beam gun by a method developed earlier (4). X-ray diffraction measurements after the photoemission experiment confirmed that the films were amorphous.

The complete experimental details and results are beyond the scope of this letter and will be published separately. Here several typical energy distribution curves (EDC's) of  $\text{Sb}_2\text{Se}_3$  are presented and their relation to the electron energy states is discussed. Fig. 1 shows EDC's at several photon energies for crystalline  $\text{Sb}_2\text{Se}_3$  with  $\vec{E}_0 \parallel a$ , and the structure plot of the major features is presented in fig. 2 for the entire photon energy range. The main features of the EDC's for crystalline  $\text{Sb}_2\text{Se}_3$  are four peaks A, B, C, and D of constant and rather well-defined initial state energy (fig. 1 and 2). We associate peaks A and B with regions of high density of states arising from narrow bands or from flat E vs. k portions of the valence band. The intensities of the four peaks strongly vary with photon energy which suggest that they correspond to direct (i.e.,  $\vec{k}$  conserving) optical transitions (5). A valley V, located 2 eV below the valence band maximum is one of the most prominent features of the EDC's for both orientations of  $\vec{E}_0$  (figs. 1, 2 and 4). A weakly resolved onset of a deeper-lying valence band at  $\sim 6$  eV below the valence band maximum, superimposed on the background of scattered electrons and on the conduction band structure, is observed as an inflection (point G) in the EDC's for  $h\nu \geq 16$  eV. The existence of this band, which shows up also in the reflectance spectrum (6), has been confirmed by x-ray photoemission spectra (7).

The lower energy ranges of the EDC's show four peaks  $P_1$  to  $P_4$  of intensity and shape strongly varying with  $h\nu$ . Since these peaks are present over the entire photon energy region with constant final state energy (fig. 2) we associate them with the regions of high densities of states in the conduction band (fig. 3). In general, such conduction band density-of-state-maxima can be filled either directly by optical excitation, or by photoexcited electrons which are inelastically scattered down from high energies (8). In our case,



these conduction band density-of-states maxima are coupled in optical transitions with the regions of high density of states in the upper part of the valence band, thus giving rise to very sharp peaks in the EDC's (e.g., the overlapping peaks D and P<sub>3</sub> for  $\vec{E}_0 \parallel a$  at  $h\nu = 10$  eV in figs. 1 and 2). Due to several largely unknown factors, e.g., the effect of matrix elements and electron-electron scattering length, no conclusions can be drawn from the relative intensity of the peaks.

The strong dependence of the relative intensity of the peaks A, B, C, and D on the orientation of  $\vec{E}_0$  (fig. 4) is attributed to the effect of the crystal field. (This dependence of the energy distribution of the joint density of states of  $\vec{E}_0$  is not observable in the reflectance or the  $\omega^2\epsilon_2$  spectrum, (6), (7)). The matrix elements for the optical transitions now include  $\vec{E}_0$  in addition to  $\vec{k}$  and  $h\nu$ . This polarization dependence of the EDC's is much stronger than that reported on other materials (9).

According to the optical sum rules (6) the upper 2 eV part of the valence band contains approximately 6 electrons per  $\text{Sb}_2\text{Se}_3$  molecule which participate in optical transitions from  $h\nu \sim 1.2$  eV (the band gap of  $\text{Sb}_2\text{Se}_3$ ) up to 3.2 eV. We attribute these six electrons to the three lone (unshared) p-pairs of Se electrons, predicted by Kastner (10). Furthermore, these weakly bonding electrons can be associated with the six weakest bonds per  $\text{Sb}_2\text{Se}_3$  molecule between the crystal layers (bond number  $\sim 0.01$ ) (11). The crystal symmetry and field determine the direction of these bonds and their energy levels by minimizing the total crystal energy and show up in the EDC's through the very strong polarization dependence of matrix elements for optical excitation from these states. Thus, the valley V separates the 6 electrons, attributed to lone p-pairs, from the rest of the weakly-bonding band located between V and point G. These latter states, which include

another 6 valence electrons per  $\text{Sb}_2\text{Se}_3$  molecule (6) have again a considerable contribution from flat E vs. k portions of the band (peaks C and D in figs. 1 and 2). These states can be attributed to the six resonant bonds of intermediate strength (bond number  $\sim 0.1$ ) (11), forming the crystal layers from infinitely long Sb-Se chains. The deeper valence band starting at  $\sim 6$  eV below the valence band maximum (point G in the EDC's) is attributed to  $\sigma$ -bonding orbitals, arising from the strongest Sb-Se bonds within the chains (bond number  $\sim 1.0$ ) (11). The strong coupling of the upper p-type part of the weakly bonding band with the high densities of states in the upper conduction band suggest the d-character of the latter states.

In amorphous  $\text{Sb}_2\text{Se}_3$  (fig. 4) peaks A, B, C and D disappear, and a broad peak, located at  $\sim 1.2$  eV below the valence band maximum is observed. In addition, two very weak conduction band structures appear, P and P', located at  $\sim 7$  and 8 eV above the valence band maximum. The broad peak is of rather constant intensity and shape with respect to  $h\nu$  suggesting that the optical transitions are non-direct, i.e.,  $\vec{k}$  conservation is not an important selection rule. As with Se and Te (12) the long-range disorder has the effect of smearing the upper conduction band structure rather than affecting the sharpness of the leading edge of EDC's. No band tailing is observed within the experimental resolution, in agreement with previous optical and photoconductivity data (13). The weaker overall structure of the conduction band allows for much better resolution of the onset of the bonding band (point G) in amorphous than in crystalline  $\text{Sb}_2\text{Se}_3$ . Of particular interest is the behavior of the Se lone p-pairs located at the top of the valence band. The separation of the upper part of the valence band by the valley V in amorphous  $\text{Sb}_2\text{Se}_3$  is much weaker yet still noticeable. The

very weak bonds, responsible formerly for holding the crystal layers together, are now randomly oriented in space, and their energy levels are determined locally by the random potential fluctuations, which result in a lack of the resonance character of these bonds (14).

In conclusion, vacuum UV photoemission spectroscopy provides a model for the density of states of  $\text{Sb}_2\text{Se}_3$ , which presents a considerably more detailed picture than the model derived from the reflectance (6) or x-ray photoemission (7). Of particular interest is the behavior of the six electrons in the top 2 eV of the valence band, attributed to the Se lone p-pairs. These states are very strongly affected by the crystal field, as demonstrated by their behavior in the transition to the amorphous phase as well as by the very strong polarization dependence of the EDC's in crystalline  $\text{Sb}_2\text{Se}_3$ .

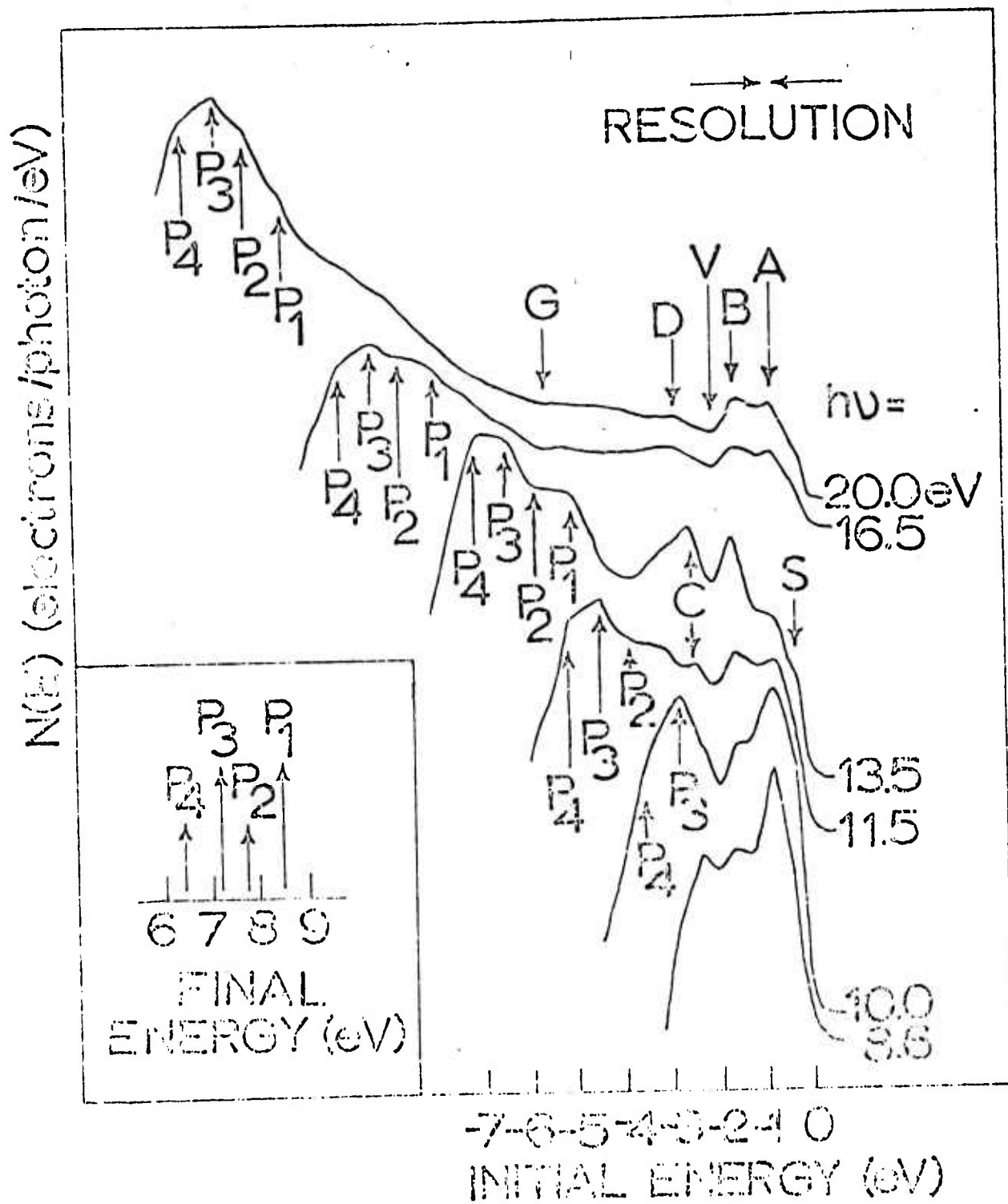
We wish to thank the staff of the University of Wisconsin Physical Science laboratory for their experimental assistance, R. Mueller for performing the x-ray diffraction, D. Davis for drawing the figures, B. Van Pelt for growing the  $\text{Sb}_2\text{Se}_3$  crystals, and Professors W.E. Spicer, F.M. Mueller and J.C. Shaffer for valuable discussions and comments on this work.

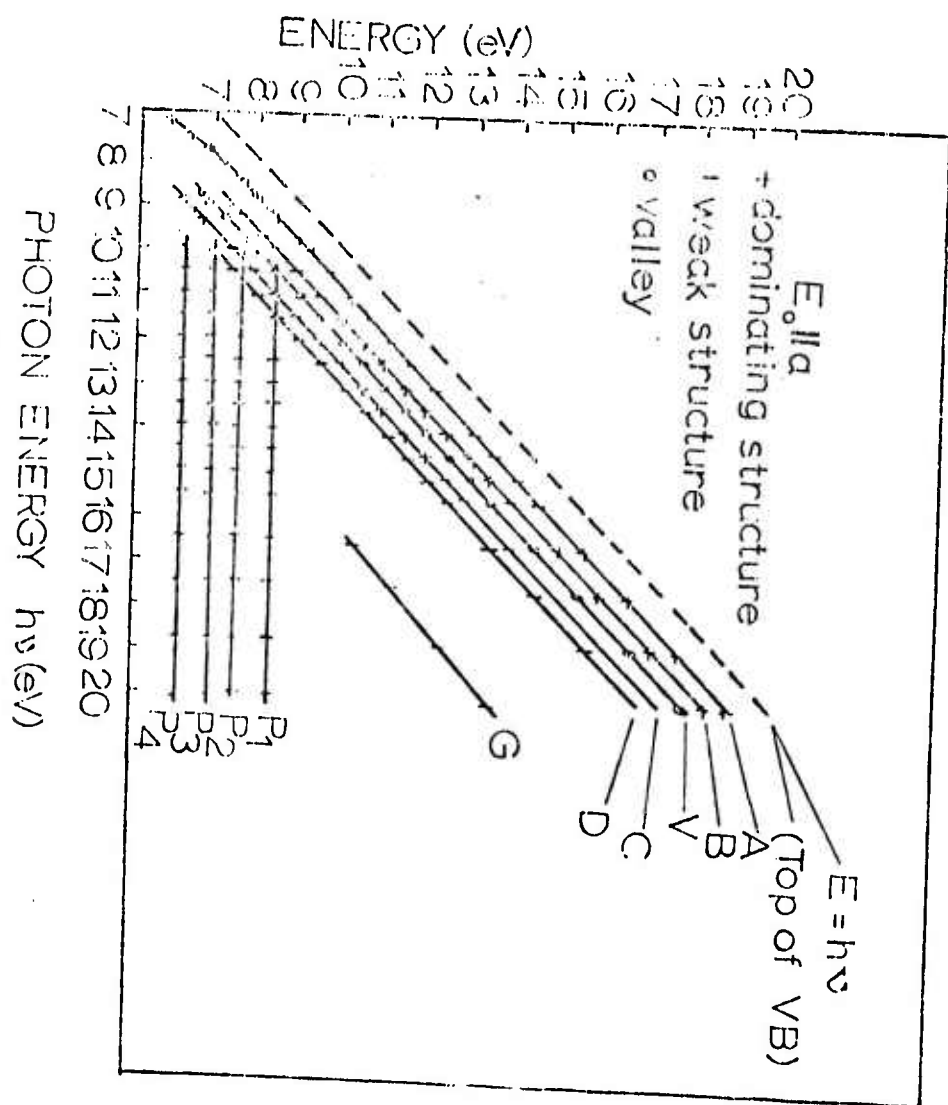
## REFERENCES

1. K. Murase, J.W. Osmun, J. Freeouf, M. Kastner and C. Wood, Bull. APS 17, (3) 345 (1972).
2. G.J. Lapeyre, A.D. Baer, P.L. Gobby, and C.F. Badgley, to be published.
3. C. Wood, B. Van Pelt, and E. Hyland, Rev. Sci. Instr., 43, 9, 1374 (1972).
4. R. Mueller and C. Wood, J. Noncryst. Solids 7, (1972) 301.
5. The question of direct transitions is complicated by the  $\vec{E}_0$  dependence of matrix elements for the transitions from these flat bands.
6. J.C. Shaffer, B. Van Pelt, C. Wood, J. Freeouf, K. Murase and J.W. Osmun, phys. stat. solidi (b), 54, 511 (1972).
7. C. Wood, J.C. Shaffer and W.G. Proctor, Phys. Rev. Letters 29, 8, 485 (1972).
8. R.A. Powell, W.E. Spicer, and J.C. McMenamin, Phys. Rev. B, 6, 8 (1972), 3050.
9. G.F. Derbenwick, Ph.D. Thesis, Stanford University (unpublished).  
G.J. Lapeyre, T. Huen and F. Wooten, Solid State Comm. 8, 1233 (1970).  
R.Y. Koyoma and L.R. Hughey in Phys. Rev. Lett. 29, 1518 (1972) report strong dependence of EDC's on the s and p polarization of the incident light for gold films. In our work, however, only s-polarized light was used.
10. M. Kastner, Phys. Rev. Lett. 28, 6, 355 (1972).
11. N.W. Tideswell, F.H. Kruse and J.C. McCullough, Acta Cryst. 10, 99 (1957).
12. L.D. Laude and B. Fitton, J. Noncryst. Solids 8-10, (1972), 971.
13. Z. Hurych, C. Wang, R. Mueller and C. Wood, J. Noncryst. Solids, 11, (1972) 153.
14. EDC's taken using the retarding field analyzer method show that the difference between the EDC's for amorphous and crystalline  $\text{Sb}_2\text{Se}_3$  can not be explained by collecting photoelectrons under a specific solid angle with the cylindrical double-pass analyzer, which would average out the structure in EDC's for amorphous  $\text{Sb}_2\text{Se}_3$ .

## Captions to Figures

- Fig. 1. EDC's for  $\vec{E}_0 || a$  (unnormalized). The insert shows the energy position of the structures  $P_1$  to  $P_4$  in the conduction band as determined with respect to the valence band maximum (VBM).
- Fig. 2. Structure plot for  $\vec{E}_0 || a$ . The final energy of structures (measured from the VBM) in the EDC's vs.  $h\nu$ .
- Fig. 3. Model densities of states for crystalline and amorphous  $Sb_2Se_3$ .
- Fig. 5. Comparison of EDC's (unnormalized) for  $\vec{E}_0 || a$ ,  $\vec{E}_0 || c$  and for amorphous  $Sb_2Se_3$ .





Reproduced from  
best available copy.



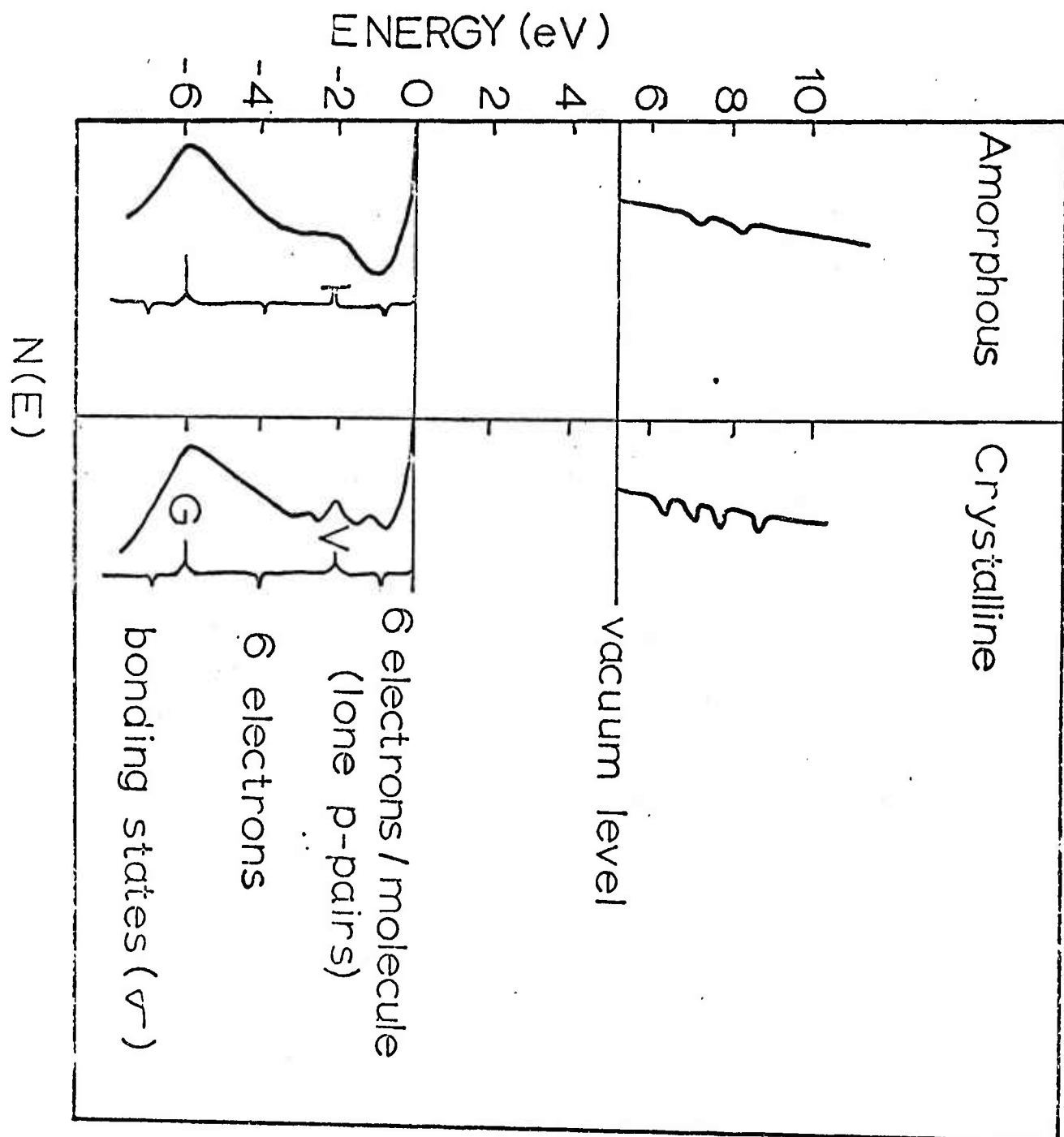


Fig. 3



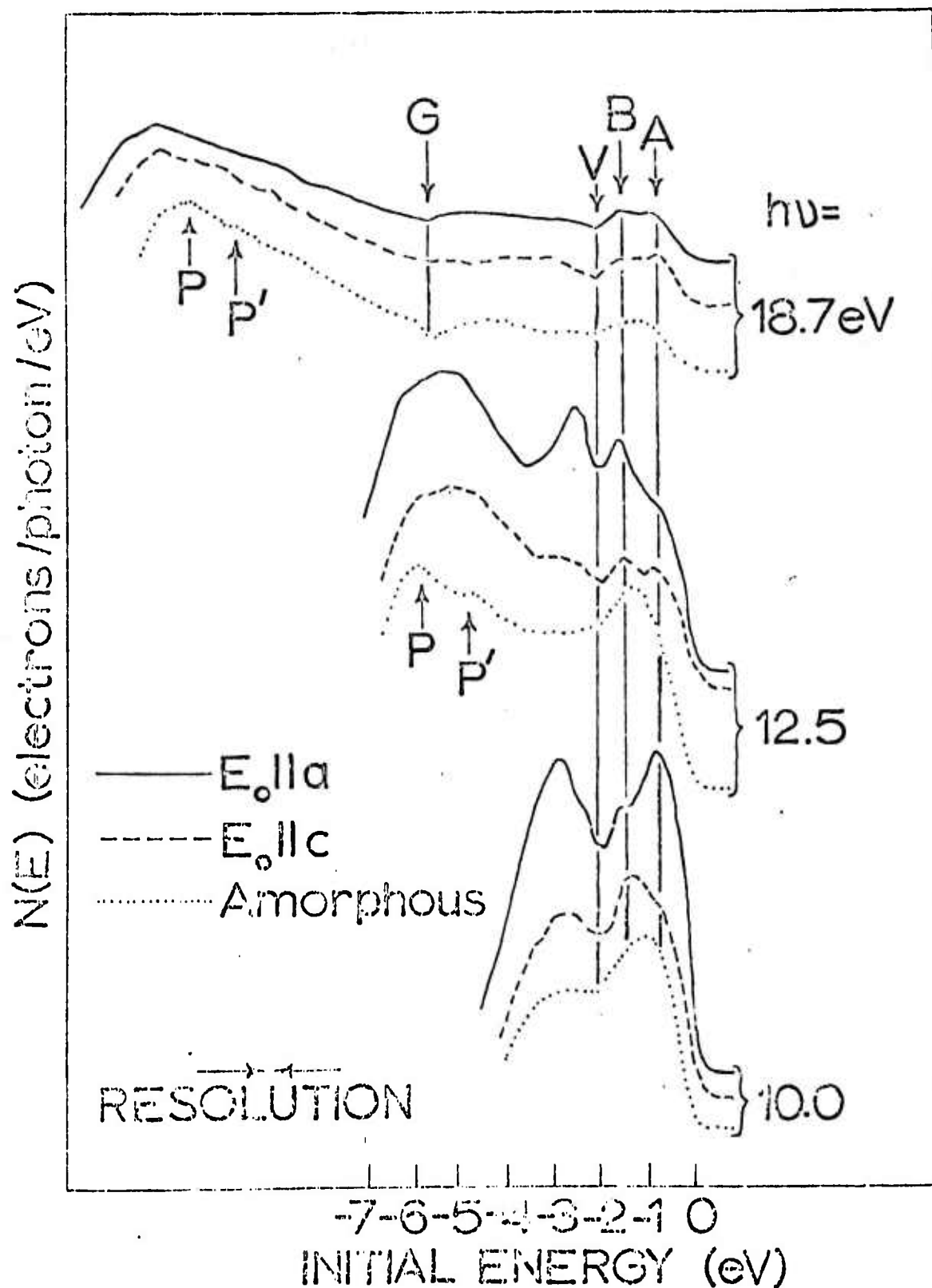


Fig. 4

Reproduced from  
best available copy.

Electronic Structure of Amorphous and Crystalline  $\text{Sb}_2\text{Se}_3$   
From Photoemission Studies Using the Synchrotron Radiation \*

Z. Hurych, C. Wood\*\* and J.C. Shaffer  
Department of Physics  
Northern Illinois University  
DeKalb, Illinois 60115

and

G.J. Lapeyre\*\*\* and A.D. Baer  
Department of Physics  
Montana State University  
Bozeman, Montana 59715

\* The Synchrotron Radiation Laboratory, University of Wisconsin is supported under Air Force Contract No. F44620-70-0029.

\*\* This work was supported by the Advanced Research Projects Agency of the Department of Defense and was monitored by the Army Research Office, Durham, under Contract No. Da-ARO-D-31-124-71-G132.

\*\*\* Work supported by the Air Force Office of Scientific Research, Office of Aerospace Research, USAF under Grant No. AFOSR-71-2061.

ABSTRACT

High resolution (0.2 eV) far UV photoemission studies ( $h\nu = 7$  eV to 35 eV) were performed to test and further develop the electronic structure of amorphous and crystalline  $\text{Sb}_2\text{Se}_3$ . The presence of the weakly bonding and bonding valence bands consistent with the chemical bonding model of this material is confirmed, and further details of the weakly bonding states are observed. The six electrons/molecule in the upper two electron volts of the weakly bonding band, attributed to the selenium lone p-pairs, are clearly separated from the rest of the weakly bonding band. These lone p-pairs are very strongly affected by the transition from the amorphous to crystalline phase.

Introduction

Experimental studies of the electronic structure of amorphous and crystalline  $\text{Sb}_2\text{Se}_3$  have been performed using ultraviolet photoemission spectroscopy (UPS) in order to test and further develop the conjectured electronic structure of this material which is based upon a chemical bonding model. Particular attention is given to the roles of the bonding and nonbonding states of the chalcogen atoms.  $\text{Sb}_2\text{Se}_3$  is interesting in that in both its amorphous and crystalline forms it displays properties characteristic of molecular solids. The structure consists of  $\text{Sb}_4\text{Se}_6$  units bonded rather weakly to one another (Tideswell et.al., 1957). Hence, the effect of the long range ordering on the electronic structure can be investigated, taking particular advantage of the strong anisotropy of the pseudo-two dimensional (layered)  $\text{Sb}_2\text{Se}_3$  crystals, so that some correlation can be made between the bonding and the electronic structure. As a supplementary study, the far UV reflectance spectra were measured for a large range of composition of the amorphous Sb-Se systems (Mueller et.al., 1973).

The electronic structure of solids can be investigated by several techniques, including UPS, XPS and optical spectroscopy (e.g., reflectance). The use of UPS with a synchrotron as a source of exciting radiation has the following advantages over other methods: (i) optical transitions can be followed over a large range (at least 30 eV) of photon energies, (ii) absolute energy positions of the maxima in the density of states (DOS) can be determined in both the valence band (VB) and the conduction band (CB) with a resolution of 0.2 eV or better. (iii) at higher values of photon energies (typically  $h\nu > 20$  eV) the experimental data can be related to the

DOS of the VB (Schevchik et.al., 1973) (Grobman and Eastman, 1972).

(iv) the natural polarization of the synchrotron radiation (with electrical vector  $\vec{E}_0$  in the median plane) allows the study of the crystal field effects on the matrix elements (Hurych et. al., 1973).

### Experimental

The photoemission spectrometer used here differs from conventional PE spectrometers in two major respects: first, the gas discharge light-source was replaced by the port of the UWPSL (University of Wisconsin Physical Sciences Laboratories) 240 MeV Synchrotron Storage Ring, and, second, the usual retarding field analyzer (Spicer and Berlund, 1964) was replaced by a double-pass electrostatic mirror (G.J. Lapeyre et.al., 1973) analyzer, in order to obtain high S/N ratio and high resolution at low light levels.

Amorphous  $\text{Sb}_2\text{Se}_3$  films of thickness 200 to 500 Å were evaporated in situ using an electron-beam gun by a method developed earlier. (Mueller and Wood, 1972) X-ray diffraction measurements following the photoemission experiment confirmed that the films were amorphous. The films were stoichiometric within 1% accuracy as determined by electron microprobe analysis. Orthorhombic single crystals of the  $\text{Sb}_2\text{Se}_3$  were grown in a zone refiner from 99.9999% purity elements and were cleaved in situ in a vacuum of  $\sim 10^{-10}$  torr. The natural cleavage plane (010) produced excellent mirror-like surfaces, which allowed the measurement of the photoemission energy distribution curves (EDC's) for polarizations of  $\vec{E}_0 \parallel a$  and  $\vec{E}_0 \parallel c$ .

### Results and Discussion

The photoemission energy distribution curves (EDC's) for amorphous  $\text{Sb}_2\text{Se}_3$  arranged with respect to the initial states are presented in fig. 1. While the detailed discussion of these data will be presented elsewhere

(Hurych et.al., 1973), the main features of the EDC's are presented here together with the structure plot where the energy of the final states is plotted vs the photon energy (fig. 2). A broad peak AB is visible at  $\sim 1.2$  eV below the VBM (fig. 1). An additional onset of the DOS is observable at  $\sim 6$  eV below the VBM (point G) in the EDC's for  $h\nu > 16$  eV, being superimposed on the smooth background of inelastically scattered electrons. All the above structure maintains a constant energy of initial states over a large range of  $h\nu$ , (figs. 1 and 2), and is therefore associated with the features of the valence band DOS. Also, two weak maxima P and P' in the conduction band DOS are observed in the low energy part of the EDC's. Fig. 3 shows that the basic features of the EDC's and the DOS of amorphous  $\text{Sb}_2\text{Se}_3$  can be compared to those of crystalline  $\text{Sb}_2\text{Se}_3$  in a rather straightforward manner. The broad peak AB in the amorphous  $\text{Sb}_2\text{Se}_3$  corresponds to two sharp peaks A and B in crystalline  $\text{Sb}_2\text{Se}_3$ . Also, the valley V, separating the upper 2 eV from the rest of the EDC's is more sharply visible in crystalline than amorphous  $\text{Sb}_2\text{Se}_3$ . The same is true for the conduction band, where four stronger structures  $P_1$  to  $P_4$  are observed in crystalline form compared to two rather weak structures P and P' in amorphous  $\text{Sb}_2\text{Se}_3$  (Hurych et.al., 1973).

At higher photon energies, the high energy region of the EDC's changes very little with  $h\nu$ , and similar to other works (Schevchick et.al., 1973), (Grobman and Eastman, 1972), portrays the basic features of the valence band DOS. The derived model DOS, using also some features of the XPS data (Wood et.al., 1972), are presented in fig. 4. There is a striking similarity between the DOS in fig. 4 and that for selenium (Schevchik et.al.). Both materials exhibit a second (bonding) valence band starting at  $\sim 6$  eV below the VBM as well as splitting of the upper (weakly bonding) band. While these two bands are observable in Se and  $\text{Sb}_2\text{Se}_3$  in the UPS as well as in far UV reflectance (Shaffer et.al., 1972), the detailed structure

in the weakly bonding band is observable in the UPS data only. Earlier we have shown (Ilurych et.al., 1973) that the upper two electron volts of the VB containing  $\sim 6$  electrons per  $\text{Sb}_2\text{Se}_3$  molecule, can be associated with the lone p-pairs of selenium. Fig. 3 shows that the lone pairs in crystalline  $\text{Sb}_2\text{Se}_3$  are characterized by two sharp peaks A and B, implying flat ( $\sim 0.4$  eV wide) E vs k bands. The strong polarization dependence of the intensity of these two peaks reflects the effect of the crystal field which determines the direction and energy levels of these states so that the total energy of the crystal is minimized. The resonance character of those lone pairs is lost in amorphous  $\text{Sb}_2\text{Se}_3$  since the Se states are determined by the random potential on local scale.

The comparison of our data with those of Se (Schevchick et.al., 1973) suggests that the lone pairs of chalcogen atoms play an important role in the formation of the upper VB of  $\overline{\text{V}}_2\overline{\text{VI}}_3$  compounds, both amorphous and crystalline, and that the basic features of the DOS are understandable in terms of chemical bonding.

In order to determine what is the minimum concentration of Se necessary to maintain a separation of the bonding and weakly bonding bands in the  $\text{Sb}_{1-x}\text{Se}_x$  systems, far UV reflectance studies of amorphous Sb-Se systems were performed (Mueller, et.al., 1973). Kramers-Kronig analysis of this data is presented in fig. 5 indicating that at Se concentration as low as 24% this separation disappears.

### Conclusion

The basic conjectures of the chemical bonding model of  $\text{Sb}_2\text{Se}_3$  are confirmed, and further information on the weakly bonding band is obtained. The six electrons/molecule in the upper band, attributed to the chalcogen lone p-pairs are clearly separated from the rest of this band, and are very strongly affected by the transition from amorphous to crystalline

$\text{Sb}_2\text{Se}_3$  as is consistent with the model of amorphous  $\text{Sb}_2\text{Se}_3$  as a random aggregate of  $\text{Sb}_4\text{Se}_6$  molecules.

Acknowledgement

We wish to thank D. Buczek and the staff of the University of Wisconsin Physical Science laboratory for their experimental assistance, R. Mueller for performing the x-ray diffraction, D. Davis and T. Knecht for drawing the figures, and B. Van Pelt for growing the  $\text{Sb}_2\text{Se}_3$  crystals.

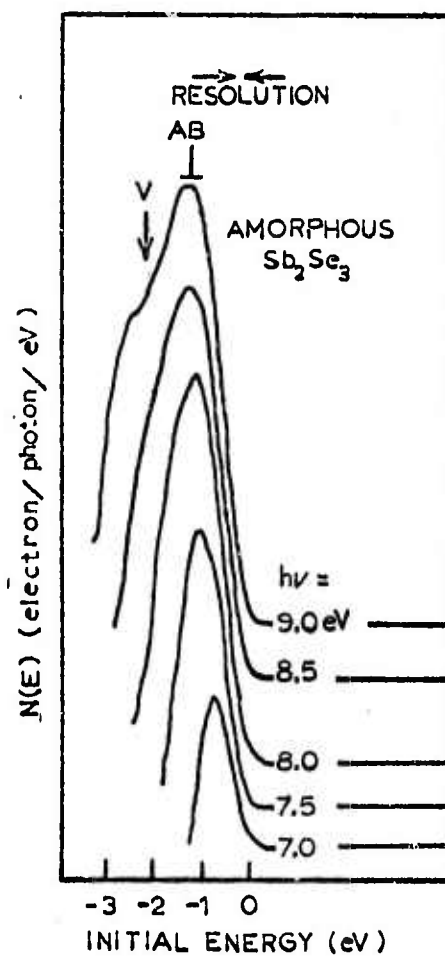


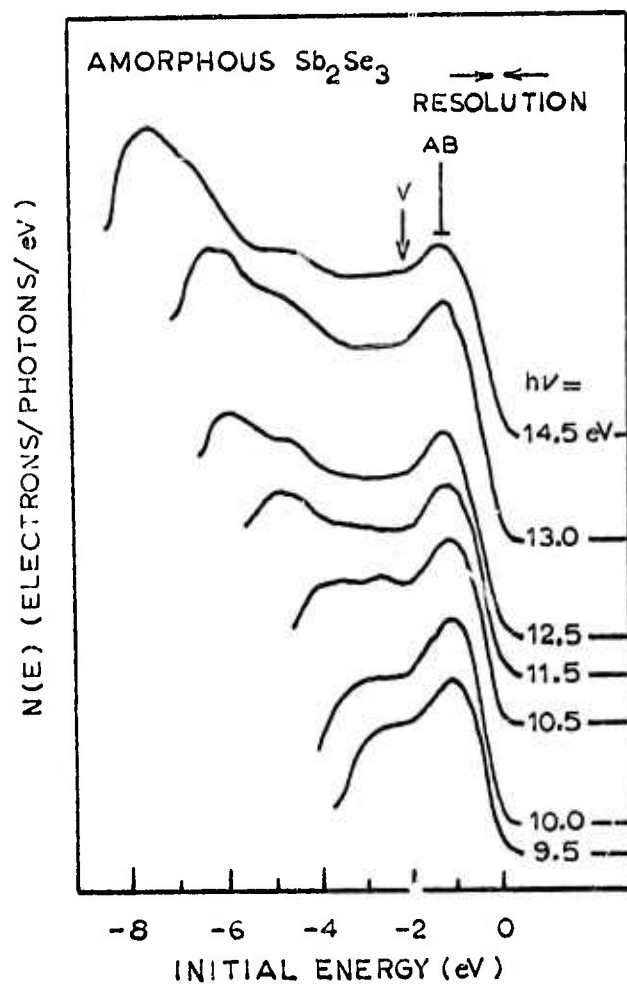
References

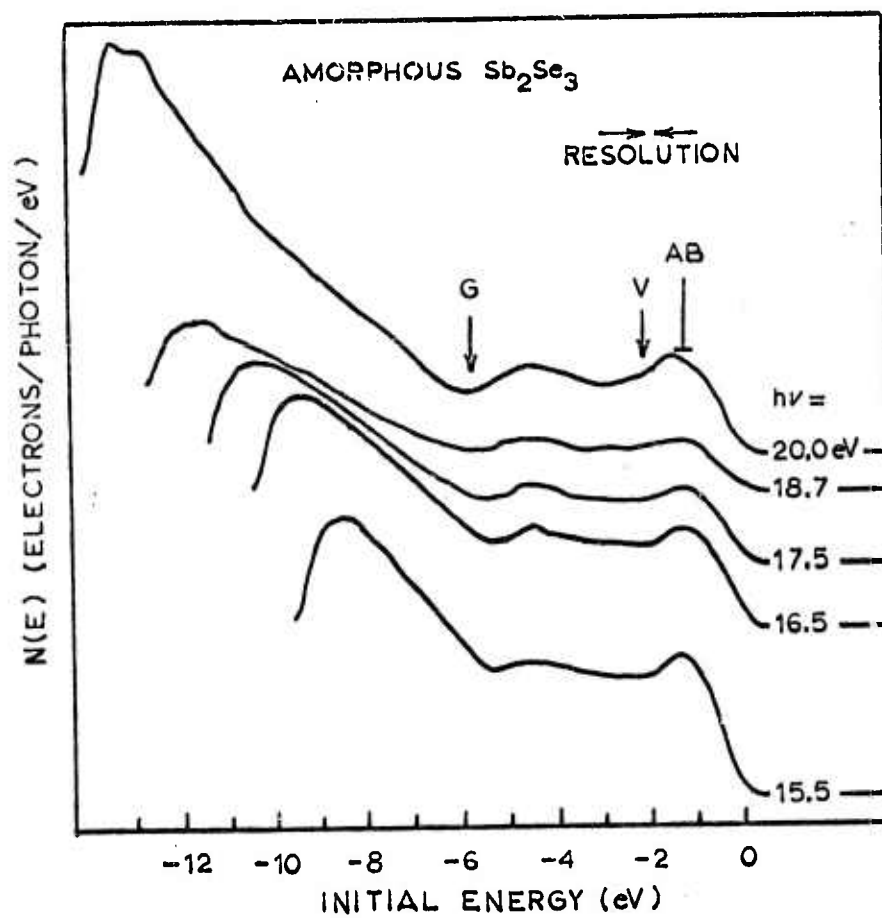
- W.D. Grobman and D.E. Eastman, Phys. Rev. Lett. 29, 1508 (1972).
- Z. Hurych, D. Buczek, C. Wood, G.J. Lapeyre and A.D. Baer, Solid State Communications; 1973, in print.
- G.J. Lapeyre, A.D. Baer, P.L. Gobby and C.I. Badgley, to be published, 1973.
- R. Mueller, J.C. Shaffer, C. Wood, Phys. Stat. Solidi (b), 59, 1973, to be published.
- R. Mueller and C. Wood, J. Noncrystalline Solids 7, 301 (1972).
- N.J. Shovchik, J. Tejeda, M. Cardona and D.W. Langer, Solid St. Communications 12, 1285 (1973).
- J.C. Shaffer, B. Van Pelt, C. Wood, J. Freeouf, K. Murase and J.V. Osmun, Phys. Stat Solidi (b), 54, 511 (1972).
- W.E. Spicer and C.N. Berglund, Rev. Sci. Instr. 35, 1665 (1964).
- N.W. Tideswell, F.H. Kruse and J.C. McCullough, Acta Cryst. 10, 99 (1957).
- C. Wood, J.C. Shaffer and W.G. Proctor, Phys. Rev. Lett. 29, 485 (1972).

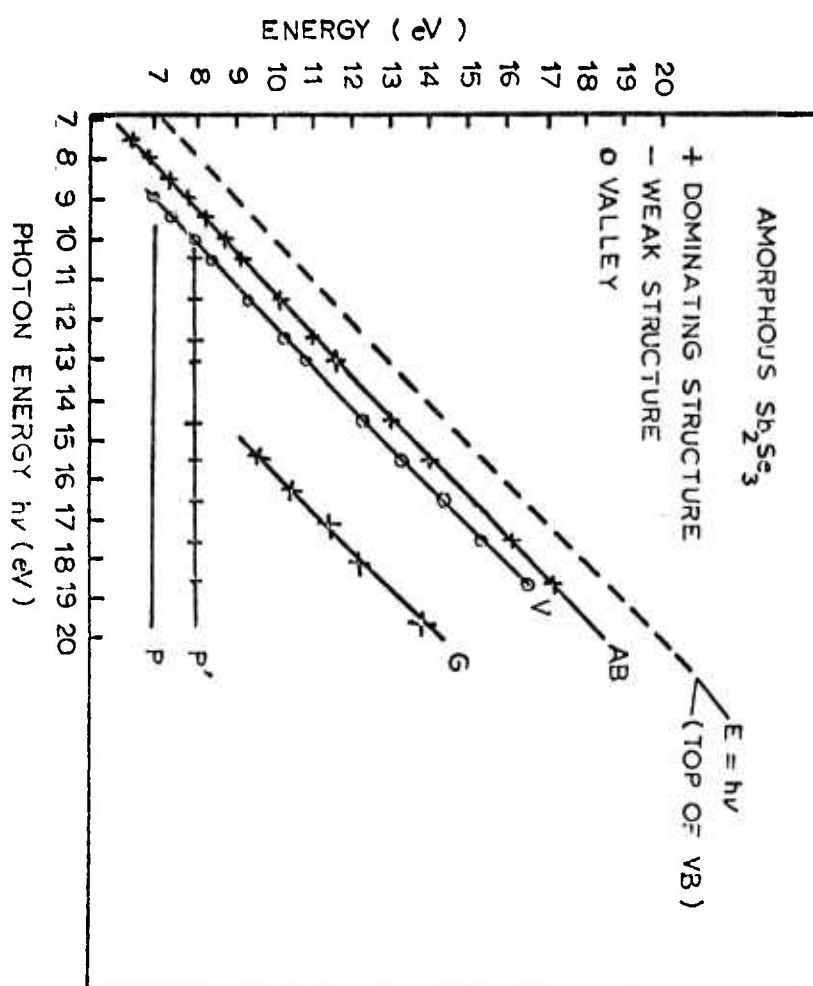
Captions to Figures

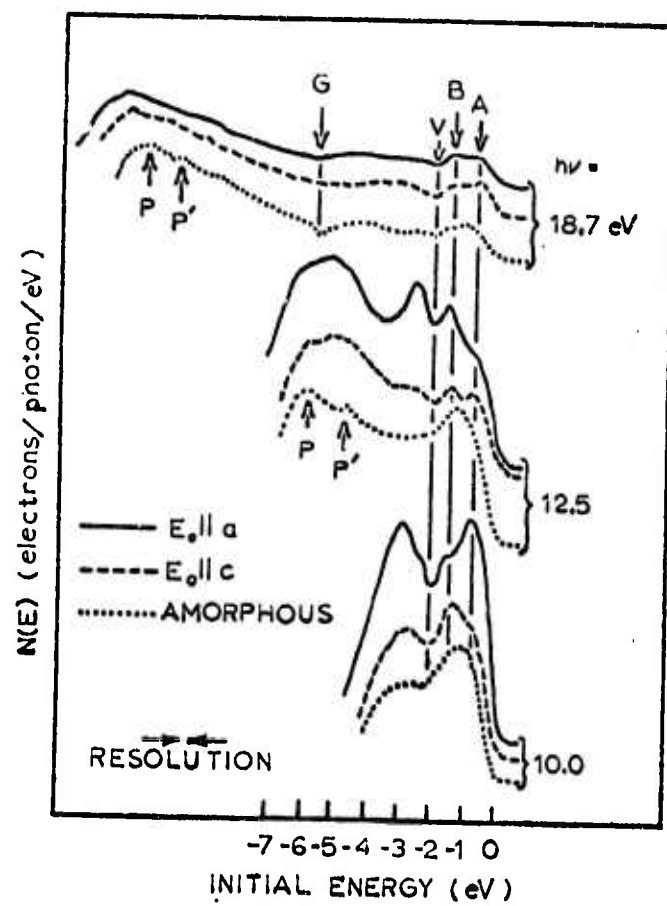
- Fig. 1. The energy distribution curves (EDC's) for amorphous  $\text{Sb}_2\text{Se}_3$ .
- Fig. 2. The structure plot for amorphous  $\text{Sb}_2\text{Se}_3$ .
- Fig. 3. Comparison of the EDC's of amorphous and crystalline  $\text{Sb}_2\text{Se}_3$ , showing also the strong polarization dependence of the EDC's in crystalline  $\text{Sb}_2\text{Se}_3$ .
- Fig. 4. Model densities of states for amorphous and crystalline  $\text{Sb}_2\text{Se}_3$ .
- Fig. 5. The imaginary part of the dielectric constant as a function of composition for the amorphous  $\text{Sb}_{1-x}\text{Se}_x$  systems.

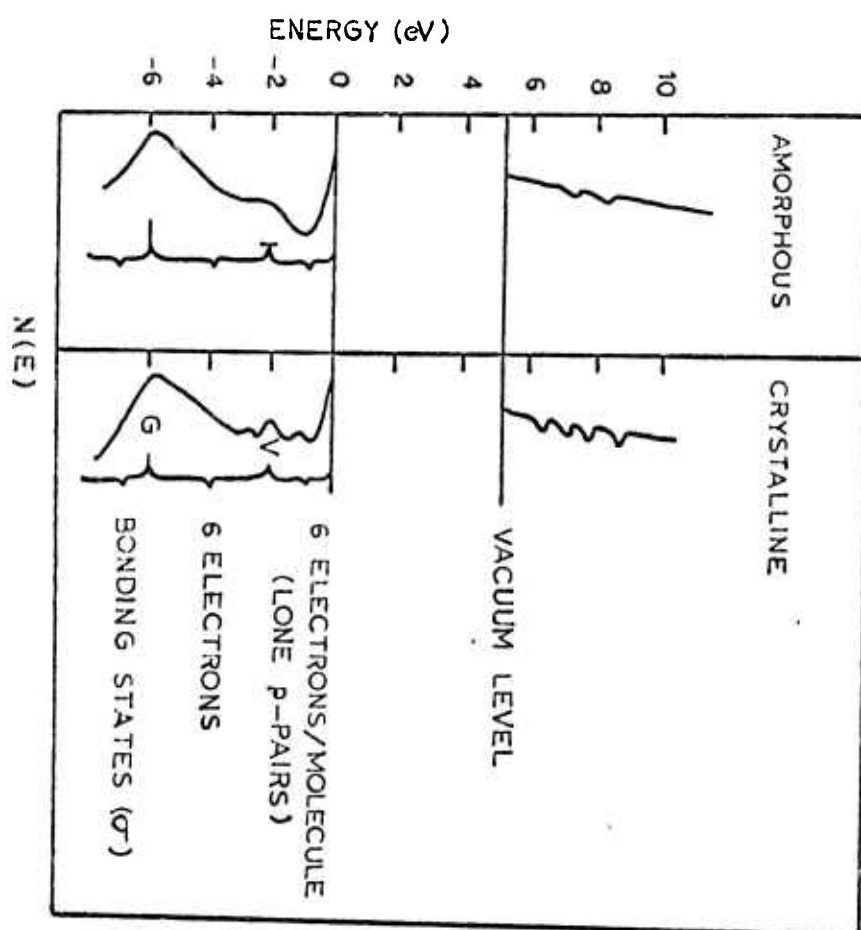




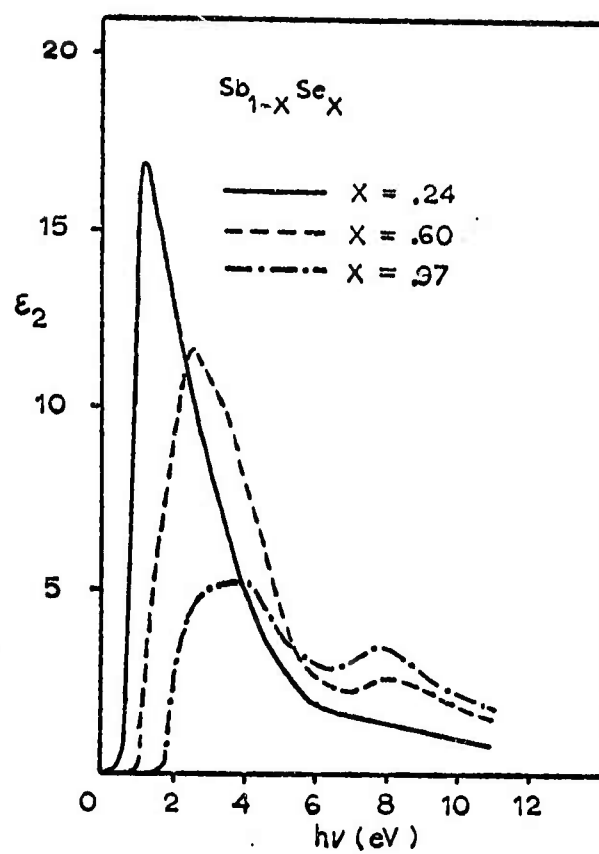












## THE PREPARATION OF AMORPHOUS THIN FILMS\*

R. MUELLER and C. WOOD

*Physics Department, Northern Illinois University, DeKalb, Illinois 60115, U.S.A.*

Received 22 February 1972

Amorphous thin films of antimony selenide of controlled composition have been prepared by vacuum evaporation. Various evaporation techniques are compared and their influence on optical properties is discussed. The optical energy gap is shown to increase with increasing selenium content.

## 1. Introduction

Certain semiconductors can be made amorphous only under drastic quenching conditions, such as vapor deposition onto a cold (compared to the melting point) substrate. Classic examples of such materials are Ge and Se amongst the elemental semiconductors and  $\text{As}_2\text{Te}_3$  and  $\text{Sb}_2\text{Se}_3$  amongst the compound semiconductors.

A serious problem, which has received little attention in the literature, arises with the latter group, i.e., one of controlling stoichiometry or of maintaining a constant predetermined composition of deposited material. In most cases the vapor above a solid or melt source is not a single species and varies with the temperature and environment of the source and vapor, e.g., whether the vapor is allowed to be in equilibrium with the source. Even if complete dissociation of the compound source occurs on evaporation it is rare that the elements have a sufficiently close vapor pressure at the chosen evaporation temperature to insure that the components impinge on the substrate in the desired concentration ratios. We have, of course, ignored the problem of sticking coefficients onto the specific substrate material. This, however, is generally of secondary consideration only, since once the first few monolayers of the compound cover the substrate, one is concerned only with the sticking coefficient onto the compound itself.

Compositional variations have often gone undetected in amorphous materials since X-ray diffraction measurements only show lack of structure.

\* This work was supported by the Advanced Research Projects Agency of the Department of Defense and was monitored by the Army Research Office, Durham, under Contract No. DA-ARO-D-31-124-71-G132.

Electron microprobe measurements are rarely employed and at best can only show variations on a gross scale (greater than microns) perpendicular to the substrate where the compositional gradient is likely to be greatest and, further, the analysis is not accurate to better than  $\sim 1$  at%. A saving grace is that amorphous materials are often not markedly compositional dependent over deviations of a few atomic %, but it is inexcusable that much data in the literature is reported on compound amorphous films with gross deviations from stoichiometry with the implication that the films are stoichiometric and, what is more, no details are given on preparation.

## 2. Preparation of antimony selenide

Let us consider the specific case of antimony selenide in the light of the above discussion. Mass spectrometric measurements by Sullivan et al.<sup>1)</sup> have shown that the equilibrium vapor species over  $\text{Sb}_2\text{Se}_3$  is predominantly  $\text{SbSe}$  and most other species present are Sb-rich compared to stoichiometry. However, this analysis applies to the condition of dynamic equilibrium between a melt and its vapor and does not correspond to the conditions applying in a conventional vacuum evaporation experiment where the vapor is immediately removed from above an open crucible. Rather, one is concerned with the dissociation vapor pressure of the element of highest vapor pressure, i.e., Se above a solid or melt of antimony selenide<sup>2)</sup> whose composition is varying as a function of time. Thus as the evaporation proceeds the source is gradually depleted of selenium and consequently, the composition of the deposit changes with time<sup>3)</sup> and with thickness.

Our initial approach to solving this problem was to force a given deposit composition by using a selenium-rich source. As an example, we found by trial and error that a source composition of  $\sim \text{SbSe}_{0.9}$  at a temperature of  $\sim 720^\circ\text{C}$  was required in order to produce a deposit of  $\text{Sb}_2\text{Se}_3$  as determined by microprobe analysis. This method necessitated using a large source of material compared with the amount of deposit required so that the composition of the source did not significantly alter with time.

A more satisfactory and convenient technique from a control viewpoint was to coevaporate Sb and Se from separate crucibles. The relative rates were monitored and controlled by two Sloan Omni II A rate-controllers. Collimating tubes were employed as shown in fig. 1 to avoid cross-contamination of the quartz crystal oscillators. By using electron-beam heating for Sb and resistance heating for Se it was possible to obtain a fairly good degree of control at a deposition rate of  $35\text{--}40 \text{ \AA}/\text{sec}$ . However, we were not able to reduce the fluctuations of the rates below  $\pm 2 \text{ \AA}/\text{sec}$ . The Se resistance-heater was in the form of a thin-walled (5 mil) stainless steel tube, pinched-off at

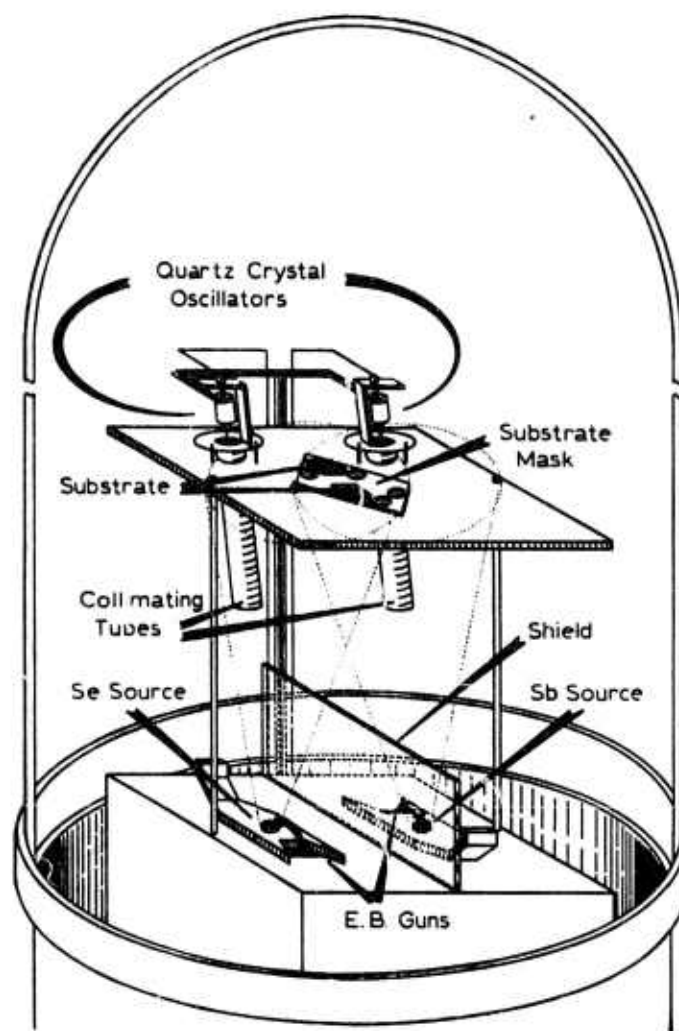


Fig. 1. Coevaporation system.

each end, thus totally enclosing the Se except for a small aperture with baffle to avoid a direct vapor path between substrate and heater. The electric current was passed through the tube.

Occasionally a vapor surge from the Se source would ruin an evaporation run. To avoid such surges, we later employed electron-beam heating for the Se source as well as for Sb. This did reduce large excursions in rates but fluctuations were at least as bad as with the resistance heater. Electron microprobe analysis showed the composition to approximately correspond to the set evaporation rates as plotted on  $x-t$  recorders by this coevaporation technique.

### 3. Optical properties

One of the purposes of this study was to examine the optical properties of amorphous antimony selenide films, deposited on fused quartz substrates, as a function of composition and the optical absorption coefficient ( $\alpha$ ) versus photon energy is shown in fig. 2. It is seen that the absorption edge obeys an approximate  $ah\nu \propto (h\nu - E_g)^2$  variation with energy as observed by Tauc et

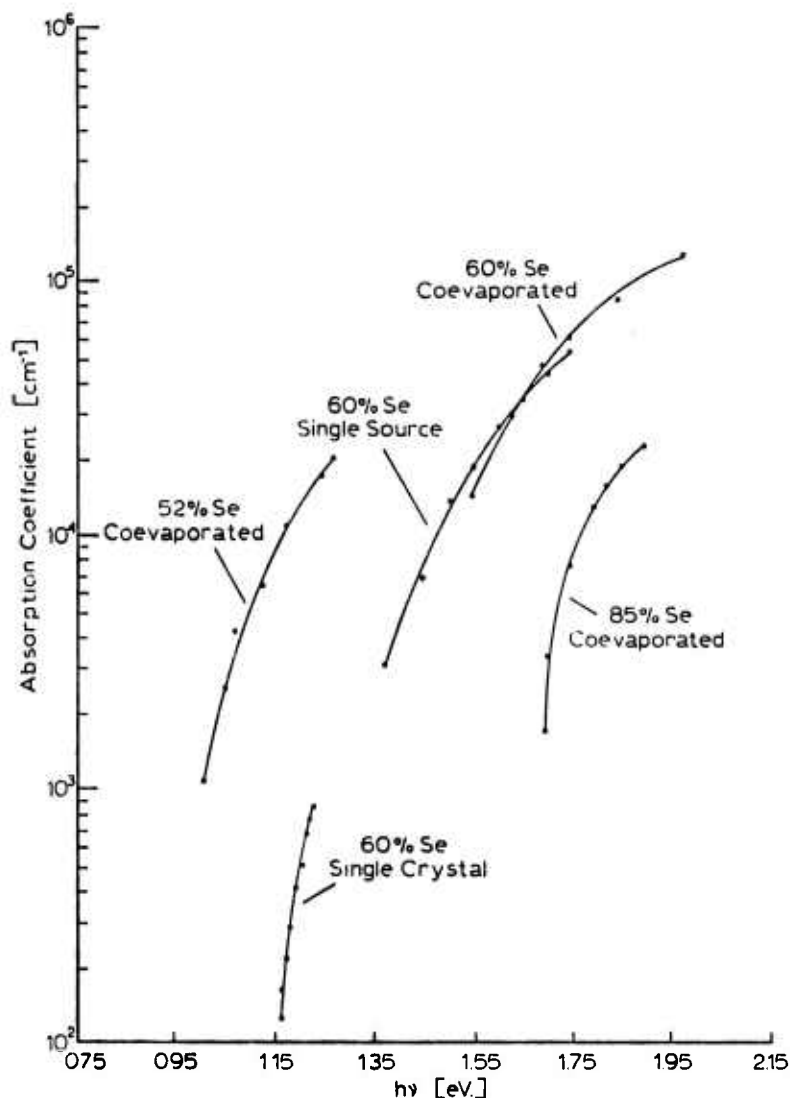


Fig. 2. Optical absorption coefficient versus photon energy.

a<sup>1,4</sup>) for amorphous Ge, suggesting the optical transitions conserve energy but not crystal momentum (fig. 3). The position of the edge decreases in energy as the Sb content increases; a variation observed previously for other elements in selenium<sup>5</sup>). Extrapolation of the curve for amorphous Sb<sub>2</sub>Se<sub>3</sub> to  $\alpha=0$  gives a value of  $E_g = 1.25$  eV which is slightly larger than the value of 1.15 eV obtained for the indirect edge in single crystal Sb<sub>2</sub>Se<sub>3</sub><sup>6</sup>).

The absorption coefficient ( $\alpha$ ) was determined from the observed transmittance ( $T_{obs}$ ) and reflectance ( $R_{obs}$ ) using the following equations<sup>7,8</sup>):

$$T_{obs} = \frac{(1 - R)^2 e^{-\alpha x}}{1 - R^2 e^{-2\alpha x}}, \quad (1)$$

and

$$R_{obs} = R(1 + Te^{-\alpha x}), \quad (2)$$

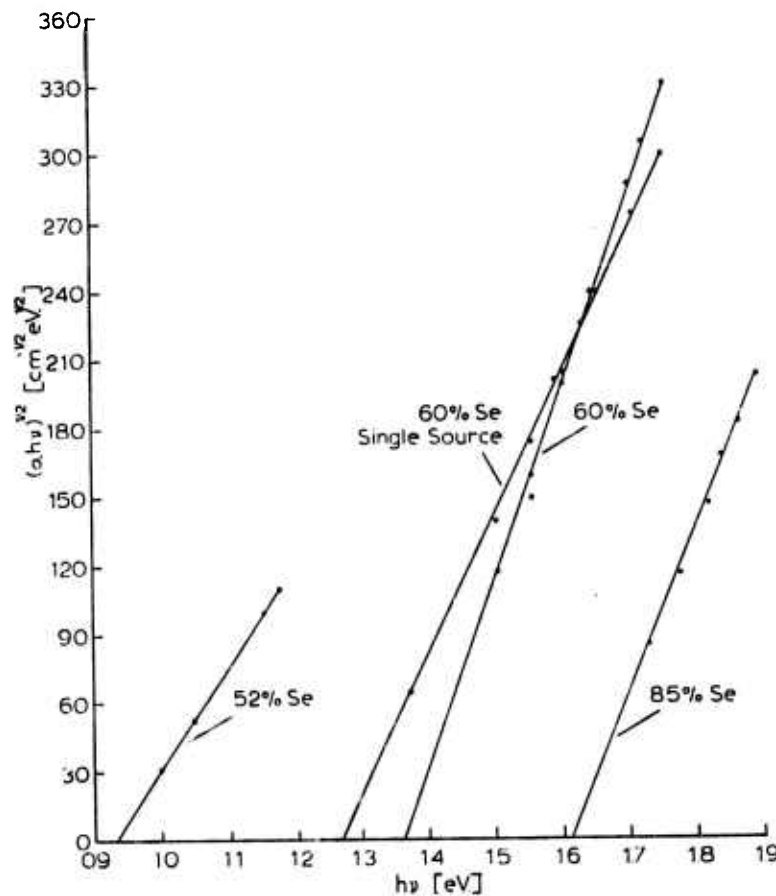


Fig. 3. Variation of absorption coefficient with photon energy.

where  $\chi$  is the film thickness. These equations could be used only in the region where the absorption was high and interference and substrate effects could be ignored. Attempts to use exact equations<sup>9)</sup>, which included interference and substrate effects, over the whole energy range failed because of

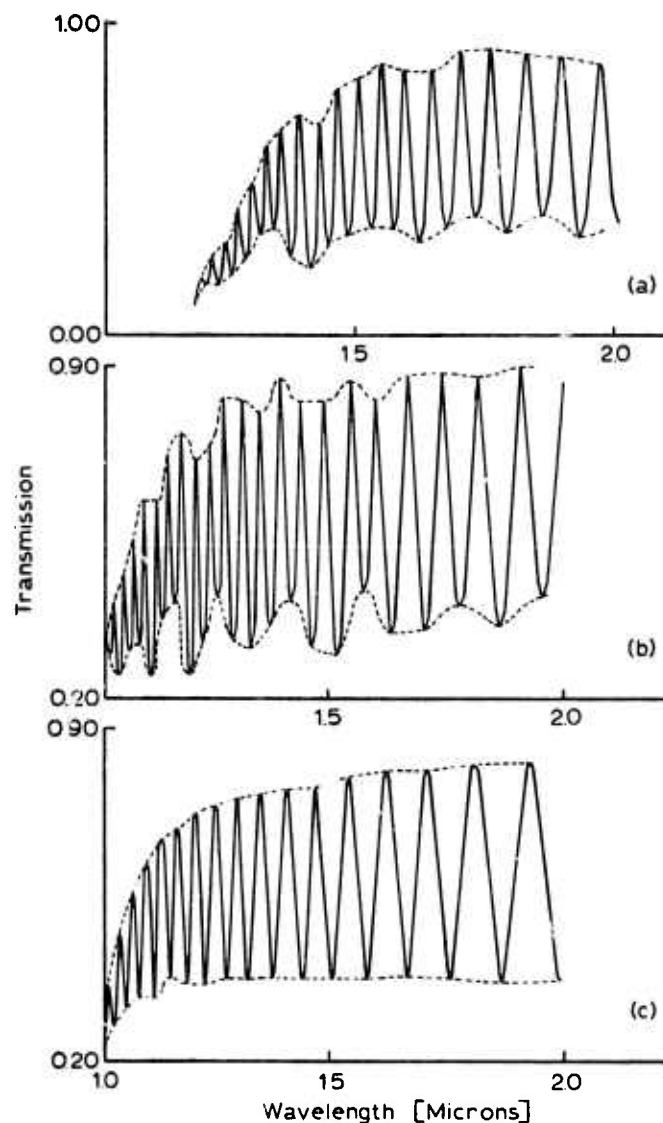


Fig. 4. Optical interference peaks in amorphous thin films. (a) Typical coevaporated film - thickness  $\sim 6.2\mu\text{m}$ . (b) Film with evaporation rates intentionally varied - thickness  $\sim 5.5\mu\text{m}$ . (c) Single source film - thickness  $\sim 4.5\mu\text{m}$ .

a slight modulation imposed on the height of the interference fringes observed beyond the absorption edge (see fig. 4). By deliberately increasing the rate fluctuations (see fig. 4) this modulation was traced to be due to the slight fluctuations in the relative evaporation rates of Sb and Se.

Accordingly, it was decided to revert to the single source evaporation process and to attempt stoichiometry control by the following means. Evaporation from melt-quenched ingot of  $\text{Sb}_2\text{Se}_3$  was carried out by electron-beam gun heating from a water-cooled hearth at sufficiently slow rates such that evaporation proceeded only from the surface, the rest of the ingot remaining solid. Initially, the higher vapor pressure element (Se) is preferentially evaporated from the surface. The process then becomes rate limited by the evaporation rate of Sb from the Sb-enriched surface and the rate of diffusion of Se to the surface. A dynamic equilibrium is thus established such that the rate at which Se is removed is controlled by the rate of evaporation of Sb; forcing the relative evaporation rates to be equal to the elemental ratio in the solid.

By micro-probe examination of the composition of a sequence of films prepared from a single source in this manner, it was established that the first few films were selenium-rich but, towards the middle of the run, equilibrium was established with the films being close to stoichiometry. At the latter stages, when the electron beam had penetrated through the source, the films reverted to non-stoichiometry again. The optical reflectance and transmittance of a typical film prepared in this fashion; fig. 4 shows complete regularity of height of the interference fringes. The optical absorption edge obtained by analysis of the data (fig. 3) shows reasonable coincidence with those obtained on coevaporated films of similar composition.

#### 4. Conclusions

It is concluded that conventional evaporation is unsatisfactory as a method of producing amorphous films of controlled composition; that with the current state-of-the-art of rate control, coevaporation is suitable only for exploratory work on composition; and surface evaporation, although more laborious for a phase-diagram type study, does yield homogeneous films of desired composition at equilibrium. Furthermore, the optical absorption edge of amorphous antimony selenides has been shown to strongly depend on composition and, hence, on the method of preparation. The optical energy gap of amorphous  $\text{Sb}_2\text{Se}_3$  closely corresponds to the indirect gap in the single crystal.



## References

- 1) C. Sullivan, J. E. Prusaczyk and K. D. Carlson, *J. Chem. Phys.* **53** (1970) 1289.
- 2) N. Kh. Abrlikosov, V. F. Bankina, L. V. Poretskaya, L. E. Shelimova and E. V. Skudnova, *Semiconducting II-VI, IV-VI and V-VI Compounds* (Plenum Press, New York, 1969) p. 194.
- 3) A. Efstatiou, D. M. Hoffman and E. R. Levin, *J. Vacuum Sci. Technol.* **6** (1969) 383.
- 4) J. Tauc, R. Grigorovici and A. Vancu, *Phys. Status Solidi* **15** (1966) 627.
- 5) J. C. Schottmiller, D. L. Bowman and C. Wood, *J. Appl. Phys.* **39** (1968) 1663.
- 6) B. Van Pelt and C. Wood, to be published.
- 7) J. A. Stratton, *Electromagnetic Theory* (McGraw-Hill, New York, 1941).
- 8) J. Tauc, in: *Progress in Semiconductors*, Vol. 9 Eds. Gibson and Burgess, (Heywood, 1965).
- 9) L. R. Gilbert, J. C. Shaffer and F. M. Mueller, to be published.

phys. stat. sol. (a) 16, K161 (1973)

Subject classification: 16; 22.6

Physics Department, Northern Illinois University, DeKalb

Photoconductivity in Crystalline and Amorphous  $\text{Sb}_2\text{O}_3$ <sup>1)</sup>

By

B. WOLFFING and Z. HURYCH

Photoconductivity measurements were performed on crystals of cubic and orthorhombic antimony oxide ( $\text{Sb}_2\text{O}_3$ ). Crystals were prepared using the vapor transport method from 6-9's purity elements as described in (1). Orthorhombic needles with growth axis in the c-direction were formed in a fused-quartz tube in the region just above 570 °C. Triangular faceted cubic crystals were formed in the region just below 570 °C. In addition, material in the form of an amorphous film was deposited on the walls of the tube. Silver paste was used to provide electrical contacts. The contacts were carefully shielded from illumination to avoid any photovoltaic effects. The samples were exposed to monochromatic light from a high intensity Baush-Lomb monochromator with a xenon source, chopped mechanically at a frequency of 37 Hz. The ac photoconductivity was measured with a Keithley 82 series lock-in amplifier.

Due to the small sample size, a quartz light pipe was used to direct the light beam to the sample. To obtain a normalized photoresponse, the monochromator light intensity was monitored in the uv region using a sodium salicylate coated EMI photomultiplier. Sodium salicylate is known to possess constant fluorescent quantum efficiency for  $\lambda < 3400 \text{ \AA}$  (2, 3). Thus the monochromator output flux could be measured with great accuracy in the region of interest. For the orthorhombic crystals a sheet polarizer was used to polarize the light parallel to the c and b axes.

For both polarization directions of orthorhombic  $\text{Sb}_2\text{O}_3$  the photoconductivity onset occurs at about 3.17 eV. Using the Moss' criterion (4) for the half-maximum photoresponse, we obtain an activation energy of 3.25 eV for  $\vec{E} \parallel \vec{b}$ , and 3.29 eV for  $\vec{E} \parallel \vec{c}$ . These values are in excellent agreement with the indirect energy gap

1) This work was supported by the Advanced Research Projects Agency of the Department of Defense and was monitored by the Army Research Office under Contract No. DA-ARO-D-31-124-72-G115.

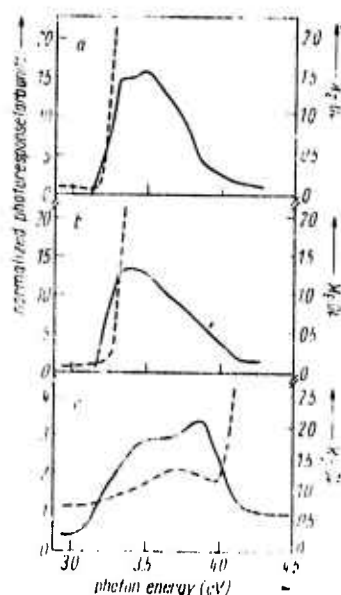


Fig. 1. Normalized photoresponse (solid line), compared with the optical absorption index (dashed line), from (1); — relative photoresponse, --- absorption index.

a) Orthorhombic  $\text{Sb}_2\text{O}_3$ ,  $\vec{E} \parallel \vec{b}$ ,

b) orthorhombic  $\text{Sb}_2\text{O}_3$ ,  $\vec{E} \parallel \vec{c}$ ,

c) cubic  $\text{Sb}_2\text{O}_3$

values of 3.25 and 3.30 eV, respectively (1).

In the case of cubic  $\text{Sb}_2\text{O}_3$  the photoconductivity onset occurs at about 3.10 eV. Fig. 1 shows an extrinsic photoresponse peak coinciding with the small peak in the optical absorption coefficient data, occurring at energies below the bandgap. Such absorption can be due to crystal impurities or to crystal lattice defects (the latter

seems to be more probable since this absorption does not show up in the orthorhombic  $\text{Sb}_2\text{O}_3$  grown from the same melt). Therefore, no attempt was made to use the Moss criterion since it is only applicable to inter-band transitions. Since the extrinsic optical absorption results in a photoconductive process we conclude that this process results in creation of free carriers rather than of excitons, unless the latter immediately dissociate. In the short wavelength region (Fig. 1) the photoresponse drops off sharply while the absorption coefficient is rising steadily, indicative of the onset of inter-band transitions. This sharp drop in photoresponse we attribute to a strong surface recombination in the higher photon energy region where the optical absorption depth is decreasing.

All attempts to measure the photoconductivity of amorphous  $\text{Sb}_2\text{O}_3$  were unsuccessful. These results were not unexpected, however, since the photosensitivity of the amorphous phase could be several orders of magnitude less than that of the crystalline phase (5). In this regard it should also be noted that even in the cubic crystal we were unable to measure the photoresponse far enough in the intrinsic absorption region, due primarily to strong surface recombination.

We wish to thank B. Van Pelt for supplying the crystals and amorphous films.

References

- (1) C. WOOD, B. VAN PELT, and A. DWIGHT, phys. stat. sol. (b) 54, 701 (1972).
- (2) F.S. JOHNSON, K. WATANABE, and R. TOUSEY, J. Opt. Soc. Amer. 41, 702 (1951).
- (3) J. HAMMANN, Z. angew. Phys. 10, 187 (1958).
- (4) T.S. MOSS, Photoconductivity in the Elements, Academic Press, New York 1952.
- (5) Z. HURYCH, R. MUELLER, C.C. WANG, and C. WOOD, J. non-cryst. Solids 11, 153 (1972).

(Received February 16, 1973)

## The Optical Properties of Amorphous and Crystalline $\text{Sb}_2\text{O}_3$ <sup>1)</sup>

By

C. WOON, B. VAN PELT, and A. DWIGHT

The optical properties of synthetic crystals of orthorhombic and cubic  $\text{Sb}_2\text{O}_3$  are compared with those of amorphous  $\text{Sb}_2\text{O}_3$ . The energy gaps in the crystals were found to correspond to indirect transitions.

Les propriétés optiques des cristaux synthétiques orthorhombique et cubique de  $\text{Sb}_2\text{O}_3$  ont été comparées avec celles de l'état amorphe de  $\text{Sb}_2\text{O}_3$ . Les séparations des bandes d'énergie pour les cristaux sont occasionnées par des transitions indirectes.

### 1. Introduction

As part of a study of the homologous series of compounds of Sb with Group VI elements we have investigated the optical properties of antimony oxide  $\text{Sb}_2\text{O}_3$  in the amorphous and crystalline forms.  $\text{Sb}_2\text{O}_3$  has two crystalline modifications: orthorhombic  $\text{Pccn}$ ,  $D_{2h}^{10}$  and cubic  $\text{Fd}\bar{3}m$ ,  $O_h^h$ . The homologous compounds  $\text{Sb}_2\text{Se}_3$  and  $\text{Sb}_2\text{S}_3$  occur only in the orthorhombic form  $\text{Pbnm}$ ,  $D_{2h}^{10}$ . Both forms of  $\text{Sb}_2\text{O}_3$  exist as natural minerals, the former as a valentinite and the latter as senarmontite. We report optical studies on synthetic crystals.

### 2. Materials Preparation

The crystals were prepared by enclosing a charge of  $\text{Sb}_2\text{O}_3$  powder in a sealed evacuated quartz tube 40 cm long and placing the tube in a temperature gradient such that the end containing the powder was at 680 °C and the other end at room temperature. Small orthorhombic needles having dimensions of a few millimetres length and fractions of 1 mm in cross-section with the growth axis in the c-direction were produced in the region of the tube above 570 °C [1]. Triangular-faceted cubic crystals of dimension several millimetres on a side were formed in the regions just below 570 °C. In addition, material deposited on the walls of the tube (or on fused quartz substrates) as an amorphous film was also investigated optically. Larger, but less perfect, orthorhombic crystals were grown by an open-tube method, using argon as a carrier gas and maintaining the  $\text{Sb}_2\text{O}_3$  powder at 675 °C and the tube at  $\geq 580$  °C.

### 3. Crystal Structure

The structure and single crystallinity of each phase was determined by X-ray diffraction. Cubic  $\text{Sb}_2\text{O}_3$  contains 16 ( $\text{Sb}_2\text{O}_3$ ) molecules per unit cell. The atomic positional parameters given by Bozorth [2] for the cubic form of  $\text{Sb}_2\text{O}_3$  are

<sup>1)</sup> This work was supported by the Advanced Research Projects Agency of the Department of Defense and was monitored by the Army Research Office, Durham, under Contract No. DA-ARO-D-31-124-71-G132.

incorrect and refined values  $x_{\text{Sb}} = 0.885$  and  $x_{\text{O}} = 0.190$  given by Almin and Westgren [3], were used in the present work. From a Debye-Scherrer powder pattern, the unit cell constant was found to be 11.152 Å, and the nearest neighbor Sb-O and O-O interatomic distances were calculated to be 1.997 and 2.94 Å, respectively, which are in good agreement with the earlier data [3], (Table 1).

Table 1  
Interatomic distances in orthorhombic  
and cubic  $\text{Sb}_2\text{O}_3$

structure	central atom	bonded atom	distance (Å) and multiplicity
cubic	Sb	O	1.997 (3)
		O	2.888 (3)
		Sb	3.627 (3)
	O	Sb	1.997 (2)
		Sb	2.888 (2)
		O	2.944 (4)
ortho-rhombic	Sb	O <sub>11</sub>	1.997 (1)
		O <sub>1</sub>	1.999 (1)
		O <sub>11</sub>	2.010 (1)
	O <sub>1</sub>	Sb	1.999 (2)
		O <sub>11</sub>	2.611 (2)
	O <sub>11</sub>	Sb	1.997 (1)
		Sb	2.010 (1)
		Sb	2.511 (1)

The orthorhombic form of  $\text{Sb}_2\text{O}_3$  consists of four  $(\text{Sb}_2\text{O}_3)$  molecules per unit cell comprising endless  $\text{Sb}_2\text{O}_3$  chains parallel to the  $c$ -axis. All Sb atoms are crystallographically equivalent but there are two different O sites in the lattice. Calculated intensities made with the atomic positional parameters reported by Buerger [4] agreed well enough with observed intensities on a Debye-Scherrer powder pattern that the literature values were assumed to be correct. The nearest-neighbor Sb-O and O-O interatomic distances were calculated to be 1.997 Å, i.e., the same as in the cubic form, and 2.61 Å, respectively. These values differ considerably from those of Wyckoff [5] although some doubt is expressed on the quoted values.

The volumes per formula weight ( $V/M$ ) were calculated to permit a comparison of packing efficiency giving values of 86.67 Å<sup>3</sup> (cubic) and 83.03 Å<sup>3</sup> (orthorhombic), indicating a more efficient packing in the high-temperature orthorhombic form.

#### 4. Optical Measurements

A Cary 14R spectrophotometer was used to make optical transmittance ( $T$ ) and, with a strong reflectance attachment, reflectance ( $R$ ) measurements on all three forms of  $\text{Sb}_2\text{O}_3$ , including  $E \parallel b$  and  $E \parallel c$  for the orthorhombic structure. Samples with naturally grown planar surfaces were chosen for the measurements, no further treatment was applied. The short-wavelength limit in the measured spectral range was set by the automated slit-width of the Cary 14R spectrophotometer reaching the fully-open position.

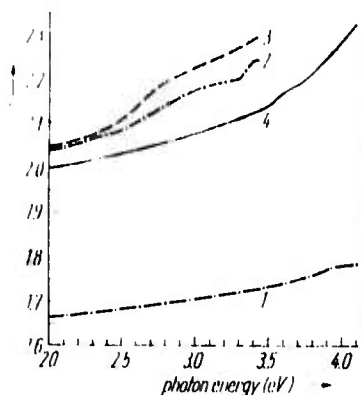


Fig. 1. Refractive indices of amorphous, orthorhombic, and cubic  $\text{Sb}_2\text{O}_3$ . (1) amorphous, thickness 60  $\mu\text{m}$ ; (2) orthorhombic,  $E||b$ , thickness 120  $\mu\text{m}$ ; (3) orthorhombic,  $E||c$ , thickness 120  $\mu\text{m}$ ; (4) cubic, thickness 830  $\mu\text{m}$ .

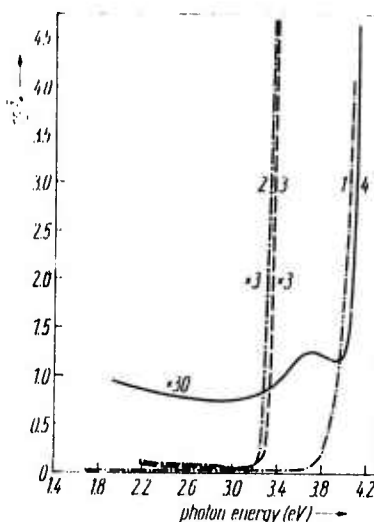


Fig. 2. Absorption indices of amorphous, orthorhombic, and cubic  $\text{Sb}_2\text{O}_3$ . (1) amorphous, thickness 60  $\mu\text{m}$ ; (2) orthorhombic,  $E||b$ , thickness 120  $\mu\text{m}$ ; (3) orthorhombic,  $E||c$ , thickness 120  $\mu\text{m}$ ; (4) cubic, thickness 830  $\mu\text{m}$ .

The absorption coefficient  $\alpha$  was calculated by computer programming the third-degree equation obtained by eliminating the front surface reflectivity,  $r$ , from the equations

$$T = \frac{(1 - r)^2 e^{-\alpha d}}{1 - r^2 e^{-2\alpha d}}, \quad (1)$$

$$R = r(1 + T e^{-\alpha d}), \quad (2)$$

i.e.,

$$(e^{-\alpha d})^3 + \left[ \left( \frac{1 - R}{T} \right)^2 - 1 + \frac{1}{T_2} \right] T(e^{-\alpha d})^2 + \left[ \left( \frac{1 - R}{T} \right)^2 - 2 \right] e^{-\alpha d} - \frac{1}{T} = 0. \quad (3)$$

These equations are valid only if the multiple reflected rays are incoherent; generally interference fringes were not observed in our samples. Sample thicknesses,  $d$ , were determined by edge viewing with a microscope fitted with a micrometer stage.

The refractive and absorption indices,  $n$  and  $k$ , were calculated from the equations

$$\alpha = \frac{4\pi k}{\lambda} \quad \text{and} \quad r = \frac{(n - 1)^2 + k^2}{(n + 1)^2 + k^2} \quad (4)$$

and are shown in Fig. 1 and 2. For the cubic sample a small rise in absorption can be seen just before the main absorption band which could be due to lattice imperfections or impurities.

The front surface reflectance is shown in Fig. 3. These measurements were made either with a sample having an irregular shaped rear surface or a correction was applied to eliminate the reflectance contribution from the rear surface. A peak at  $\approx 3.4$  eV can be observed in the reflectance spectrum of the orthorhombic sample for  $E||b$  which may be related to the onset of direct transitions.

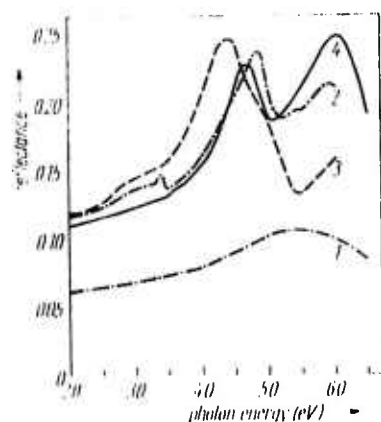


Fig. 3. Front surface reflectance spectra of amorphous, orthorhombic, and cubic  $\text{Sb}_2\text{O}_3$ . (1) amorphous; (2) orthorhombic,  $E \parallel b$ ; (3) orthorhombic,  $E \parallel c$ ; (4) cubic.

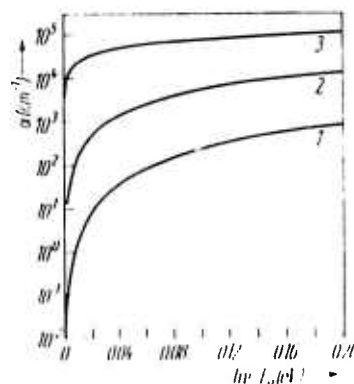


Fig. 4. Theoretical plots of (1) indirect allowed, (2) direct forbidden, and (3) direct allowed transitions.

It appeared possible to fit part of the absorption edge in all samples to any of the standard energy dependences on photon energy  $h\nu$ , namely,  $(\alpha n h\nu)^2$  for direct allowed,  $(\alpha n h\nu)^{2/3}$  for direct forbidden, and  $(\alpha h\nu)^{1/2}$  for indirect allowed transitions [6]. However, if both the magnitude of  $\alpha$  and its rate of change with  $h\nu$  is taken into account then it becomes possible to choose between them. The generalized curve in Fig. 4 greatly assists in making a choice. Here, for a photon energy range corresponding to the measured range at the absorption edge, we have plotted

$$\alpha n h\nu = 2.68 \times 10^5 (h\nu - \Delta E)^{1/2} \quad (5)$$

for direct allowed transitions,

$$\alpha n h\nu = 1.8 \times 10^5 (h\nu - \Delta E)^{3/2} \quad (6)$$

for direct forbidden transitions, and

$$\alpha h\nu = B (h\nu - \Delta E)^2 \quad (7)$$

for indirect allowed transitions, ignoring the small correction for phonon energy, and assuming a value of the proportionality constant  $B \approx 10^5$  in order to obtain

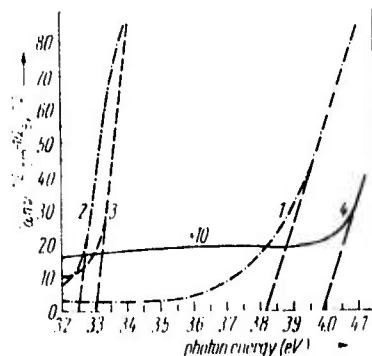


Fig. 5. Experimental plots of the absorption coefficient for all three forms of  $\text{Sb}_2\text{O}_3$  assuming indirect transitions. (1) amorphous, thickness 60  $\mu\text{m}$ ; (2) orthorhombic,  $E \parallel b$ , thickness 120  $\mu\text{m}$ ; (3) orthorhombic,  $E \parallel c$ , thickness 120  $\mu\text{m}$ ; (4) cubic, thickness 830  $\mu\text{m}$ .



values of  $\alpha$  comparable with the experimental values. This constant is about two orders of magnitude higher than that of Ge and Si [7] and one order of magnitude higher than for  $\text{Sb}_2\text{Se}_3$  [8, 9] and GaP [10], although values of  $B/\Delta E^2$  [6] are comparable.

A comparison of Fig. 4 with the experimental results shows from the magnitude of  $\alpha$  and  $d\alpha/d(h\nu)$  that an indirect transition is responsible for the low-energy part of the absorption edge in both single crystal forms of  $\text{Sb}_2\text{O}_3$  (Fig. 5). The following values of  $B$  were obtained from the slopes:  $B(E \parallel b) = 1.4 \times 10^5$ ,  $B(E \parallel c) = 2.1 \times 10^5$ , and  $B(\text{cubic}) = 9.9 \times 10^4 \text{ cm}^{-1} \text{ eV}^{-1}$ . From the intercepts the following indirect energy gap values were obtained: for the orthorhombic crystal,  $\approx 3.25 \text{ eV}$  for  $E \parallel b$ ,  $\approx 3.30 \text{ eV}$  for  $E \parallel c$  and for the cubic crystal  $\approx 4.0 \text{ eV}$ ; neglecting the small correction due to the phonon energies.

The absorption edge of the amorphous form was also found to obey an approximate  $(\alpha n h\nu)^{1/2}$  dependence on photon energy  $h\nu$  showing conservation of energy but not crystal momentum [11], and a value of  $\approx 3.8 \text{ eV}$  was obtained for the intercept of the amorphous phase.

### 5. Discussion

It is seen above that the optical properties in the vicinity of the energy gap of  $\text{Sb}_2\text{O}_3$  conform to other members of the homologous series. The absorption edges begin with indirect transitions, as for  $\text{Sb}_2\text{S}_3$  and  $\text{Sb}_2\text{Se}_3$ , the reflectance spectrum is characteristic of group V-VI compounds, and the magnitude of the reflectance is depressed and smoothed on the crystalline to amorphous transition, as is general for group V-VI compounds and many other materials. However, the large shift of the energy gap to higher energies on the orthorhombic crystalline to amorphous transformation is in strong contrast with  $\text{Sb}_2\text{Se}_3$  in which the indirect edge of the crystalline orthorhombic phase and the edge in the amorphous phase coincide [12].

There appears to be no rule as to which way the energy gap should shift on loss of long-range order. Energy gaps may shift to higher energies (Se, Te [13]), remain the same (Ge [14],  $\text{Sb}_2\text{Se}_3$  [12]), or shift to lower energy ( $\text{As}_2\text{Se}_3$ ,  $\text{As}_2\text{S}_3$  [15]) at the crystalline to amorphous transformation. Part of the problem lies in the uncertainty as to which region of the absorption edge in the two phases should be compared. Certainly one would expect the more weakly bonded (second, third, etc. nearest-neighbor) atoms and, therefore, the indirect transitions to be most strongly affected by structural randomization. For a more definitive grasp of the effects of randomization on the electronic structure the whole spectrum including direct transitions should be compared. We are currently attempting to grow thinner crystals of larger area to obtain more accurate optical data at higher photon energies.

These results, however, suggest that the short-range order in amorphous  $\text{Sb}_2\text{O}_3$  approximates more closely to that of the cubic than the orthorhombic form, a conclusion somewhat supported by the looser packing of the cubic form and by the Mössbauer studies of Long et al. [16] where the quadrupole splitting in the amorphous phase more closely corresponds to that of the cubic structure.

In order to relate the optical to the crystallographic structure in the two crystalline forms of  $\text{Sb}_2\text{O}_3$ , a calculation of bond number,  $n$ , was made for each of the bonds listed in Table I using the equation for bond length [17]:

$$D(n) = D(1) - 0.6 \log_{10} n. \quad (8)$$

where the single bond length  $D(1) = r_A + r_B - 0.08 |\chi_A - \chi_B| = 2.022 \text{ \AA}$  for Sb-O. The valence ( $\Sigma n$ ) indicates that the valencies of Sb and O are fully satisfied by the first nearest neighbors, i.e., the coordination number is 3 for Sb and 2 for O. Therefore, in contrast to other V-VI compounds where it has been suggested that the valence bands arise from resonating p-bonds [18], it appears that in  $\text{Sb}_2\text{O}_3$  the valence and conduction bands arise from bonding ( $\sigma$ ) (or lone-pair states [19]) and antibonding ( $\sigma^*$ ) states, respectively. Both optical absorption measurements and bond length determinations show that these bands are somewhat closer in energy in the orthorhombic than in the cubic structure.

#### Acknowledgement

We are indebted to L. R. Gilbert for assistance with the computer programming of the optical data.

#### References

- [1] W. B. PEARSON, Handbook of Lattice Spacings and Structures of Metals, Pergamon Press, 1958.
- [2] R. M. BOZORTH, J. Amer. Chem. Soc. **45**, 1621 (1923).
- [3] K. E. ALMIN and A. WESTEREN, Ark. Kemi, Miner. Geol. **15B**, 1 (1942).
- [4] M. J. BURGESS, Crystal Structure Analysis, Wiley, 1960.
- [5] R. W. G. WYCKOFF, Crystal Structures, Vol. 2, Interscience Publishers, 1960 (p. 6).
- [6] R. A. SMITH, Semiconductors, Cambridge 1961.
- [7] G. A. MACFARLANE and V. ROBERTS, Phys. Rev. **97**, 1714 (1955); **98**, 1865 (1955).
- [8] V. V. SMOLEY, S. D. SHUTOV, and S. N. SHERSTATSKII, Academy of Sciences, Moldavian SSR, 183 (1969).
- [9] B. VAN PRET and C. WOOD, to be published.
- [10] E. J. JOHNSON, Semiconductors and Semimetals, Vol. 3, Ed. R. K. WILLARDSON and A. C. BEER, Academic Press (Inc.), 1967.
- [11] J. TURE, R. GUGOROVICI, and A. VANCE, phys. stat. sol. **15**, 627 (1966).
- [12] C. WOOD, Z. HURYCH, and J. C. SHAFFER, Proc. 4th Internat. Conf. Amorphous and Liquid Semicond., J. non-crystall. Solids, **8**, 209 (1972).
- [13] J. STUKE, Translation of talk presented at the German Physical Society Meeting, Munich 1969.
- [14] T. M. DONOVAN, E. J. ASHLEY, and W. E. SPICER, Phys. Letters (Netherlands) **32A**, 85 (1970).
- [15] R. ZALLEN, R. E. DREWS, R. L. EMERALD, and M. L. SLADE, Phys. Rev. Letters **26**, 1564 (1971).
- [16] G. G. LONG, J. G. STEVENS, and L. H. BOWEN, Inorg. Nucl. Chem. Letters **5**, 799 (1969).
- [17] L. PAULING, The Nature of the Chemical Bond, Cornell University Press, New York 1960 (p. 221).
- [18] E. MOOSER and W. B. PEARSON, J. Phys. Chem. Solids **7**, 65 (1958).
- [19] M. KASTNER, Phys. Rev. Letters **28**, 355 (1972).

(Received August 29, 1972)

## PHOTOCONDUCTIVITY IN AMORPHOUS $\text{Sb}_{1-x}\text{Se}_x$ LAYERS\*

Z. HURYCH, R. MUELLER, C. C. WANG and C. WOOD

*Department of Physics, Northern Illinois University, DeKalb, Illinois 60115, U.S.A.*

Received 3 March 1972

The photoconductive spectral response of amorphous  $\text{Sb}_{1-x}\text{Se}_x$  films as a function of composition shows that an excess of Sb or Se causes a shift toward smaller or larger activation energies, respectively, when compared with stoichiometric Sb-Se films ( $x = 0.50$ ). This shift agrees with the shift of the optical absorption edge. An estimate of the density of states at the quasi-Fermi level for amorphous  $\text{Sb}_x\text{Se}_{1-x}$  gives values of at least  $10^4$  greater than the single crystal material.

### 1. Introduction

Amorphous  $\text{Sb}_2\text{Se}_3$  is one of the least investigated of the V-VI compound semiconductors. There exists little experimental data on photoconductivity<sup>1-3</sup>, and there the sample compositions were not well defined. Because of large difference in the vapor pressure of the two constituents, conventional evaporation from a single source of  $\text{Sb}_2\text{Se}_3$  does not yield stoichiometric  $\text{Sb}_2\text{Se}_3$  films<sup>4</sup>. Using a controlled co-evaporation procedure we have produced  $\text{Sb}_{1-x}\text{Se}_x$  films in a large range of compositions with  $x$ -values from 0.52 up to 0.86, so that the effect of the  $x$ -value on photoconductive spectral response and the photosensitivity  $\mu\tau$  could be investigated.

### 2. Preparation of samples

Samples deviating from stoichiometry were prepared by co-evaporation of Sb from an electron beam gun and Se from a resistor heater onto room temperature quartz substrates<sup>5</sup>. Two Sloan ONMI 11A quartz crystal monitors and controllers were used, and the evaporation rate of both Sb and Se separately monitored and recorded on  $x-y$  plotters. For the stoichio-

\* This research was supported by the Advanced Research Projects Agency of the Department of Defense and was monitored by the Army Research Office, Durham, under Contract No. DA-ARO-D-31-127-71-G132.

metric composition,  $\text{Sb}_2\text{Se}_3$ , samples were prepared both by coevaporation and by a modified single source evaporation using an electron beam gun<sup>4</sup>). Gold contacts were evaporated onto the substrates in a separate vacuum system prior to film deposition. Antimony contacts were evaporated onto substrates during the same vacuum cycle before the  $\text{Sb}_{1-x}\text{Se}_x$  films were deposited. The background pressure was  $\sim 10^{-8}$  torr. The composition of samples was determined by electron microprobe with an accuracy of  $\sim 1$  at %. The films were found to be amorphous both by X-ray and electron diffraction<sup>5</sup>).

### 3. Photoconductivity

Photoconductivity of  $\text{Sb}_{1-x}\text{Se}_x$  films with gold contacts was investigated for various compositions corresponding to the  $x$ -values in the range of 0.52 up to 0.86. The spectral dependence of photoconductivity was measured using Bausch and Lomb High Intensity Grating Monochromators. Light was mechanically chopped at various frequencies between 16 and 80 cps and the photosignal was synchronously detected using PAR HR-8 lock-in amplifier. The results are plotted as a change in conductivity per incident photon flux versus photon energy in fig. 1. This figure clearly shows the strong dependence of the photoconductive spectral response on sample composition. The set of curves in figs. 1a and 1b is divided by the curve for the stoichiometric  $\text{Sb}_2\text{Se}_3$  film ( $x = 0.60$ ) with a photoconductivity activation energy  $E_a = 1.4$  eV as determined by Moss' criterion<sup>6</sup>). The coevaporated and electron beam evaporated films gave essentially the same spectral response. It is seen that with increasing Sb content ( $x < 0.60$ ) the activation energy and the photoconductivity onset move toward lower energy, while the higher Se content ( $x > 0.60$ ) shifts the response toward higher energies with respect to  $\text{Sb}_2\text{Se}_3$  film. The effect of composition on the position of the photoconductivity onset was always found to correspond to the change in fundamental optical absorption edge position<sup>7</sup>). This dependence of  $E_a$  on composition is similar to that of melt-quenched amorphous  $\text{Sb}_{1-x}\text{Se}_x$ , published by Mostovski et al.<sup>7</sup>). The structure present on the onset edge of some films is due to the optical interference as shown by comparison with the absorbance (fig. 2). For comparison, fig. 1 also shows the photosensitivity of single crystalline  $\text{Sb}_2\text{Se}_3$  with  $E_a = 1.1$  eV.

The lux ampere characteristics were investigated and were found linear over 2 orders of magnitude. It was difficult to extend these measurements to lower light intensities due to the low photosensitivity of films.

Even though the contacts were carefully shielded from illumination during measurements to avoid any photovoltaic effects, some effect of contact material was observed on the spectral response (fig. 3) when Sb or Au con-

tact were used. However, we found this contact effect was much weaker than that reported in ref. 2.

The absolute photoconductivity was measured at  $h\nu = 1.65$  eV. The chopped light illuminated the sample through a light pipe of known diameter. From the absolute photoconductivity  $\Delta\sigma$ , the product  $(\mu\tau)$  was calculated using a relation

$$\Delta\sigma = \eta q (\mu\tau) A I_0 / t h\nu,$$

where  $A$  is the sample absorptance,  $t$  is the sample thickness,  $q$  is the elec-

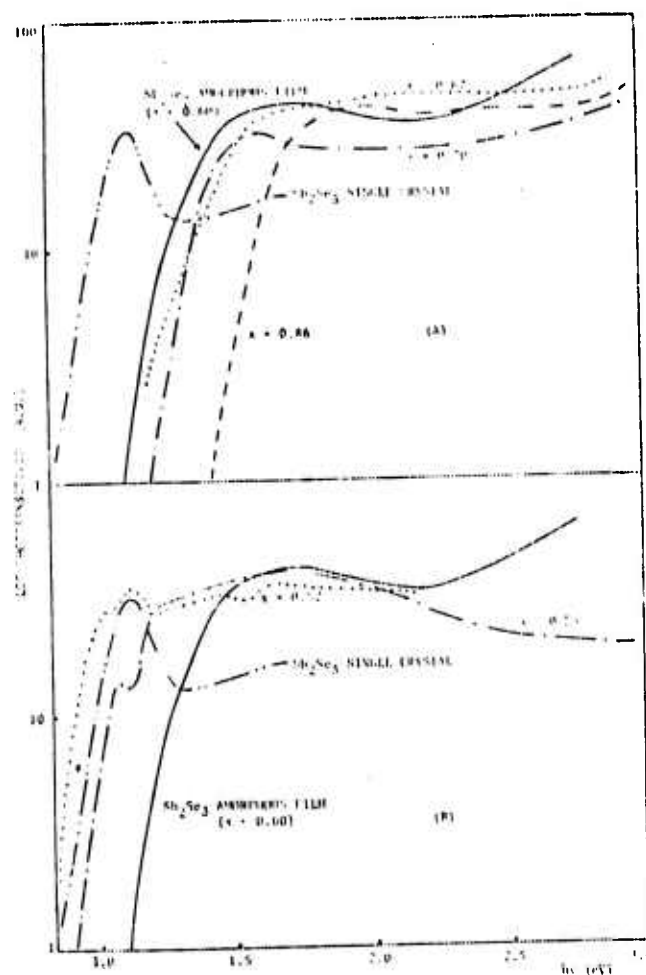


Fig. 1. Relative photosensitivity of  $\text{Sb}_{1-x}\text{Se}_x$  films. (a) Se rich films; (b) Sb rich films.

tronic charge and  $I_0$  is the light flux. The quantum efficiency  $\eta$  was assumed to be one. The light flux was determined using a calibrated thermopile.

The values of the  $\mu\tau$  (where  $\tau$  is the lifetime of excess carriers) were found to be in the range of  $6 \times 10^{-10}$  up to  $2 \times 10^{-9}$  cm<sup>2</sup>/V. The value of  $\mu\tau$  for single crystalline Sb<sub>2</sub>Se<sub>3</sub> was found to be  $3 \times 10^{-5}$  cm<sup>2</sup>/V.

A direct display of the decay of the photoconductive pulse was generally impossible because the photosensitivity of the films was very low and the signal was often below the noise level. The photoconductive response time was measured from the phase shift between the light pulse and the photoconductive response using a method described in ref. 8. The values of the

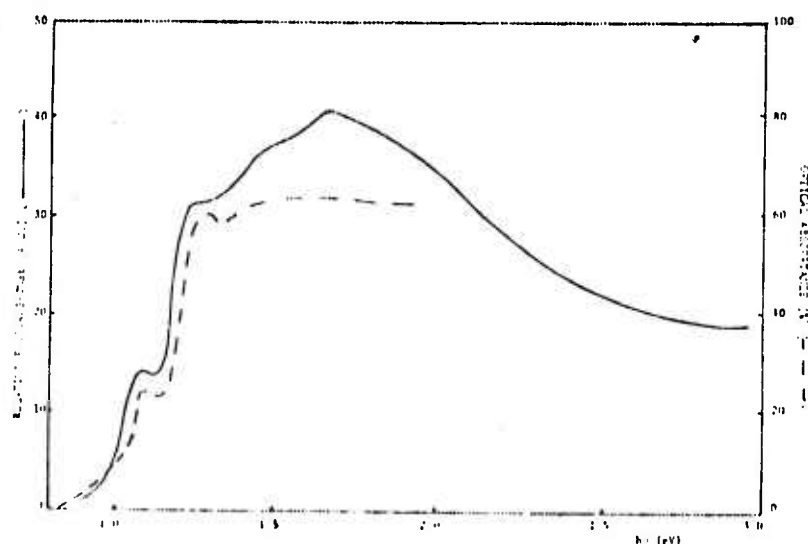


Fig. 2. Relative photoresponse and optical absorbance for Sb<sub>2</sub>Se<sub>3</sub> film with  $\lambda = 0.52 \mu$ .

response time were  $10^{-3}$  to  $10^{-2}$  sec for films compared to 400  $\mu$ sec for single crystal. It should be noted that this method measured the "effective" response time, i.e. those components of the pulse which contribute to the largest area of the pulse. This means that this method cannot resolve the very fast initial rise and fall of the pulse which is found, e.g., for amorphous As<sub>2</sub>Te<sub>3</sub><sup>(9)</sup> or GeTe<sup>(10)</sup> and which was associated with the recombination lifetime.

#### 4. Discussion

The photoconductivity spectral response shows a strong dependence on composition which can be used to explain the difference in spectral response

between our stoichiometric  $Sb_2Se_3$  films and those reported by Kolomiets et al.<sup>1,2</sup>). Their films were prepared by conventional evaporation from a source of  $Sb_2Se_3$  which we found produces nonstoichiometric films with composition depending on the temperature of the source and the stage of the evaporation cycle due to preferential evaporation of Se. The discrepancy between their results and ours can therefore be explained by an excess of Se in their samples.

Comparing the spectral response of amorphous with crystalline  $Sb_2Se_3$ , one finds no significant difference between the sharpness of the onset for these two different modifications. Even though a diffuse onset of photo-

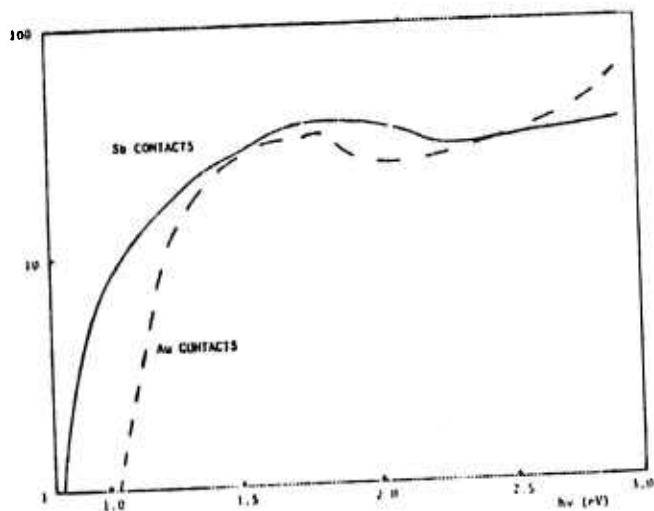


Fig. 3. Effect of Sb or Au contacts on the spectral photoconductive response of  $Sb_{1-x}Se_x$  films.

conductivity (or of optical absorption) is usually considered as a proof for the existence of localized states in the gap, the presence of a sharp onset does not preclude the existence of these states. The explanation is given by much lower values of matrix elements for electronic transitions between localized and extended states<sup>11,12</sup>). Similarly, sharp onsets of photoconductivity and optical absorption edge were found previously for amorphous  $Si^{13}$  and  $Ge^{14}$ ). All these measurements suggest that even though the process of photoconductivity includes both optical and transport properties, the information about the localized states from the photoconductive edge coincides with the optical densities rather than with the densities obtained from electrical or magnetic measurements. It is known<sup>14</sup>) that the effective

"optical" density of localized states in the gap can be a few orders of magnitude lower than the density obtained from transport measurements.

While from the absolute photoconductivity one can easily obtain the product  $\mu\tau$ , the separation of this product into its two constituents has to include some model for transport of carriers. For example, the model proposed by Weiser and Brodsky<sup>10</sup> for amorphous  $\text{As}_2\text{Te}_3$  assumes that excited carriers move along or just above the "mobility edge", and  $\tau$  was equated to the carrier lifetime having a value of  $\sim 10^{-8}$  sec thus giving mobility values of the order of 0.1 to 1  $\text{cm}^2/\text{V sec}$ , which is just on the boundary between a localized and delocalized conductivity mechanism. The opposite approach was taken by Kolomiets<sup>15</sup> who associates  $\tau$  with the response time of  $\sim 10^{-4}$  sec, controlled by trapping effects, and completely neglects the initial fast part of the photopulse. The corresponding values of  $\mu$  are thus in the  $10^{-4}$  to  $10^{-1}$   $\text{cm}^2/\text{V sec}$  region corresponding to localized mobility. The time  $10^{-4}$  sec then corresponds to the "lifetime" of a hopping carrier between traps.

If we assume a delocalized mobility value of the order 1  $\text{cm}^2/\text{V sec}$  in our films then, because the  $\mu\tau$  product has values of the order  $10^{-9}$  to  $10^{-10}$   $\text{cm}^2/\text{V}$ , the recombination lifetime has to be in the range  $10^{-9}$  to  $10^{-10}$  sec. The immediate consequence is that there must then exist recombination centers or deep traps of very large cross-section approximately in the middle of the pseudogap. The order of magnitude of the density of traps can be estimated from following kinetic conditions. The light intensity used corresponds to the generation rate  $g \sim 10^{19}/\text{cm}^3 \text{ sec}$  averaged over the absorption length. In the steady state condition the density of free carriers ( $n$ ) must be equal to  $g\tau$ , where  $\tau$  is the free carrier lifetime. Taking the average value of  $\mu\tau$  to be  $1 \times 10^{-9}$   $\text{cm}^2/\text{V}$ , the lifetime of non-localized carriers has a value  $\tau \sim 10^{-9}$  sec, yielding  $n \sim 10^{10}/\text{cm}^3$ . Now trapped carriers of density  $n_t$  result in a response time  $\tau_{\text{resp}}$  longer than  $\tau$  by the factor  $\tau_{\text{resp}}/\tau = (n_t + n)/n \sim n_t/n$ . In our case  $\tau_{\text{resp}}/\tau = 10^{-4}/10^{-9} \sim 10^5$ , yielding  $n_t \sim 10^{15}/\text{cm}^3$ . From the total number of trapped carriers  $n_t$  we can then estimate the total number of trapping states  $N_t$  between the mobility edges assuming that the trapped carriers are in thermal equilibrium with the conduction or valence bands. Even though the trapping states should be thought to be distributed continuously throughout the gap with the density  $N_t/\text{cm}^3 \text{ eV}$ , the major part of carriers are trapped at the levels within a slice  $kT$  of the quasi-Fermi level  $F_1^*$ . The condition of thermal equilibrium then yields<sup>16)</sup>

$$\frac{n_t}{n} = \frac{N_t^* kT}{N_c} \exp \frac{F_1^*}{kT},$$

with  $N_c \sim 10^{19}/\text{cm}^3$  being the effective density of states in the conduction



band. Because the above equation includes two unknowns ( $N_t^*$ ,  $E_t^*$ ) it is useful to consider  $E_t^*$  as a parameter and calculate the corresponding values of  $N_t^*$ . This is done in table 1, which clearly indicates that  $E_t^* \approx 0.3$  eV, since the density of states inside the gap cannot exceed the band densities. There must exist, also, a lower limit for  $E_t^*$  because the very low lifetime  $10^{-9}$  sec requires the existence of recombination centers of rather high concentration which would lie between the quasi-Fermi levels for electrons and holes (assuming equal recombination cross-sections for electrons and holes). Assuming that  $E_t^*$  is somewhere in the interval 0.3 eV to 0.5 eV from the non-localized states, we get rather high densities of states ( $10^{18}$  up to  $10^{21}/\text{cm}^3$ ) deep inside the pseudogap.

TABLE I  
Concentration of trapping states  $N_t^*$  at the quasi-Fermi level  $E_t^*$  as a function of distance of  $E_t^*$  from the band edge

$E_t^*$ (eV) from the band edge	$N_t^*$ ( $\text{eV cm}^{-3}$ ) <sup>-1</sup>
0.1	$8 \cdot 10^{14}$
0.2	$1.3 \cdot 10^{15}$
0.3	$2.5 \cdot 10^{15}$
0.4	$4 \cdot 10^{16}$
0.5	$8 \cdot 10^{17}$
0.6	$1.3 \cdot 10^{18}$
0.7	$8 \cdot 10^{18}$

Similar calculations were performed for single crystalline  $\text{Sb}_2\text{Se}_3$  comparing again the response time and the internal photosensitivity  $\mu\tau$ , assuming a mobility of  $45 \text{ cm}^2/\text{V sec}$  (7). In this case we found that the density of trapping states at the quasi-Fermi level must be lower by at least a factor of  $2 \times 10^3$  than that for the amorphous films thus giving values  $10^{14}$  up to  $10^{16}/\text{cm}^3$  eV for crystalline  $\text{Sb}_2\text{Se}_3$ . This fact is of particular importance if we realize that both amorphous and crystalline  $\text{Sb}_2\text{Se}_3$  exhibit a photoconductive onset of similar sharpness despite quite different values of states inside the gap.

### 5. Conclusion

It is shown that for amorphous  $\text{Sb}_{1-x}\text{Se}_x$  films the position of the photoconductive edge coincides with the optical absorption edge and depends strongly on film composition. This edge is located at 1.4 eV for stoichiometric  $\text{Sb}_2\text{Se}_3$  films. The sharpness of the photoconductive onset for amorphous  $\text{Sb}_2\text{Se}_3$  is similar to that of single crystal  $\text{Sb}_2\text{Se}_3$ , thus giving

no direct evidence for the band tailing into the pseudogap. On the other hand, the analysis of the photoconductivity kinetics yields much higher density states deep inside the pseudogap, with values  $\sim 8 \times 10^{17}$  to  $10^{21}/\text{eV cm}^3$  which are closer to densities of states obtained from transport rather than from optical measurements.

### References

- 1) B. T. Kolomeets, V. M. Lyubin and D. V. Tarkhin, *Fiz. Tverd. Tela* **1** (1959) 899 [English Transl. *Soviet Phys. Solid State* **1** (1960) 819].
- 2) V. M. Lyubin and V. S. Muzhinski, *Soviet Phys. Semiconductors* **3** (1970) 1408.
- 3) A. F. Istaitieh, D. M. Hoffman and E. R. Fevig, *J. Vacuum Sci. Technol.* **6** (1969) 384.
- 4) R. Mueller and C. Wood, *J. Non-Crystalline Solids* **7** (1972) 301.
- 5) H. Krause, to be published.
- 6) T. S. Moos, *Photoconductivity in the Elements* (Academic Press, New York, 1952).
- 7) A. A. Mostovskii, L. G. Timoteeva and O. A. Timoteev, *Soviet Phys.-Solid state* **6** (1964) 389.
- 8) Z. Hurych and C. Wang, *J. Sci. Instr.* **5** (1972) 11.
- 9) K. Weiser and M. H. Brodsky, *Phys. Rev. B* **1** (1970) 791.
- 10) W. F. Howard and R. Ito, *Phys. Rev. B* (1970) 4709.
- 11) H. Cretzschke, *J. Non-Crystalline Solids* **6** (1971) 49.
- 12) J. D. Dow and J. J. Hopfield, *J. Non-Crystalline Solids* **8-10** (1972) 664.
- 13) D. L. Pierce, C. G. Ribling and W. F. Spicer, *J. Non-Crystalline Solids* **8-10** (1972) 959.
- 14) T. M. Donovan, W. F. Spicer and J. M. Bennett, *Phys. Rev. Letters* **22** (1969) 1158.
- 15) B. T. Kolomeets, Yu. V. Rukhlyadev and V. P. Shilo, *J. Non-Crystalline Solids* **5** (1970-71) 402.
- 16) A. Rose, *Concepts in Photoconductivity and Allied Problems* (Wiley, New York, 1963).
- 17) J. Black, E. M. Conwell, L. Seige and C. W. Spencer, *J. Phys. Chem. Solids* **2** (1957) 240.

---

## A method for determining photoconductive response times

Z Hurych and C Wang

Department of Physics, Northern Illinois University,  
DeKalb, Illinois 60115, USA

MS received 2 August 1971

**Abstract** It is shown how the photoconductive response time  $\tau_0$  can be readily determined from the phase shift between the exciting radiation and the photocurrent using a lock-in amplifier technique.

A standard method of measuring AC photocurrents which employs chopped light can be easily modified to yield also the photoconductive response time  $\tau_0$ . If a photoconductor with response time  $\tau_0$  is illuminated by symmetrical square wave pulses of frequency  $f$ , the first harmonic frequency of the photocurrent is delayed with respect to the exciting radiation by a phase  $\phi_0$ , where

$$\phi_0 = 2\pi f\tau_0. \quad (1)$$

This phase shift  $\phi_0$  can be easily measured using a lock-in amplifier as a phase sensitive detector. In order to obtain a good accuracy in  $\phi_0$ ,  $f$  must be chosen of the order of  $1/\tau_0$ . This note indicates how additional phase changes due to the electronic equipment can be eliminated.

In AC photoconductivity measurements, the exciting light pulses are usually produced by a light chopper, where the same blade chops the light illuminating the sample and also the light from an auxiliary light source which is placed in

front of a photosensitive detector P. P thus provides a signal coherent with the exciting light, which is used as a reference for the lock-in amplifier. In photocurrent measurements, the phase of the lock-in amplifier is adjusted to the value  $\phi_1$  for maximum mixer output. Clearly,

$$\phi_1 = \phi_0 + \phi_E + \phi_G + \phi_P \quad (2)$$

where the subscripts 0, E, G, P are symbols for the phase shifts due to the sample, electronic equipment, geometry of the light chopper and the photodetector P with its electronic circuit, respectively.

The sample is subsequently replaced by another 'reference' photodetector R, with a very short response time  $\tau_R$  so that the corresponding phase delay

$$\phi_R = 2\pi f\tau_R \quad (3)$$

is much smaller than  $\phi_0$ . Then without any change in electronic circuits or geometry of the equipment, the phase of the lock-in amplifier is again adjusted to a value  $\phi_2$  for maximum mixer output, so that according to equation (2)

$$\phi_2 = \phi_R + \phi_E + \phi_G + \phi_P \quad (4)$$

From (2) and (4) we obtain

$$\phi_0 = (\phi_1 - \phi_2) + \phi_R \quad (5)$$

and the photoconductive response time  $\tau_0$  is then determined from equation (1). If  $\tau_R \ll \tau_0$ ,  $\phi_R$  in equation (5) can be neglected.

An orthorhombic  $\text{Sh}_2\text{Se}_3$  single crystal was used to compare this technique with the 'graphical' method, where  $\tau_0$  is determined from the decay of the photocurrent pulses observed on an oscilloscope. Very good agreement was obtained for  $\tau_0$  in the range 400–80  $\mu\text{s}$  using a PAR HR-8 lock-in amplifier and  $f = 700$  Hz (Hurych, Wang and Wood 1971a). The variation of  $\tau_0$  in the above range was achieved by partial filling of traps using a dc light background of variable intensity. As the reference photodetector R, a Texas Instrument silicon light sensor LS 600 with a response time of 15  $\mu\text{s}$  was used. This method was used to determine the response time in epitaxial YbTe and YhSe (Hurych *et al.* 1971b).

Due to the use of a lock-in amplifier, the method described above can be used for measurements of  $\tau_0$  even in the case of photosignals well below the noise level. Thus this method is applicable to very poor photoconductors, or can be applied to good photoconductors at very low light levels or low drift fields if it is desirable to eliminate space charge effects, and is particularly useful when other graphical signal averaging instruments, such as box car integrators, are not available.

A few errors are associated with this method; for example, equation (1) neglects the finite width  $d$  (usually a few millimetres) of the illuminated part of the sample. This introduces an error  $\Delta\phi_0$  of the order of a few per cent, as  $\Delta\phi_0 \approx d/L$ , where  $L$  (typically 10–20 cm) is the length of the segment of the chopping blade corresponding to one light pulse. Another source of error ( $\sim 1\%$ ) is the reproducibility of the phase shift dial of the lock-in amplifier. (Since this method measures the difference  $\phi_1 - \phi_2$ , the absolute accuracy of the phase shift is not important.) Finally, the value  $\tau_0$  determined from equations (1) and (5) is the exact response time only if the rise and fall of the photocurrent are symmetrical and obey the exponential dependence on time. Otherwise  $\tau_0$  would be an 'effective' or average response time. The above condition for exponential rise and decay is very nearly obeyed in the case of semiconductors with a very low concentration of traps, where the response time  $\tau_0$  is close to the recombination

lifetime of minority carriers (Rose 1963, Mort 1968). Such materials are rather poor photoconductors, and the application of the above method is particularly advantageous.

#### Acknowledgments

This research was supported by the Advanced Research Projects Agency of the Department of Defense and was monitored by the Army Research Office, Durham, under Contract No. DA-ARO-D-31-124-70-G77. The author would like to thank Dr C Wood for his valuable discussions.

#### References

- Hurych Z, Wang C and Wood C 1971a *Bull. Am. Phys. Soc.* **16** 400
- Hurych Z, Wang C and Wood C 1971b *Phys. Letters* **34A** 291–2
- Rose A 1963 *Concepts in Photoconductivity and Allied Problems* (New York, London: Interscience) pp 18–22
- Mort J 1968 *J. Appl. Phys.* **39** 3543–9
- Journal of Physics E: Scientific Instruments 1972 Volume 5  
Printed in Great Britain

## OPTICAL AND TRANSPORT PROPERTIES OF AMORPHOUS $\text{Sb}_2\text{Se}_3$ \*

C. WOOD, Z. HURYCH and J. C. SHAFFER

*Physics Department, Northern Illinois University, DeKalb,  
Illinois 60115, U.S.A.*

The optical absorption, reflectivity, electrical conductivity, photo-conductivity, and photo-emission have been studied in amorphous films of  $\text{Sb}_2\text{Se}_3$ . The films were prepared by coevaporation thus allowing strict control of composition. Comparison with data on  $\text{Sb}_2\text{Se}_3$  single crystals show marked similarity of properties and in particular, show that the forbidden energy gap values closely correspond. Furthermore, in contrast to published data, on similar amorphous systems such as  $\text{As}_2\text{Te}_3$ <sup>1)</sup>, the structure at the band edges appears to be quite sharp, thus showing no evidence of a mobility gap.

### 1. Materials preparation

Throughout the work described in this contribution the intent has been to compare the properties of amorphous thin films of antimony selenide with crystalline  $\text{Sb}_2\text{Se}_3$ . Much effort has been made to ensure that the composition of the films can be made closely approximate to that of the crystal and that the films are, indeed, amorphous.

The films were prepared by the technique of coevaporation onto fused quartz substrates. Separate quartz crystal oscillators monitored and controlled the rates of deposition of Sb evaporated from an electron-beam gun and Se from a resistance heated crucible. Films could be obtained with a variety of compositions, and though the principal interest herein is with films of composition near to that of the stoichiometric crystal, we report some results on other samples.

The degree of order of these films has been checked by electron diffraction<sup>2)</sup> and the stoichiometric films were found to be amorphous to the resolution of this technique ( $\sim 20 \text{ \AA}$ ). Mössbauer spectroscopy has been carried out<sup>3)</sup> on both crystalline and amorphous samples and indicates that the short-range order of Sb in the amorphous films differs from that in the crystals. Differential thermal analysis of the samples allowed a determination of a crystallization

\* This research was supported by the Advanced Research Projects Agency of the Department of Defense and was monitored by the Army Research Office Durham, under Contract No. D-ARO-D-31-124-71-G132.

temperature, of  $\sim 180^\circ\text{K}$ ; however, no softening temperature ( $T_g$ ) has been determined due to the small mass of the samples. The composition of the samples has been determined by both micro-probe analysis and by conventional X-ray emission methods. The compositions are probably accurate to the order of 1 at %.

## 2. The energy band gap

It has been known for some time that  $\text{Sb}_2\text{Se}_3$  is a semiconducting compound with a band gap 1.0–1.2 eV at room temperature<sup>4</sup>). The photoconductivity spectra of amorphous and polycrystalline films have been measured<sup>4</sup>) and, from the threshold, the band gap of the amorphous samples was found to be 1.6 eV and that of the polycrystalline samples 1.3 eV. As will be pointed out below, these results are not consistent with those reported here and may be explained by compositional deviations in the samples used in previous work.

In fig. 1 the absorption constant, determined from reflectivity and transmission measurements, of a thin (250 Å) and thick (5.8  $\mu\text{m}$ ) film of composition approximating that of the crystalline material is compared with single crystal data using unpolarized light. Similar data for an Sb excess and a Se excess film are also displayed. The absorption constant in the region of the edge shows an  $\alpha^{1/2}$  dependence on photon energy, for the single crystal. It is apparent from this dependence and the reflectivity curves that the transition giving rise to the edge at  $\sim 1.1$  eV in the crystal is a direct one with a superimposed indirect tail<sup>5</sup>). The absorption coefficient for the amorphous films exhibits no simple relationship with energy.

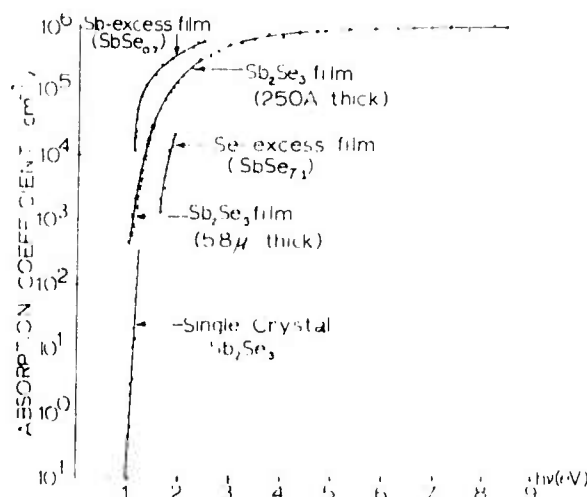


Fig. 1. The optical absorption spectra of single crystal  $\text{Sb}_2\text{Se}_3$  and amorphous films of  $\text{Sb}_x\text{Se}_y$ .

The resistivity of the stoichiometric amorphous films is comparable to that of the crystal. Preliminary values of the thermal activation energies computed from the slopes of the resistivity versus temperature curves are  $\sim 1.0$  eV and  $\sim 0.5$  eV for the crystal and amorphous films, respectively. The former value is in good agreement with published values<sup>6)</sup> and with the optical data. For the films, a value of approximately one-half the estimated band gap appears to be commonly found for amorphous materials<sup>7)</sup>.

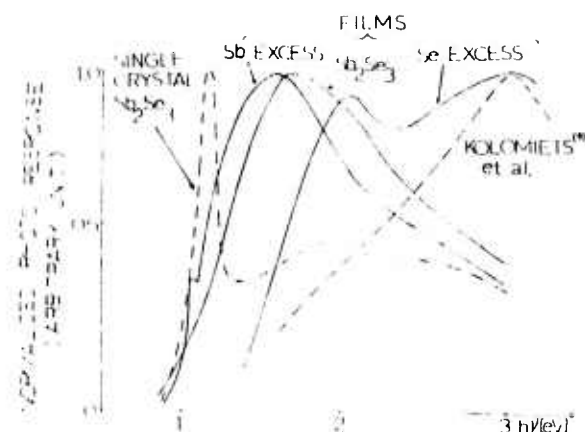


Fig. 2. The photoconducting spectral response of single crystal  $\text{Sb}_2\text{Se}_3$  and amorphous films  $\text{Sb}_x\text{Se}_y$ .

In fig. 2 the photocurrent response spectra of a crystalline sample and several amorphous films of different compositions  $\text{Sb}_x\text{Se}_y$  are shown. The photoconductive activation energy ( $\lambda_1$ )<sup>8)</sup> of the crystalline sample and for the stoichiometric amorphous film of composition  $\text{Sb}_2\text{Se}_3$  are 1.1 eV and 1.3 eV, respectively. There appears to be no evidence of band tailing in the spectral distribution curves.

### 3. Visible to ultraviolet optical properties

The near normal incidence reflectivity of the natural cleavage plane of  $\text{Sb}_2\text{Se}_3$  to unpolarized light and for light polarized  $\parallel a$  and  $\parallel c$  orientations is shown in fig. 3 for the spectral region 0 eV to 11.0 eV. The data is less reliable in the unpolarized light case because of a wavelength-dependent horizontal polarizing component in the Cary 14-R spectrophotometer<sup>9)</sup>. The data exhibits a broad region of high reflectivity extending from about 1.0 eV to about 7.0 eV. In addition much individual structure associated with critical points may be discerned in this region which is in essential agreement with

the data of Shutov et al.<sup>5</sup>). The front surface reflectivity of an amorphous film of  $\text{Sb}_2\text{Se}_3$ , 5.8  $\mu\text{m}$  thick, is also presented in fig. 3 over the same spectral region. For the particular film there is no measurable transmission in this range and therefore, the measured reflectivity can be compared to that of the bulk single crystal. The reflectivity was found to be somewhat lower than that of the single crystal in agreement with results on other amorphous materials<sup>10</sup>).

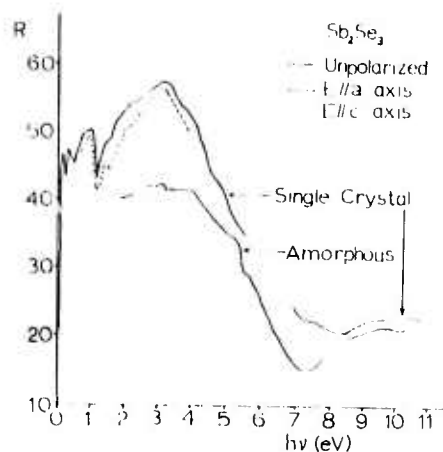


Fig. 3. Near-normal incidence optical reflectivity spectra of single crystal and amorphous  $\text{Sb}_2\text{Se}_3$ .

#### 4. Photoemission

The results of some preliminary photoemission measurements are presented in fig. 4. The photoelectric yield ( $Y$ ) and the energy distribution curves (EDC) of photoemitted electrons were measured and compared for single crystalline and amorphous  $\text{Sb}_2\text{Se}_3$ . The measurements were performed in vacuum in the range  $10^{-10}$  torr. The single crystals were cleaved in the natural cleavage plane ( $1b$ ) in situ. The amorphous films of composition  $\text{Sb}_2\text{Se}_3$  were prepared in the belljar apparatus and transferred under a dry inert atmosphere to the photoemission chamber and, therefore, because of this exposure, the data is less reliable. The chamber is being modified to prepare the films in situ.

The values of photoelectric threshold as obtained from the  $Y^{1/3}$  versus  $h\nu$  extrapolation<sup>11</sup>) were 5.7 eV for films and 6.4 eV for crystals.

From the EDC which represent the joint density of electronic states (JDOES) between the valence and conduction bands, an attempt was made to construct the effective valence and conduction band density of states.



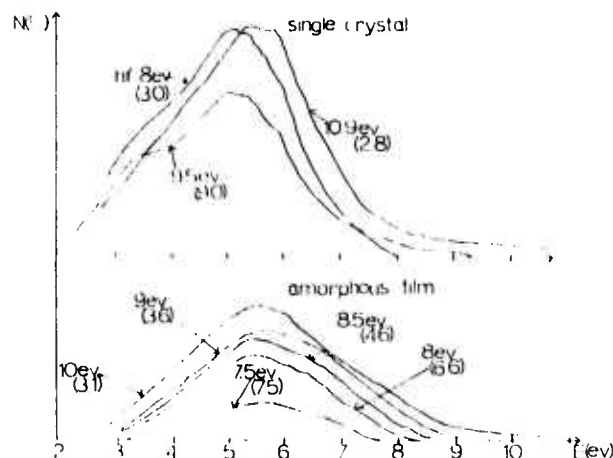


Fig. 4. Photoemission energy distribution  $N(E)$  versus energy ( $E$ ) above the top of the valence band of single crystal and amorphous  $\text{Sb}_2\text{Se}_3$ .

In the case of the amorphous material, the JDOES could be satisfactorily interpreted in terms of indirect transitions, i.e., no pronounced dependence of matrix elements on  $k$  (but possibly a dependence on  $h\nu$ ), for photon energies of 7 eV to 11.8 eV, with no evidence of sharp structure in the valence or conduction band. For the single crystal, direct transitions were dominant together with slight additional structure which could be explained in terms of indirect transitions, with constant matrix elements due probably to a localized or flat  $E$  versus  $k$  band. A more detailed assignment of these transitions at present is a difficult task as the band structure calculations are not available, and the results of group theory selection rules have been applied so far only to the region of the interband minimum, which is inaccessible to photoemission measurements due to the work function of investigated materials.

### 5. Conclusions

In summary we find marked similarities between the properties of single crystal and amorphous  $\text{Sb}_2\text{Se}_3$  and little evidence of extensive band tailing into the forbidden band gap as one would expect to find from a mobility gap consideration.

### Acknowledgements

The authors wish to acknowledge the valuable assistance of the following graduate students: R. Afshar, D. Buezek, L. Gilbert, R. Mueller, B. Van Pelt and C. Wang.

## References

- 1) K. Weiser and M. H. Brodsky, Phys. Rev. B **1** (1970) 791.
- 2) B. Krause, to be published.
- 3) S. L. Ruby, L. R. Gilbert and C. Wood, Bull. Am. Phys. Soc. **16** (1971) 303.
- 4) N. Kh. Abrikosov, V. F. Bankina, L. V. Poretskaya, L. E. Shelimova and E. V. Skudnova, *Semiconducting II-VI, IV-VI and V-VI Compounds* (Plenum Press, New York, 1969) p. 187.
- 5) S. D. Shutov, V. V. Sobolev, Y. V. Popov and S. N. Shestatskii, Phys. Status Solidi **31** (1969) K23.
- 6) M. V. Kot and S. D. Shutov, Tr. Fiz. Poluprovodnikov, Kishinevsk. Univ. **1** (1962) 47.
- 7) E. A. Fagen and H. Fritzsche, J. Non-Crystalline Solids **2** (1970) 170.
- 8) T. S. Moss, *Photoconductivity in the Elements* (Academic Press, New York, 1952).
- 9) M. E. Hill, A. L. Olson and L. W. Nichols, Appl. Optics **7** (1968) 1437.
- 10) J. Tauc, in: *Optical Properties of Solids*, Eds. S. Nudelman and S. S. Mitra (Plenum Press, New York, 1969).
- 11) R. C. Eden, Ph.D. Thesis, Stanford University (1967) p. 249.

## THE AMORPHOUS Sb-Se SYSTEM\*

C. WOOD, R. MUELLER and L.R. GILBERT

*Physics Department, Northern Illinois University, DeKalb, Illinois 60115, USA*

Received 12 January 1973 and in revised form 25 April 1973

Essentially the complete compositional range of the amorphous Sb-Se system has been prepared in thin-film form by a simple evaporation technique. Optical and transport properties have been measured as a function of composition.

### 1. Introduction

As pointed out in a previous paper [1] considerable care is required in the preparation of amorphous materials by vacuum evaporation if a given composition is desired and, further, that physical properties, e.g. the optical energy gap, change appreciably as a function of composition. It is, therefore, of interest to investigate amorphous systems as a function of a wide range of known compositions and to construct a type of 'phase diagram'. This can be a very laborious procedure by conventional methods and the purpose of this paper is to describe a method whereby such an investigation is facilitated and to apply this method to a particular amorphous system, namely, Sb-Se. The basic technique has been employed in the past to prepare crystalline films [2, 3] and composites [4] but not, to our knowledge, to prepare amorphous films, i.e., its most appropriate use, where equilibrium phase diagrams are inapplicable.

### 2. Experimental apparatus

The apparatus is very similar in design to that described earlier [1]. Sb and Se are coevaporated from two Airco-Temesco electron beam (EB) guns whose relative rates of evaporation are controlled by two Sloan Omni H-A rate controllers<sup>†</sup>. However,

\* This work was supported by the Advanced Research Projects Agency of the Department of Defense and was monitored by the Army Research Office under Contract No. DA-ARO(D-31-124-72-G115). We wish also to acknowledge financial support by the Council of Deans of Northern Illinois University.

<sup>†</sup> Footnote, see next page.

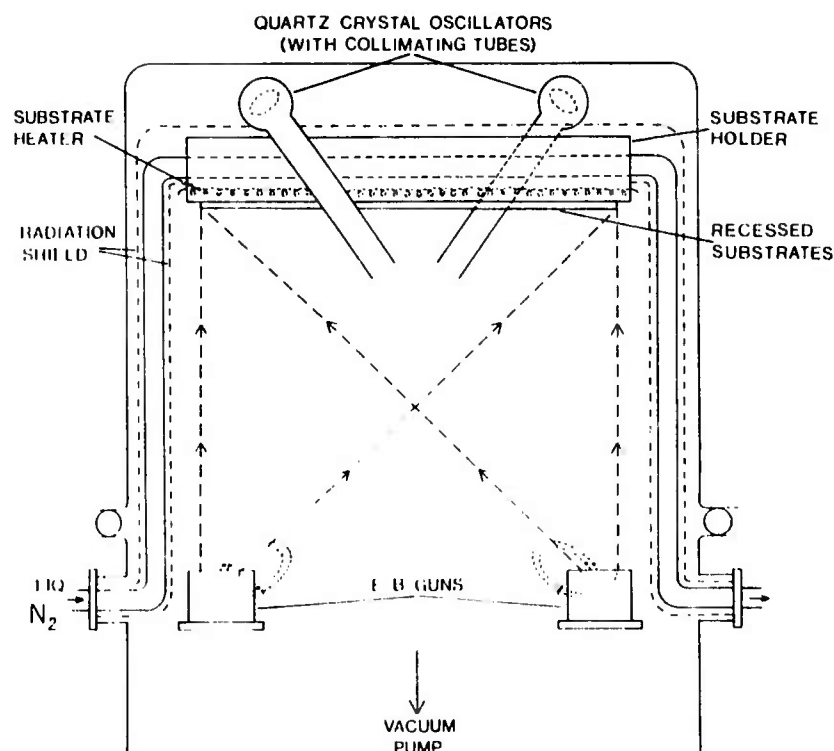


Fig. 1. Co-evaporation system.

the major difference between systems is that in this instance the EB guns are widely separated (diametrically opposed) in the bell-jar and the substrate holder is  $\sim 14$  in (35.6 cm) long, i.e., nearly equal in length to the  $\frac{1}{2} \times \frac{1}{2}$ " (1.27 cm  $\times$  1.27 cm) diameter of the bell-jar (fig. 1). Thus a total of about 28 square fused-quartz substrates can be accommodated in a holder. The juxtaposition of one end of the substrate holder to one crucible and its remoteness from the other crucible ensures the formation of a strong composition gradient along the length of the holder; the actual value of the gradient and the film thickness depends on the density of Sb and Se, and on the height of the holder above the crucibles.

Our present system incorporates two such holders situated at different heights above the crucibles, clamped on the copper tubing cooled by liquid  $N_2$ . Hence, for a given ratio of evaporation rates from the two EB guns a broad sampling of compositions in thick films is obtained in the lower rack and a smaller compositional gra-

<sup>1</sup> The operation of these controllers has been greatly improved by the redesign of the quartz crystal oscillator by Dr. D.F. Newell of the Industry and Technology Department, N.I.U.

dient about the composition ratio of interest is obtained in thin films from the upper rack. Furthermore, the substrates can be held at temperatures between liquid  $N_2$  and room temperature.

### 3. Film preparation

In this experiment the evaporations were carried out in a pressure of  $\sim 10^{-7}$  mm Hg. or lower, and the ratio of evaporation rates ( $\text{\AA}/\text{sec}$ ) for Sb:Se was chosen to be 1.0, thus  $Sb_2Se_3$  occurred near the center of the substrate holder. The substrates were held at room temperature throughout the evaporation. The compositions of selected films were determined by electron microprobe analysis and are plotted in fig. 2.

A theoretical plot of film thickness ( $t$ ) and composition ( $f$ ), where  $f$  is the at% Se at point  $x$ , for the lower and upper substrate racks is also shown in fig. 2. A best fit to the experimental thickness data was obtained assuming an Sb:Se rate ratio

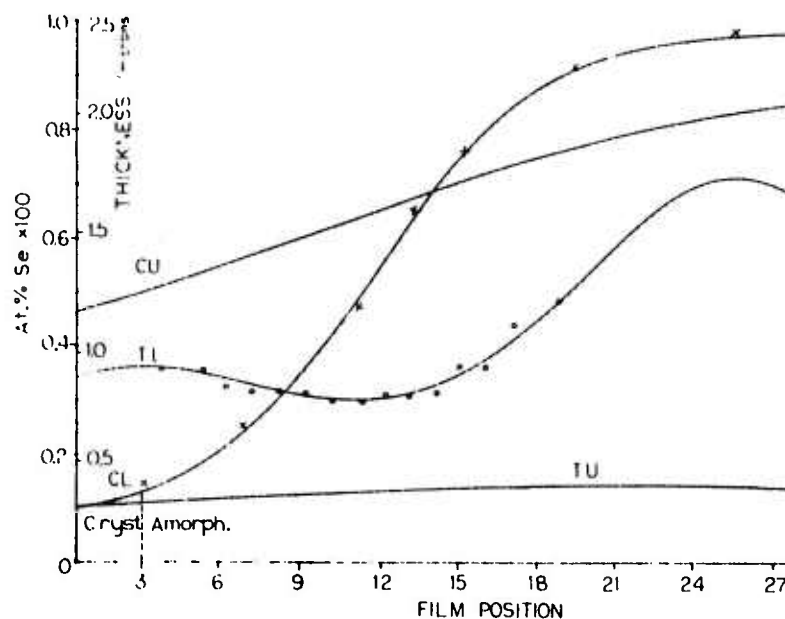


Fig. 2. Theoretical curves of composition ( $C$ ) and film thickness ( $T$ ) versus film position in upper ( $U$ ) and lower ( $L$ ) substrate holders. ( $x$ )- $\mu$ -probe data, ( $o$ )-thicknesses determined by interferometry.

( $W_{\text{Sb}}, W_{\text{Se}}$ ) of 0.7 instead of 1.0. These curves were plotted using the equations\*:

$$t_{\text{SbSe}} = t_{\text{0Sb}} \left[ 1 + \left( \frac{r}{h} \right)^2 \right]^{-2} + t_{\text{0Se}} \left[ 1 + \left( \frac{d}{h} \cdot \frac{r}{h} \right)^2 \right]^{-2}, \quad (1)$$

$$f_{\text{Se}} = \left[ 1 + \frac{W_{\text{Se}}^2 A_{\text{Se}}}{W_{\text{Sb}}^2 A_{\text{Sb}}} \left( 1 + \frac{d^2}{h^2} - \frac{2dr}{h^2} \right)^2 \right]^{-1}, \quad (2)$$

where  $t_{\text{0Se}}, t_{\text{0Sb}}$  are the thicknesses directly above the respective sources;  $A_{\text{Se}}, A_{\text{Sb}}$  are the atomic weights of selenium and antimony;  $d$  is the separation of the sources; and  $h$  is the height of the rack. For this system,  $d$  equals 12.3 in (31.2 cm),  $h_{\text{lower}}$  equals 7.0 in (17.8 cm) and  $h_{\text{upper}}$  equals 17.1 in (43.4 cm). Eqs. (1) and (2) include the assumption of a cosine distribution from each  $\frac{3}{4}$  in diameter source. At low evaporation rates,  $\sim 1$  to  $1\frac{1}{2}$  Å/sec such as used in this experiment, this appears to be a reasonable assumption. However, Smith [5] has shown that at high rates of evaporation from EB guns a virtual source exists and, therefore, the source position and evaporation distribution are rate dependent.

Although both elements can be prepared in the amorphous form, amorphous Sb is stable only at low temperatures for thick films ( $\sim$  microns) or for very thin films ( $\sim 10^2$  Å) at room temperature [6, 7]. X-ray diffraction measurements showed that all except the extremely Sb-rich films were amorphous in the present experiment. The demarcation is shown in fig. 2 for the composition curve of the lower substrate holder (CL). One film at this boundary appeared to be amorphous initially but crystallized on standing for a period of approximately one week. An indication of this transformation was first noticed optically by the initial appearance of infra-red optical transmission and transmission interference fringes and their later disappearance. The transformation was verified by X-ray diffraction.

#### 4. Optical measurements

In order to survey the optical properties of the films as a function of composition every alternate substrate in the sequence in the holder was selected for measurement. Because of the compositional variation across the substrate only a 1 mm wide strip of the center section, perpendicular to the composition gradient, was measured.

A Cary 14 R spectrophotometer with a Strong [8] reflectance attachment was used to make optical transmittance ( $T$ ) and reflectance ( $R$ ) measurements. Since the films were deposited on fused-quartz substrates, true  $R$ 's and  $T$ 's for the films were obtained from observed values  $R_{\text{obs}}$  and  $T_{\text{obs}}$  by using the following equations [9, 10] (without a substrate in the reference beam):

\* These equations are essentially the same as in ref. [4] but expressed in terms of atomic weights.

$$T = \frac{T_{\text{obs}}(1 - R'_1 R'_s)}{(1 - R'_s)} \quad (3)$$

$$R = R_{\text{obs}} \frac{T_1^2 R'_s}{(1 - R'_1 R'_s)} \quad (4)$$

where  $R'_1$  the reflectance at the substrate-film interface was assumed to be  $\approx R_{\text{obs}}$ ,  $R'_s = (1 - n_s)^2 / (1 + n_s)^2$  and the refractive index of the substrate  $n_s = 1.43$ .

The absorption coefficient ( $\alpha$ ) was calculated by computer programming the third-degree equation obtained by eliminating the front surface reflectivity,  $r$ , from the equations:

$$T = \frac{(1 - r)^2 e^{-\alpha l}}{1 - r^2 e^{-2\alpha l}} \quad (5)$$

$$R = r(1 + T e^{-\alpha l}) \quad (6)$$

i.e.,

$$(e^{-\alpha l})^3 + \left[ \left( \frac{1 - R}{T} \right)^2 - 1 + \frac{1}{T^2} \right] T(e^{-\alpha l})^2 + \left[ \left( \frac{1 - R}{T} \right)^2 - 2 \right] e^{-\alpha l} - \frac{1}{T} = 0. \quad (7)$$

These equations are valid only if the multiple-reflected rays are incoherent; and were applied only in the range where interference fringes were not observed. The short wavelength limit of the measured spectral range was set by the automatic slit-width of the Cary 14 R spectrophotometer reaching the fully-open position. Sample thicknesses,  $l$ , were determined by multiple interference of reflected light using a microscope fitted with a Watson interference objective. The refractive and absorption indices,  $n$  and  $k$ , were calculated from the equations:

$$\alpha = \frac{4\pi k}{\lambda}, \quad r = \frac{(n - 1)^2 + k^2}{(n + 1)^2 + k^2} \quad (8)$$

The absorption edges were found to obey the relation for non-direct transitions [11, 12]

$$\alpha h\nu = B(h\nu - E_g)^2, \quad (9)$$

showing conservation of energy but not crystal momentum. If the intercepts of the extrapolated curves in fig. 3 are taken as the values of the optical energy gap ( $E_g$ ) then one finds a tremendous variation in  $E_g$  from  $\sim 1.9$  eV to  $\sim 0.4$  eV on increasing the Sb:Se ratio. Corresponding values for  $B$  ranged from  $10^6$  to  $2 \times 10^5 \text{ cm}^{-1} \cdot \text{eV}^{-1}$  (table 1).

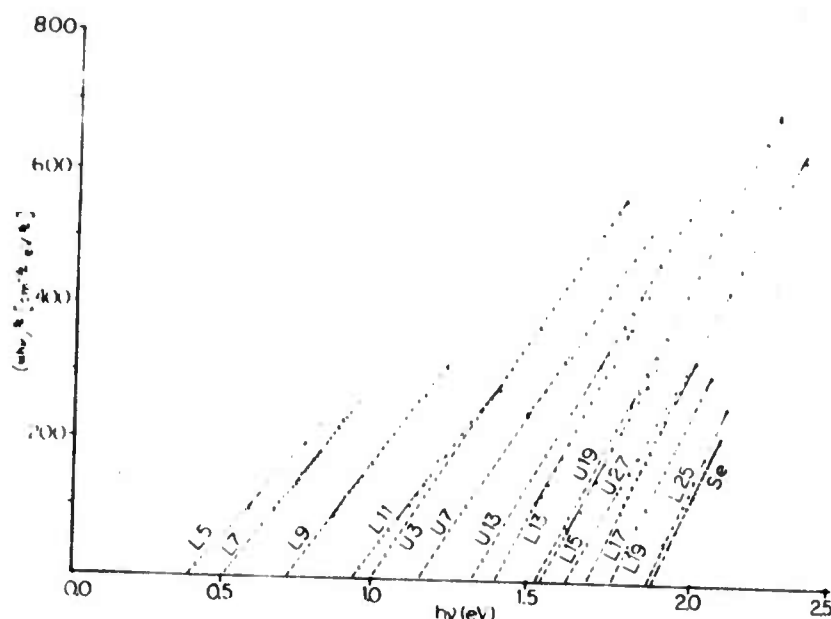


Fig. 3. Square-root dependence of absorption coefficient ( $\alpha$ ) on photon energy ( $h\nu$ ) for Sb-Se films of varying compositions shown in fig. 2.

From classical dispersion theory [13] the real part of the dielectric constant is given by:

$$n^2 - k^2 = 1 + \frac{Ne^2}{mc_0} \frac{\omega_0^2 - \omega^2}{(\omega_0^2 - \omega^2)^2 + \omega^2 \gamma^2} \quad (10)$$

In the limiting case at high frequencies, and where  $n^2 \gg k^2$ ,

$$n^2 - 1 = \frac{Ne^2}{mc_0} \frac{1}{(\omega_0^2 - \omega^2)} \quad (11)$$

and at low frequencies, where  $\omega \rightarrow 0$ ,

$$n^2 - 1 = \frac{Ne^2}{mc_0 \omega_0^2} \quad (12)$$

The high frequency values of  $n$  for four representative films were obtained from eqs. (7) and (8) in the region of non-interference, and the low frequency values, where  $k$  is small, were obtained from the positions of the maxima and minima in the interference region using the expressions:



Table I  
Optical and electrical parameters of amorphous Sb-Se films as a function of composition.

Film No.	At % Se	$E_g$ (eV)	$B$ (cm <sup>-1</sup> ·eV <sup>-1</sup> × 10 <sup>5</sup> )	$\Delta E_0$ (eV)	$\sigma_0 \exp(\gamma/k)$ (ohm <sup>-1</sup> ·cm <sup>-1</sup> × 10 <sup>3</sup> )	$\Delta E_1$ (eV)
L4	15			0.255	1.37	$1.37 \times 10^{-2}$
L5	17.5	0.40	2.7			
L6	20.5			0.308	3.45	$1.07 \times 10^{-2}$
L7	24.5	0.51	3.4			
L8	29			0.347	1.97	$9.44 \times 10^{-3}$
L9	34.5	0.72	3.7			
L10	41			0.458	1.25	$8.98 \times 10^{-3}$
L11	47.5	0.95	3.8			
L12	55			0.591	1.08	$9.43 \times 10^{-4}$
L13	62	1.39	5.0			
L14	68.5			0.656	0.12	$1.36 \times 10^{-4}$
L15	74.5	1.55	7.8			
L16	80			0.674	0.0017	$7.1 \times 10^{-4}$
L17	84	1.68	9.2			
L19	90	1.77	8.8			
L22a)	94.5	1.89	10	0.89	0.20	$3.5 \times 10^{-3}$
L25	97					
L26a)	97.5			1.04	2.06	$3.7 \times 10^{-3}$
U3	50	1.00	5.0			
U7	56.5	1.16	6.5			
U9	60	1.36	15.2			
U10	62			0.647	0.54	
U12	65			0.649	0.32	
U13	67	1.33	5.5			
U19	76	1.54	8.6			
U27	84	1.63	7.1			$8.8 \times 10^{-4}$

a) Sandwich electroded samples.

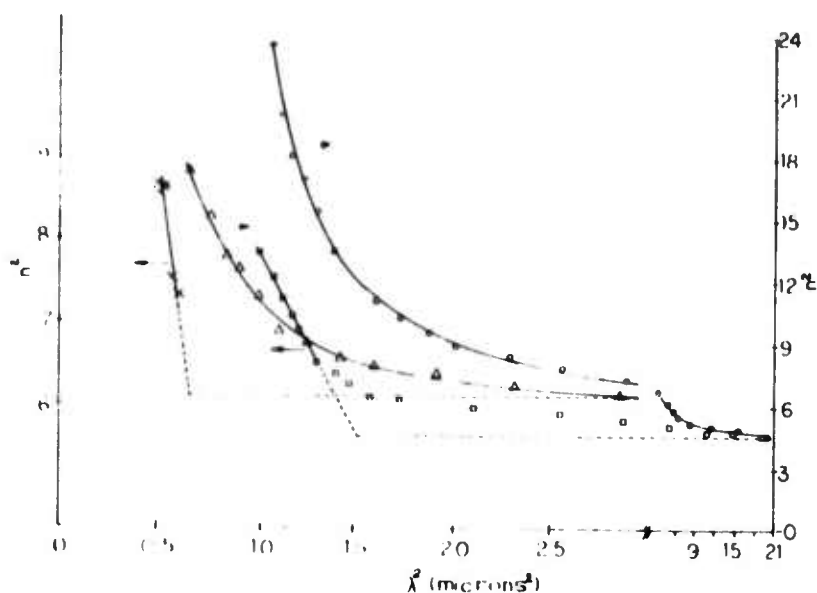


Fig. 4. Square of refractive index ( $n$ ) versus square of wavelength ( $\lambda$ ). Experimental (Sample 1.13): (x)  $n$  calculated from eqs. (7) and (8); ( $\Delta$ )  $n$  determined from interference maxima and minima, eq. (11). Theoretical: (o)  $n$  generated from eq. (10); (o)  $n$  determined from interference maxima and minima generated from Abè's equations.

$$2nd = m\lambda, \quad m = \lambda_2/(\lambda_1 - \lambda_2). \quad (13)$$

A plot of  $n^2$  versus  $\lambda^2$  for a typical film is shown in fig. 4. Extrapolations of the curves to  $\omega \rightarrow \infty$  and  $\omega \rightarrow 0$  yield values (table 2) for the high frequency ( $\epsilon_\infty$ ) and low frequency ( $\epsilon_0$ ) dielectric constants, respectively, as shown by eqs. (11) and (12). The high frequency values are not very reliable because of the limited range of experimental values of  $n$ .

Table 2  
High ( $\epsilon_\infty$ ) and low ( $\epsilon_0$ ) frequency dielectric constants obtained from extrapolation of curves in fig. 4.

Sample	$\epsilon_0$	$\epsilon_\infty$
1.25	5.8	12.3
1.19	7.2	13.75
1.13	12.8	33.5
1.7	20.7	54.0

As can be seen from fig. 4, a considerable error is introduced in the high frequency region if the  $n$  values determined from interference fringes are used for the extrapolation, as employed by Chandhari et al. [14]. This is further illustrated by the plot in fig. 4 of theoretical values of  $n$ , determined from eq. (10) for  $\omega_0 = 3.0 \times 10^5 \text{ sec}^{-1}$  and  $g = 1.5 \times 10^{14} \text{ sec}^{-1}$ . Using the same values of  $n$  and  $k$  in Abeles equations [15] interference fringes were generated and the values of  $n$  determined from the positions of the maxima and minima (eq. (13)) were plotted. The two theoretical curves are seen to diverge considerably at high frequencies as is observed experimentally.

One cannot determine the free-carrier relaxation time and, hence, the charge carrier mobility, from the intersection of these two regions, as suggested by Chaudhari et al. [14]. For high-resistivity materials, with very low free-carrier concentrations, such as discussed here and in ref. [14], the dispersion of the refractive index is due to an absorption band, not free carriers as they supposed. The lack of absorption at long wavelengths is confirmation that we are not dealing with dispersion due to free charge carriers in either the high or low optical frequency range.

### 5. Conductivity measurements

Alternating in the holder with the substrates for optical measurements were substrates which were electroded for conductivity measurements. The electrodes consisted of four strips of baked-on liquid-bright platinum. After film deposition these substrates were clamped to a copper block inside a copper radiation-shield attached to the cold-finger of an Air-Products Cryotip Dewar. Contact was made to the platinum by phosphor-bronze strips.

Up to  $10^{13}$  ohms the resistances were measured by passing a known dc current through the outer two electrodes and, with a Keithley 604 Differential Electrometer (input impedance  $10^{14}$  ohms), measuring the voltage drop across the inner two electrodes spaced 2 mm apart. Any potential barrier effects at contacts were thus avoided. Above  $10^{13}$  ohms the resistances were determined from the current flowing with 500 V applied across two electrodes. In films where the resistance variation with temperature required both two- and four-probe measurements  $\ln R$  versus  $1/T$  curves coincided showing that contact potential barriers could be ignored. For films of greater than  $10^{15}$  ohms resistance, i.e., films with  $> 80$  at % Se, a sandwich electrode structure was used. Teflon insulation was used throughout. The apparatus was calibrated with a series of standard resistances of up to  $10^{13}$  ohms. The temperature of the film was measured by attaching a calibrated chromel-constantan thermocouple to the film side of the substrate. The resistance was monitored both in the cooling and warming cycle. If sufficient time was allowed for the films to come to temperature equilibrium these curves coincided. The warming cycle had the slowest rate of change and generally was used for analysis. No hysteresis was observed between repeated cycles.

The results of these measurements are plotted in fig. 5. The activation energies

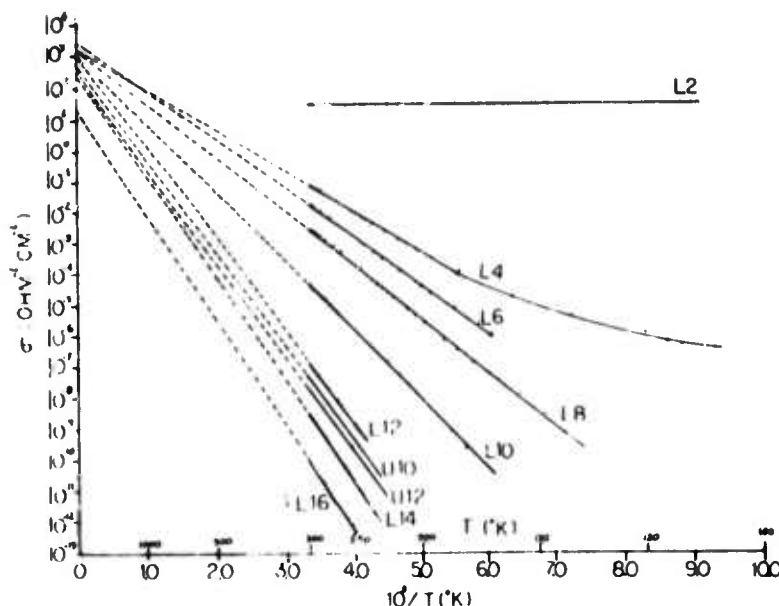


Fig. 5. Electrical conductivity ( $\sigma$ ) versus reciprocal of absolute temperature ( $T$ ).

were determined from a least-squares fit to the equation:

$$\sigma = \sigma_0 \exp\left(-\frac{\Delta E}{kT}\right). \quad (14)$$

For conduction in extended states  $\Delta E$  represents the energy difference between the Fermi energy ( $E_F$ ) and the majority carrier band edge (e.g. the valence band edge,  $E_v$ ). For intrinsic conduction the Fermi level is close to the center of the forbidden band and consequently  $\Delta E = \frac{1}{2}E_g$  [16]. If we assume  $\Delta E$  to be a linear function of temperature

$$\Delta E = \Delta E_0 - \gamma T, \quad (15)$$

then the activation energies obtained from the plots in fig. 5 are the extrapolated values ( $\Delta E_0$ ) to  $T = 0$  K and not the actual values of  $\Delta E$  at  $T = 0$  [11, 17].

The pre-exponential term,  $\sigma_0$ , includes the charge carrier mobility and density of states and can be shown to be nearly invariant with respect to temperature for both conventional acoustic-mode lattice scattering in crystals and diffusive-type mobility [11, 18] developed for disordered materials. Generally,  $\sigma_0$  is not strongly temperature dependent compared to the exponential term in eq. (14) and is expected to lie in the range  $10^2$  to  $10^3$  ohm $^{-1}$  cm $^{-1}$  [11].

If the charge carriers are excited into localized states at the band edges then  $\Delta E = E_F - E_B + \Delta W_1$ , where  $\Delta W_1$  is the activation energy for hopping conduction and the localized states occupy the energy range  $E_B - E_V$  [11]. Here,  $\sigma_0$  is expected to be  $\sim 10^{-2}$  to  $10 \text{ ohm}^{-1} \cdot \text{cm}^{-1}$  [11]. A straight line can be obtained on a  $\ln \sigma$  versus  $1/T$  plot if the mobility does not vary rapidly between  $E_B$  and  $E_V$ .

If hopping conduction occurs between localized states near the Fermi energy then  $\Delta E = \Delta W_2 \sim \frac{1}{2}$  width of the defect band [11]. Again, a straight line  $\ln \sigma$  versus  $1/T$  plot can be obtained, with  $\sigma_0 \lesssim 10^{-2} \text{ ohm}^{-1} \cdot \text{cm}^{-1}$ , if hopping is between nearest neighbors. Otherwise,

$$\ln \sigma = A - B/T^{1/4}. \quad (16)$$

It is seen in fig. 5 that all but the extremely Sb-rich films yield a straight line on the  $\ln \sigma$  versus  $1/T$  plot. Values of  $\sigma_0 \exp(\gamma/k)$ , obtained by extrapolating the curves to  $1/T = 0$  were found to be  $\sim 10^3 \text{ ohm}^{-1} \cdot \text{cm}^{-1}$  on the Sb-rich of  $\text{Sb}_2\text{Se}_3$  and then to progressively decrease to  $\sim 10 \text{ ohm}^{-1} \cdot \text{cm}^{-1}$  with increasing Se content (c.f. fig. 8). The extreme Sb-rich films were crystalline and showed metallic conductivity. The low temperature region of the  $\ln \sigma$  versus  $1/T$  plot for the film lying just on the amorphous side of the phase boundary, showed some curvature which would be fitted to the form of eq. (16). However, an estimate of the density of states from  $B = 2[\alpha^3/kN(E_F)]^{1/4}$  yielded an unrealistic value of  $N(E_F) \sim 10^{42} \text{ eV}^{-1} \cdot \text{cm}^{-3}$  and so cannot be interpreted straightforwardly in terms of the Mott model. Annealing to produce an acceptable density of states value [19] could not be employed here because of the propensity to crystallization.

## 6. Thermoelectric measurements

The Seebeck coefficient ( $S$ ) was measured on a number of the films used for resistivity measurements in an attempt to determine the position of the Fermi level.

Several choices of expressions for Seebeck coefficient are available for amorphous semiconductors [11]. If the current is carried primarily by electrons (or holes) in the vicinity of the Fermi energy ( $E_F$ ) then:

$$S = \pm \frac{1}{3} \pi^2 \frac{k^2 T}{e} \left[ \frac{d(\ln \sigma)}{dE} \right]_{E=E_F}. \quad (17)$$

An equation of this general form is applicable to hopping conductivity and, for example, to a half-filled impurity or defect band.

For a one-carrier non-degenerate system in which a mean free path ( $L$ ) can be defined:

$$S = \pm \frac{k}{e} \left( \frac{\Delta E}{kT} + A \right), \quad (18)$$

where  $\Delta E = E_F - E_V$ , is the energy difference between the Fermi energy and the band edge in which conduction is taking place, i.e. conduction or valence band, and as mentioned above, is temperature dependent, e.g. eq. (15). The constant  $A$  may take on various values depending on the energy dependence of the charge-carrier relaxation time, e.g.  $A = 2$  for acoustical-mode lattice scattering [20]. If a mean free path cannot be defined, i.e.  $L <$  the lattice spacing, and the energy dependence of the density of states (and, hence, the conductivity) is assumed to be linear then  $A = (1 + \text{terms of order } T)$ .

For a two-carrier system the individual contributions of electrons (e) and holes (h) to the Seebeck coefficient are subtractive [21]:

$$S = \frac{\sigma_e S_e + \sigma_h S_h}{\sigma_e + \sigma_h}, \quad (19)$$

In the intrinsic conductivity range where the electron and hole concentrations are equal

$$S = \frac{k}{e} \frac{b-1}{b+1} \left[ \frac{\Delta E_0}{kT} + A \right], \quad (20)$$

where  $b = \mu_e/\mu_h$ , the ratio of electron to hole mobility.

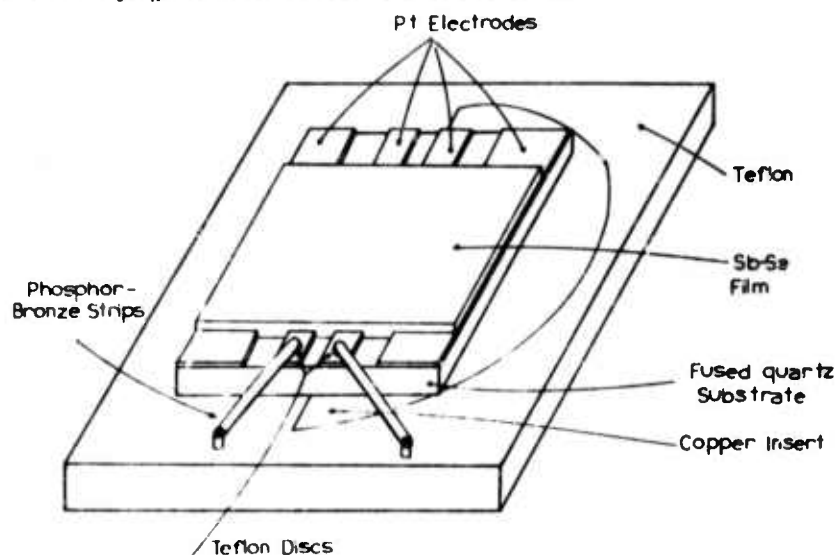


Fig. 6. Diagram of electroded substrate showing spring contacts for thermo-emf measurements. Spring contacts, without teflon discs, were used for electrical conductivity measurements.

In the experimental arrangement a Pt wire and a chromel-constantan thermocouple were pressed into contact with two of the platinum electrodes on the substrate using teflon discs attached to phosphor-bronze strips (fig. 6). A Keithley 604 differential voltmeter was connected to the platinum leads to measure the Seebeck voltage across the film and then to the two thermocouples, connected differentially, to measure the temperature gradient. A temperature gradient of  $\sim 5^\circ\text{C}$ , near room temperature, was established in the films perpendicular to the platinum electrodes by placing the substrate on a half-copper, half-teflon heatsink (fig. 6) and heating the copper by a hot plate. In a separate experiment a Pb film was evaporated onto a Pt-electroded substrate and the absolute Seebeck coefficient of the electrodes was determined to be  $2\mu\text{V}/^\circ\text{C}$  with constantan leads.

Values of  $S$  for various films are plotted against composition in fig. 7. All values were positive showing the majority carriers to be holes. Since for most films there

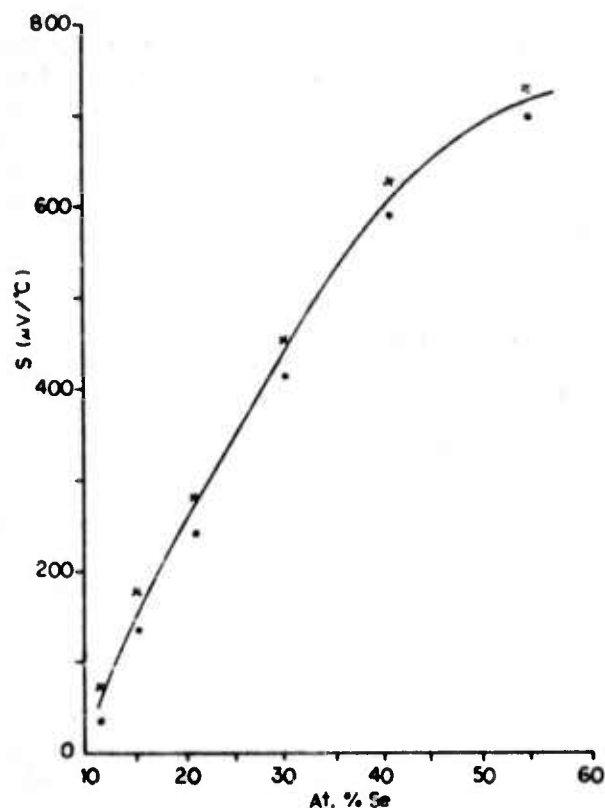


Fig. 7. Room temperature Seebeck coefficient versus film composition. (x) constantan or (o) platinum leads to sample.

was no evidence of impurity or defect band conductivity, either from the temperature dependence of the conductivity or from the magnitude of  $\sigma_0$ , eq. (17) was rejected. Values for  $\Delta E_0$  obtained from eq. (18), for any reasonable assumed value for  $A$  and  $\gamma$ , could not be reconciled with the  $\Delta E_0$  values obtained from  $\ln \sigma$  versus  $1/T$  curves. We were, therefore, forced to conclude that eq. (19) is applicable, i.e., the Fermi level is fixed near the middle of the energy gap and both holes and electrons are contributing to the Seebeck coefficient. If we assume that the Fermi level is in the middle of the gap for  $\text{Sb}_2\text{Se}_3$ , i.e., intrinsic conductivity, and substitute in eq. (20) the value for  $\Delta E_{ij}$  from the  $\ln \sigma$  versus  $(1/T)$  data, putting  $A = 1$  and  $\gamma = 3.5 \times 10^{-4} \text{ eV/}^\circ\text{C}$ , we can compute a value for  $b$  of 0.39.

## 7. Discussion

Attention has been drawn to the importance of annealing or depositing amorphous films near the crystallization temperature,  $T_c$ , to obtain reliable optical and conductivity data [22–24]. Sb-Se films cannot be annealed because of the tendency to crystallize. Amorphous Sb films, of thickness  $> 10^3 \text{ \AA}$ , crystallize well below room temperature and amorphous Se crystallizes at  $\sim 100^\circ\text{C}$ . The highest  $T_c$  reported for this system was  $170^\circ\text{C}$  at the composition  $\text{Sb}_2\text{Se}_3$  [25]. Because of the slow deposition rates ( $\sim 2 \text{ \AA/sec}$ ), the high vacuum ( $\sim 10^{-7} \text{ mm Hg}$ ), and the proximity of the substrate temperature during deposition to  $T_c$ , it was thought unlikely that further annealing would produce changes in film structure, while still remaining amorphous.

From straight-line slopes of the  $\ln \sigma$  versus  $1/T$  curves it is evident that the Fermi level is pinned in the gap. We cannot say whether this is due to a high local density of defect states in the gap as envisaged by Davis and Mott [26] or to a charge neutrality condition involving localized states tailing into the gap and overlapping, i.e., the CFO model [27]. Although the Fermi energy could not be determined unambiguously by thermo-emf measurements (the low Seebeck coefficient values clearly indicate a two-carrier mode of conduction) the results suggest that it is located near the middle of the gap.

The optical gap ( $E_g$ ) at room temperature and the thermal activation energy ( $\Delta E_0$ ) are shown in fig. 8 as a function of composition. A break in both curves occurs in the vicinity of  $\text{Sb}_2\text{Se}_3$ . At this composition  $2\Delta E_0 \approx E_g(0)$  where  $E_g(0)$  is the value of  $E_g$  extrapolated to 0 K [28] from which we might infer a symmetrical distribution of states with the Fermi level pinned near the center of the gap. Since  $\Delta E$  strictly represents the difference between the Fermi level and the valence-band edge, no great importance should be attached to the fact that  $2\Delta E > E_g$  at high Sb concentrations or  $< E_g$  at high Se concentrations. One cannot justifiably assume that the difference between  $2\Delta E$  and  $E_g$  represents the energy spread of the localized levels at the band edge as supposed by Weiser and Brodsky [29] for amorphous  $\text{As}_2\text{Te}_3$  (where  $2\Delta E < E_g$ ) or by Chandhari et al. [14] for amorphous  $3\text{As}_2\text{Se}_3 \cdot 2\text{Sb}_2\text{Se}_3$  films (where  $2\Delta E > E_g$ ). Possible reasons for this difference are:



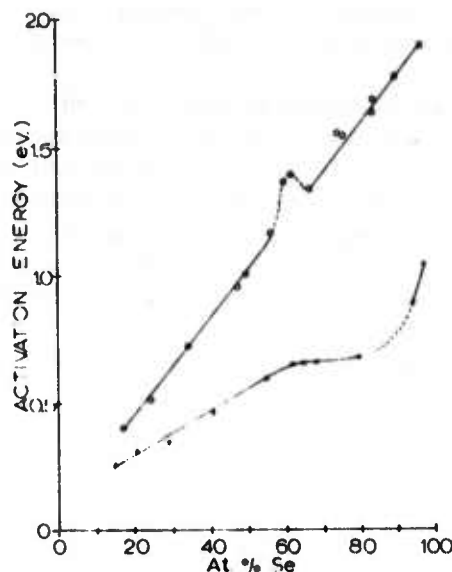


Fig. 8. Optical (○) and thermal (x) activation energies as a function of film composition.

(i) the Fermi level may be fixed away from the middle of the gap either by a high density of defect (or impurity) states [26] or by a different energy distribution of localized states tailing into the gap [27];

(ii) the value of  $\Delta E_0$  obtained from the  $\ln \sigma$  versus  $(1/T)$  curves represents the extrapolated value to absolute zero assuming a linear variation (constant  $\gamma$ ) of  $\Delta E$  with temperature, which is not generally equal to the true values of  $\Delta E$  at absolute zero [11, 17];

(iii) the optical energy gap is difficult to define since the lower part of the absorption edge is generally exponential with  $h\nu$  and of uncertain origin [11] (does not obey Urbach's rule) and, at higher photon energies, obeys a power law of the form  $\alpha h\nu \propto (h\nu - E_g)^n$  where  $0.5 \leq n \leq 3$ , which, depending on the assumptions used in the derivation, will give a different meaning to the value of  $E_g$  as determined by extrapolation;

(iv) the variation of the optical gap  $E_g$  between absolute zero and room temperature is generally assumed linear for comparison with  $\Delta E$ , which is rarely the case;

(v) the demarcation between localized and non-localized states at the band edges is not clearly defined and depends to some extent on the localized state's distribution in energy [11].

Values of  $\sigma_0 \exp(\gamma/k) \sim 10^3 \text{ ohm}^{-1} \cdot \text{cm}^{-1}$  are found for compositions on the Sb-rich side of  $\text{Sb}_2\text{Se}_3$ . On the Se-rich side the values steadily decrease to  $\sim 10 \text{ ohm}^{-1} \cdot \text{cm}^{-1}$ . Assuming an average value of 60 for  $\exp(\gamma/k)$  (i.e., the value obtained

from optical measurements for amorphous  $\text{Sb}_2\text{Se}_3$  between 200 K and 300 K) [29] for all compositions then the magnitude of  $\sigma_0$  suggests conduction in extended states for the Sb-rich films and conduction in localized states at the band edges for the Se-rich films.

The optical data showed an expected increase in the high ( $\epsilon_\infty$ ) and low frequency ( $\epsilon_0$ ) dielectric constants, with increasing Sb (metallic-bonding) content. Absorption coefficients ( $\alpha$ ) ranged from  $10^3$  to  $10^5 \text{ cm}^{-1}$  for the particular experimental conditions (film thickness, spectrometer sensitivity, etc.) and fitted well to an  $(\alpha h\nu)^{1/2}$  versus  $h\nu$  relationship for non-direct transitions showing the  $k$ -conservation selection rule is relaxed. An exponential tail was not observed or expected for these high absorption constants. The slope ( $B$ ) of the curves showed a steady increase with increasing Se-content.

Davis and Mott [26] have shown that  $B$  can be related to the energy spread ( $\Delta E_1$ ) in localized states at the band edge by

$$B = \frac{4\pi\sigma_0}{nc\Delta E_1} \quad (21)$$

where it is assumed that the optical transitions are occurring between extended and the localized states and that  $\sigma_{\text{opt}} \sim \sigma_0$ . Table 1 lists the values of  $\Delta E_1$  calculated from the slopes assuming  $\exp(\gamma/k) = 60$ . It can be seen that the values are very small  $\sim 10^{-2}$  to  $10^{-4} \text{ eV}$  with a minimum near 80 at % Se. However, when  $\sigma_0$  drops much below a value  $\sim 10^2 \text{ ohm}^{-1} \cdot \text{cm}^{-1}$ , it can no longer be assumed to be  $\sim \sigma_{\text{opt}}$  and eq. (21) cannot be used to determine a value of  $\Delta E_1$ . The small values of  $\sigma_0$  at high Se content may suggest that conduction occurs by hopping in localized states, and that the values we calculate for  $\Delta E_1$  are not significant, but this is pure conjecture. A second difficulty arises namely, that even in the range of high  $\sigma_0$  the values obtained for  $\Delta E_1$  are very much smaller than the photon energy range ( $> \text{several tenths eV}$ ) over which eq. (9) applies.

We are forced to conclude that the assumption of parabolic bands used by Taue [12] in the derivation of eq. (9) is more applicable to our films, that there is no evidence of appreciable band tailing, i.e. the band edges are fairly sharp, and the low values of  $\sigma_0$  at high Se concentrations are the result of a low diffusion-type mobility in extended states rather than hopping in localized states. Cohen [18] has estimated that this Brownian-motion conductivity extends from  $\sim 5 \text{ cm}^2/\text{V} \cdot \text{sec}$  down to  $10^{-2} \text{ cm}^2/\text{V} \cdot \text{sec}$  which, coupled with the decreasing gap with Se-content, would well encompass the range of conductivities encountered in our films.

Further support for these conclusions is given by a comparison of conduction in amorphous  $\text{Sb}_2\text{Se}_3$  and conduction in a single crystal of intrinsic  $\text{Sb}_2\text{Se}_3$  [30]. Between 300 K and 100 K, the conductivity in the  $c$ -direction of the single crystal was characterized by an activation energy of 0.63 eV with  $\sigma_0 \sim 33 \text{ ohm}^{-1} \cdot \text{cm}^{-1}$  and  $\sigma$  (room temp)  $\sim 5 \times 10^{-8} \text{ ohm}^{-1} \cdot \text{cm}^{-1}$ . This compares with the amorphous film of  $\text{Sb}_2\text{Se}_3$ , which has an activation energy of 0.625 eV,  $\sigma_0 \sim 12 \text{ ohm}^{-1} \cdot \text{cm}^{-1}$  and  $\sigma$

(room temp)  $\sim 2 \times 10^{-8} \text{ ohm}^{-1} \cdot \text{cm}^{-1}$  and shows that the mobility is comparable in both phases. Furthermore, assuming 'intrinsic' conduction for the amorphous  $\text{Sb}_2\text{Se}_3$  film, the mobility ratio,  $b$ , from eq. (20) was found to be very close to the value of  $\frac{1}{3}$  determined by Black et al. [31] for a single crystal of  $\text{Sb}_2\text{Se}_3$ . Black et al. [31] estimated the hole mobility in crystalline  $\text{Sb}_2\text{Se}_3$  to be approximately  $45 (m_0^2/m_e m_h)^{3/4}$ . Optical absorption [32] and photoconductive spectral response [33] measurements on single crystal and amorphous  $\text{Sb}_2\text{Se}_3$  show almost identical values for the energy gap, again, showing the properties of the two phases are remarkably similar\*.

The continuous change in energy gap and conductivity with composition lends support to the view that foreign atoms incorporated in an amorphous solid tend to satisfy their valency requirements rather than act as donor or acceptor impurities. Sb, when added to amorphous Se, probably reduces the  $\text{Se}_8$  ring concentration (as with As) [35] and acts as a branching or cross-linking agent between the Se linear polymer chains, replacing the weak bonds between chains with stronger covalent bonds. The fact that the addition of Sb reduced the glass-forming capability of Se [36] from the melt is more related to modification of the coordination (it becoming more metallic) in the melt than to cross-linking in the solid. Amorphous  $\text{Sb}_2\text{Se}_3$  has a higher crystallization temperature than amorphous Se. The peak in optical energy gap occurring at  $\text{Sb}_2\text{Se}_3$  could be associated with an ordering in the amorphous phase into molecular units corresponding to the crystalline form; but this is not supported by Mössbauer [37] or electron diffraction studies [38].

The following hypothesis based on a chemical bonding model is advanced to account for the tremendous variation of energy gap with composition. The valence band in undoped amorphous Se is assumed to arise from the non-bonding (lone-pair) 4p states and the conduction band from anti-bonding  $\sigma^*$  states arising from p-orbitals [39]. From the relative energy positions of the molecular states of Sb and Se, the addition of Sb to Se would provide unoccupied Sb  $\sigma^*$  (anti-bonding) states just below the Se  $\sigma^*$  conduction band and Sb  $\sigma$  (bonding) states below the Se (non-bonding or lone-pair) valence band [40]. However, Sb-Se bonds will be formed which will probably be of the resonating p-type. At low concentrations of Sb, these bonds will create localized  $\sigma^*$  states below the Se  $\sigma^*$  band. At higher concentrations of Sb the states will become delocalized and form the conduction band and, in addition, the valence band will probably take on a resonating p-state character, first producing localized and then delocalized states, as the composition  $\text{Sb}_2\text{Se}_3$  is approached. The general overlap of the states and the consequent broadening of the bands would account for the decrease of optical activation energy between pure Se and  $\text{Sb}_2\text{Se}_3$ . A further increase in Sb concentration would result in its domination of the band structure, and particularly the interaction of the Sb 5d orbitals, which at very high Sb concentrations would produce appreciable overlap into the energy gap. Near pure Sb, these orbitals

\* Switching has also been observed in both amorphous and crystalline phases of  $\text{Sb}_2\text{Se}_3$ , cf. ref. [34].

would be depressed into the valence band, causing the conductivity to be metallic upon crystallization.

An added reason for the decrease in band-gap with Sb concentration could be due to the effect of compositional disorder [40]. Lone-pair electrons adjacent to Sb atoms will have higher energies than those remote from Sb atoms, causing a broadening and tailing of the lone-pair valence band of Se. This effect could account for the shallower slope of the  $(\alpha h\nu)^{1/2}$  versus  $h\nu$  curves with increasing Sb concentration.

#### Acknowledgements

We wish to thank Dr. J. C. Shaffer for valuable discussions and comments on this work.

#### References

- [1] R. Mueller and C. Wood, *J. Non-Crystalline Solids* 7 (1972) 301.
- [2] S.A. Vikshinsky, *New Method of Metallographic Analysis of Alloys* (Gov. Tekh. izdat, 1944).
- [3] M.V. Kot and I.P. Molodyan, *Uchenye Zapiski Khimiev Univ.* 39 (1959) 49.
- [4] W.J. Ostrander and C.W. Lewis, *Trans. Natl. Vacuum Symp.* 8 (1961) 881.
- [5] H.R. Smith, *Society of Vacuum Coaters Annual Meeting*, Detroit, Mich. March 5-6 (1969).
- [6] L.S. Palatnik and V.M. Kosevich, *Soviet Phys. Cryst.* 3 (1958) 716.
- [7] J. Cohen, *J. Appl. Phys.* 25 (1954) 798.
- [8] J. Strong, *Procedures in Experimental Physics* (Prentice-Hall, N.J., 1938) p. 376.
- [9] T.M. Donovan, W.E. Spicer, J.M. Bennet and E.J. Ashley, *Phys. Rev.* 2 (1970) 397.
- [10] H.E. Bennett and J.M. Bennett, *Phys. of Thin Films*, ed. G. Haas and R.E. Thun, Vol. 4 (Academic Press, N.Y., 1967) p. 31.
- [11] E. Davis and N.F. Mott, *Electronic Processes in Non-Crystalline Materials* (Clarendon, Oxford, 1971).
- [12] J. Tauc, *Optical Properties of Solids*, ed. F. Abèles (North-Holland, Amsterdam, 1970).
- [13] T.S. Moss, *Optical Properties of Semiconductors* (Butterworths, London, 1961).
- [14] P.K. Chaudhari, F.R. Chenette and A. Van Der Ziel, *J. Appl. Phys.* 43 (1972) 3145.
- [15] F. Abèles, *Ann. d. Phys.* 5 (1950) 596, 706.
- [16] J.S. Blakemore, *Electrical Communication* (June, 1952) p. 131.
- [17] H. Fritzsche, *J. Non-Crystalline Solids* 6 (1971) 49.
- [18] M.H. Cohen, *J. Non-Crystalline Solids* 4 (1970) 391.
- [19] A. Lewis, *Phys. Rev. Letters* 29 (1972) 1555.
- [20] A.F. Joffe, *Semiconductor Thermoelements* (Infosearch, London, 1957).
- [21] V.A. Johnson, *Progress in Semiconductors* 1 (1956) 82.
- [22] W.E. Spicer, T.M. Donovan and J.E. Fischer, *J. Non-Crystalline Solids* 8-10 (1972) 122.
- [23] M.L. Theye, *Mat. Res. Bull.* 6 (1971) 103.
- [24] P.A. Walley and A.K. Jonscher, *Thin Solid Films* 1 (1967) 367; 2 (1968) 327.
- [25] L.R. Gilbert and C. Wood, *Bull. Am. Phys. Soc.* 16 (1971) 500.
- [26] E.A. Davis and N.F. Mott, *Phil. Mag.* 22 (1970) 903.
- [27] M.H. Cohen, H. Fritzsche and S.R. Ovshinsky, *Phys. Rev. Letters* 22 (1969) 1065.
- [28] B. Van Pelt and C. Wood, to be published.

- [29] K. Weiser and M.H. Brodsky, *Phys. Rev.* 1 (1970) 791.
- [30] L.R. Gilbert and C. Wood, to be published.
- [31] J. Black, E.M. Conwell, L. Selge and C.W. Spencer, *J. Phys. Chem. Solids* 2 (1957) 240.
- [32] C. Wood, Z. Hurych and J.C. Shaffer, *J. Non-Crystalline Solids* 8-10 (1972) 209.
- [33] Z. Hurych, R. Mueller, C.C. Wang and C. Wood, *J. Non-Crystalline Solids* 11 (1972) 153.
- [34] S. Luby, J. Cervenak, J. Kubek, M. Marcin and J. Šedláček, *Czech. J. Phys.* B21 (1971) 878;  
L.G. Gribnyak, *Sov. Phys.-Semicond.* 6 (1972) 478;  
N.S. Platakis and H.C. Gatos, *Phys. Stat. Sol.* a 13 (1972) K1.
- [35] G. Lucovsky, *Mater. Res. Bull.* 4 (1969) 505.
- [36] R.W. Hjalsty and H. Krebs, *J. Non-Crystalline Solids* 1 (1969) 399.
- [37] S.L. Puby, L.R. Gilbert and C. Wood, *Phys. Letters* 37A (1971) 453.
- [38] L.I. Tartarinova, *Kristallografiya* 4 (1959) 678.
- [39] E. Mooser and W.B. Pearson, *Progress in Semiconductors* 5 (1960) 103.
- [40] M. Kastner, *Phys. Rev. Letters* 28 (1972) 355.

THE AMORPHOUS  $Sb_{1-x}Te_x$  SYSTEM\*

C.M. Garner, L.R. Gilbert and C. Wood

Physics Department  
Northern Illinois University  
DeKalb, Illinois 60115

Amorphous films of  $Sb_{1-x}Te_x$ , where  $0.11 \leq x \leq 0.86$ , have been prepared by coevaporation. Crystallization temperatures occur near room-temperature for all compositions and appear to depend on film thickness. The optical and transport properties have been investigated as a function of temperature. Optical band gaps at room-temperature,  $E_g$ , ranged between 0.3 to 0.7 eV and decreased non-linearly with temperature. For the composition  $Sb_2Te_3$ ,  $E_g \sim 0.7$  eV, in contrast to the semi-metallic character of the crystalline form. All compositions were p-type with the Fermi-level close to the middle of the gap. The results have been interpreted in terms of the chemical bonding.

\* This work was supported by the Advanced Research Projects Agency of the Department of Defense and was monitored by the Army Research Office under Contract No. DA-ARO-D-31-124-72-G115.

### Introduction

As part of a continuing study of the properties of amorphous antimony chalcogenides [1], we report below on an investigation of the amorphous (a)  $\text{Sb}_{1-x}\text{Te}_x$  system. As with other members of this family of compounds, the  $\text{Sb}_{1-x}\text{Te}_x$  system can be readily prepared in the amorphous form only by quenching from the vapor phase and then, due to its more metallic bonding, only with somewhat more difficulty than other members of this series.

We are aware of only one other report in the literature on the preparation of a- $\text{Sb}_{1-x}\text{Te}_x$ . This is the work of Andrievskii et al. [2] in which a- $\text{Sb}_2\text{Te}_3$ , was prepared by vapor deposition onto a substrate of nitrocellulose lacquer held at 20°C. This result is contrary to our experience in which it was found necessary to cool fused-quartz or sapphire substrates to temperatures approaching that of liquid  $\text{N}_2$  in order to obtain amorphous deposits. Our films were presumably somewhat thicker than those of Andrievskii et al. since they were performing electron diffraction studies, but they claimed that their results were not dependent upon thickness. Furthermore, from the method of preparation, there is some doubt as to the composition of their films in that vaporization occurs by decomposition into the gaseous species  $\text{Sb}_4$ ,  $\text{Sb}_2\text{Te}_2$ ,  $\text{Sb}_2$  and  $\text{SbTe}$  [3,4] and, also, that disproportionation occurs into two phases above the solidus temperature in the range 11 to 60 at% Te [5]. Hence, it is extremely unlikely that evaporation from an  $\text{Sb}_2\text{Te}_3$  source will yield the same composition of deposit. We did not find it so for  $\text{Sb}_2\text{Se}_3$  [6].

A few electrical measurements have been reported on thin films of  $\text{Sb}_2\text{Te}_3$  by other workers [7,8] but these appear to have been crystalline and, because the preparation method is the same as above, are of doubtful composition.

Of particular interest in the amorphous-crystalline transformation of



the Sb-Te system is the effect on the band structure of the loss of long-range-order, and the possible change in short-range-order. Crystalline (c)  $\text{Sb}_2\text{Te}_3$  (rhombohedral,  $\text{C}_{33}\text{D}_{3d}^5$ ) is either a semimetal or a narrow gap semiconductor. From the optical data of Sehr and Testardi [9] the band gap is not greater than 0.21 eV and, because of degeneracy effects (Burstein shift [10]), may be considerably smaller. An estimate by Smirnov et al. [11] of the effect of degeneracy on the position of the optical absorption edge places the band gap at  $\sim 0.03$  eV. The conductivity is always found to be p-type despite numerous attempts by different investigators to produce n-type material by impurity doping or by deviations from stoichiometry. Free carrier concentrations are always found to be in the range  $10^{19}$  to  $10^{20} \text{ cm}^{-3}$  [12, 13, 14]. It has been suggested that a wrong-atom defect is responsible for this characteristic conductivity [12].

#### Preparation

Amorphous thin films in two thickness ranges,  $\sim 400\text{\AA}$  and  $\sim 2000\text{\AA}$ , were prepared by a coevaporation method onto an elongated substrate, as described elsewhere [1]. The elements were of high purity (6-9's) and the evaporation was carried out at rate  $\sim 2\text{\AA}/\text{sec}$  in a pressure of  $< 10^{-7}$  torr. The substrate holders were cooled with liquid  $\text{N}_2$  and contained some fused-quartz and, for better thermal transfer, some sapphire substrates. During evaporation, the temperature of the surface of the fused-quartz substrates was  $\sim 120^\circ\text{K}$  and of the sapphire  $\sim 100^\circ\text{K}$ . Compositions of selected films were determined by microprobe analysis and fitted to theoretical curves of composition versus substrate position [1].

#### Structure and Annealing Effects

The films were determined to be initially amorphous in the range 11 to



86 at% Te by x-ray diffraction. Standing at room-temperature progressively resulted in the thick ( $\sim 2000 \text{ \AA}$ ) films at the ends of the composition range undergoing conversion to the crystalline form. The greatest stability of the amorphous structure occurred in the Sb-rich range of compositions. After several weeks, all thick films except sample L9 had crystallized. The degree of crystallinity of the thin ( $\sim 400 \text{ \AA}$ ) films was less certain because of the smaller amount of material present to diffract x-rays. However, over the complete composition range ( $0.4 \leq x \leq 0.8$ ) of these films, no crystallinity was detected until the films were heated above room temperature.

The electrical conductivity at room-temperature increased by at least an order of magnitude in films held at room-temperature for a period of about one week. At the Sb-rich end of the system sample L4 exhibited metallic-like conductivity when first measured, whereas some Te-rich films (U16 and U26) exhibited this type of conductivity progressively in time, although all three films appeared to be amorphous from x-ray and optical gap determinations. The effect on the electrical conductivity of annealing at room-temperature for several days between temperature-cycles is shown in Fig. 1 for a film of composition 80 at% Te. After this film had been crystallized by heating it to  $200^{\circ}\text{C}$ , its room temperature-conductivity increased by an order of magnitude above the last result shown in Fig. 1.

For several selected thin films ( $\sim 400 \text{ \AA}$  thickness) of widely differing composition the conductivity measurements were extended above room-temperature. The films were heated at a rate of  $\sim 2^{\circ}\text{C}/\text{min}$  in a static atmosphere of argon at a pressure of slightly more than 1 atmosphere. A marked increase in conductivity over one or more orders of magnitude at a particular temperature was taken as an approximate indication of the amorphous-crystalline phase transformation. The crystal-

lization temperature was taken to be at the point of maximum slope and this data is plotted in Fig. 2. Crystallization was confirmed to have occurred by x-ray diffraction measurements.

### Optical and Transport Properties

Details of measurement of optical, electrical and thermo-emf measurements have been reported elsewhere [1]. Only the results of these measurements will be reported here. Measurements were made only on films that were amorphous and, because of annealing effects, were performed as rapidly as possible after film preparation; within 48 hours in the case of optical measurements.

Fig. 3 shows a plot of the square-root dependence of the optical absorption coefficient ( $\alpha$ ) on photon energy ( $h\nu$ ) for a range of compositions. The absorption edge ( $E_g$ ) was determined from the intercepts of the curves in Fig. 3 with the abscissa. The variation of  $E_g$  with temperature was obtained for four samples of different compositions and is plotted in Fig. 4.

Fig. 5 shows a plot of the log of conductivity ( $\log \sigma$ ) versus reciprocal temperature ( $T^{-1}$ ) between room and liquid- $N_2$  temperature for a number of compositions. All higher temperature data fit well to this linear dependence. At lower temperatures the data points for a number of films fall below the straight line. These data points were reproducible for repeated temperature-cycles if the time lapse between cycles was small. We do not suspect any measurement error because this behavior was not observed for the other, and in some cases, more highly resistive amorphous material systems, e.g., Sb-Se, Ge-Se, and Ge-Te [15], using the same apparatus.

Thermo-emf measurements at room-temperature, employing a temperature gradient of  $< 10^\circ\text{C}$ , showed the films to be p-type throughout the composition range. The Seebeck coefficient values are plotted in Fig. 6.

In Fig. 7 we have plotted the optical activation energy at room-temperature ( $E_g$ ); the value of  $E_g$  extrapolated to absolute zero temperature ( $\Delta E_g(0)$ ) using the data in Figs. 3 and 4; and the thermal activation energy extrapolated to 0°K ( $\Delta E_0$ ) from the slopes of the curves in Fig. 5 as a function of composition.

The results of all these measurements are summarized in Table 1, in which  $B \text{ cm}^{-1}\text{eV}^{-1}$  is the square of the slope of the curves in Fig. 3 and  $\sigma_0 \text{ ohm}^{-1}\text{cm}^{-1}$  is obtained from the intercept ( $\sigma_0 \exp \gamma/k$ ) with  $1/T = 0$  axis of the curves in Fig. 5.

### DISCUSSION

Preliminary evaporations of thick films ( $\sim 1$  micron) of  $\text{Sb}_{1-x}\text{Te}_x$  on to room-temperature or liquid- $\text{N}_2$  cooled substrates produced only crystalline films. Thin films,  $\sim 400 \text{ \AA}$  and  $2000 \text{ \AA}$ , were prepared in this study in order to stabilize the amorphous structure. Sb, for example, is known to be stable in the amorphous phase at room-temperature only if the films are extremely thin (16)(17). Similar considerations appear to apply to the  $\text{Sb}_{1-x}\text{Te}_x$  system. In the present study all films  $\sim 2000 \text{ \AA}$  thickness had crystallized on standing at room-temperature for several weeks, whereas films  $\sim 400 \text{ \AA}$  thickness in the composition range  $0.11 \leq x \leq 0.86$  appeared, by x-ray diffraction, to remain amorphous. Optical and transport measurements (Figs. 3,4 and 5) made on these very thin films immediately after preparation appear to exhibit standard semiconducting characteristics. However on standing at room-temperature for extended periods pronounced changes in conductivity occurred (Fig. 1) with eventual conversion to a semi-metallic character. The type of substrate used for film deposition, e.g., fused quartz or sapphire, did not appear to influence either the tendency to crystallization or the conductivity of the films.

From Fig. 2, the thin films appear to be below their crystallization temperatures at room-temperature  $T_c$ . It should be noted, however, that our values of  $T_c$  were not determined by thermodynamic methods and simply represent the stage where the crystallite size and volume fraction have increased to the extent that conducting paths have developed between electrodes (18)(19). However, in the Ge-Te system, Messier and Roy (20) have shown a close correspondence exists between  $T_c$  determined from conductivity measurements and published values.

From the marked time-dependent properties of these films we infer that the mass diffusion rates, at room-temperature and above, must be quite high in the  $a\text{-Sb}_{1-x}\text{Te}_x$  system. The glass transition temperature ( $T_g$ ) could be below room-temperature, which would account for the pronounced annealing effects (Fig. 1). Marked changes in conductivity have been observed at  $T_g$  by other investigators in the Ge-Te (20) and Ge-As-Te (21) amorphous systems, and distinction has been made between these transitions and the crystallization temperatures, ( $T_c$ ), the latter generally occurring at temperatures  $50^\circ\text{C}$  to  $150^\circ\text{C}$  above  $T_g$ . The curves in Fig. 1 closely resemble those of Pinto (21) and Johnson and Quinn (22) on successively heating Ge-As-Te amorphous films to higher temperatures. Pinto associates the temperature at which transitions from semiconducting to semimetallic characteristics occur with  $T_g$ . Johnson and Quinn associate these conductivity changes with a thermally induced conductive surface layer. The latter mechanism does not seem likely in our films since we would expect a greater conductivity change in the thinner films with the smaller bulk which is contrary to our findings. We also annealed our films under a static positive pressure of argon to suppress surface evaporation which could give rise to conducting layers. It appears more likely that, immediately after deposition,

heterogeneous crystallization is slowly taking place on a microscale of the type observed by Moss and deNeufville (18) in the  $\text{Ge}_{1-x}\text{Te}_x$  system at  $T_g$ . We have no way to detect this and this is the reason why the optical and transport measurements were performed as rapidly as possible after film preparation. We do not believe our thin films are crystalline to any marked degree because of the orders of magnitude changes in conductivity, which we associate with  $T_c$ , occur at  $\sim 100^\circ\text{C}$  to  $150^\circ\text{C}$ , i.e., well above room-temperature.

The square root dependence of the optical absorption coefficient on photon energy in Fig. 1 suggests that non-direct transitions are responsible for the absorption edge in the range  $\alpha \sim 10^3$  to  $10^5 \text{ cm}^{-1}$ , in common with many amorphous materials (23). The slopes of these curves ( $B^{1/2}$ ) gave values for  $B$  in the range  $5 \times 10^6$  to  $2 \times 10^7 \text{ cm}^{-1}\text{eV}^{-1}$  which are appreciably higher than values commonly encountered in amorphous materials (23) and show that the absorption edges are fairly sharp in the measured range.

The most striking feature of this amorphous system is the surprisingly large value of the band gap over the whole compositional range (Fig. 7). The crystalline counterparts, where they exist, all have much smaller or negligible band gaps. Sb, for example, in the crystalline form is a semimetal but exhibits semiconducting properties in the amorphous form (24)(25) (the optical gap is unspecified). The band gap in Te more than doubles from 0.33 eV to 0.73 eV on transforming to the amorphous phase (26)(27). As mentioned above, for c- $\text{Sb}_2\text{Te}_3$   $E_g$  is  $< 0.2 \text{ eV}$  and probably is  $\sim 0.03 \text{ eV}$ , whereas, from Fig. 6,  $E_g$  is  $\sim 0.7 \text{ eV}$  for the amorphous phase. Considerable changes in short-range order (SRO), as well as the disruption of long range order, would be expected to occur in the crystalline-amorphous transformation in order to account

for these large shifts in band gap. Electron diffraction studies by Andrievskii et al. (2) have shown that the SRO in c- and a-Sb<sub>2</sub>Te<sub>3</sub> do not correspond and further that the first coordination sphere in a-Sb<sub>2</sub>Te<sub>3</sub> is at 2.78 Å compared with the shortest Sb-Te bond distance of 3.07 Å in c-Sb<sub>2</sub>Te<sub>3</sub>, indicating that the bonding is stronger in the amorphous form.

The optical band gap appears to hover around the value for amorphous Te (~ 0.7 eV) from 80 at % Te (films of higher Te concentration were crystalline) down to ~ 35 at% Te, where each Sb atom must have at least one Sb nearest neighbor. The band gaps then decrease rapidly down to 0.3 eV at ~ 11 at% Te, (films of lower Te concentration were crystalline).

In contrast, the thermal activation energies varied little over most of the amorphous composition range (with the exception of sample L4 which, although amorphous, exhibited semimetallic properties). These are the values extrapolated to 0°K. Applying an approximate correction to these values for the changing gap with temperature (Fig. 2) would suggest that, irrespective of composition, the Fermi-level is fixed at ~ 0.2 eV from the valence band edge (the Seebeck coefficients are positive) at room-temperature. The marked dip in Seebeck coefficient for compositions between 60 and 70 at% Te (Fig. 6) cannot, therefore, be due to a shift in Fermi-level. Values of the Seebeck coefficient, calculated on the basis of a one-carrier system, were at least a factor of two higher than the experimental values. This suggests that both electrons and holes are contributing to the Seebeck coefficient and that, in the range 60 to 70 at% Te, the electron contribution increases (perhaps due to a mobility increase) although the Fermi-level remains approximately fixed.

From the magnitudes of  $\sigma_0$ , listed in Table 1, conduction appears to take place in extended states for composition up to ~ 50 at % Te



and by hopping in localized states at the band edges (23) beyond this composition. However, the intercepts,  $\sigma_0 \exp (\gamma/k)$ , of the  $\ln \sigma$  vs  $1/T$  curves in Fig. 5 were all  $\sim 10^4 \text{ ohm}^{-1}\text{cm}^{-1}$ . Values for  $\sigma_0$  were obtained from these intercepts by estimating  $\gamma$  from Fig. 4. These values are not highly reliable because the temperature variation ( $\beta$ ) of the optical energy gap was generally found to be non-linear. Values of  $\gamma \sim \beta/2$  were determined from the slopes of the curves in Fig. 4 over the temperature range  $200^\circ\text{K}$  to  $300^\circ\text{K}$ , i.e., the range in which straight lines were obtained in the  $\ln \sigma$  vs  $1/T$  curves.

The general downward curvature of the  $\ln \sigma$  vs  $1/T$  curves at low temperature is contrary to normal behavior but could be explained by a shift of the Fermi-level towards the center of the gap as the temperature is lowered (the distribution of states in the gap is unknown). It cannot be explained by the non-linear temperature dependence of the gap (c.f. Fig. 4) which would give rise to a slight upward curvature, as verified by a theoretical fit to the data.

An estimate of the relative positions of the molecular state energies of Sb and Te can be made from  $\epsilon_2$  spectra and atomic ionization energies (28). This suggests that the antibonding ( $\sigma^*$ ) states of Te-Te bonds and of Sb-Sb bonds have roughly the same energy. Thus, the conduction band energy would be expected to change very little on alloying Sb with Te. The lone-pair p-states in Te should be located well above the bonding ( $\sigma$ ) states of Sb-Sb bonds and therefore should predominate in the formation of the valence band from pure Te to quite high concentrations of Sb in the  $\text{Sb}_{1-x}\text{Te}_x$  system. This scheme would account for the rather compositionally independent optical band gap. At higher concentrations of Sb appreciable numbers of Sb-Sb bonds are formed until eventually the band gap approached that of (amorphous) Sb. The lone-pair band in the  $\text{Sb}_{1-x}\text{Se}_x$  system appears to play a similar role as a function of composition (29).

The  $\text{Sb}_2\text{Te}_3$  crystalline structure is built-up of multiple five-fold atomic layers (30):  $\text{Te}^{(1)} - \text{Sb} - \text{Te}^{(2)} - \text{Sb} - \text{Te}^{(1)}$ . Each  $\text{Te}^{(1)}$  atom has three Sb neighbors in the same multiple layer and three next-nearest  $\text{Te}^{(1)}$  neighbors in the adjacent layer. In their bonding scheme for the  $\text{C}_{33}$ -type structures, Mooser and Pearson (31) conclude that some covalent bonding exists between two adjacent  $\text{Te}^{(1)}$  sheets.\* This model was rejected by Drabble and Goodman (30) for  $\text{Bi}_2\text{Te}_3$  on the basis that the presence of these resonating bonds (required to satisfy the coordination) would produce an empty orbital in the valence shell of some atoms (because of the electron promotion necessary to give rise to the resonance) and would thus lead to metallic-like behavior, whereas  $\text{Bi}_2\text{Te}_3$  is a semiconductor. This argument is not applicable to  $\text{Sb}_2\text{Te}_3$  which does show a metallic-like behavior. As an alternative, Drabble and Goodman proposed that the Te and Bi atoms form hybrid  $\text{sp}^3\text{d}^2$  orbitals in which the s and p-electrons of  $\text{Te}^{(2)}$  and the s electrons of Bi become unpaired and occupy free d-orbitals. The p-electrons in  $\text{Te}^{(1)}$  atoms are used only in bonding to the three nearest-neighbor Bi atoms, i.e., the bonding between  $\text{Te}^{(1)}$  atoms of adjacent layers is solely of the van der Waal type.

We suggest that some resonant covalent bonding between  $\text{Te}^{(1)}$  layers does exist in c- $\text{Sb}_2\text{Te}_3$  because of its semimetallic character. However, in the crystalline to amorphous transformation  $\text{Te}^{(1)}$  interlayer resonant bonding would be absent which could now give rise to semi-conducting characteristics and, with the decrease in nearest-neighbor distance (2), an appreciable band gap.

\* The distance between  $\text{Te}^{(1)}$  atoms in adjacent layers ( $3.62 \text{ \AA}$  in  $\text{Sb}_2\text{Te}_3$ ) is appreciably less than the sum of the van der Waal radii ( $4.4 \text{ \AA}$ ).



## References

1. C. Wood, R. Mueller and L.R. Gilbert, J. Non-Cryst. Solids (to be published).
2. A.I. Andrievskii, I.D. Nabitovich and Ya. V. Voloshchuk, Sov. Phys, Cryst. 7 (1963) 704.
3. R.F. Porter and C.W. Spencer, J. Chem. Phys. 32 (1960) 943.
4. V.S. Ban and B.E. Knox, J. Chem. Phys. 52 (1970) 248.
5. A. Brown and B. Lewis, J. Phys. Chem. Solids 23 (1962) 1597.
6. R. Mueller and C. Wood, J. Non-Cryst. Solids 7 (1972) 301.
7. N.S. Rajagopalan and S.K. Ghosh, Physica 29 (1963) 234.
8. V.D. Deokar and A. Goswami, Indian J. Pure Appl. Phys. 4 (1966) 288.
9. R. Sehr and L.R. Testardi, J. Phys. Chem. Solids 23 (1962) 1219.
10. E. Burstein, Phys. Rev. 93 (1954) 632.
11. I.A. Smirhov, A.A. Andreev and V. Kutasov, Soviet Phys. - Solid State 10 (1968) 1403.
12. T.C. Harman, B. Paris, S.E. Miller and H.L. Goering, J. Phys. Chem. Solids, 2 (1957) 181.
13. J. Black, E.M. Cornwell, L. Seigle, and C.W. Spencer, J. Phys. Chem. Solids, 2 (1957) 240.
14. B. Ronnlund, O. Beckman and H. Levy, J. Phys. Chem. Solids 26 (1965) 1281.
15. C. Wood, L.R. Gilbert, R. Mueller and C.M. Garner, J. Vacuum Sci. Tech. 10 (1973) 739.
16. G.A. Kurov and Z.G. Pinsker, Sov. Phys. Cryst. 1 (1956) 320.
17. L.S. Palatnik and V.M. Kosevich, Sov. Phys. Cryst. 3 (1959) 716; 4 (1960) 37.
18. S.C. Moss and J.P. deNeufville, Mat. Res. Bull. 7 (1972) 423.
19. C.H. Champness and R.H. Hoffmann, J. Non-Cryst. Solids 4 (1970) 138.

20. R. Messier and R. Roy, Mat. Res. Bull. 6 (1971) 749.
21. R. Pinto, J. Non-Cryst. Solids 6 (1971) 187.
22. R.T. Johnson and R.K Quinn, J. Appl. Phys. 43 (1972) 3875.
23. E.A. Davis and N.F. Mott, Electronic Processes in Non-Crystalline Materials (Clarendon, Oxford, 1971).
24. J. Cohen, J. Appl. Phys. 25 (1954) 798.
25. E. Mooser and W.B. Pearson, Progress in Semiconductors 5 (1960) 103.
26. H. Keller and J. Stuke, Phys. Status Solidi 8 (1965) 831.
27. J. Stuke, German Physical Society Meeting, Munich, 1969.
28. M. Kastner, Phys. Rev. Lett. 28 (1972) 355.
29. R. Mueller, J.C. Shaffer and C. Wood, Phys. Stat. Sol. (in print).
30. J.R. Drabble and C.H.L. Goodman, J. Phys. Chem. Solids 5 (1958) 142.
31. E. Mooser and W.B. Pearson, J. Phys. Chem. Solids 7 (1958) 65.

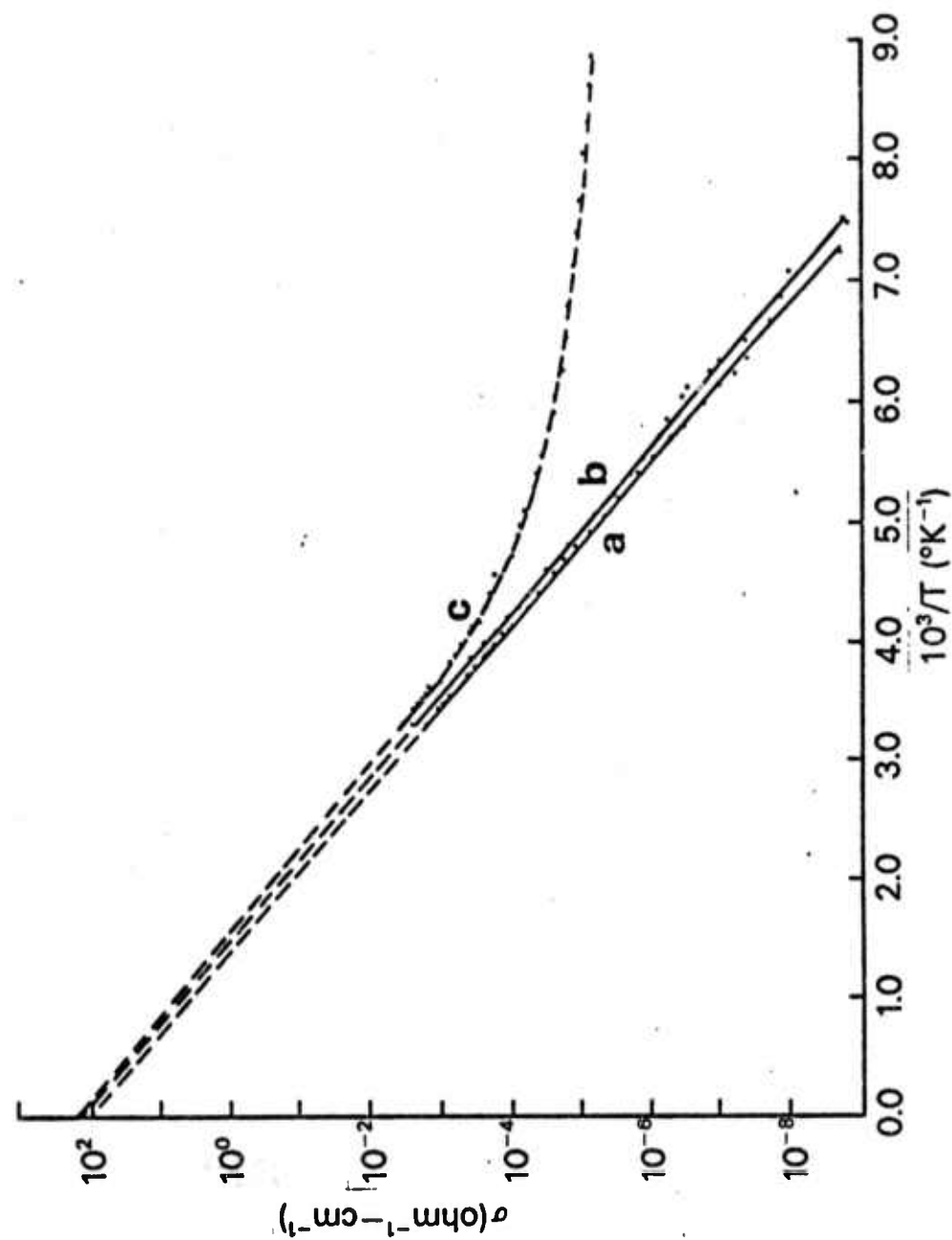
Table 1

Optical and Electrical Parameters of  $\alpha\text{-Sb}_{1-x}\text{Te}_x$   
Films as a Function of Composition

Film #	At % Te	Thickness $\text{\AA}$	$E_g$ (eV)	$B$ ( $\text{cm}^{-1}\text{ev}^{-1}$ ) $\times 10^6$	$\Delta E_o$ (eV)	$\sigma_o$ $\text{ohm}^{-1}\text{cm}^{-1}$	Seebeck Coefficient ( $\mu\text{v}/^\circ\text{C}$ )
L1	11.0	1510	0.30	7.9			
L3	13.5	1590	0.44	7.4			
L4	15.5	1600			semi- metallic		+ 12.
L6	20.5	1540			0.26	$4.7 \times 10^3$	+290.
L7	24.0	1490	0.48	6.2			
L9	33.0	1390	0.54	6.7			
U4	46.5	480			0.35	$1.1 \times 10^3$	+330.
U5	48.0	490	0.75	11.1			
U10	56.5	510			0.33	$3.3 \times 10^1$	+340.
U11	58.0	520	0.74	18.6			
U12	60.0	530			0.30	$8.9 \times 10^1$	+310.
U14	63.5	530			0.31	$1.5 \times 10^1$	+100.
U15	65.0	540	0.73	17.9			
U16	67.0	550			semi- metallic		+ 98.
U19	71.5	550	0.67	10.0			
U26	80.0	520			0.28	$2.6 \times 10^1$	+290.
U27	80.5	510	0.76	12.5			

### Figure Captions

1. Effect of annealing at room-temperature on the electrical conductivity of film U-26.
  - a - measured 2½ days after evaporation
  - b - measured 5 days after evaporation
  - c - measured 6 days after evaporation
2. Crystallization temperature versus film composition.
3. Square-root dependence of absorption coefficient ( $\alpha$ ) on photon energy ( $h\nu$ ).
4. Variation of optical bandgap ( $E_g$ ) with temperature (T). U15 and U27 - sapphire substrates; U11 and L9 - fused quartz substrates.
5. Log electrical conductivity ( $\sigma$ ) versus reciprocal of absolute temperature (T).
6. Room-temperature Seebeck coefficient versus film composition.
7. Optical activation energy at room-temperature (X), optical activation energy extrapolated to 0°K(0), and thermal activation energy ( $\Delta$ ) extrapolated to 0°K versus film composition.



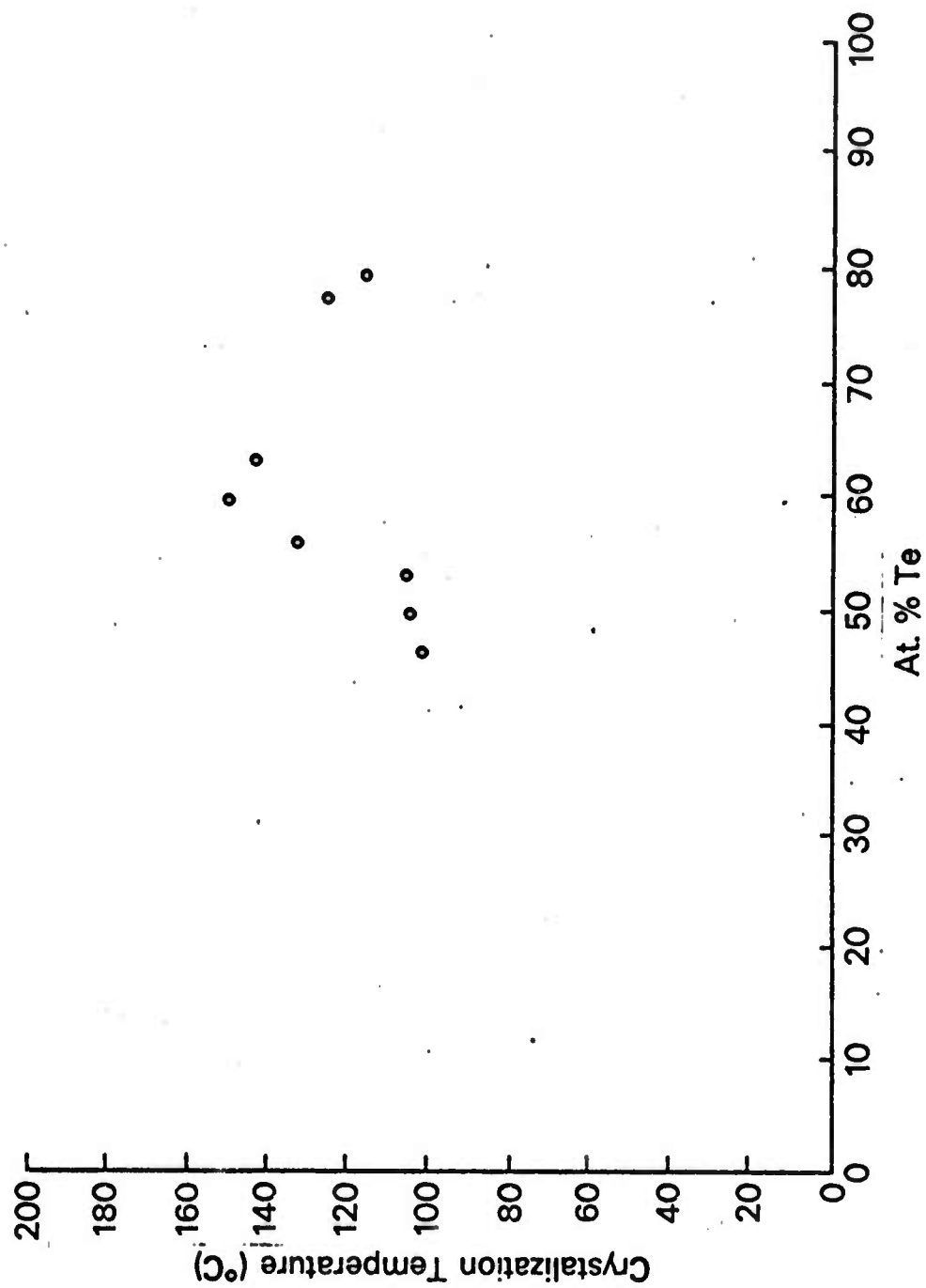


Fig. 2. Garner et al.

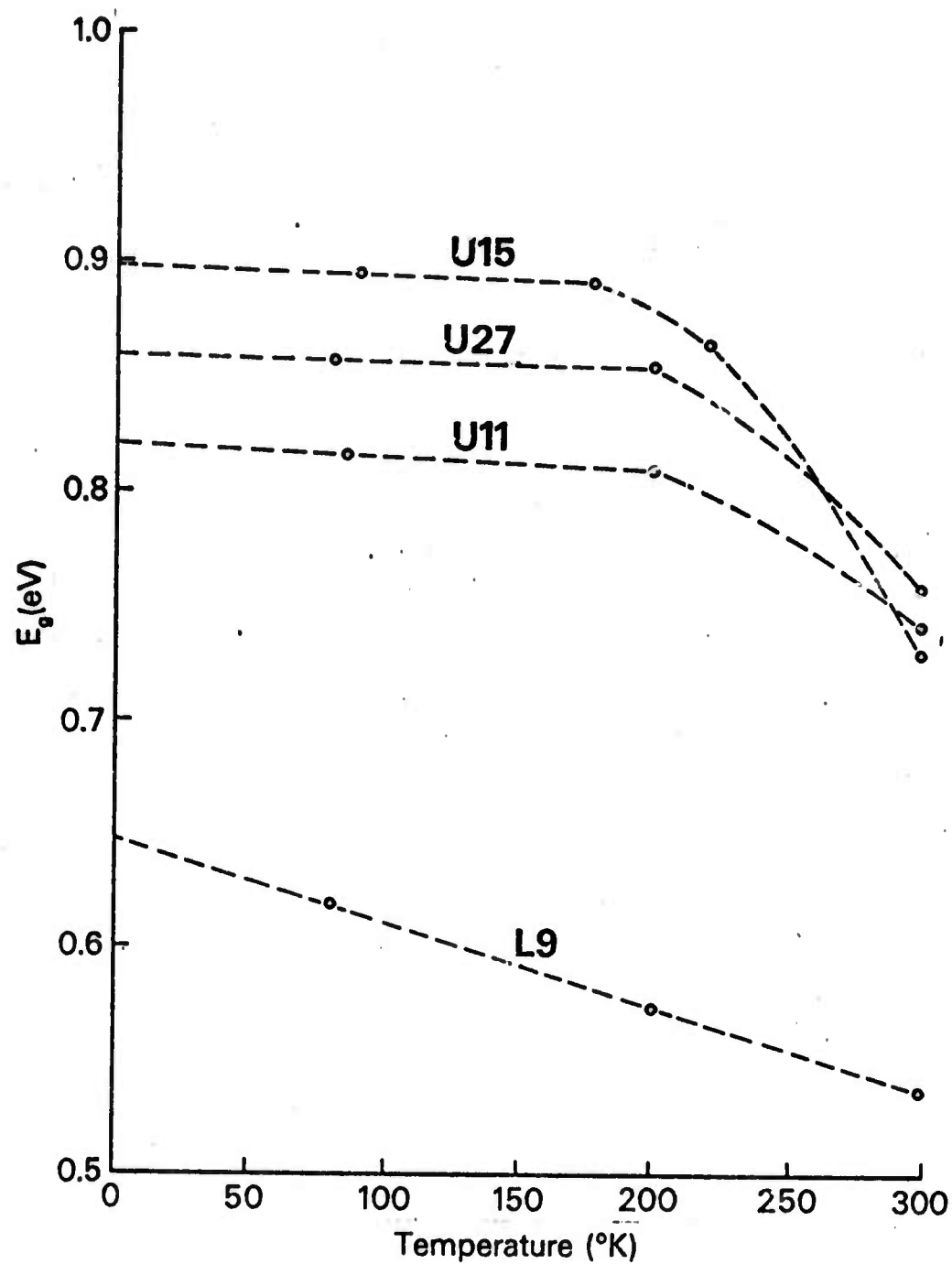


Fig. 4. Garner et al.

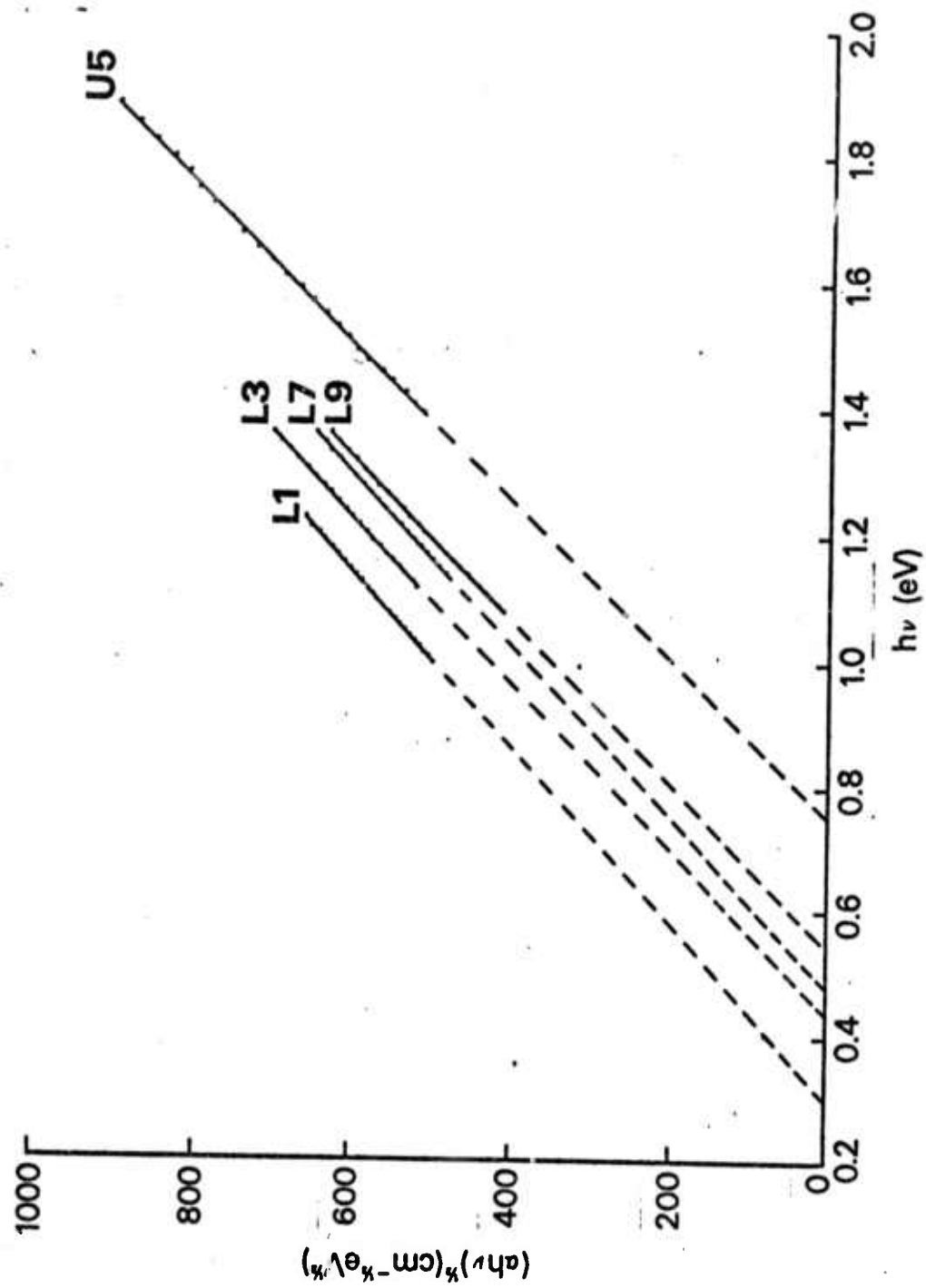


Fig. 3 Carrier study



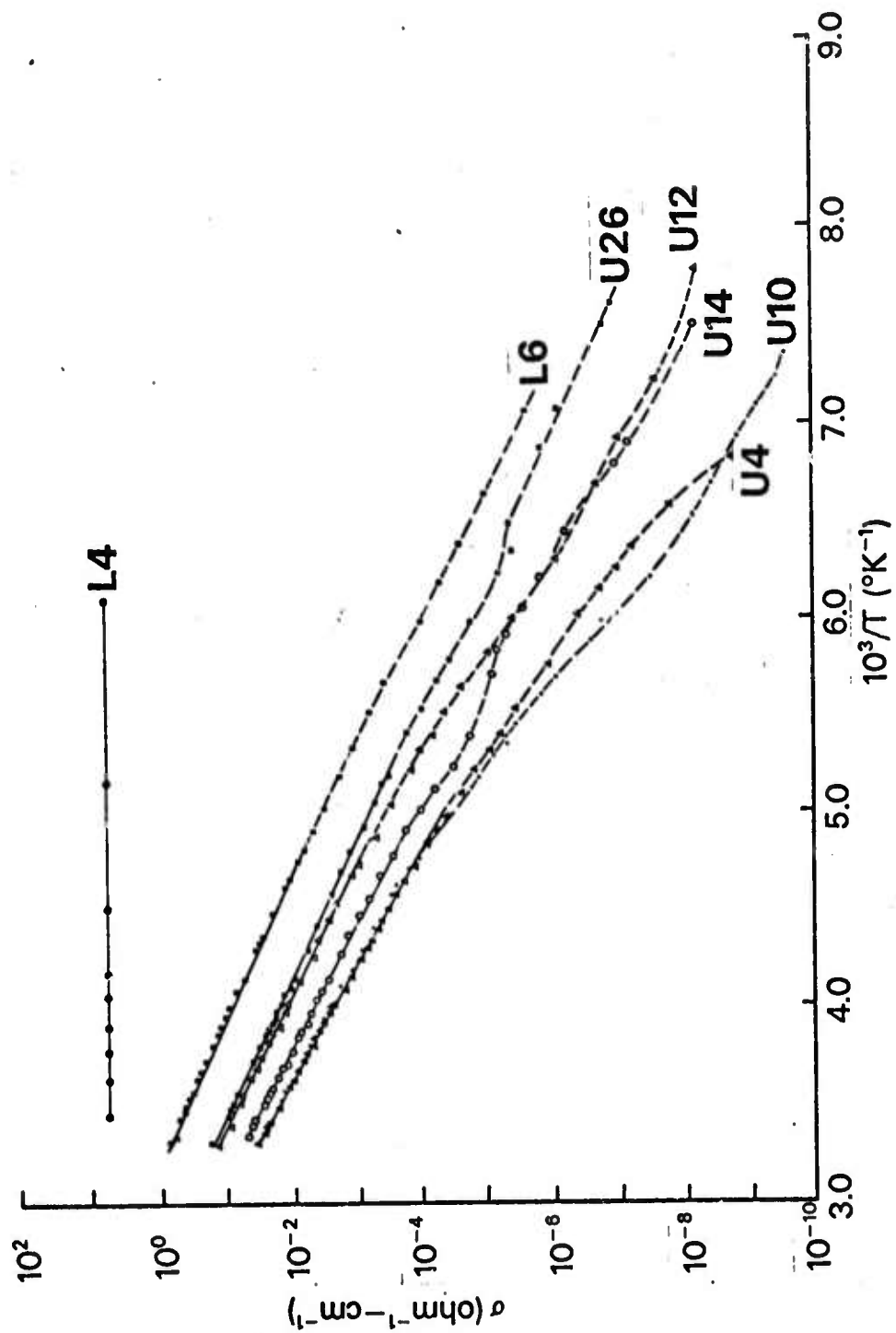


Fig. 5. Conductivity vs.  $1/T$ .

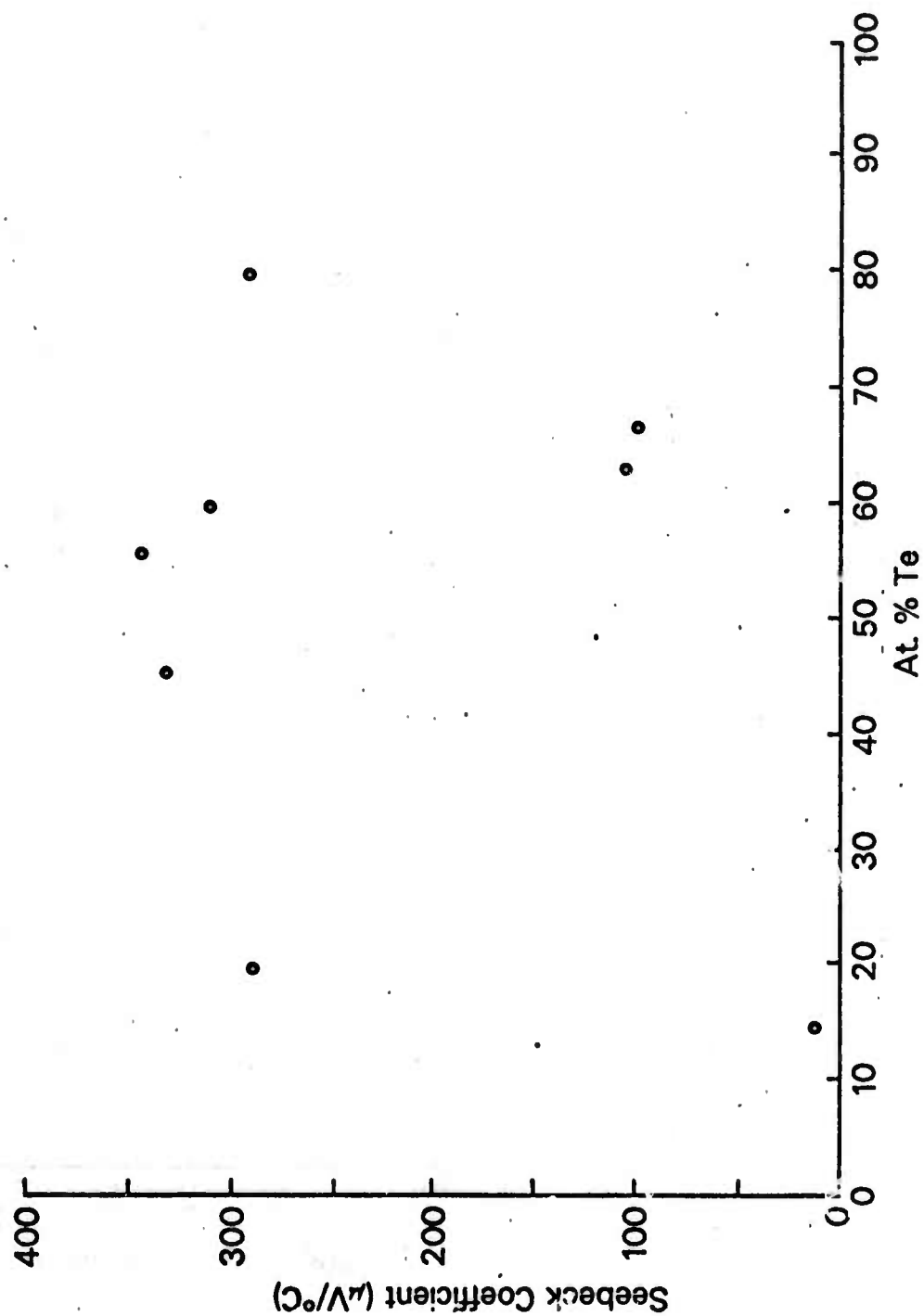


Fig. - Garnet et al

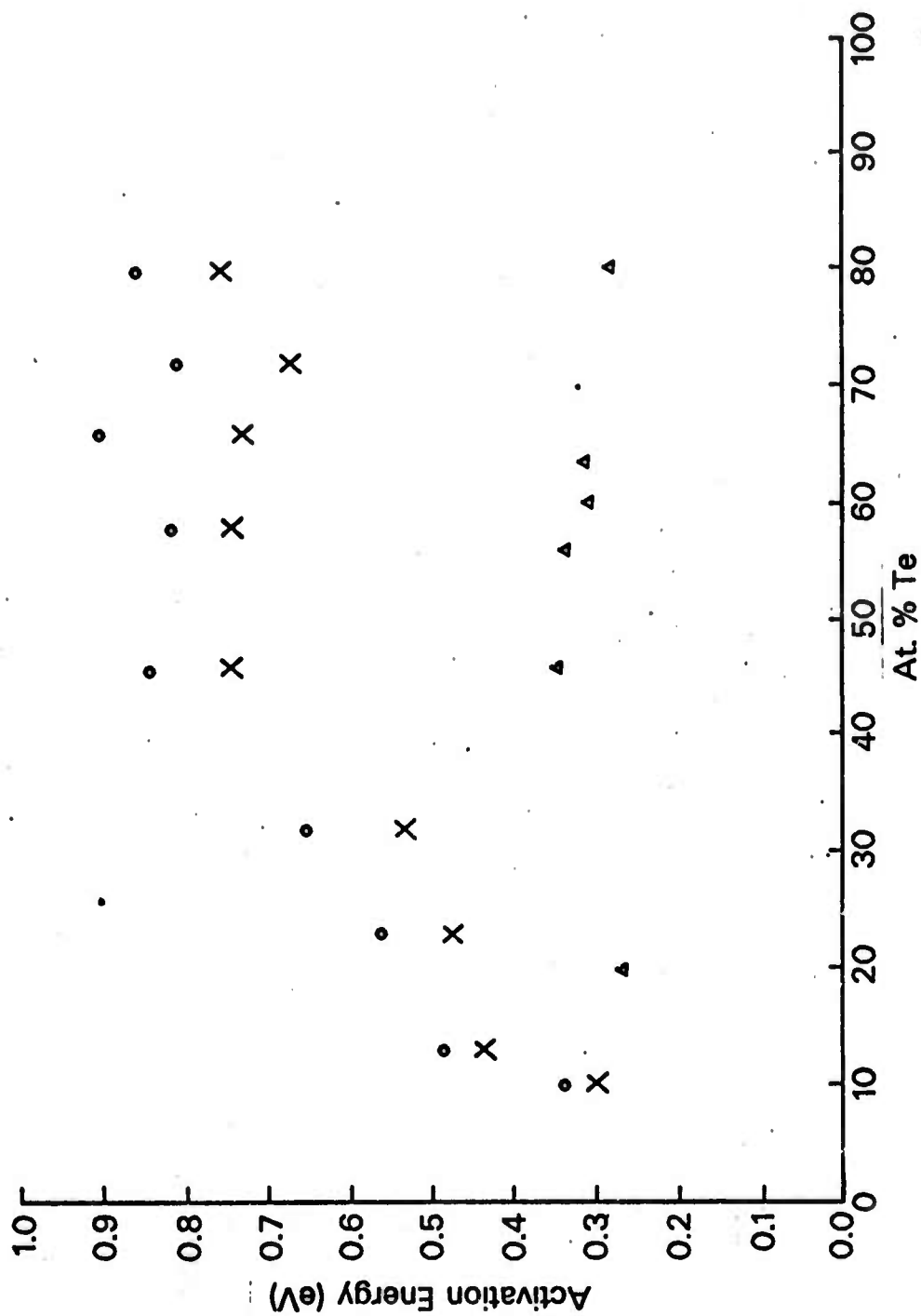


Fig. 7 Continued

# Amorphous Thin Films\*

C. Wood, L. R. Gilbert, R. Mueller, and C. M. Garner

Physics Department, Northern Illinois University, DeKalb, Illinois 60115

(Received 1 May 1973)

The optical and transport properties of the binary amorphous systems Sb-Se, Ge-Se, and Ge-Te, have been investigated as a function of composition. Essentially the whole amorphous phase of each system was prepared in a single evaporation by an elongated substrate coevaporation technique. The optical band gap varied fairly smoothly between the values for amorphous end components. Most films exhibited  $\ln \sigma$  vs  $T^{-1}$  relationships. Except for the Sb-Se system, the  $\sigma_a$  values lay in the hopping conductivity range. Those Ge chalcogenide films showing  $\ln \sigma$  vs  $T^{-1/4}$  hopping conductivity behavior generally converted to a  $T^{-1}$  variation after annealing. The thermal activation energies and thermocouple measurements showed the Fermi levels to be fixed well away from the band edges in the forbidden gap. Delocalization of states in the gap of a-Ge with increasing chalcogen content was not observed. The results have been interpreted in terms of chemical bonding.

## INTRODUCTION

One of the main purposes of this study was to determine the influence of chemical bonding on the properties of amorphous solids. To this end, we have selected several binary systems on the basis of the molecular ionization energies of the end components and attempted to trace development of these energies across the whole phase diagram.

Since the preparation of a whole amorphous binary system can be quite laborious, we have developed a vacuum coevaporation technique whereby the complete compositional range can be prepared in one evaporation. The method is particularly suited to the preparation of amorphous materials where the systems are not governed by equilibrium phase diagram considerations. It is possible, therefore, to examine a continuous change in physical properties over a wide compositional range. We have applied this method to an investigation of the amorphous systems Sb-Se, Ge-Se, and Ge-Te.

## MATERIALS PREPARATION

A brief description of the evaporation system follows. A more detailed description has been reported elsewhere.<sup>1</sup> Basically, the apparatus consisted of a Varian oil-pumped bell-jar system with two widely spaced Arco Temescal 270° electron beam (EB) guns, each gun being controlled by modified Sloan Omni HA quartz-crystal-oscillator evaporation-rate controllers. An elongated substrate holder of length equal to the spacing between the EB guns, i.e., nearly the width of an 18-in. bell jar, and capable of being maintained at any temperature between room and liquid N<sub>2</sub> temperature, was situated above and in line with the EB guns. A series (~30) of fused quartz substrates, in which each alternate substrate was electrodeposited, was held in juxtaposition in the holder. Thus each substrate received a different ratio of the two elements because of differing proximity to the two EB guns (the exact ratio being controlled by the settings of the evaporation rate controllers), i.e., compositions over a wide range were prepared simultaneously.

Our present system incorporated two such holders

situated at different heights above the crucibles. Hence, for a given ratio of evaporation rates from the two EB guns, a broad sampling of compositions in thick films was obtained in the lower rack and a smaller compositional gradient about a preselected composition was obtained in thin films from the upper rack.

In this experiment the evaporations were carried out in a pressure of  $< 10^{-7}$  mm Hg, or lower, at extremely low evaporation rates ( $< 1$  to  $2 \text{ \AA/sec}$ ). The substrates were held at room temperature throughout the evaporation. The compositions of selected films were determined by electron microprobe analysis and, from the geometry of the system and the measured evaporation rates, the composition was calculated<sup>1</sup> as a function of position in the holder.

## OPTICAL MEASUREMENTS

In order to survey the optical properties of the films as a function of composition, every alternate substrate in the sequence in the holder could be selected for measurement. Because of the compositional variation across the substrate, only a 3-mm-wide strip of the center section, perpendicular to the composition gradient, was measured.

A Cary 14 R spectrophotometer with a Strong<sup>2</sup> reflectance attachment was used to make optical transmittance  $T$  and reflectance  $R$  measurements. From these measurements, the refractive and the absorption indices and the absorption constant were calculated by a method reported in Ref. 1.

The absorption edges were found to obey the relation for nondirect transitions<sup>3,4</sup>:

$$\alpha h\nu = B(h\nu - E_g)^2, \quad (1)$$

showing conservation of energy but not crystal momentum. The intercepts of the  $(\alpha h\nu)^{1/2}$  vs  $h\nu$  curves extrapolated to  $\alpha=0$  were taken as the values of the optical energy gap  $E_g$ .

## CONDUCTIVITY MEASUREMENTS

Alternating in the holder with the substrates for optical measurements were substrates which were

electroded for conductivity measurements. The electrodes consisted of four strips of haked-on liquid-bright platinum, so that four-probe measurements could be made. Measurements were made between room and liquid  $N_2$  temperature.

Thermal activation energies were determined from a least-squares fit to the equation

$$\sigma = \sigma_0 \exp(-\Delta E/kT), \quad (2)$$

For conduction in extended states,  $\Delta E$  represents the energy difference between the Fermi energy  $E_F$  and the majority carrier band edge (e.g., the valence band  $E_v$ ). If we assume  $\Delta E$  to be a linear function of temperature,

$$\Delta E = \Delta E_0 - \gamma T, \quad (3)$$

then the activation energy obtained from the plots of Eq. (2) is the extrapolated value ( $\Delta E_0$ ) to  $T = 0$  K and not the actual values of  $\Delta E$  at  $T = 0$  K.<sup>3,4</sup> Generally,  $\sigma_0$  is not strongly temperature dependent compared to the exponential term in Eq. (2) and is expected to lie in the range  $10^2$ – $10^4 \Omega^{-1} \text{ cm}^{-1}$ .

If the charge carriers are excited into localized states at the band edge, then  $\Delta E = E_F - E_{LC} + \Delta W_0$ , where  $\Delta W_0$  is the activation energy for hopping conduction and the localized states occupy the energy range  $E_{LC} - E_v$ .<sup>3</sup> Here  $\sigma_0$  is expected to be  $\sim 10^{-7}$ – $10 \Omega^{-1} \text{ cm}^{-1}$ .

If hopping conduction occurs between localized states near the Fermi energy, then  $\Delta E = \Delta W_2 \sim \frac{1}{2}$  width of the defect band. If hopping is between nearest neighbors, Eq. (2) is followed with  $\sigma_0 \lesssim 10^{-2} \Omega^{-1} \text{ cm}^{-1}$ . If variable range hopping occurs, the conductivity variation has the form<sup>4</sup>

$$\ln \sigma = A' - B'/T^{1/2}, \quad (4)$$

### THERMOELECTRIC MEASUREMENTS

The Seebeck coefficient  $S$  at room temperature was measured on a number of the films used for resistivity measurements.

For a one-carrier nondegenerate system in which a mean free path  $L$  can be defined,

$$S = A \left( \frac{k(\Delta E)}{e(kT + 1)} \right), \quad (5)$$

where  $\Delta E = E_F - E_v$  is the energy difference between the Fermi energy and the band edge in which conduction is taking place, i.e., conduction or valence band. As mentioned above,  $\Delta E$  is temperature dependent; c.f. Eq. (3). The constant  $A$  may take on various values depending on the energy dependence of the charge-carrier relaxation time, e.g.,  $A = 2$  for acoustical-mode lattice scattering.<sup>6</sup> If a mean free path cannot be defined, i.e.,  $L$  is less than the lattice spacing, and the energy dependence of the density of states is assumed to be linear, then  $A = (1 + \text{terms of order } T)$ .

For a two-carrier system, the individual contributions of electrons  $e$  and holes  $h$  to the Seebeck coefficient are

subtractive<sup>7</sup>:

$$S = \frac{\sigma_e S_e + \sigma_h S_h}{\sigma_e + \sigma_h}, \quad (6)$$

### Sb-Se SYSTEM

Although both elements can be prepared in the amorphous form, amorphous Sb is stable only at low temperatures for thick films ( $\sim$ mirrors) or for very thin films ( $\sim 10^2 \text{ \AA}$ ) at room temperature.<sup>8,9</sup> X-ray diffraction measurements showed that all except the extremely Sb-rich ( $>85 \text{ at.}\%$ ) films were amorphous in the present experiment.

Attention has been drawn to the importance of annealing or depositing amorphous films near the crystallization temperature  $T_c$  to obtain reliable optical and conductivity data.<sup>10–12</sup> Sb-Se films cannot be annealed much above room temperature because of the tendency to crystallize or phase segregate.<sup>13</sup> Amorphous Sb films of thickness  $>10^2 \text{ \AA}$ , crystallize well below room temperature and amorphous Se crystallizes at  $\sim 100^\circ \text{C}$ . The highest  $T_c$  reported for this system was  $170^\circ \text{C}$  at the composition  $\text{Sb}_2\text{Se}_3$ .<sup>14</sup> Because of the slow deposition rates ( $\sim 2 \text{ \AA/sec}$ ), the high vacuum ( $\sim 10^{-7}$  mm Hg), and the proximity of the substrate temperature during deposition to  $T_c$ , it was thought unlikely that further annealing would produce changes in film structure.

Absorption coefficients  $\alpha$  ranged from  $10^3$  to  $10^5 \text{ cm}^{-1}$  for the particular experimental conditions (film thickness, spectrometer sensitivity, etc.) and fitted well to an  $(\alpha h\nu)^{1/2}$  vs  $h\nu$  relationship for nondirect transitions. An exponential tail was not observed or expected for these high absorption constants. The slope ( $B'$ ) of the curves showed a steady increase with increasing Se content.

It was found that all but the extremely Sb-rich films ( $>85 \text{ at.}\%$  Sb) yielded straight lines on the  $\ln \sigma$  vs  $1/T$  plot. Values of  $\sigma_0 \exp(\Delta E/kT)$  obtained by extrapolating the curves to  $1/T = 0$  were found to be  $\sim 10^3 \Omega^{-1} \text{ cm}^{-1}$  on the Sb-rich side of  $\text{Sb}_2\text{Se}_3$  and then progressively to decrease with increasing Se content to a minimum of  $\sim 10 \Omega^{-1} \text{ cm}^{-1}$  at  $80 \text{ at.}\%$  Se, and then increase again to  $10^4 \Omega^{-1} \text{ cm}^{-1}$ . Because of their very high resistance ( $>10^6 \Omega$ ), the extreme Se-rich films were measured using a sandwich electrode structure. The extreme Sb-rich films were crystalline and showed metallic conductivity. The low temperature region of the  $\ln \sigma$  vs  $1/T$  plot for a film lying just on the amorphous side of the phase boundary showed some curvature which could be fitted to the form of Eq. (4).

All Seebeck coefficient values for samples with up to  $55 \text{ at.}\%$  Se were positive (Fig. 4) showing the majority carriers to be holes. Beyond this composition, the resistances were too high to allow measurement. Values for  $\Delta E_0$  obtained from Eq. (5) for any reasonable assumed value for  $A$  and  $\gamma$  could not be reconciled with the  $\Delta E_0$  values obtained from  $\ln \sigma$  vs  $1/T$  curves. We were, therefore, forced to conclude that Eq. (6) is

applicable, i.e., the Fermi level is fixed near the middle of the energy gap and that both holes and electrons are contributing to the Seebeck coefficient.

The optical gap  $E_g$  at room temperature and the thermal activation energy  $\Delta E_a$  at absolute zero temperature is shown in Fig. 1 as a function of composition.

### Ge-Se SYSTEM

Both elements Ge and Se can be prepared in thick amorphous thin film form by deposition onto room-temperature substrates. Consequently, the complete system was found to be amorphous by x-ray diffraction.

Data is available in the literature<sup>17,18</sup> on annealing, and glass and crystallization temperatures for limited ranges of compositions of melt quenched glasses have been reported. These values are not directly translatable to thin films<sup>19</sup> and significant differences have been observed even for various methods of thin film preparation, for example, whether sputtered or evaporated,<sup>17,19</sup> and for different degrees of high vacuum.<sup>20</sup> Therefore, it was found necessary to anneal our films in small progressive steps in temperature.

The optical absorption coefficients, which again ranged between  $10^3$  and  $10^5$  cm<sup>-1</sup>, fitted well to the  $(\alpha h\nu)^{1/2}$  vs  $h\nu$  relationship both before and after annealing. However, the slopes ( $B$ ) slightly decreased and the intercepts ( $E_g$ ) slightly increased on annealing, with most marked changes occurring around the compositions GeSe and GeSe<sub>2</sub>.

Most films obeyed a  $\ln \sigma$  vs  $1/T$  dependence and, for these, annealing also increased the thermal activation energies  $\Delta E_a$ ; but, in addition, it converted a number of Ge-rich films (> 32 at.% Se) obeying a  $\ln \sigma$  vs  $T^{-1}$  hopping conductivity-type relationship, over at least part of the temperature range, to a  $\ln \sigma$  vs  $1/T$  dependence.

It was found that  $\sigma_a$  ranged between  $10^{-4}$  and  $1 \Omega^{-1}$  cm<sup>-1</sup> for the as-deposited films, for compositions between 0 and 50 at.% Se, with a sharp minimum occurring near GeSe<sub>2</sub> of  $\sim 10^{-6} \Omega^{-1}$  cm<sup>-1</sup>, and then increased again beyond this point.  $\gamma$  was determined from the temperature variation of the optical gap. Annealing increased the values of  $\sigma_a$  by less than a factor of 5 in the range 0-50 at.% Se. Films beyond 50 at.% Se have not been annealed, to date.

Thermocent measurements at room temperature showed the Seebeck coefficient to be  $n$  type for the Ge-rich compositions to 45 at.% Se, the limit of our measurements, and to increase monotonically with Se content (Fig. 4).

Again, we have plotted the optical ( $E_g$ ) and thermal ( $\Delta E_a$ ) activation energies as a function of composition in Fig. 2. Here, we also show the effects of annealing.

### Ge-Te SYSTEM

Since Te is normally crystalline as deposited at room temperature, only films up to the composition 90 at.%

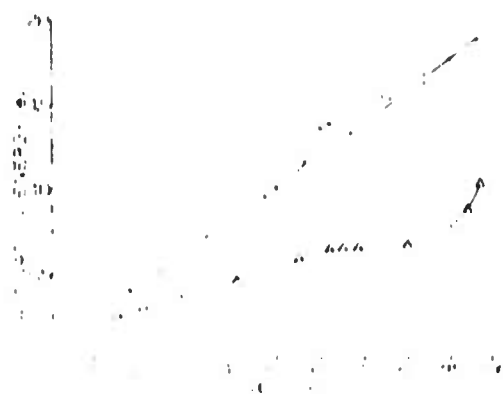


FIGURE 1. Ge-Se System. Optical and thermal activation energy vs composition.  $\bullet$ ,  $E_g$  (as deposited);  $\Delta$ ,  $\Delta E_a$  (as deposited).

Te were found to be amorphous by x-ray diffraction. Although we used published data on annealing<sup>17</sup> as a guide, we found that our samples crystallized well below the temperatures listed. Therefore, we had to resort to annealing in stages.

Some prior work on sputtered films of this system was reported by Rockstad and de Nerville.<sup>21</sup> Our results are in substantial agreement with theirs if we compare our as-deposited films with their annealed ones; even though our optical band gap is defined differently and most of our conductivity-temperature dependences fitted a straight-line  $\ln \sigma$  vs  $T^{-1}$  behavior over the whole temperature range down to liquid N<sub>2</sub> temperatures. An important exception is that, as with Ge-Se, a number of the Ge-rich films exhibited a  $\ln \sigma$  vs  $T^{-1}$  behavior before annealing, and a  $\ln \sigma$  vs  $T^{-1}$  relationship afterwards.

The optical absorption edges fitted the  $(\alpha h\nu)^{1/2}$  vs  $h\nu$  relationship quite well in the range  $\alpha > 10^3$  cm<sup>-1</sup>. Generally, annealing slightly increased the value of  $E_g$  above the as-deposited values; the slope ( $B$ ) was significantly changed only in the vicinity of GeTe<sub>2</sub>, where it was lowered.

In contrast to the behavior of the optical gap  $E_g$ , and to the behavior of the thermal activation energy  $\Delta E_a$  in the Ge-Se system,  $\Delta E_a$  in this system decreased on annealing.

In the as-deposited films, a large scatter in  $\sigma_a$  values was obtained, generally ranging between 1 and  $10^5 \Omega^{-1}$  cm<sup>-1</sup>, with a maximum at GeTe<sub>2</sub> and a marked minimum of  $10^{-4} \Omega^{-1}$  cm<sup>-1</sup> in the range 70-80 at.% Te. Again  $\gamma$  was obtained from the temperature dependence of the optical gap. After annealing, the  $\sigma_a$  values decreased by a factor of between 2 and 10, except for the range 70-80 at.% Te, where the values increased to the same order as the other films.

The room-temperature Seebeck coefficient was  $n$  type in the Ge-rich end of the system up to 36 at.% Te and  $p$  type beyond this composition (Fig. 4).

Figure 3 shows a plot of  $E_g$  at room temperature and  $\Delta E_a$ , both as a function of composition and annealing.

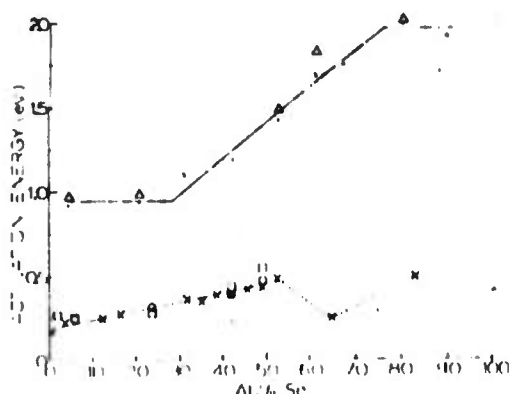


FIGURE 2. Ge-Se system. Optical and thermal activation energy vs composition: ●,  $E_g$  (as deposited); △,  $E_g$  (first anneal); ×,  $\Delta E_a$  (as deposited); ○,  $\Delta E_a$  (first anneal); □,  $\Delta E_a$  (second anneal). The first annealing temperature was 200 °C for samples containing less than 55 at.% Se and 160 °C for samples greater than 55 at.% Se. The second annealing temperature was 50° higher.

## DISCUSSION

For all three systems, the optical energy gaps vary fairly smoothly with composition from values corresponding to the band gaps of the amorphous end components. In the Ge-Se and Ge-Te systems, the gaps remain fairly constant over quite a large composition range near the end components. As the concentration of Ge decreases, the forbidden gap remains constant until 70 at.% Ge, where Se-Se or Te-Te bonds are formed. At the extreme Ge-rich ends of the Ge-Se and Ge-Te systems the Fermi levels are located  $\sim 0.2$  eV from the conduction band edge. This value is close to the impurity activation energy of Se and Te in crystalline Ge<sup>22</sup> and is at least suggestive that the localized states fixing the position of the Fermi level are due to the addition of these atoms. The correspondence between the Fermi-level position with respect to the conduction band in Ge-Se and Ge-Te is quite close in both systems until compositions GeSe and GeTe are reached. With further increase of chalcogen concentration, the optical band gap, however, decreases for Ge-Te while it increases for Ge-Se. At approximately 40 at.% Te, the Fermi level for Ge-Te is located near the center of the gap. For this reason, the sign of the thermopower changes beyond this composition. There is no doubt that we are dealing with a two-carrier system and that the marked deviation between the Seebeck coefficient values beyond  $\sim 45$  at.% chalcogen (Fig. 4) is due to the more rapid movement of the valence band away from the conduction band in Ge-Se than in Ge-Te.

The Sb-Se system shows a more linear change in optical and thermal band gap than the Ge-Se and Ge-Te systems. Also, the Fermi level appears to be closer to the middle of the gap over the whole composition range than in the Ge chalcogenides.

Over the entire Ge-Se and Ge-Te systems, the magnitude of  $\sigma_a$  observed both before and after annealing indicated that conductivity was either by hopping at the band edges or by Brownian-type motion.<sup>23</sup>

$\sigma_a$  values for the Sb-Se system, based on the value of  $\gamma$  at Sb<sub>2</sub>Se<sub>3</sub>, indicate this type of conductivity from 60 to 80 at.% Se, and conduction in extended states outside this composition range.

Since the conductivity obeys a  $\ln \sigma$  vs  $T^{-1}$  behavior for many films over quite a wide temperature range, the Fermi level must be fixed in the gap although generally, not in the center of the gap. We presume this is due to a high density of localized states in the region of the Fermi level.

In those films which could not be fitted to  $\ln \sigma$  vs  $T^{-1}$  because of the possibility of several conduction mechanism obeying different temperature dependences, the interpretation of the conductivity was not unambiguous.

Presumably, Sb or Ge, when added to Se or Te, act as a branching or cross-linking agent between the linear polymer chains with Sb in threefold, Ge in fourfold and Se or Te in two-fold coordination. Radial distribution studies by Betts *et al.*,<sup>24</sup> on the Ge-Te system and by Fawcett *et al.*,<sup>25</sup> on the Ge-Se system suggest that a random covalent model applies over the whole composition range, i.e., that Ge is tetrahedrally coordinated and that the chalcogen is twofold coordinated, but not exclusively to unlike atoms as in a chain crossing model. However, at low concentrations of Ge in Se, both models seemed applicable.

A completely ordered system can exist at the compositions Sb<sub>2</sub>Se<sub>3</sub>, GeSe<sub>2</sub>, and GeTe<sub>2</sub>, where bonding is completely between dissimilar atoms, which could account for slight  $E_g$  maxima at these compositions.<sup>21</sup> However, this necessitates the introduction of an amorphous cluster model<sup>26</sup> to account for the amorphous structure. On each side of these compositions, anion-anion or cation-cation bonds will be formed causing the value of  $E_g$  to progressively change with composition. Similarly, ordering into a threefold coordination at amorphous GeTe has been suggested<sup>27</sup> to account for thermodynamic properties which could be related to the minimum we observe in  $\Delta E_a$ . The rather flat varia-

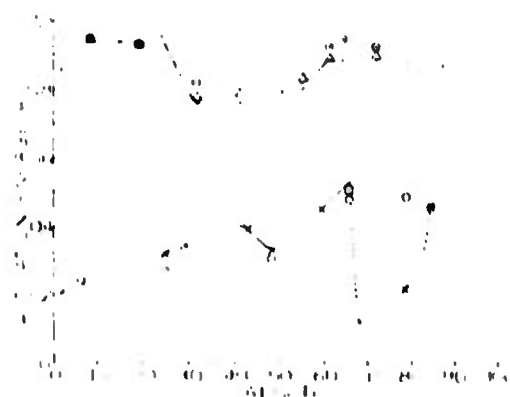


FIGURE 3. Ge-Te system. Optical and thermal activation energy vs composition: ●,  $E_g$  (as deposited); △,  $E_g$  (first anneal); ○,  $E_g$  (second anneal); ×,  $\Delta E_a$  (as deposited); ○,  $\Delta E_a$  (first anneal); □,  $\Delta E_a$  (second anneal). The first annealing temperature decreases linearly from 200 °C at 0 at.% Te to 140 °C at 50 at.% Te. For samples greater than 50 at.% Te, the first annealing temperature was 100 °C. The second annealing temperature was approximately 50° higher over the entire range.





FIGURE 1. Room Temperature thermoelectricity vs composition for the Sb-Se, Ge-Se, Ge-Te systems: (O) Sb-Se, ( $\Delta$ ) Ge-Se, ( $\square$ ) Ge-Te.

tion of  $E_g$  with composition at each end of the Ge-Te and Ge-Se systems could be associated with phase separation of amorphous phases<sup>11</sup> although, in this case, we would have expected a marked change in the variations of  $E_g$  with composition on annealing. The electrical properties vary less smoothly with composition, probably as a result of a strong compositional and structural dependence.

Following the work of Mosser and Pearson,<sup>22</sup> Kastner,<sup>23</sup> Zallen *et al.*,<sup>24</sup> and Shaffer *et al.*,<sup>25</sup> we present the following hypothesis to explain the compositional dependence of the electronic structure of these systems.

At the extreme chalcogen-rich end of the systems, we would expect the valence band to principally arise from the lone-pair  $p$  band, and the conduction band principally from the  $\sigma^*$  antibonding band of the chalcogen. Similarly, at the extreme Si or Ge end of the range, we would expect the valence band to principally arise from the  $\sigma$  bonding band, and the conduction band from the  $\sigma^*$  antibonding band. (In the case of Si, the overlap of the  $5d$  level with the energy gap has been proposed to account for its semimetallic nature.<sup>26</sup>) From the relative energy positions of the molecular states of Sb, Ge, Se, and Te, we would expect at the intermediate range of compositions that the valence band arises principally from the lone-pair  $p$  band of the chalcogen, and the conduction band from resonating Si-Se  $p$  bands or  $sp^3$  hybridized Ge-Se or Ge-Te bands.

Heavy emphasis was placed in this work on the preparation and measurement of the Ge-rich compositions in the expectation that a delocalization of lone-pair  $p$  states could be observed.<sup>27</sup> However, none was observed from either the optical or transport data. Perhaps a too-simple-minded view of the translation of the

relative energy positions of molecular states into a solid has been taken and that the lone-pair states do not fall within the forbidden gap of Ge. Alternatively, one can argue that the introduction of levels within the band is not sufficient by itself, but that the occupancy, i.e., Fermi-level position with regard to the levels, is equally important.<sup>28</sup> Further work is planned to elucidate these points.

\*This work was supported by the Advanced Research Projects Agency of the Department of Defense and was monitored by the Army Research Office under Contract No. DA-ARO(D-1) 124-72 G115.

<sup>1</sup>C. Wood, R. Mueller, and L. R. Gilbert, in *J. Non-Cryst. Solids*, (to be published).

<sup>2</sup>J. Strong, *Procedures in Experimental Physics* (Prentice-Hall, Englewood Cliffs, N.J., 1958), p. 376.

<sup>3</sup>E. Davis and N. F. Mott, *Electronic Processes in Non-Crystalline Materials* (Clarendon, Oxford, 1971).

<sup>4</sup>J. Van, *Optical Properties of Solids*, edited by F. Abeles (North-Holland, Amsterdam, 1970).

<sup>5</sup>H. Fritzsch, *J. Non-Cryst. Solids* **6**, 49 (1971).

<sup>6</sup>A. F. Joffe, *Semiconductor Thermoelements* (Infosearch, London, 1957).

<sup>7</sup>V. A. Johnson, *Prog. Semicond.* **1**, 82 (1956).

<sup>8</sup>I. S. Patainsk and V. M. Kosevich, *Sov. Phys.-Crystallogr.* **3**, 716 (1958).

<sup>9</sup>J. Cohen, *J. Appl. Phys.* **25**, 798 (1954).

<sup>10</sup>W. E. Spicer, T. M. Donovan, and J. F. Fisher, *J. Non-Cryst. Solids* **10**, 122 (1972).

<sup>11</sup>M. L. Thye, *Mater. Res. Bull.* **6**, 103 (1971).

<sup>12</sup>P. A. Walley and A. K. Jonscher, *Thin Solid Films* **1**, 367 (1967); *Thin Solid Films* **2**, 327 (1968).

<sup>13</sup>M. H. Myers and J. S. Berkes, *J. Non-Cryst. Solids* **8-10**, 804 (1972).

<sup>14</sup>L. R. Gilbert and C. Wood, *Bull. Am. Phys. Soc.* **16**, 500 (1971).

<sup>15</sup>A. Feltz, H. J. Bannier, F. J. Lippmann, and W. Muhl, *J. Non-Cryst. Solids* **8-10**, 64 (1972).

<sup>16</sup>D. B. Dove, J. Chang, and B. Molnar, *J. Non-Cryst. Solids* **8-10**, 376 (1972).

<sup>17</sup>S. K. Dahl and K. L. Chapin, *J. Appl. Phys.* **41**, 2196 (1970).

<sup>18</sup>R. Messier and R. Roy, *Mater. Res. Bull.* **6**, 749 (1971).

<sup>19</sup>W. F. Howard and R. Tsu, *Phys. Rev. B* **1**, 4709 (1970).

<sup>20</sup>J. M. Donovan and M. L. Knotek, *Bull. Am. Phys. Soc.* **18**, 453 (1973).

<sup>21</sup>H. K. Rockstad and J. P. de Neufville, 11th Int. Conf. on Phys. Semicond., Warsaw, Poland, 1972.

<sup>22</sup>E. H. Putley, *Phys. Status Solidi* **6**, 571 (1964).

<sup>23</sup>M. H. Cohen, *J. Non-Cryst. Solids* **4**, 391 (1970).

<sup>24</sup>E. Belis, A. Diencinck, and C. W. Bates, *J. Non-Cryst. Solids* **8-10**, 364 (1972).

<sup>25</sup>R. W. Fawcett, C. N. J. Wagner, and C. S. Cargill, *J. Non-Cryst. Solids* **8-10**, 369 (1972).

<sup>26</sup>D. Turnbull and D. E. Polk, *J. Non-Cryst. Solids* **8-10**, 19 (1972).

<sup>27</sup>Third Semi-Annual Technical Report Contract No. DAH015-70 C D187, Advanced Research Projects Agency, Washington, D. C., 1972.

<sup>28</sup>E. Mosser and W. B. Pearson, *Prog. Semicond.* **5**, 103 (1960).

<sup>29</sup>M. Kastner, *Phys. Rev. Lett.* **28**, 355 (1972).

<sup>30</sup>R. E. Drews, R. L. Emerald, M. L. Slatle, and R. Zallen, *Solid State Comm.* **16**, 293 (1972).

<sup>31</sup>J. C. Shaffer, B. Van Pelt, C. Wood, J. Freehuff, K. Murase, and J. W. Osmun, *Phys. Status Solidi* **54**, 511 (1972).

<sup>32</sup>D. Adler (private communication).



## A Zone Refiner for Crystal Growth\*

C. WOOD, B. VAN PELT, AND E. HYLAND

*Department of Physics, Northern Illinois University, DeKalb, Illinois 60115*

(Received 20 January 1972)

A horizontal zone refiner has been developed for crystal growth of group V-VI compounds. Tin-oxide coated fused quartz tubes were used as transparent heating elements.

It is fairly common practice to utilize a horizontal zone refiner to grow single crystals.<sup>1</sup> Not only can the shape of the freezing interface be conveniently viewed (almost an essential for good crystal growth), but also there is the additional convenience that some purification can be effected before the attempt is made to grow a crystal. It may be added that superior zone purification is effected if the conditions encourage good crystal growth since it is well known that impurities tend to segregate at grain boundaries.

If the material has a high vapor pressure at the melting point or is a compound with a tendency to dissociate at the melting point, then it becomes necessary to control the temperature of the whole environment of the material in order to suppress evaporation or dissociation. Evaporation or dissociation still occurs, but a dynamic equilibrium is set up between the melt and walls of the vessel enclosing the ingot. In the case of dissociation of a compound, the element having the highest vapor pressure tends to evaporate preferentially. The walls of the enclosure are thus maintained at a temperature which corresponds to a higher vapor pressure for the free element than the pressure of that element above the compound at its melting point. This furnace enclosure also acts as an afterheater, which greatly assists in the growth of single crystals, but often obstructs clear viewing of the freezing interface.

We have been growing single crystals of antimony chalcogenides, e.g.,  $\text{Sb}_2\text{S}_3$ ,  $\text{Sb}_2\text{Se}_3$ ,  $\text{Sb}_2\text{Te}_3$ , which tend to dissociate on melting (melting points in the range 600–700°C) and have devised a system which overcomes the difficulty of viewing. A schematic diagram is shown in

Fig. 1. The temperature of the hot zone is sensed by a Chromel-Alumel thermocouple junction positioned in the center of the zone and suspended inside the inner furnace tube. The arms of the thermocouple extend from opposite ends of the furnace tube and are supported by a frame attached to the traveling zone carriage. The thermocouple controls the power supplied to the furnaces, which are wired in series, through a Leeds and Northrup Speedomax W Azar recorder. The compounds are sealed off inside an evacuated fused quartz capsule which is placed inside the furnace tube.

The central feature of the apparatus is a tin-oxide conductive coating on the exterior of fused quartz tubing.<sup>2</sup> This has been utilized to provide both the stationary furnace tube enclosing the whole ingot and the shorter traveling heater which supplies the additional heat necessary for the molten zone. The tin-oxide coating can be made thick (~30–170  $\Omega/\text{square}$ ) while still remaining very transparent (the growth interface can be clearly seen through both tubes) and can be operated continuously at temperatures up to 700°C without deterioration.

Silver paste supplied by Engelhard Industries, Inc. painted in strips around the tube and fired on at ~600°C provides a suitable electrical contact to the tin-oxide. It is essential not to contact the tin-oxide directly since hot spots are formed which craze the oxide coating. Stainless steel foil wrapped and bolted around the silver paste contact or stainless steel U-shaped bars (preferably gold coated) in which the tube can be nestled are satisfactory.

The main difficulty experienced in the development of this apparatus was nonuniformity of the tin-oxide coating. For good crystal growth it is essential that the temperature conditions do not vary at different parts of the tube, which implies uniformity of conductive coating. A coated tube supplied by Corning Glass Works, although remarkably uniform considering it was hand coated, was inadequate for our purposes. Since better uniformity of coating was not available, we therefore set up a spray coating system (using the formula described in Ref. 2) on a traveling lathe. The problem of maintaining the tube surface at ~520°C during spraying was overcome by inserting a Nichrome wound furnace tube inside the fused quartz tube to be coated and relying mainly upon radiant heat to maintain the surface temperature. Best results were obtained with freshly mixed solutions of tin-chloride.

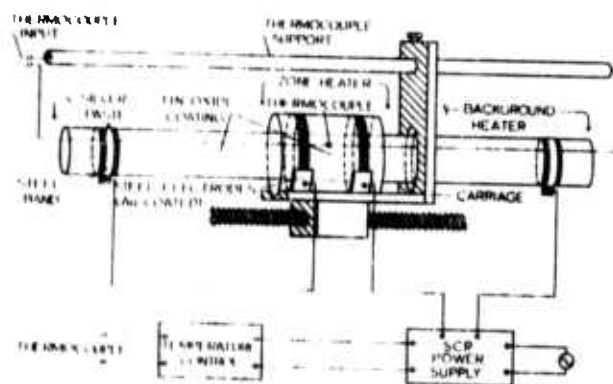
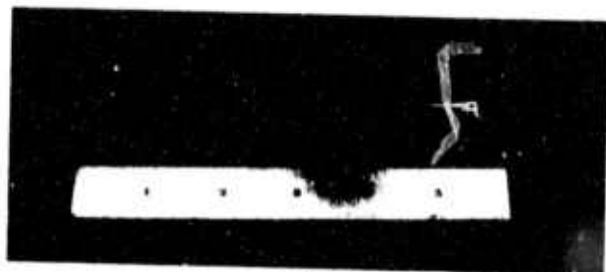


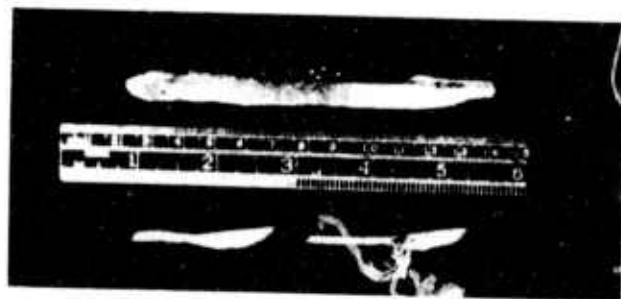
FIG. 1. Horizontal zone refiner.



(a)



(b)



(c)

FIG. 2. (a)  $\text{Sb}_2\text{Se}_3$  single crystal. Freezing occurred from the right. (b) Same  $\text{Sb}_2\text{Se}_3$  ingot cleaved. Large cleavage face (010) uppermost. (c) Cleaved  $\text{Sb}_2\text{Te}_3$  ingot (above ruler) with large cleavage face toward ruler and cleaved  $\text{Sb}$  ingot (below ruler).

As is well known, the ideal shape of a freezing front is slightly concave, i.e., the molten zone forms the shape of a slightly concave lens, so that the first part of the front to freeze does so on the crystal nuclei and not on foreign nuclei on the walls of the tube. This condition is easily achieved by lowering the heat input to the molten zone and thus increasing the relative contribution of the thermal conduction along the bar to the heat losses. Too small a heat input will cause the axis along the center of the molten zone to freeze across completely while the edges still remain molten. Too large a heat input will give rise to a convex shape.

Examples of some of the crystals grown in this type of apparatus are shown in Fig. 2. The shape of the freezing front used on a single crystal of  $\text{Sb}_2\text{Se}_3$  can be seen in Fig. 2(a). The ingot was not uniform in cross section and shows the freezing front shape in a height step.

The tin oxide coating is quite versatile as a heating element and specially shaped heating zones can easily be fabricated by painting the electrodes to the desired configuration. Also, it is comparatively simple to construct a heater with multiple heating zones for rapid zone refining by painting many electrodes on a tin-oxide coated tube and shorting out alternate coatings.

The authors are indebted to B. Hanson for assistance with temperature control and construction of an electrical power supply for the tin-oxide tubes.

\* Research supported by the Advanced Research Projects Agency of the Department of Defense and monitored by the Army Research Office, Durham, under Contract No. DA-ARO-D-31-124-71-G132.

<sup>1</sup> G. Pfann, *Zone Melting* (Wiley, New York, 1959), p. 153.

<sup>2</sup> Proceedings of the Eleventh Symposium on the Art of Glassblowing, American Scientific Glassblowers Society, 1966, p. 128.

# MÖSSBAUER STUDIES OF AMORPHOUS AND CRYSTALLINE ANTIMONY SELENIDES

S. L. RUBY \*

Argonne National Laboratory, Argonne, Illinois 60439, USA

L. R. GILBERT and C. WOOD \*\*

Northern Illinois University, DeKalb, Illinois 60115, USA

Received 2 November 1971

Amorphous films of  $\text{SbSe}_x$ , with  $0.5 < x < 9$ , were studied with the Mössbauer effect. The spectra are all similar to each other but different from that of crystalline  $\text{Sb}_2\text{Se}_3$ . Despite the poor resolution, it is clear that the material condensed from vapor is not micro-crystalline.

Amorphous films of  $\text{SbSe}_x$ , with  $0.5 < x < 9$  and tens to microns thick, were prepared by vacuum evaporation onto quartz substrates at room temperature and were studied by use of Mössbauer resonance spectra taken at 4°K. Films of various composition were obtained by partial evaporation of large quenched ingots having different Se/Sb ratios. The compositions of the films were determined by electron microprobe and or X-ray emission spectroscopy. The Se/Sb ratios of ingot and film frequently were found to be quite different; e.g., an  $\text{Sb}_2\text{Se}_3$  source ( $x = 1.5$ ) produced a film with  $x = 9$ . The crystalline  $\text{Sb}_2\text{Se}_3$  measured for comparison was in the form of a powdered sample of a single crystal.

The  $\text{Sb}_2\text{Se}_3$  crystal is orthorhombic  $\text{Pbnm}(\text{D}_{2h}^{16})$  consisting of infinite chains parallel to the  $c$  axis. In each unit cell are two equally populated types of Sb sites and three types of Se sites. The strongest bonds are within the chains, where the Sb-Se bond distances range from 2.576 to 2.777 Å, while the separations of "non-bonded" Sb-Se pairs range from 2.98 to 3.74 Å [1]. Two computer fits to the experimental Mössbauer spectrum of a powdered sample of crystalline  $\text{Sb}_2\text{Se}_3$  are shown in fig.1. The solid line in the upper plot is the unsuccessful fit obtained when a single Sb lattice site was assumed; in the lower plot the computer was allowed two different but equally populated Sb sites. The

goodness-of-fit criterion  $\chi^2$  shrinks from 7.3 in the upper fit to 1.2 in the lower. In this Mössbauer spectrum, the isomer shifts for the two sites (which measure the over-all electronic charge density at the nucleus) were -4.2 and -7.1 mm/s relative to  $\text{InSb}$ .

The spectra of amorphous films in the composition range  $0.5 < x < 9$  were obtained at 4°K with a  $\text{CaSnO}_3(\text{Sb})$  source in a conventional Mössbauer spectrometer. As seen from the typical spectrum shown in fig.2 and from the results in table 1, the spectra for all compositions of amorphous  $\text{SbSe}_x$  consisted of a single peak at a position intermediate between the double peaks of the crystalline  $\text{Sb}_2\text{Se}_3$ . For a single antimony site and a pure quadrupole inter-

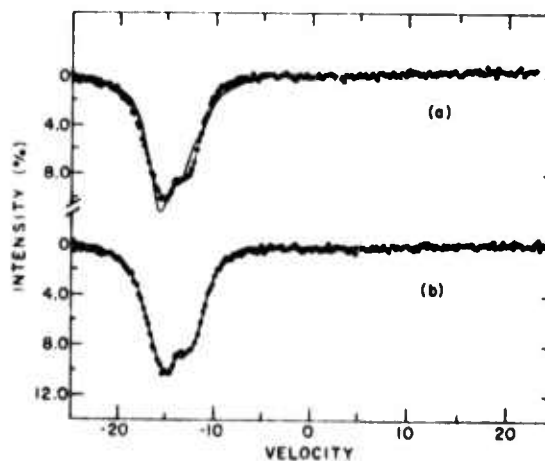


Fig.1. Dual fittings to the spectrum from crystalline  $\text{Sb}_2\text{Se}_3$ . (a) Corresponds to a single site of Sb, while (b) corresponds to two-equally populated sites.

\* Work performed under the auspices of the U.S. Atomic Energy Commission.

\*\* This research was supported by the Advanced Research Projects Agency of the Department of Defense and was monitored by the Army Research Office, Durham, under Contract no. D-ARO-D-31-124-71-G132.

Table 1  
Quadrupole splittings  $e^2qQ$  and isomer shifts  $S$  of  
amorphous and crystalline samples of  $SbSe_x$ .

Composition $x = Se/Sb$	$e^2qQ$ (mm/s)	$S^a$ (mm/s)
0.3	9.6	-14.0
1.1	9.7	-14.4
2.0	10.8	-13.4
1.5	10.9	-13.6
0.5	11.5	-13.0
1.5 (Crystalline)	7.9	-12.6
	8.4	-15.5

a) As measured relative to a  $CaSnO_3$  source. Relative to  $InSb$ , add 8.1 mm/sec.

action, the Mössbauer spectrum of  $^{121}Sb$  (in which the transition is between nuclear levels with spins  $\frac{1}{2}$  and  $\frac{3}{2}$ ) is an asymmetric octet; but in the present case the individual lines cannot be resolved because the quadrupole splitting is not large enough in comparison with the natural line width (2.1 mm/s).

The data for the amorphous films could be moderately well fitted ( $\chi^2 < 3$ ) by assuming a single site for which each member of the octet has a normal width ( $\Gamma = 2.8$  mm/s), the quadrupole shift  $e^2qQ = 10.5 \pm 1$  mm/s and the isomer shift  $S = -5.1 \pm 0.5$  mm/s. Giving the computer more freedom by allowing additional sites could further decrease  $\chi^2$ , but the values of  $e^2qQ$  and  $S$  for the individual sites would still fall within the ranges given above. (For comparison,  $S = -6.0, 0$  and  $12.3$  mm/s for  $SbF_3$ ,  $InSb$  and the  $(SbF_6)^-$  ion, respectively; and  $e^2qQ = 18.7$  and  $0$  for  $Sb_2O_3$  and  $InSb$ , respectively [2].) The simplest interpretation is that in all these amorphous  $SbSe_x$  films, regardless of their composition, the nearest-neighbor environment is quite uniform. However, we do not understand why the Mössbauer spectra should be so similar for such a wide range of compositions over which considerable changes should occur in the Sb environment.

Taken together, the spectra show that the short-range order in  $SbSe_x$  differs from that in the crystalline solid and indicates that the environments of the antimony sites in the amorphous solid are quite homogeneous, i.e., they are characterized by a narrow range in coordination number and in bond length. This viewpoint is supported by electron-diffraction studies [3]: intensity and radial-distribution curves indicate that both the coordination number and the nearest-neighbor distance decrease in the transition from the crystalline to the amorphous phase of " $Sb_2Se_3$ ". Because of the method of preparation used, the amorphous phase was probably Se-rich.) In con-

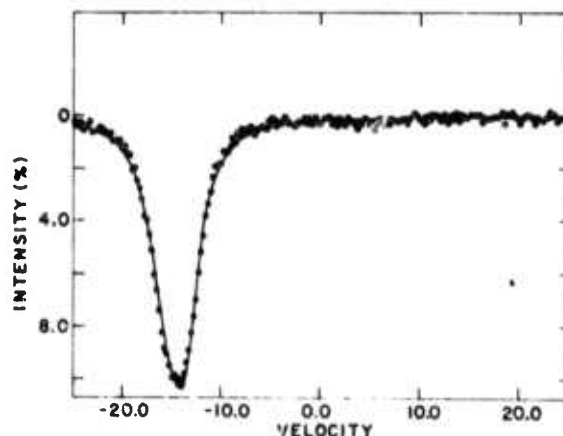


Fig. 2. Spectrum from a  $SbSe_{2.0}$  amorphous film fitted with a single site.

trast,  $As_2S_3$  and  $GaAs$  in the amorphous phase were shown to retain the configuration inherent in the crystalline phase.

Similar results have been obtained for  $Fe(PO_3)_3$  in both the glassy and the crystalline form [4]. Detailed analysis shows that the spectra correspond to two sites for the glassy samples but only one for the crystal. The quadrupole splittings in the glass are 3 and 8 times those in the crystal and the line widths are perhaps 4 times as large. For iron phosphate, therefore, the glass has more sites and more site distortion than the crystal. For  $Sb_2Se_3$ , it is clear that the two sites seen in the crystal are replaced by many in the glass but that the properties of the latter sites are closely similar (little site distortion).

The above results shed significant light on the nature of amorphous or glassy solids. In particular, they are relevant to the controversy on whether a solid condensed from a vapor is truly a glass or consists of microcrystals - especially for  $Sb_2Se_3$  and other materials from which the glass cannot readily be formed by quenching from a melt. The answer appears to be that the solid so formed is not a collection of microcrystals in equilibrium and therefore is presumably a glass.

The authors wish to thank Dr. C. W. Kimball for many helpful discussions.

#### References

- [1] W. W. Tidswell, F. W. Kruse and J. C. McCullough, *Acta Cryst.* 10 (1957) 99.
- [2] S. I. Ruby, *Mössbauer effect methodology* (Plenum Press, New York, 1967) vol. 3, p. 203.
- [3] L. I. Tartarova, *Kristallografiya* 4 (1959) 678.
- [4] C. R. Kurkjian and D. N. E. Buchanan, *Phys. Chem. Glasses* 5 (1964) 63.

# Mössbauer investigation of $\text{Sn}_x(\text{As}_2\text{Se}_3)_{1-x}$ glasses\*

S. P. Taneja, A. E. Dwight, L. Gilbert, W. C. Harper,  
C. W. Kimball & C. Wood

Physics Department, Northern Illinois University, DeKalb, Illinois

Mössbauer measurements on  $^{119}\text{Sn}$  nuclei in  $\text{Sn}_x(\text{As}_2\text{Se}_3)_{1-x}$  ( $x=2.5, 5.0, 8.0$ , and  $10.0$  at%) glasses have been made at 4.2, 77.3, and 298 K. The chemical reactions suggested by Shkolnikov are confirmed. However, contrary to his findings, the present results, combined with those of Borisova et al., show that the chemical kinetics are sensitive to the method of preparation of the glass. Although x-ray measurements indicate that no long-range order exists in the amorphous samples, the Mössbauer results indicate that the local environment about Sn atoms is similar for all compositions; that is, a high degree of local chemical order exists. Moreover, the long-range disorder in the glass affects the isomer shift and quadrupolar coupling at Sn atoms only to second order. The Debye temperature for Sn atoms differs by about 40 K between the crystal ( $\sim 140$  K) and the glass ( $\sim 100$  K).

The ternary systems of amorphous chalcogenide semiconductors have been the subject of intensive investigation in the past.<sup>(1, 2)</sup> This class of materials has recently taken on more significance with the discovery of switching effects and possible device applications.<sup>(3)</sup> The addition of group IV elements to the arsenic chalcogenides has been found to have significant effects on softening temperature, microhardness, and electrical conductivity. These changes in the physical properties have been ascribed to the crosslinking of the chain-like structure by the group IV element.<sup>(1)</sup>

A Mössbauer study of  $^{119}\text{Sn}$  in  $\text{Sn}_x(\text{As}_2\text{Se}_3)_{1-x}$  glasses, where  $x=2.5, 5.0, 8.0$ , and  $10$  at%, has been made at 298, 77.3, and 4.2 K to study further the nature of the glass-crystal transition and the role of the group IV element in a switching glass. The isomer shift, the centroid of the absorption pattern, reflects the electronic structure of the Sn atom and its vibrational energy. The quadrupolar interaction reflects both the electronic structure and the noncubic nature of the environment of the atom. In a disordered system distributions of both isomer shift and quadrupolar coupling should occur and the line breadth and shape should reflect the dispersion of these distributions. The Debye temperature may be obtained by measuring the temperature dependence of the Mössbauer absorption.

\* This research was supported by the Advanced Research Projects Agency of the Department of Defense and was monitored by the Army Research Office, Durham, under Contract No. DA-ARO-D-31-127-71-0132.

## Experimental

The samples were prepared from 99.9999% grade materials. Arsenic and selenium were outgassed by subliming in a vacuum and then sealed in a fused quartz ampoule, in the appropriate ratio, under a pressure of  $\sim 10^{-5}$  mm Hg. The ampoule was placed in a rocking furnace at 630°C for about 12 h and then quenched in a brine solution at about 200 K.

To prepare a single crystal of  $\text{SnSe}_2$ , high purity Sn and outgassed Se were mixed and sealed in an evacuated quartz ampoule; excess Se was used in order to avoid a mixed phase of  $\text{SnSe}$  and  $\text{SnSe}_2$ . The ingot was placed in a three zone furnace and the temperature was slowly raised to 680°C over a period of four days. One of the end zones and the middle zone were cooled at 4 deg. C/h to solidify the ingot from one end. Crystalline  $\text{SnSe}$  was prepared in a similar fashion using equal percentages of Sn and Se.

All samples were tested by x-ray analysis. Debye-Scherrer patterns, using a Cu target, show diffuse bands characteristic of amorphous systems for  $x=2.5, 5.0$ , and  $8.0$ . Similar patterns for the samples containing 10% Sn show the amorphous phase and have, in addition, five lines of a crystalline phase of which four may be indexed as lines of  $\text{SnSe}$  as shown in Table 1. The crystallised specimens containing 10% Sn are found to be predominantly in the  $\text{SnSe}$  phase.

The Mössbauer absorbers were prepared by powdering the amorphous compounds and encapsulating them in a cold-setting plastic. The sample thicknesses were 5–10 mg/cm<sup>2</sup> of natural tin. The Mössbauer source was  $^{119}\text{Sn}$  in  $\text{BaSnO}_3$  at 298 K, and the spectra were recorded with a conventional spectrometer in the constant acceleration mode. All data were fitted by computer to Lorentzian lines using the least squares method.

Table 1. Analysis of x-ray film for the 10% Sn amorphous sample

$t_0$	$d_0$ (Å)	Source for SnSe on ASTM Card
m	2.90	2.98
m	2.86	2.87
w	2.35	2.39
w	1.98	Uncertain, also not seen on SnSe sample
w	1.82	1.84



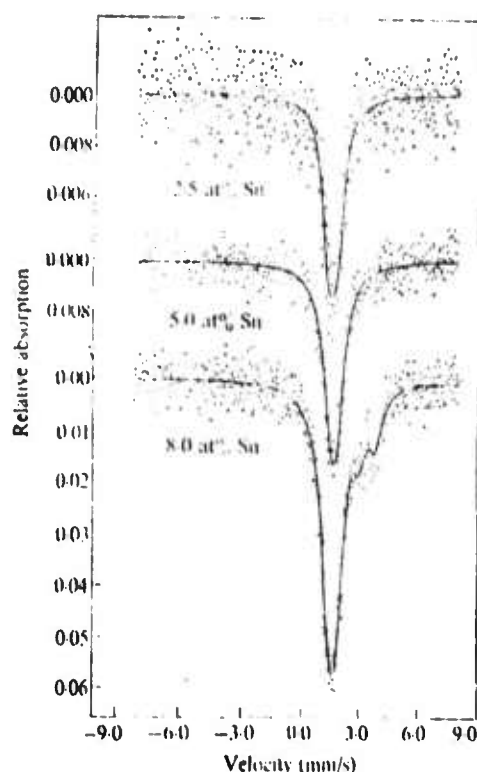
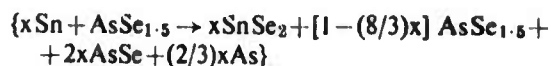


Figure 1. The Mössbauer spectra of amorphous samples at 77.3K. The solid line is a least squares fit to the model described in the text

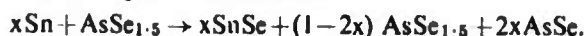
### Results and discussion

The effect of tin on the microhardness and conductivity of semiconducting  $\text{As}_2\text{Se}_3$  glasses has been studied by Shkolnikov.<sup>(4)</sup> The hardness and conductivity change significantly after 5% Sn is added and Shkolnikov suggested that a chemistry in which  $\text{SnSe}_2$  occurs at low tin concentrations and  $\text{SnSe}$  at high concentrations may account for such behaviour. None of his suggested reactions contains any compound of tin with arsenic. Also, he found that air cooled and quenched Sn-As-Se glasses were almost equally amorphous. Borisova *et al.*<sup>(5)</sup> have examined the  $^{119}\text{Sn}$  Mössbauer effect in  $\text{Sn}_x(\text{As}_2\text{Se}_3)_{1-x}$  glasses formed by cooling in air, and concluded that only  $\text{SnIV}$  occurred in the glassy state but that the glass-crystal mixtures exhibited both the  $\text{SnII}$  and  $\text{SnIV}$  absorption lines. The present authors' Mössbauer measurements on Sn-As-Se glasses quenched to low temperature from the melt, show quantitative differences in the chemical kinetics from those observed by Borisova *et al.*

Typical Mössbauer spectra at 77.3K for amorphous samples containing 2.5, 5.0, and 8.0% Sn are shown in Figure 1, and for those containing 10% Sn in Figure 2. Tin occurs in only one phase at concentrations of 2.5 and 5.0%, but a second phase appears in the spectra of the samples containing both 8.0 and 10.0%. Although the limit of solubility of tin in the quenched glassy state has been set by Kolomiets *et al.*<sup>(6)</sup> as about 7%, the second phase does not correspond to either  $\alpha$ - or  $\beta$ -Sn. The reaction chemistry given by Shkolnikov<sup>(4)</sup> for low Sn concentrations is



and for higher concentrations



As the Sn concentration increases, the Sn atom changes its valence from +4 to +2 and the free As combines with Se to give a further increase in the  $\text{AsSe}_{1.5}$  content.

Crystalline  $\text{SnSe}_2$  is trigonal ( $\text{CdI}_2$ -C6 type) and all Sn atoms are in equivalent sites; crystalline  $\text{SnSe}$  is orthorhombic ( $\text{GeS}$ -B16 type) and all Sn atoms are in equivalent sites. A doublet is expected for both  $\text{SnSe}$  and  $\text{SnSe}_2$  and these spectra are shown in Figure 3. The spectra of the amorphous samples containing low concentrations of tin are similar to the spectrum of  $\text{SnSe}_2$ , and at higher concentrations a spectrum characteristic of  $\text{SnSe}$  appears. Slight but significant differences between the patterns for amorphous and crystalline samples are discussed below. The spectra are similar to those of Borisova *et al.*, but the relative quantities of  $\text{SnSe}_2$  and  $\text{SnSe}$  for similar concentrations of tin differ. Apparently the chemical kinetics are dependent on method of sample preparation in contrast with Shkolnikov's findings. The dominant phase in the crystalline samples is  $\text{SnSe}$ , but this phase also appears in the amorphous samples. X-ray analysis shows no crystallinity for the 8% samples quenched to low temperatures but the Mössbauer patterns show the presence of both  $\text{SnSe}$  and  $\text{SnSe}_2$ .

The Mössbauer results are given in Table 2. Within statistical error the quadrupolar coupling and line width ( $\Gamma \sim 0.9$  mm/s) are independent of composition for both  $\text{SnIV}$  and  $\text{SnII}$  sites in the amorphous samples. If the identity of atoms about a given Sn atom were to vary on the basis of random occupation of sites, local

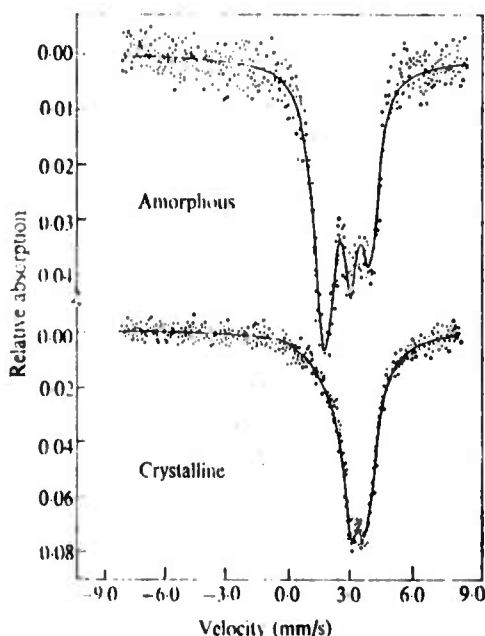


Figure 2. The Mössbauer spectra of amorphous and crystalline samples containing 10% Sn at 77.3K

**Table 2.** Results of the analysis of Mössbauer Spectra of  $\text{Sn}_x(\text{As}_2\text{Se}_3)_{1-x}$ ;  $\delta$  is the isomer shift relative to  $\text{BaSnO}_3$ ,  $\Delta$  is the quadrupole splitting ( $= (1/2)e^2qQ$ ), and the subscripts 1 and 2 denote values corresponding to tin valencies of IV and II, respectively

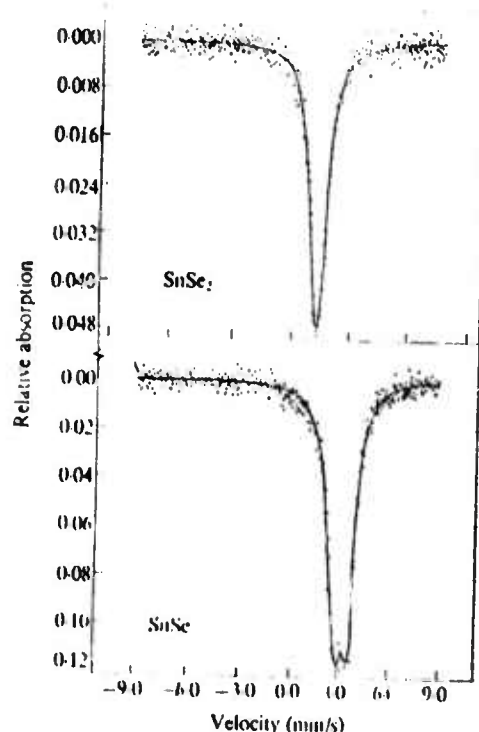
Temperature (K)	Composition (at %)	$\delta_1$ (mm/s)	$\delta_2$ (mm/s)	$\Delta_1$ (mm/s)	$\Delta_2$ (mm/s)
<b>Amorphous</b>					
77.3	2.5	$1.68 \pm 0.04$	—	$0.42 \pm 0.10$	—
77.3	5.0	$1.69 \pm 0.14$	—	$0.33 \pm 0.14$	—
77.3	8.0	$1.69 \pm 0.02$	—	$0.46 \pm 0.06$	—
298.0	10.0	$1.66 \pm 0.02$	$3.49 \pm 0.06$	$0.51 \pm 0.06$	$0.96 \pm 0.04$
77.3	10.0	$1.67 \pm 0.02$	$3.32 \pm 0.02$	$0.50 \pm 0.06$	$0.82 \pm 0.08$
4.2	10.0	$1.69 \pm 0.02$	$3.39 \pm 0.02$	$0.50 \pm 0.06$	$0.93 \pm 0.04$
			$3.43 \pm 0.02$	$0.50 \pm 0.06$	$0.96 \pm 0.04$
<b>Crystalline</b>					
298.0	10.0*	$\sim 1.62$	$3.27 \pm 0.02$	$\sim 0.50$	—
77.3	10.0*	$1.62 \pm 0.08$	$3.32 \pm 0.02$	$0.50 \pm 0.18$	$0.74 \pm 0.02$
298.0	$\text{SnSe}_2$	$1.33 \pm 0.02$	—	$\sim 0.0$	$0.78 \pm 0.02$
77.3	$\text{SnSe}_2$	$1.35 \pm 0.02$	—	$\sim 0.0$	—
298.0	$\text{SnSe}$	—	$3.28 \pm 0.02$	$\sim 0.0$	—
77.3	$\text{SnSe}$	—	$3.33 \pm 0.02$	—	$0.74 \pm 0.10$ $0.79 \pm 0.02$

\* Less than 6% of the area at 298K corresponds to SnIV. A small quantity of an unidentified third phase is observed at  $\delta \approx 0.53$  mm/s with  $\Delta \approx 0.99$  mm/s

fluctuations in composition would be expected to lead to a distribution of electric field gradient tensors and a line broadening which was dependent upon composition.<sup>(7)</sup> The near constancy of isomer shift, quadrupolar coupling, and line width are interpreted to mean that the Sn atom has a similar local environment for all compositions; i.e. a high degree of local order exists about the Sn sites and, further, the local

chemical order closely resembles that of  $\text{SnSe}$  and  $\text{SnSe}_2$  for SnII and SnIV atoms respectively. Moreover, the symmetrical, and only slightly broadened, lines for Sn in the glass indicate that the electronic structure of the Sn atom and the electric field gradient at the atoms are affected to only second order by the long-range disorder and composition change in the glasses. The long-range disorder in the amorphous systems leads to small, systematic differences in the isomer shift and quadrupolar coupling between amorphous and crystalline systems.

Debye temperatures, for  $\text{Sn}$  are estimated to be from the temperature dependence of the Mössbauer absorption  $\theta\mu \approx 145 \pm 10\text{K}$  in crystalline  $\text{SnSe}_2$ ,  $\theta\mu \approx 130 \pm 10\text{K}$  in crystalline  $\text{SnSe}$ ,  $\theta\mu \approx 100 \pm 10\text{K}$  in the  $\text{Sn-As-Se}$  glass SnIV and  $\theta\mu \approx 90 \pm 10\text{K}$  in SnII. Within the error of the measurement ( $\pm 10\text{K}$ ) the same Debye temperature fits the data from 4.2 to 77.3K and from 77.3 to 298K; it is, therefore, inferred that the glass-crystal transition takes place above room temperature.

**Figure 3.** The Mössbauer spectra of samples of crystalline  $\text{SnSe}_2$  and  $\text{SnSe}$  at 77.3K

## References

- Kolomiets, B. T. (1964). *Phys. stat. Solidi* 7, 359.
- Hilton, A. R., Jones, C. E. & Brau, M. (1966). *Physics Chem. Glasses* 7 (4), 105.
- Pearson, A. D., Northover, W. R., Dewald, J. F. & Peck, W. F. (1962). *Advances in glass technology*. Plenum Press, New York.
- Kolomiets, B. T. & Levedev, E. A. (1963). *Radiotekh. Electron.* 8, 209.
- Eaton, E. L. (1964). *J. Am. Ceram. Soc.* 47, 554.
- Ovshinky, S. R. (1968). *Phys. Rev. Lett.* 21, 1450.
- Shkolnikov, E. V. (1966). *Solid state chemistry*, p. 142. (Edited by E. V. Borisova). Consultants Bureau, New York.
- Borisova, Z. V., Vasilev, L. N., Seregin, P. P. & Shipatov, V. T. (1970). *Soviet Phys. Semiconductors* 4 (3), 4.3.
- Kolomiets, B. T., Goryanova, N. A. & Shilo, V. P. (1960). *Collection: The glassy state*. Izd. Akad. Nauk. SSSR, Moscow, p. 456.
- Preston, R. S., Lam, D. J., Nevitt, M. V., Van Osternburg, D. O. & Kimball, C. W. (1966). *Phys. Rev.* 149, 440.

MÖSSBAUER SPECTROSCOPY OF AMORPHOUS SEMICONDUCTORS AND  
GLASSES CONTAINING ANTIMONY, TIN, AND IRON: A REVIEW<sup>†</sup>

S.P. Taneja, C.W. Kimball and J.C. Shaffer

Department of Physics, Northern Illinois

University, DeKalb, Illinois

ABSTRACT

A comprehensive review is given of Mössbauer studies of bond character, electronic structure and glass-crystal transition in amorphous semiconductors and glasses containing antimony, tin and iron. The isomer shift is correlated with electron density (calculated from HFSCF) at the tin and antimony nuclei to delineate electronic structure in amorphous tin and antimony chalcogenides. The Debye temperature is computed for tin chalcogenides. Comprehensive data on Mössbauer parameters are presented along with an extensive bibliography.

I. INTRODUCTION

Mössbauer measurements have become a major tool for the investigation of the electronic properties of amorphous materials. In disordered systems distributions of isomer shift, quadrupolar coupling and hyperfine interaction occur. The line breadths and shapes reflect the dispersion of these distributions. Isomer shift and quadrupolar splittings are related to the valence state and coordination of the atom in the glass. The Mössbauer fraction yields the strength of the binding of the Mössbauer atom.

<sup>†</sup>Based on work performed under the auspices of an ARPA grant (ARO, Durham).



A brief discussion of current models of amorphous and glassy systems is given. A general review of recent Mössbauer work follows. A few typical studies are discussed in detail.

## II. GENERAL THEORIES OF STRUCTURE OF GLASSES

An understanding of the structure of glass is based on a knowledge of how a glass is formed. Normally on cooling a solution, crystals precipitate at a certain temperature, the liquidus temperature. For glass forming materials, when the temperature drops about 100°C below the liquidus temperature, the rate of growth of crystals becomes so small, due to increased viscosity of the melt, that the substance remains a liquid. As the temperature is decreased further, the viscosity increases so much that the non-crystalline structure is frozen in. The glass is characterized by its non-crystalline nature and a lack of any long range order.

According to the random network theory of Zachariasen(1), silica glass is formed of three dimensional random networks of alternate atoms of silicon and oxygen in long cross-linked chains. The random nature of these networks causes each atom to have a slightly different environment. Elements which can form such linked chains are called glass formers. This random network theory predicts that glass has a very open structure which is well suited for holding other elements called network modifiers. The crystalline theory of the structure of glass proposes that glass is made up of more or less deformed crystals bound together by regions with a low degree of order. This theory calls for marked deviations in chemical composition of the glass from point to point. A synthesis of both models is probably necessary to correctly describe some glasses. The random network implies that bonds are not all alike. Differences between bonds can account for the fact that glass does not have a fixed melting point, but rather there is a temperature range over which it becomes less viscous and finally becomes a regular liquid. Since the viscosity becomes very high as the temperature is lowered, strains and inhomogeneities are frozen in when the glass is quenched.

One of the important tools in studying glass structure

has been x-ray diffraction. X-ray patterns can be analyzed to give radial distribution curves which give the probability of finding a second atom at a given distance from the first. One difficulty with x-ray diffraction techniques is that x-rays are not very selective, since the radial distributions overlap in more complex systems.

### III. MÖSSBAUER EFFECT IN AMORPHOUS SEMICONDUCTORS AND GLASSES

Mössbauer spectroscopy has been recognized for some time as a useful technique for obtaining information about the structural behavior of antimony, tin and iron atoms in amorphous semiconductors and glasses. The first observation of the Mössbauer effect in glass was made by Pollak et. al.(2) who made a qualitative study of  $\text{Fe}^{57}$  in fused quartz and Pyrex glass. Subsequent work appeared on alkali silicate, iron metaphosphate, borate and phosphate glasses. An excellent review of this early Mössbauer work was published by Kurkjian(3). The present paper reviews the recent Mössbauer studies on amorphous semiconductors and glasses with antimony, tin and iron as components.

#### A. Antimony: Amorphous and Crystalline Chalcogenides

The VB-VIB (chalcogenide) semiconductors have become of substantial interest in recent years because of potential device applications(4,5). Optical and transport properties have been studied in both crystalline and amorphous phases. In crystalline form the semiconductors of composition  $(\text{VB})_2(\text{VIB})_3$  have been of greatest interest(6). The system  $(\text{VB})_x(\text{VIB})_y$  can exist over wide ranges of composition in particular cases in amorphous form. More complex amorphous materials may be obtained by the addition of elements from, e.g., columns IV and VII of the periodic table. Amorphous materials with Sb as the VB component may be studied by Mössbauer spectroscopy ( $\text{Sb}^{121}$ ) yielding structural information (e.g., stereochemical changes on the crystalline to amorphous transition) and valuable insight into the chemical bonding in these materials. The latter is particularly important since  $(\text{VB})_2(\text{VIB})_3$  compounds crystallize in a variety of complex crystal structures (see below) obviating, for the present, band structure calculations, and the pro-

Table I  
Mössbauer Results for Amorphous and Crystalline Antimony Compounds

Compound	Temp (°K)	I.S. ( $\delta$ )* (mm/sec)	Q.S. ( $\Delta$ ) (mm/sec)	Line Width ( $\Gamma$ ) (mm/sec)	Ref.
<u>OXIDES</u>					
Sb <sub>2</sub> O <sub>3</sub> (amorphous)	80	-11.35 $\pm$ 0.10	18.6 $\pm$ 1.0	3.60 $\pm$ .2	8
(crystalline)	80	-11.32 $\pm$ 0.12	18.3 $\pm$ 0.70	3.14 $\pm$ .10	8
$\alpha$ -Sb <sub>2</sub> O <sub>4</sub> (crystalline)	80	0.6 $\pm$ .03	-6.1 $\pm$ 1.0	3.31 $\pm$ .15	8
Sb <sub>2</sub> O <sub>4</sub> (crystalline)	80	-14.36 $\pm$ 0.06	16.4 $\pm$ 0.60	3.13 $\pm$ .14	8
		1.06 $\pm$ .02	-4.3 $\pm$ 1.1	3.49 $\pm$ .13	8
<u>SULFIDES</u>					
Sb <sub>2</sub> S <sub>3</sub> (amorphous)	80	-12.74 $\pm$ 0.17		5.22 $\pm$ .18	9
(crystalline)	80	-14.32 $\pm$ 0.11		4.31 $\pm$ .17	9
Sb <sub>2</sub> S <sub>5</sub>	80	-12.11 $\pm$ 0.09		5.27 $\pm$ .29	9
Sb <sub>2</sub> Se <sub>3</sub> (amorphous)	4.2	-13.6 <sup>†</sup>	10.9		10
(crystalline)	4.2	-12.6; -15.5 <sup>†</sup>	7.9; 8.4		10
Sb <sub>2</sub> Te <sub>3</sub> (crystalline)	80	-15.3 $\pm$ 0.20			11

\* Isomer shift relative to SnO<sub>2</sub> or BaSnO<sub>3</sub>.

† Isomer shift relative to CaSnO<sub>3</sub>.

properties of these materials must be interpreted with phenomenological models based upon the assumed chemical bonding and its systematic variation(7). Mössbauer studies have been made on  $\text{Sb}_2\text{O}_3$  in both crystalline and amorphous form by Long et. al.(8).  $\text{Sb}_2\text{S}_3$  has been investigated by Stevens and Bowen(9) both as a crystal and as an amorphous solid.  $\text{Sb}_2\text{Se}_3$  has been studied by Ruby et. al.(10) in both crystalline and amorphous form and, in addition, these investigators performed Mössbauer measurements on a series of  $\text{Sb}_x\text{Se}_y$  compositions in amorphous form.  $\text{Sb}_2\text{Te}_3$  has been investigated in its crystalline form by Birchall and Della Valle(11). The results of these investigations as well as those from work on associated compounds(8,9) are summarized in Table I.

Since the  $\text{Sb}_2\text{X}_3$  compounds and their amorphous forms are typical of VB-VIB materials, Mössbauer results can contribute to the elucidation of the chemical bonding and stereochemistry of these materials. With this in mind crystal structures of the  $\text{Sb}_2\text{X}_3$  compounds are briefly described in conjunction with Mössbauer results on both crystalline and amorphous samples.

$\text{Sb}_2\text{O}_3$  crystallizes in two polymorphs.  $\alpha\text{-Sb}_2\text{O}_3$  is a complex cubic structure with space group  $\text{Fd}\bar{3}\text{m}$  with 16  $\text{Sb}_2\text{O}_3$  units in the unit cell(12). As is seen in Table I, the isomer shift and quadrupolar coupling in the amorphous  $\text{Sb}_2\text{O}_3$  closely correlate to those in the cubic crystal. The orthorhombic-Pccn polymorph has also been investigated by Long et. al.(8) and has virtually identical isomer shift.

$\text{Sb}_2\text{S}_3$ , stibnite, crystallizes in a complex orthorhombic structure with space group  $\text{Pnma}$  with four  $\text{Sb}_2\text{S}_3$  units in the unit cell and two non-equivalent Sb sites(13). As is made clear by Stevens and Bowen(9), these two Sb sites were not resolved in their Mössbauer study (it should be noted that their crystalline materials were not precisely stoichiometric). On the crystalline to amorphous transition there is an apparent variation in the isomer shift but this is difficult to interpret, since the two-site spectrum was not resolved in the experiment on the crystalline material.

$\text{Sb}_2\text{Se}_3$  crystallizes in the same structure as  $\text{Sb}_2\text{S}_3$ (14) (with virtually identical lattice constants) and thus also has two non-equivalent Sb sites. Ruby et. al.(10) were

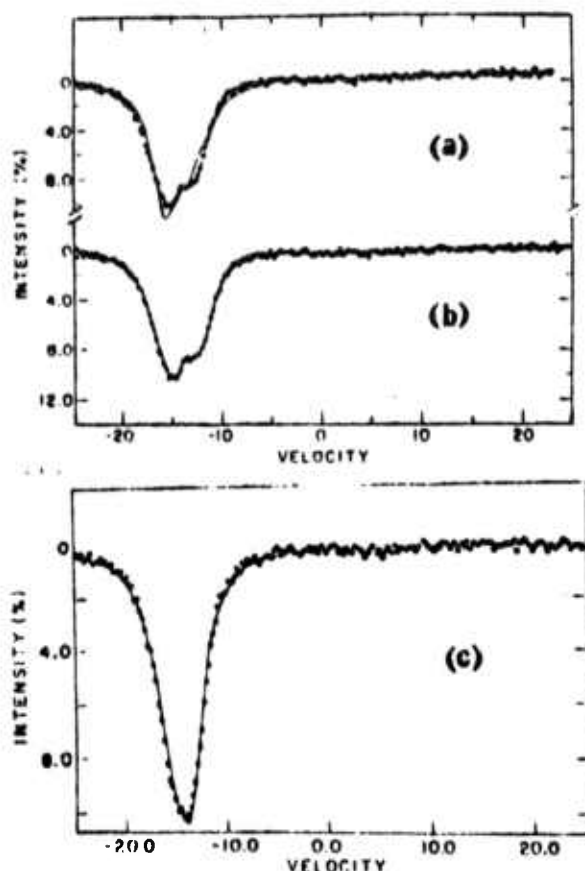


Figure 1. Spectrum from (a) crystalline  $\text{Sb}_2\text{Se}_3$  corresponds to a single site of Sb, (b) corresponds to two equally populated sites, (c)  $\text{SbSe}_{2.0}$  amorphous film fitted with single site. (From Ruby et. al.)<sup>18</sup>

able to resolve the contributions from these two different sites in both isomer shift and quadrupolar coupling. In comparing the results on the crystalline and amorphous materials (see Figure 1) these workers concluded that it was impossible to fit their amorphous spectrum with any two Sb-site model. Their result indicates a distribution of antimony sites in the amorphous material with nearly identical short range environment. Moreover, the Mössbauer parameters are close to the average of the crystalline parameters. The same workers found only small changes in

Mössbauer spectra with composition through a series of amorphous materials of the type  $\text{Sb}_x\text{Se}_y$ . Since the composition varied over a broad range they were unable to explain this insensitivity.

$\text{Sb}_2\text{Te}_3$  crystallizes in a trigonal (rhombohedral) structure of space group  $R\bar{3}m$  having a single antimony site in the unit cell(15). Its isomer shift as measured by Birchall and Della Valle(11) is larger than the mean isomer shift in  $\text{Sb}_2\text{Se}_3$ . As the material is difficult to prepare and maintain in the amorphous phase, no Mössbauer data, as yet, has been obtained on amorphous  $\text{Sb}_2\text{Te}_3$ .

Much speculation has been made about the chemical bonding in the chalcogenide semiconductors(7,13,14,16,17). Most of this has been based upon crystallographic structure in these materials and their optical properties. Kastner(18,19) following the classic work of Phillips(20) and Van Vechten(21) on the tetrahedral semiconductors, has interpreted the optical response of several chalcogenide semiconductors in terms of a simplified chemical bonding model. In this model the higher occupied electronic states are assigned to lone p-pair (L.P.) non-bonding orbitals on the chalcogen atoms while the bonding ( $\sigma$ ) orbitals form deeper valence states. The highest s electrons of both the group V and group VI atoms are well below the  $\sigma$  states in energy and may be regarded as core states. The conduction band is composed of the  $\sigma^*$ (anti-bonding) states associated with the  $\sigma$ (bonding) orbitals. The  $\sigma$ -orbitals are thought to be essentially p-type with little or no s-p hybridization occurring(22). In this picture the lone p-pairs are sensitive to the "ionicity" (electron transfer) in the material and, it is speculated(19), draw nearer to the  $\sigma$  bonding states as the ionicity increases. The optical measurements on the series  $\text{Sb}_2\text{X}_3$  ( $\text{X} = \text{O}, \text{S}$  and  $\text{Se}$ )(23,24,25) indicate decreasing ionicity as the chalcogen increases in atomic number. This is inferred from the qualitative trend of the main absorption bands in these materials to separate further (these bands arise from the  $\text{L.P.} \rightarrow \sigma^*$  and  $\sigma \rightarrow \sigma^*$  transitions) as the chalcogen varies from O to Se. The optical data for  $\text{Sb}_2\text{Te}_3$  suggests(26) that the chemical bonding in this compound is somewhat different from that of the other Sb chalcogenides. Based upon the measured isomer shifts of these materials, it is concluded that the charge density at the Sb nuclei increases in magnitude in the sequence O, S,

Se to Te in  $Sb_2X_3$ . One can estimate the p electron configuration of Sb on the basis of the Hartree-Fock calculations of Ruby et. al.(27). If one assumes that the deep-lying  $5s^2$  electrons remain unaffected, then the result of this procedure indicates increased  $Sb \rightarrow X$  electron transfer in the order O, S, Se and Te. This conclusion is contradictory to that from the optical data.

Upon the transition to the amorphous state only small differences in isomer shift are found between crystal and amorphous material. This tends to corroborate the insensitivity of the deep  $5s^2$  electrons to the details of the chemical bonding in these materials which is understood principally in terms of p-bonding without significant s-p hybridization(22). It should be emphasized that the chalcogenide semiconductors both as crystals and as glasses are in an early stage of understanding of their detailed structure. Much additional work on Mössbauer spectra and its comparisons with other measurements will be necessary in order to establish more precisely, the stereochemistry and electronic structure in these materials.

#### B. Tin: Amorphous Chalcogenide Semiconductors

The ternary system, Sn-As-Se has recently taken on technological significance with the discovery of switching effects and possible applications(28). The addition of group IV elements to the arsenic chalcogenides has been found to have significant effects on softening temperature, microhardness and electrical conductivity. These changes in the physical properties have been ascribed to the cross-linking of the chain-like structure by the group IV elements(29).

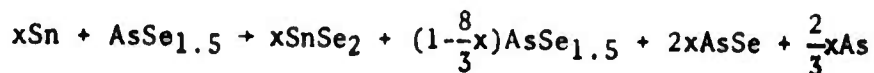
Mössbauer studies in the amorphous Sn-As-Se have been made by Borisova et. al.(30) and Taneja et. al.(31) at various concentrations and temperatures. The nature of the glass-crystal transition and the role of the group IV elements in the microchemistry of a switching glass have been studied. Mössbauer studies in this system have also been made by Vasil'ev et. al.(32) and Bartenev et. al.(33).

The effect of tin on the microhardness and conductivity of semiconducting  $As_2Se_3$  glasses had been studied by Shkol-

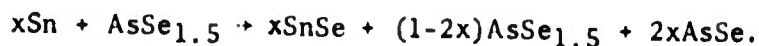


nikov(34). The hardness and conductivity change significantly after 5% Sn is added. Shkolnikov suggested that a chemistry in which  $\text{SnSe}_2$  occurs at low tin concentrations and  $\text{SnSe}$  at high concentrations may account for such behavior. Also, he found that air cooled and quenched Sn-As-Se glasses were almost equally amorphous. Borisova et. al.(30) have examined the  $\text{Sn}^{119}$  Mössbauer Effect in Sn-As-Se glasses formed by cooling in air and concluded that only Sn IV occurred in the glassy state but that the glass-crystal mixture exhibited both the Sn II and Sn IV absorption lines.

Figure 2a shows the Mössbauer spectra of Taneia et. al.(31) at liquid nitrogen temperature for amorphous samples containing 2.5%, 5.0% and 8% Sn. Figure 2b shows Mössbauer spectra of 10% Sn in amorphous and crystalline form(31). Tin occurs in only one phase at concentrations of 2.5 and 5.0%, but a second phase appears in the spectra of the samples containing 8.0 and 10.0% Sn. This result is consistent with the limit of solubility of tin (~7%) in the quenched glassy state set by Kolomiets et. al.(35). The reaction chemistry given by Shkolnikov(34) for low Sn concentrations is



and for higher tin concentrations



As the Sn concentration increases, the Sn atom changes its nominal valence from +4 to +2 and the free As combines with Se to give a further increase in the  $\text{AsSe}_{1.5}$  content. None of the suggested reactions contain any compound of tin with arsenic.

Crystalline  $\text{SnSe}_2$  is trigonal ( $\text{CdI}_2\text{-C}_6$  type) and all Sn atoms are in equivalent sites; crystalline  $\text{SnSe}$  is orthorhombic ( $\text{GeS-B}_{16}$  type) and all Sn atoms are in equivalent sites. A doublet is expected for both  $\text{SnSe}$  and  $\text{SnSe}_2$  (Figure 2c).

The spectra of amorphous samples of low concentrations of tin are similar to the spectrum of  $\text{SnSe}_2$  and at higher



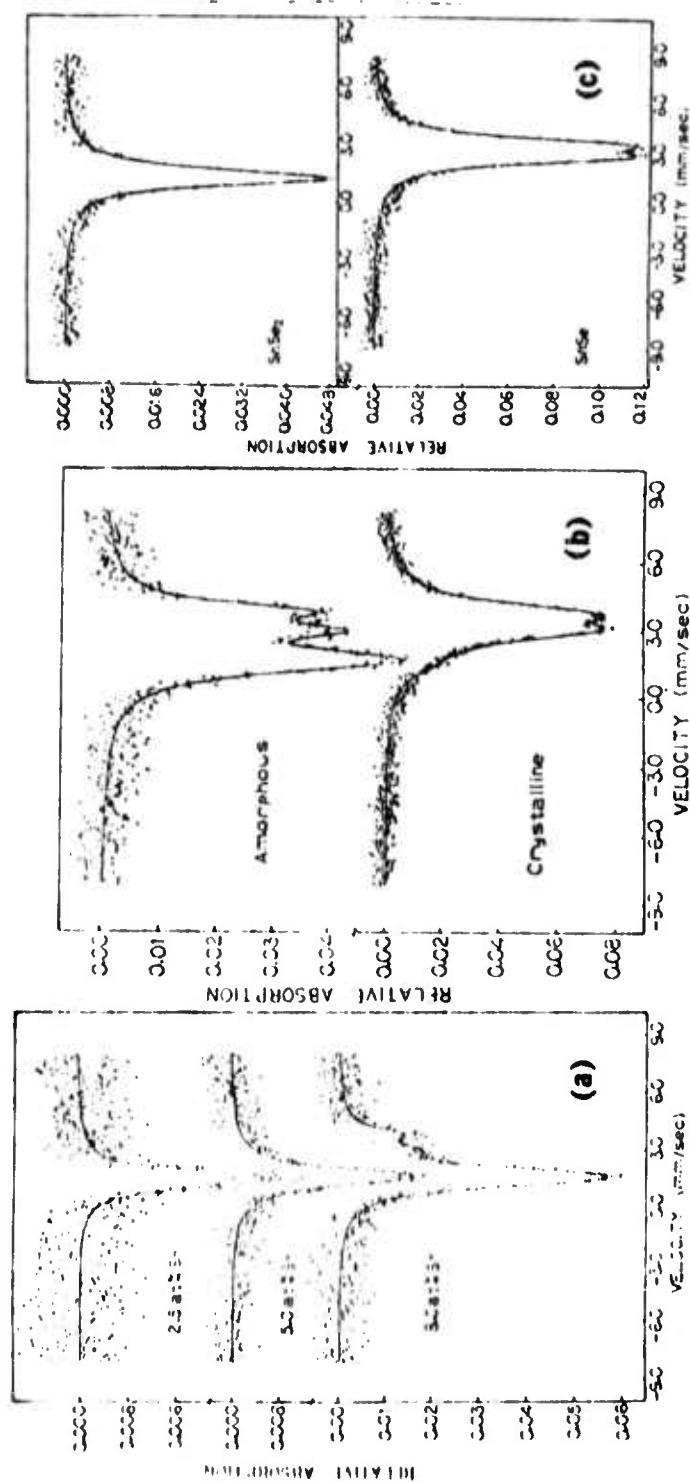


Figure 2. Mössbauer spectra of (a) amorphous samples containing 2.5%, 5% and 8% Sn (b) amorphous and crystalline samples containing 10% Sn (c) crystalline  $\text{SnSe}_2$  and  $\text{SnSe}$ , all at 77.3 K. (from Taneja et. al.)<sup>31</sup>



concentrations a spectrum characteristic of SnSe appears. The spectra shown are similar to those of Borisova et. al. (30) but the relative quantities of SnSe<sub>2</sub> and SnSe for similar concentrations of tin differ. Apparently, the chemical kinetics are dependent on the method of sample preparation in contrast with Shkolnikov's findings. The dominant phase in the crystalline samples is SnSe but this phase also appears in the amorphous samples. X-ray analysis shows no crystallinity for the 8% samples quenched to low temperatures, but the Mössbauer patterns show the presence of both SnSe and SnSe<sub>2</sub>.

The Mössbauer results are given in Table II. Within statistical error the quadrupolar coupling and line width ( $\Gamma \approx 0.9$  mm/sec) are independent of composition for both SnIV and SnII sites in the amorphous samples. The near constancy of isomer shift, quadrupolar coupling, and line width is interpreted to mean that the Sn atom has a similar local environment for all compositions; i.e., a high degree of local order exists about Sn sites and, further, the local chemical order closely resembles that of SnSe and SnSe<sub>2</sub> for SnII and SnIV atoms, respectively. Moreover, the symmetrical, and only slightly broadened, lines for Sn in the glass indicate that the electronic structure of the Sn atoms and the electric field gradient at the atoms are affected to only second order by the long-range disorder and composition change in the glasses. The long-range disorder in the amorphous system leads to small, systematic differences in the isomer shift and quadrupolar coupling between amorphous and crystalline systems.

From the temperature dependence of the Mössbauer absorption, Taneja et. al. (31) estimate the Debye temperature for Sn to be  $\theta_D \approx (145 \pm 10)$  K in crystalline SnSe<sub>2</sub>,  $\theta_D \approx (130 \pm 10)$  K in crystalline SnSe, and  $\theta_D \approx (100 \pm 10)$  K as SnIV and  $\theta_D \approx (90 \pm 10)$  K as SnII in Sn-As-Se glass. It is inferred from the temperature dependence of the  $\theta_D$  that the glass-crystal transition takes place above room temperature.

The Hartree-Fock calculations of Ruby et. al. (27) and measured isomer shift indicate that the electronic structure of SnIV in the above systems closely corresponds to that of  $\alpha$ -tin ( $sp^3$ ). SnII has a shift which is close to the tin halides, namely, between SnCl<sub>2</sub> and SnF<sub>2</sub>.

Table II

Results of the Analysis of Mössbauer Spectra of  $\text{Sn}_x(\text{As}_2\text{Se}_3)_{1-x}$ .  $\delta$  is the isomer shift relative to  $\text{BaSnO}_3$ .  $\Delta$  is the quadrupole splitting ( $-\frac{1}{2}e^2qQ$ ) (31)\*\*

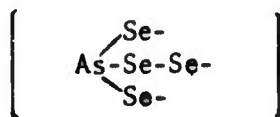
Temperature (°K)	Composition x (atomic %)	$\delta_1^+$ mm/sec	$\delta_2^+$ mm/sec	$A_1$ mm/sec	$A_2$ mm/sec
<u>Amorphous</u>					
77.3	2.5	$1.68 \pm .04$	-	$0.42 \pm .10$	-
77.3	5.0	$1.69 \pm .14$	-	$0.33 \pm .14$	-
77.3	8.0	$1.69 \pm .02$	$3.49 \pm .06$	$0.46 \pm .06$	$0.96 \pm .08$
298.0	10.0	$1.66 \pm .02$	$3.32 \pm .02$	$0.51 \pm .06$	$0.82 \pm .04$
77.3	10.0	$1.67 \pm .02$	$3.39 \pm .02$	$0.50 \pm .06$	$0.93 \pm .04$
4.2	10.0	$1.69 \pm .02$	$3.43 \pm .02$	$0.50 \pm .06$	$0.96 \pm .04$
<u>Crystalline</u>					
298.0	10.0*	$1.62$	$3.27 \pm .02$	$0.50$	$0.74 \pm .02$
77.3	10.0*	$1.62 \pm .08$	$3.32 \pm .02$	$0.50 \pm .18$	$0.78 \pm .02$
293.0	$\text{SnSe}_2$	$1.33 \pm .02$	-	$0.0$	-
-	$\text{SnSe}_2$	$1.35 \pm .02$	-	$0.0$	-
-	$\text{SnSe}$	-	$3.28 \pm .02$	-	$0.74 \pm .10$
77.3	$\text{SnSe}$	-	$3.33 \pm .02$	-	$0.79 \pm .02$

\* The subscripts 1 and 2 for  $\delta$  and  $A$  denote values corresponding to tin valencies of IV and II, respectively.

\*\* Less than 6% of the absorption at 298°K corresponds to  $\text{SnIV}$ . A small quantity of an unidentified third phase is observed at  $\delta = 0.53$  mm/sec with  $A = .99$  mm/sec.

From Taneja et al.

Vasil'ev et. al. (32) concluded from their Mössbauer studies that in case of the glass  $\text{AsSe}_{1.5}\text{Sn}_{0.3}$  (excess selenium), the structure of the glass network is mainly formed from structural  $\text{AsSe}_{3/2}$  units joined by selenium bridges



whereas in the case of glass with selenium deficit ( $\text{AsSe}_{0.95}\text{Sn}_{0.05}$ ) the structural units are  $\text{As}_2\text{Se}_{4/2}$  with As-As bonds,



Furthermore, the immediate environment of tin in glass is similar to that of  $\text{SnSe}_2$ , i.e., the Sn atoms form structural  $\text{SnSe}_{6/3}$  units in the glass.

#### C. Tin: Silicate, Borate and Phosphate Glasses

Mössbauer studies of alkali tin silicate and borate glasses have been made by several workers (36-40). Mössbauer spectra of glasses containing tin differ from the spectrum of  $\text{SnO}_2$  by a small chemical shift and slightly broader width (36). Mitrofanov and Sidarov (37) noted the absence of quadrupolar splitting in silicate glasses and only a small splitting in borate glasses. In alkali free glasses tin is present as  $\text{SnII}$  but in alkali glasses no  $\text{SnII}$  is found. Evestrop'ev et. al. (40) studied the alkali-tin-(silicate, borate, germanate and phosphate) glasses and measured the temperature dependence of Mössbauer fraction  $f$  for some of these glasses as well as the  $f$  dependence on the composition. Evestrop'ev et. al. (40) find that the temperature dependence of  $f$  for  $\text{SnO}_2$  fits well into the framework of the Debye model, whereas the  $f$  dependence for  $\text{NaO}_2\text{-SnO}_2\text{-SiO}_2$  glass is complex. They observed similar behavior in other silicate glasses and explained this behavior with a model in which tin containing glasses are formally considered as systems containing tin atoms as impurities.

Table III

## Mössbauer Parameters of Tin Containing Glasses(40)

Composition of Glass	$\delta^*$ (mm/sec)	$\Delta$ (mm/sec)
Na <sub>2</sub> O-SnO <sub>2</sub> -SiO <sub>2</sub>	-0.20 $\pm$ 0.05	0.40 $\pm$ 0.07
Na <sub>2</sub> O-SnO <sub>2</sub> -B <sub>2</sub> O <sub>3</sub>	-0.10 $\pm$ 0.05	0.60 $\pm$ 0.07
Na <sub>2</sub> O-SnO <sub>2</sub> -GeO <sub>2</sub>	-0.06 $\pm$ 0.05	0.50 $\pm$ 0.07
Na <sub>2</sub> O-SnO <sub>2</sub> -GeO <sub>2</sub> (crystal)	-0.10 $\pm$ 0.05	0.30 $\pm$ 0.07
Na <sub>2</sub> O-SnO-P <sub>2</sub> O <sub>5</sub>	3.60 $\pm$ 0.05	1.80 $\pm$ 0.07

\* I.S. relative to CaSnO<sub>3</sub>.

Table IV

Parameters of Mössbauer Spectra of Glasses  
Na<sub>2</sub>O-SnO<sub>2</sub>-SiO<sub>2</sub> Produced Under Reducing Conditions(40)

Composition of Glass	$\delta^*$ , SnII (mm/sec)	$\delta^*$ , SnIV (mm/sec)	$\Delta$ EQ (mm/sec)	SnII/ SnIV
13%-35%-52%	2.8 $\pm$ 0.05	-0.2 $\pm$ 0.05	1.75 $\pm$ 0.07	1.10
13%-5%-82%	2.8 $\pm$ 0.05	-0.2 $\pm$ 0.05	1.75 $\pm$ 0.07	0.85

\* I.S. relative to CaSnO<sub>3</sub>.

For silicate and borate glasses  $f$  was found to decrease with increasing  $\text{Na}_2\text{O}$  or  $\text{SnO}_2$  content. For germanate glasses  $f$  does not depend on the composition. Table III presents the data on the chemical shift and quadrupole splitting for glasses prepared under oxidizing conditions. The chemical shift for silicate, borate and germanate glasses corresponds to that of  $\text{SnIV}$ ; although the shift differs somewhat from that of  $\text{SnO}_2$ . The presence of only a small quadrupolar splitting in silicate, borate and germanate glasses is interpreted by these workers<sup>(40)</sup> to imply the existence of long-range order in these glasses. Tin occurs only as  $\text{SnII}$  in phosphate glasses. When the glass is formed under reducing conditions,  $\text{SnII}$  appears even in silicate glasses (Table IV) and the fraction of  $\text{SnII}$  increases with increasing Sn concentration in the glass. Evstrop'ev et. al. concluded that at sufficiently high concentrations of tin,  $\text{SnII}$  also appears in silicate glasses formed under oxidizing conditions. Thus the chemical equilibrium which exists in these glasses between  $\text{SnIV}$  and  $\text{SnII}$  is displaced toward  $\text{SnII}$  as the tin content is increased.

Bartenev et. al.<sup>(39)</sup> also studied the alkali-tin-silicate glasses. A negative chemical shift indicates an increase in the degree of ionicity of Sn-O bonds through the series of Li-Na-K glasses. The ionic character of the chemical bond increases in these glasses with an increase in cation radius of alkali metal. From the temperature dependence of  $f$  values it was concluded that the rigidity of the bonds decreases with increasing ionicity of the chemical bonds in alkali silicate glasses.

#### D. Iron: Amorphous Alloys

Mössbauer studies have been made to examine the nature of magnetism in amorphous alloys. Tsuei et. al.<sup>(41)</sup> and Bonder et. al.<sup>(42)</sup> have measured the magnetic hyperfine field as a function of temperature and composition in amorphous Fe-P-C.

The Mössbauer spectra of alloys at different phosphorus concentrations<sup>(42)</sup> are shown in Figure 3. The lines of the magnetic hyperfine pattern are found to be greatly broadened in the amorphous alloys relative to those in pure iron (Figure 3a). The broadening is attributed to disorder in the

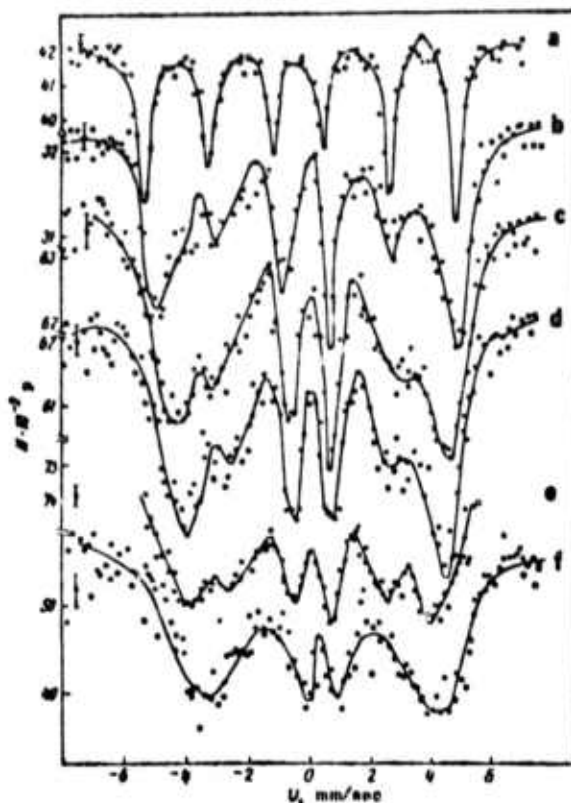


Figure 3. Mössbauer spectra of amorphous alloys of iron and phosphorus at 295 K. Phosphorus content: a - pure iron, b - 9.0, c - 12.4, d - 16.8, e - 19.6 and f - 24.4% (From Bonder et. al.)<sup>42</sup>.

neighbor shells about an Fe atom and to the spread in inter-atomic distance of these neighbors throughout the amorphous alloy.

The mean field at Fe nuclei diminishes linearly as the phosphorus concentration increases (see Figure 4a). The effective hyperfine field ( $H_{\text{eff}}$ ) is found to depend mainly on the nearest neighbor environment of Fe atoms. Bonder et. al.<sup>(42)</sup> explain the reduction in field and an increase in the shift with increasing concentration in terms of

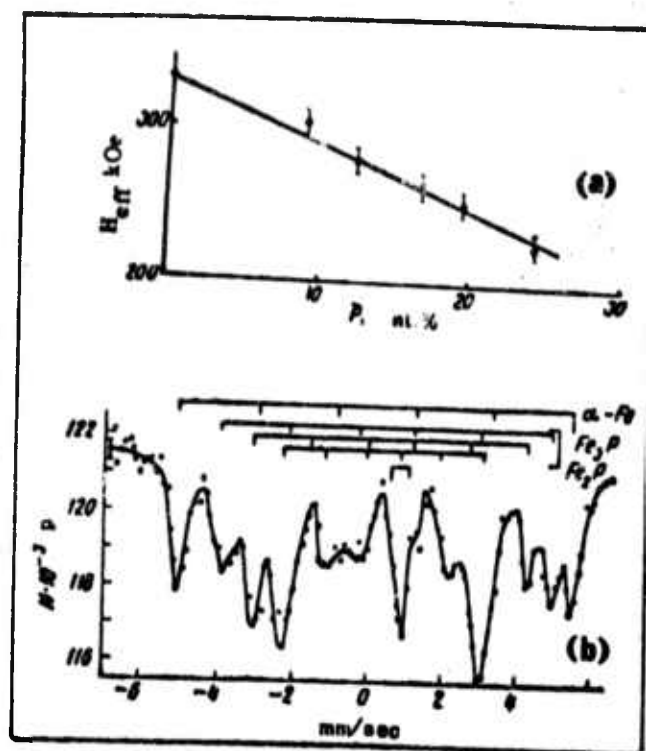


Figure 4. (a) Concentration dependence of the effective hyperfine splitting in iron-phosphorus alloy, (b) Mössbauer spectrum of alloy at 295 K with 19.6% P. (From Bonder et. al.)<sup>42</sup>

transfer of electrons from P and C atoms to the 3d band in Fe. The solubility of phosphorus in iron at room temperature is less than 1%. The amorphous alloys of iron-phosphorus are therefore metastable and, with annealing, transform into a mixture of crystalline phases. Figure 4b shows the Mössbauer spectrum of such a sample with 19.6% phosphorus, annealed at 673 K for one hour. The spectrum fits well to a combination of the absorption pattern of  $\alpha$ -iron,  $Fe_3P$  and  $Fe_2P$ .



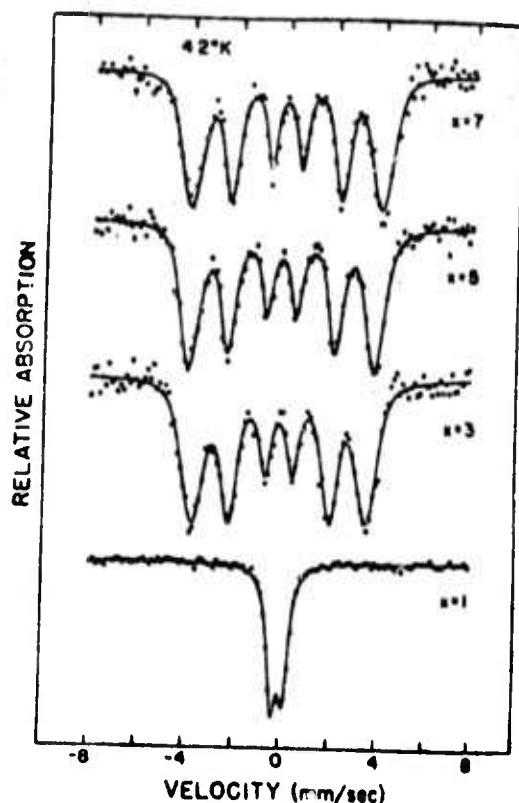


Figure 5. Mössbauer spectra of amorphous  $\text{Fe}_x\text{Pd}_{80-x}\text{Si}_{20}$  alloys at liquid helium temperature (From Sharon and Tsuei)<sup>43</sup>

Sharon and Tsuei<sup>(43)</sup> have made similar measurements on Fe-Pd-Si amorphous alloys at 4.2, 77 and 295 K with varying concentration of Fe and Pd. Above  $T_c$  the presence of many non-equivalent Fe positions in the random alloy give rise to a superposition of many isomer shifted quadrupolar patterns which result in an asymmetric total pattern.

Figure 5 shows the magnetic hyperfine patterns of amorphous Fe-Pd-Si alloys at 4.2 K. To a good approximation the electric quadrupole interaction has vanished in

these spectra. The fact that six peaks are clearly resolved and quite symmetric in shape suggests that the hyperfine field distribution is rather narrow and also symmetric about its average value. The data were fitted with a Gaussian distribution of fields:

$$P(H) = \frac{1}{\sqrt{2\pi\Delta_0^2}} \exp\left(-\frac{(H-H_0)^2}{2\Delta_0^2}\right)$$

where  $H_0$  and  $\Delta_0$  are average hyperfine field and standard deviation respectively. These values along with the line widths, average isomer shift and quadrupole splitting are listed in Table V.

Table V

Values of line width ( $\Gamma_1$ ,  $\Gamma_2$ ), quadrupole splitting ( $\Delta$ ) isomer shift ( $\delta$ ) hyperfine field ( $H_0$ ) and standard deviation ( $\Delta_0$ ) for amorphous Fe-Pd-Si alloys (From Sharon & Tsuei)<sup>43</sup>

Composition	$\Gamma_1^a$ (mm/sec)	$\Gamma_2^a$ (mm/sec)	$\Delta^a$ (mm/sec)	$\delta^a$ (mm/sec) <sup>†</sup>	$H_0^b$ (koe)	$\Delta_0^b$ (koe)
Fe <sub>1</sub> Pd <sub>79</sub> Si <sub>20</sub>	0.348	0.394	0.413	-0.095		
Fe <sub>3</sub> Pd <sub>77</sub> Si <sub>20</sub>	0.398	0.406	0.431	-0.088	226.5	18.8
Fe <sub>5</sub> Pd <sub>77</sub> Si <sub>20</sub>	0.447	0.471	0.466	-0.070	240.8	16.2
Fe <sub>7</sub> Pd <sub>73</sub> Si <sub>20</sub>	0.485	0.516	0.544	-0.047	248.3	20.6

a measurements at 295 K

b measurements at 4.2 K

<sup>†</sup> isomer shift relative to Co<sup>57</sup> in Cu

Sharon and Tsuei<sup>(43)</sup> proposed a model in which the Pd atoms play very little or no role in the magnetic ordering. In terms of a band picture, the Fermi level is high enough

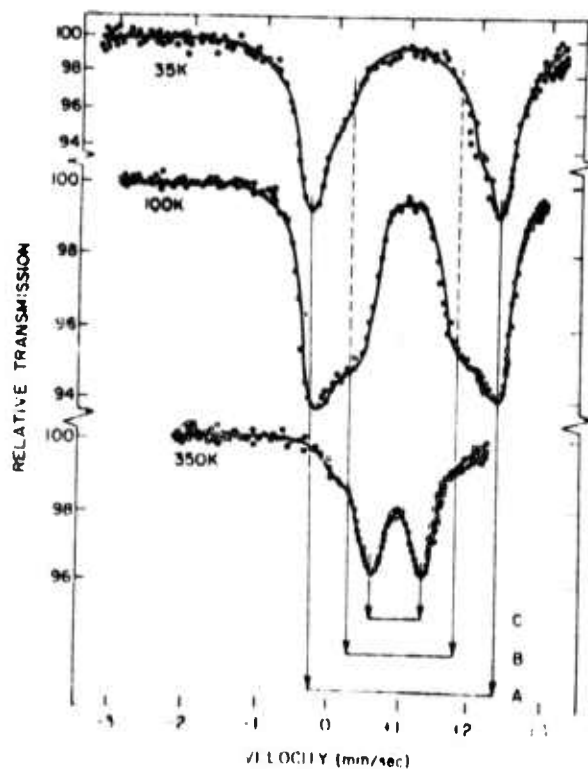


Figure 6. Mössbauer spectra of amorphous  $\text{FeCl}_2$  sample at 35, 100 and 350 K (From Boyle et. al.)<sup>44</sup>.

so that the states which arise from the 4d orbitals of Pd are completely filled; electron transfer from Si fills the d holes of Pd. The magnetic interaction between Fe atoms takes place via the conduction electrons and is locally ferromagnetic.

Boyle et. al.<sup>(44)</sup> have studied the temperature dependence of magnetic hyperfine field of amorphous  $\text{FeCl}_2$  to examine the sharpness of the magnetic transition. The Curie temperature is found to be 22 K. The quadrupolar splitting observed at 24 K is  $\sim 2.5$  times the value found in crystalline  $\text{FeCl}_2$ . At 8 K an average hf field of about

85 koe is present in addition to the quadrupole interaction found at 24 K. At 15 K the magnetic hf field is reduced to 45 koe.

Figure 6 shows the Mössbauer spectrum of an amorphous  $\text{FeCl}_2$  sample upon warming well above the critical temperature. Three distinctly different quadrupole spectra appear which are denoted by A, B and C. A pure quadrupole spectrum A (with  $e^2qQ = 5.3$  mm/sec) is observed immediately above  $T_c$ . At about 30 K, the spectrum B (with  $e^2qQ = 3.2$  mm/sec at 77 K) starts to grow in. Around 380 K the sample is largely converted into phase B, but at the same time phase C begins to appear. Conversion to C is achieved at about 400 K. The quadrupolar splitting of phase C ( $e^2qQ = 1.7$  mm/sec at 300 K) identifies this phase to be crystalline  $\text{FeCl}_2$ . Recooling to 8 K produces a spectrum which is typical of antiferromagnetic crystalline  $\text{FeCl}_2$ .

Boyle et. al. conclude that there exists a sharp magnetic transition in amorphous  $\text{FeCl}_2$ , that the amorphous system transforms to crystalline  $\text{FeCl}_2$  via an intermediate phase, and that the transformation is irreversible. Similar behavior was observed in other amorphous halides.

### E. Iron in Glasses

The behavior of iron in glasses has been discussed in detail by Kurkjian<sup>(3)</sup>. Consequently, only a brief discussion of later work will be given. As pointed out by Kurkjian, the structural picture of iron in glass is quite complicated. The Mössbauer results on iron silicate glasses<sup>(45)</sup>, iron borate glasses<sup>(46)</sup> and iron borosilicate glasses<sup>(47,48)</sup> have been compiled in Table VI.

Bukrey et. al.<sup>(46)</sup> made Mössbauer measurements to identify crystal formation in the iron-borate glass system containing up to 35 wt %  $\text{Fe}_2\text{O}_3$ . Figure 7 shows their Mössbauer absorption spectra of  $\text{Fe}^{3+}$  in paramagnetic  $\text{Na}_2\text{O-B}_2\text{O}_3\text{-Fe}_2\text{O}_3$  glass at room and liquid nitrogen temperatures. The spectra remain unchanged over the range 10-30 wt %  $\text{Fe}_2\text{O}_3$ . The main feature of the spectra of all these glasses was a resolved quadrupole doublet. Bukrey et. al. attributed the significant broadening in width to incomplete relaxation

Table VI  
Mössbauer Parameters for Some Complex Glasses

Composition	$\delta^*$ (mm/sec)	$\Delta$ (mm/sec)	$\Gamma$ (mm/sec)
Iron-Silicate- Glasses (with 7-15 wt% of $\text{Fe}_2\text{O}_3$ ) <sup>45</sup>	$\text{Fe}^{3+}$ $0.37 \pm 0.03$	$0.85 \pm 0.05$	0.75
	$\text{Fe}^{2+}$ $1.12 \pm 0.05$	$2.00 \pm 0.10$	
Iron-Borate- Glasses (with 10-30 wt% of $\text{Fe}_2\text{O}_3$ ) <sup>46</sup>	$\text{Fe}^{3+}$ $0.3 - 0.5^\dagger$	1.0	0.7
Iron-Boro- Silicate- Glasses (with 8 wt% $\text{Fe}_3\text{O}_4$ ) <sup>47</sup>	$\text{Fe}^{3+}$ $0.07 \pm 0.02^{**}$	$0.69 \pm 0.04$	$0.72 \pm 0.04$
	$\text{Fe}^{2+}$ $0.80 \pm 0.01$	$2.08 \pm 0.03$	$0.90 \pm 0.04$

\* I.S. relative to  $\text{Co}^{57}$  in Cr.

† Varies from liquid nitrogen to room temperature.

\*\* I.S. relative to  $\text{Co}^{57}$  in Cu, add .378 mm/sec to convert it relative to  $\text{Co}^{57}$  in Cr.

of the magnetic hyperfine field. It was shown that samples containing as high as 30 wt %  $\text{Fe}_2\text{O}_3$  can be prepared for which no hfs appeared. The appearance of hyperfine splitting was roughly correlated with the method of cooling the melt of the glass sample. Figure 8 shows a series of Mössbauer spectra for glass samples in the range of 30-35 wt %  $\text{Fe}_2\text{O}_3$  which exhibit hfs at room temperature. The order in which the spectra appear in Figure 8 is not according to increasing wt %  $\text{Fe}_2\text{O}_3$ , since hfs appearance was not simply dependent on the concentration but also on the method of preparation. The uppermost curve shows the quadrupole

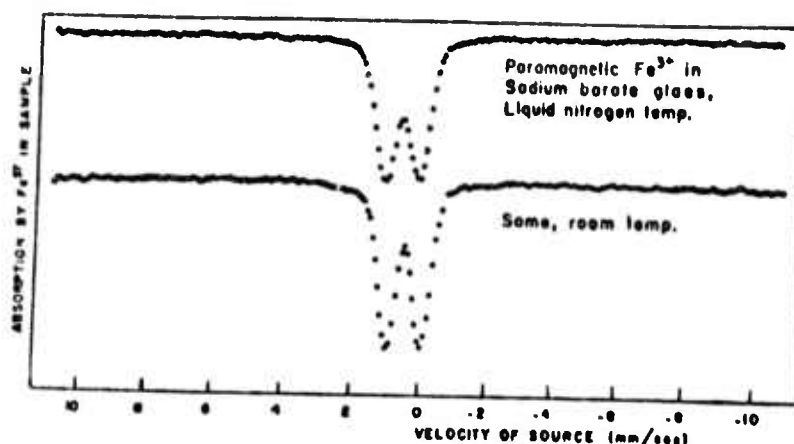


Figure 7. Mössbauer spectra of  $\text{Fe}^{3+}$  in  $\text{Na}_2\text{O}-\text{B}_2\text{O}_3$  glass at liquid nitrogen and room temperature (From Bukrey et. al.)<sup>46</sup>

split doublet due to iron in glassy material as well as a weak hfs pattern characteristic of  $\text{Fe}_2\text{O}_3$ . Bukrey<sup>(49)</sup> has recently pointed out that the spectrum attributed to  $\text{Fe}_2\text{B}$  in the complex spectrum shown in Figure 8(d), turns out to have a hyperfine field different from that of  $\text{Fe}_2\text{B}$  by about 20 koe. Therefore, the spectrum is not due to  $\text{Fe}_2\text{B}$  which is consistent with the x-ray analysis. Thus, he pointed out that the behavior of iron in this glass is far more complex than first imagined<sup>(46)</sup> since the "non- $\text{Fe}_2\text{B}$ " spectrum as well as 12 other lines in the data, remain unassigned to any known iron compounds. From the values of the isomer shift and quadrupole splitting, it was found that the iron ions in these borate glasses are in  $\text{Fe}^{3+}$  state in regions surrounded by 6-8 oxygens.

Taragin and Eisenstein<sup>(47,48)</sup> studied the borosilicate glasses. The Mössbauer spectrum for 8 at. %  $\text{Fe}_3\text{O}_4$  in borosilicate glass at room temperature is shown in Figure 9 and the corresponding Mössbauer parameters are listed in

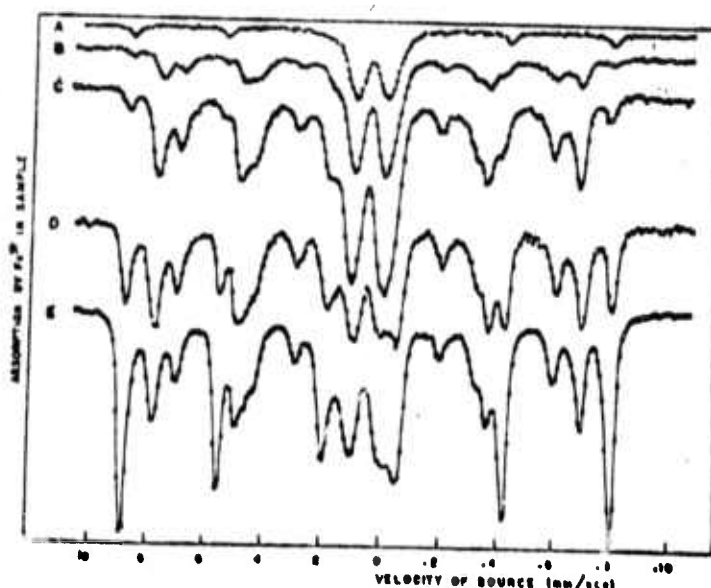


Figure 8. Mössbauer spectra of crystalline material in the glass samples. B and C contain 30 wt %  $\text{Fe}_2\text{O}_3$ ; A, D and E contain 35 wt. %  $\text{Fe}_2\text{O}_3$  (From Bukroy et. al.)<sup>46</sup>.

Table VI. Data at 80 K showed no significant difference from room temperature spectra. By comparing the isomer shift values with other iron containing glasses, it was found that both ferrous and ferric iron were present in borosilicate glasses. By correlating the data on isomer shift and quadrupole splitting with coordination number it was found that both  $\text{Fe}^{2+}$  and  $\text{Fe}^{3+}$  are in sites with predominantly tetrahedral symmetry. Taragin and Eisenstein concluded that ferric ions almost certainly replace  $\text{Si}^{4+}$  in  $\text{SiO}_4$  tetrahedra; i.e.,  $\text{Fe}^{3+}$  occurs as a glass former. Further, unusual broadening of the Mössbauer line probably arises from the presence of  $\text{Fe}^{2+}$  in diverse surroundings.

Finally, it is worthwhile to mention that a number of Mössbauer studies have been made on frozen aqueous solutions<sup>(50,52)</sup>. Recently, Ruby<sup>(53)</sup> has presented a short review on this subject. Mössbauer effect has also been

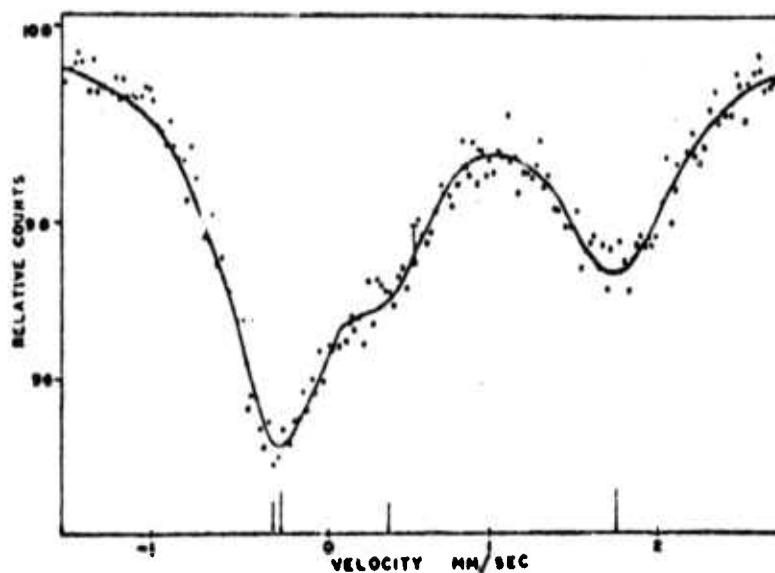


Figure 9. Mössbauer spectrum of Iron Borosilicate glass at room temperature (From Targin and Eisenstein)<sup>47</sup>

applied to the study of the glass-crystal transition in polymers<sup>(54)</sup> and methanol<sup>(55)</sup>.

#### IV. REFERENCES

1. W.H. Zachariasen, J. Amer. Chem. Soc. 54, 3841 (1932); J. Chem. Phys. 3, 162 (1935).
2. H. Pollak, M. De Coster and S. Amelinckx, in: Proc. Second International Conf. on the Mössbauer Effect, Saclay, 1961, Eds. D.M.J. Compton and A.H. Schoen (Wiley, New York, 1962) p. 298.
3. C.R. Kurkjian, J. Non-Cryst. Solids 3, 157 (1970).
4. Fundamentals of Amorphous Semiconductors, National Academy of Sciences, Washington, D.C. (1972).



5. Critical Reviews in Solid State Sciences, vol. 2, no. 3, Chemical Rubber Company, Cleveland, Ohio, editors; D.F. Schuele, and R.W. Hoffman (1971).
6. J. Black, E.M. Conwell, L. Seigle and W. Spencer, J. Phys. Chem. Solids, 2, 240 (1957).
7. E. Mooser and W.B. Pearson, J. Phys. Chem. Solids, 7, 65 (1958).
8. G.C. Long, J.G. Stevens and L.H. Bowen, Inorg. Nucl. Chem. Letters, 5, 799 (1969).
9. J.G. Stevens, L.H. Bowen, Mössbauer Effect Methodology, (Ed. I.J. Gruverman), Plenum Press, Vol. 5, 27 (1969).
10. S.L. Ruby, L. Gilbert and C. Wood, Physics Letters, 37A, 453 (1971).
11. T. Birchall and B. Della Valle, Chem. Comm. 675 (1970).
12. K.E. Almin and A. Westgren, Arkiv. Kemi. Min, Geol, 15B, 22 (1941-42).
13. S. Scavnicar, Z. fur. Krist. 114, 85 (1960).
14. N.W. Tideswell, F.H. Kruse and J.C. McCullough, Acta. Cryst. 10, 99 (1957).
15. J.R. Drabble and C.H. Goodman, J. Phys. Chem. Solids, 5, 142 (1958).
16. I.V. Batarunas, A.S. Karpus, A.I. Andryulus, and P.O. Balyulis, Chemical Bonds in Semiconductors and Solids, ed. W.N. Sirota, Trans. Consultants Bureau, New York, (1967) p. 199.
17. A.S. Karpus and I.V. Batarunas, Chemical Bonds in Semiconductors and Solids, ed. N.N. Sirota, Trans. Consultants Bureau, New York, (1967), p. 203.
18. M. Kastner, Phys. Rev. Letters, 28, 355 (1972).
19. M. Kastner, Phys. Rev. (in press).
20. J.C. Phillips, Rev. Mod. Phys. 49, 317 (1970).

21. J.A. Van Vechten, *Phys. Rev.* 182, 891 (1969).
22. V.I. Kruglov and T.M. Zimkina, *Sov. Phys.-Solid State*, 10, 170 (1968).
23. S.D. Shutov, V.V. Sobolev, Y.V. Popov, and S.N. Sheshtskii, *Phys. Stat. Sol.* 31, K23 (1969).
24. J.C. Shaffer, B. Van Pelt, C. Wood, J. Freeouf, K. Murase and J.W. Osmun, *Phys. Stat. Sol.* 54B, 571 (1972).
25. V.V. Sobolev, S.D. Shutov, Yu. V. Popov, and S.N. Sheshtskii, *Phys. Stat. Sol.* 30, 349 (1968).
26. C. Wood, B. Van Pelt and A. Dwight, *Phys. Stat. Sol.* 54B, 701 (1972).
27. S.L. Ruby, G.M. Kalvius, G.B. Beard, and R.E. Snyder, *Phys. Rev.* 159, 239 (1967).
28. A.D. Pearson, W.R. Northover, J.F. Dewalel, and W.F. Peck, *Advances in Glass Technology*, Plenum Press, New York, (1962).
29. B.T. Kolomiets, *Phys. Stat. Sol.* 7, 359 (1964).
30. Z.U. Borisova, L.N. Vasil'ev, P.P. Seregin and V.T. Shipatov, *Sov. Phys.-Semiconductors*, 4, 433 (1970).
31. S.P. Taneja, A.E. Dwight, L. Gilbert, W.C. Harper, C.W. Kimball and C. Wood, *Phys. Chem. Glass.* 13, 153 (1972).
32. L.N. Vasil'ev, P.P. Seregin and V.T. Shipatov, *Inorganic Materials*, 7, 1841 (1972).
33. G.M. Bartenev, A.D. Tsyganov, S.A. Dembovskii and V.I. Mikhailov, *J. of Structural Chem.* 12, 853 (1972).
34. L.V. Shkol'nikov, *Solid State Chemistry*, (edited by E.V. Borisova) Consultant Bureau, New York, 1966, p. 142.
35. B.T. Kolomiets, N.A. Goryanova and V.P. Shilo, *Collection: The Glassy State* Izd. Akad. Nauk, SSSR. Moscow, p. 456 (1960).

36. V.A. Bryukhanov, V.I. Goldanskii, N.N. Delyagin, L.A. Koryto, E.F. Makarov, I.P. Suzdalev and V.S. Shpinel, Soviet Physics-JETP, 16, 321, (1963).
37. K.P. Mitrofanov and T.A. Sidorov, Soviet Physics-Solid State, 9, 693 (1967).
38. I.P. Polozova and P.P. Seregin, Soviet Physics-Solid State, 10, 1196 (1969).
39. G.M. Bartenev, S.M. Brekhovskikh, A.Z. Varisov, L.M. Landa and A.D. Tsyganov, Soviet Physics-Solid State, 12, 972 (1970).
40. K.S. Evstrop'ev, V.G. Bezrodnyi, P.P. Seregin and V.T. Shipatov, Inorganic Materials, 6, 685 (1970).
41. C.C. Tsuei, G. Longworth and S.C.H. Lin, Phys. Rev. 170, 603 (1968).
42. V.V. Bonder, V.A. Povitskiy and YE.F. Makarov, Phys. Metals & Metallogr. 30, 166 (1972).
43. T.E. Sharon and C.C. Tsuei, Solid State Communications, 9, 1923 (1971).
44. A.J.F. Boyle, G.M. Kalvius, D.M. Gruen, J.R. Clifton and R.L. McBeth, J. Phys. (Paris) Colloq. 32 suppl. C1-224 (1971).
45. A.A. Belyustin, Yu. M. Ostanevich, A.M. Pisarevskii, S.B. Tomilov, U. Bai-Shi and L. Cher, Soviet Physics-Solid State, 7, 1163 (1965).
46. R.K. Bukrey, P.E. Kenealy, G.B. Beard and H.O. Ber, J. Appl. Phys. 40, 4289 (1969).
47. M.F. Taragin and J.C. Eisenstein, J. Non-Crystalline Solids, 3, 311 (1970).
48. M.F. Taragin, Ph.D. Thesis (1970) Univ. Microfilm.
49. R.R. Bukrey (private communication).
50. B. Brunot, U. Hauser, W. Neuwirth, and J. Bolz, Z. Physik, 249, 125 (1971).

51. B. Brunot, U. Hauser, W. Neuwirth, and J. Bolz, Z. Physik, 249, 134 (1971).
52. S.L. Ruby and I. Pelah, Mössbauer Effect Methodology (Ed. I.J. Gruverman), Plenum Press, Vol. 6, 21 (1970).
53. S.L. Ruby, Proc. on Application of Mössbauer Effect, (Plenum Press), Israel, August, 1972.
54. S. Reich and I. Michaeli, J. Chem. Phys. 56, 2350 (1972).
55. A. Simopoulos, H. Wickman, A. Kostikas and D. Petrides, Chem. Phys. Letters, 7, 615 (1970).

Talk presented at Ninth International Conference on Crystallography,  
Tokyo, Japan, August 1972.

XVI Crystal surfaces, surface reactions, thin film and epitaxy

XVI-7. MECHANISM OF CRYSTAL GROWTH IN THIN FILMS OF  
Sb<sub>x</sub>Se<sub>y</sub> CAUSED BY ELECTRON IRRADIATION. By H.  
Brigitte Krause, Physics Department, Northern Illinois  
University, DeKalb, Illinois, U. S. A.

Thin films of Sb<sub>x</sub>Se<sub>y</sub> ranging from Sb<sub>1</sub>Se<sub>3</sub> to Sb<sub>3.5</sub>Se<sub>3</sub> were investigated by electron spectroscopy and selected area electron diffraction. Most samples, originally amorphous, crystallized in the electron beam. Although size and shape of the resulting crystallites, ranging from thin fibers to well defined single crystal domains varied considerably, the diffraction patterns for all compositions indicated a perfect or defect Sb<sub>2</sub>S<sub>3</sub> structure. In some cases superlattices were observed. The composition of the reflecting crystallites, although not stoichiometric, differed from the specimen composition since some of the antimony segregated by diffusion. The crystallization occurred also at low temperatures, for instance, down to -125°C. The crystals formed at the various temperatures were stable only while in the electron beam. The mechanism of reversible and irreversible changes with the electron energy and with temperature will be discussed.

The author thanks Dr. Charles Wood and Mr. R. Mueller for supplying the thin films.